

*Modulation of conformational space and  
dynamics of unfolded outer membrane  
proteins by periplasmic chaperones*

**DISSERTATION**

**zur Erlangung des akademischen Grades**

**Doctor of Philosophy**

**(Ph.D.)**

vorgelegt

**dem Bereich Mathematik und Naturwissenschaften  
der Technischen Universität Dresden**

von

**Neharika Chamachi**

geboren am 18. März 1991 in Karnataka, Indien

Eingereicht am 19. November 2020 und verteidigt am 28. April 2021

Die Dissertation wurde in der Zeit von 11/2016 bis 11/2020 im B CUBE – Center for Molecular Bioengineering der Technischen Universität Dresden angefertigt.

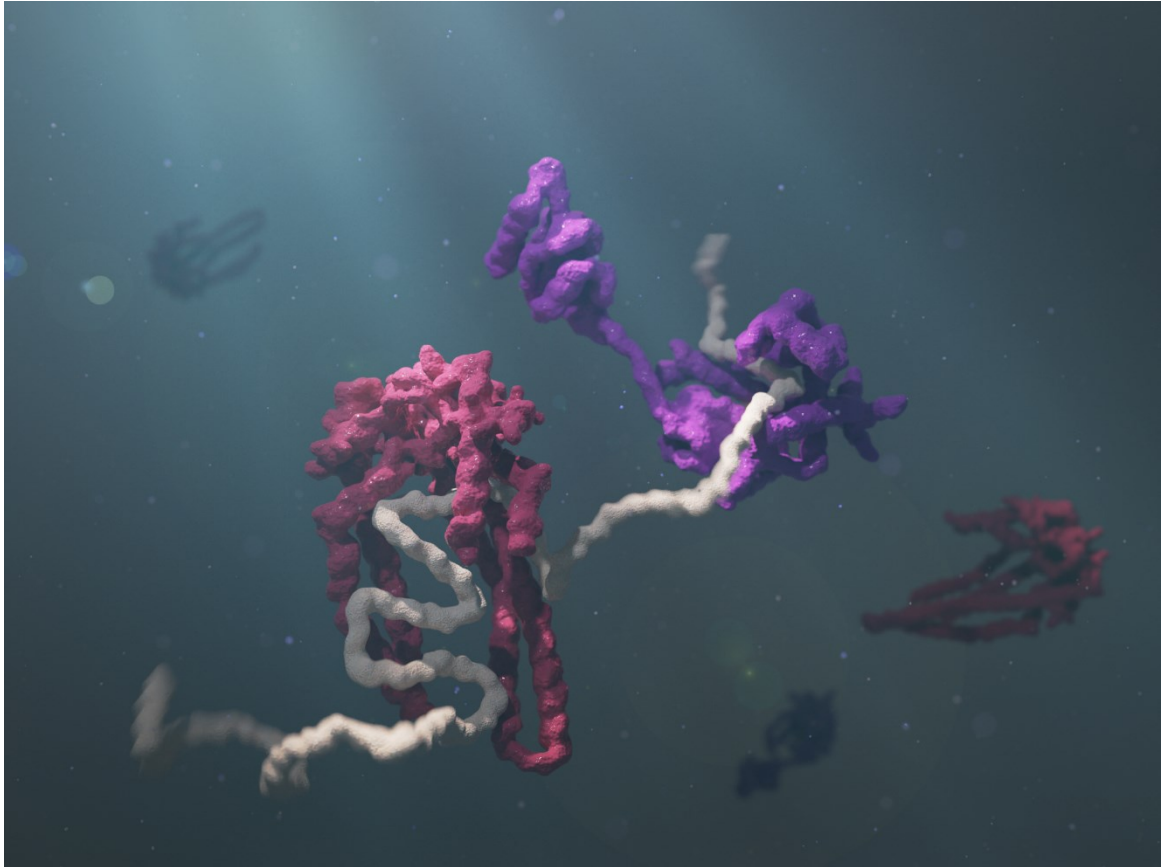
Gutachter: Prof. Dr. Michael Schlierf  
Prof. Dr. Karim Fahmy



‘...and later, lying on the deck of his boat gazing at the immense, starry sky, the tiny mouse Amos, a little speck of a living thing in the vast living universe, felt thoroughly akin to it all. Overwhelmed by the beauty and mystery of everything, he rolled over and over and right off the deck of his boat and into the sea.’

- From ‘Amos & Boris’ by William Steig





An illustration of outer membrane protein interaction with periplasmic chaperones.

- Designed by Dr. Andreas Hartmann.



# Summary

Beta-barrel outer membrane proteins (OMPs) present on the outer membrane of Gram-negative bacteria are vital to cell survival. Their biogenesis is a challenging process which is tightly regulated by protein-chaperone interactions at various stages. Upon secretion from the inner membrane, OMPs are solubilized by periplasmic chaperones seventeen kilodalton protein (Skp) and survival factor A (SurA) and maintained in a folding competent state until they reach the outer membrane. As periplasm has an energy deficient environment, thermodynamics plays an important role in fine tuning these chaperone-OMP interactions. Thus, a complete understanding of such associations necessitates an investigation into both structural and thermodynamic aspects of the underlying intercommunication. Yet, they have been difficult to discern because of the conformational heterogeneity of the bound substrates, fast chain dynamics and the aggregation prone nature of OMPs. This demands for use of single molecule spectroscopy techniques, specifically, single molecule Förster resonance energy transfer (smFRET).

In this thesis, upon leveraging the conformational and temporal resolution offered by smFRET, an exciting insight is obtained into the mechanistic and functional features of unfolded and Skp/SurA - bound states of two differently sized OMPs: OmpX (8  $\beta$ -strands) and outer membrane phospholipase A (OmpLA – 12  $\beta$ -strands). First, it was elucidated that the unfolded states of both the proteins exhibit slow interconversion within their sub-populations. Remarkably, upon complexing with chaperones, irrespective of the chosen OMP, the bound substrates expanded with localised chain reconfiguration on a sub-millisecond timescale. Yet, due to the different interaction mechanisms employed by Skp (encapsulation) and SurA (multivalent binding), their clients were found to be characterised by distinct conformational ensembles. Importantly, the extracted thermodynamic parameters of change in enthalpy and entropy exemplified the mechanistically dissimilar functionalities of the two chaperones. Furthermore, both Skp and SurA were found to be capable of disintegrating aggregated OMPs rather cooperatively, highlighting their multifaceted chaperone activity. This work is of significant fundamental value towards understanding the ubiquitous chaperone-protein interactions and opens up the possibility to design drugs targeting the chaperone-OMP complex itself, one step ahead of the OMP assembly on the outer membrane.





# Contents

List of Figures .....	11
List of Abbreviations .....	13
Chapter 1 Introduction.....	15
Chapter 2 Theoretical Background.....	19
2.1 Protein - chaperone interactions.....	20
2.2 Protein - chaperone interactions involved in outer membrane protein (OMP) biogenesis.....	28
2.3 Single molecule Förster resonance energy transfer (smFRET) to study OMP-chaperone interactions .....	40
Chapter 3 Optimisation of the labelling strategy for smFRET experiments .....	49
3.1 Refolded conformation of outer membrane phospholipase A (OmpLA) is sensitive to dimethyl sulfoxide .....	50
3.2 Labelling efficiencies are site-specific.....	53
3.3 Denaturing conditions significantly improve labelling.....	55
3.4 Summary .....	58
Chapter 4 Denatured OMP ensembles undergo slow structural interconversion.....	61
4.1 Denaturing a smaller OMP: 8 $\beta$ -stranded OmpX .....	62
4.2 Denaturing a bigger OMP: 12 $\beta$ -stranded OmpLA .....	69
4.3 Summary .....	75
Chapter 5 Expanded chaperone bound OmpX displays fast chain dynamics .....	77
5.1 OmpX expands on a timescale of hours in aqueous solution .....	78
5.2 Trimeric Seventeen kilodalton protein (Skp <sub>3</sub> ) and Survival factor A (SurA) bound OmpX is expanded and comprises of fast reconfiguring species .....	80
5.3 SurA interacts with OmpX at a relatively low entropic cost .....	86
5.4 Skp and SurA act as disaggregases under cellular stress.....	90
5.5 Summary .....	93
Chapter 6 Trimeric Skp pushes and pulls OmpLA.....	97
6.1 OmpLA exhibits a compact state in aqueous environment .....	98
6.2 OmpLA is partially encapsulated by Skp <sub>3</sub> and lacks distinct conformational change upon complexing with SurA.....	99

6.3	Skp <sub>3</sub> binds OmpLA with a relatively low entropic cost .....	104
6.4	Summary .....	108
Chapter 7 Conclusion and Outlook .....		111
Appendix 8.1 Fast inter-domain dynamics of SurA in solution .....		121
8.1.1	SurA shows quick distance fluctuations between its C-terminal and P1 domains in absence of its substrate .....	121
8.1.2	Distance between ends of C-terminal and P2 domains remain unchanged upon substrate binding .....	124
8.1.3	Summary .....	125
Appendix 8.2 Lifetime based filtering of DNA-origami coupled molecules. ....		127
8.2.1	Distinguishing differently labelled DNA origami by evaluating acceptor lifetime during smFRET experiments .....	128
8.2.2	Probing FRET efficiency of the origami coupled DNA rulers. ....	130
8.2.3	Conformational states of DNA hairpin are not perturbed upon coupling to DNA origami .....	132
8.2.4	Summary .....	135
Appendix 8.3 Materials and Methods.....		137
8.3.1	Site directed Mutagenesis .....	137
8.3.2	Expression, purification, refolding and labelling of OMPs .....	141
8.3.3	Expression, purification, refolding and labelling of chaperones .....	146
8.3.4	Derivation of correction factor, $\gamma$ .....	149
8.3.5	Probability density analysis (PDA) results of denaturant concentration range with OmpLA variants.....	149
8.3.6	Modelling the aqueous and chaperone bound OmpX state heterogeneity.....	151
8.3.7	Calculation of autocorrelation function .....	152
8.3.8	Sequence of DNA rulers and hairpin .....	154
8.3.9	Calculation of FRET-two-channel kernel-based density distribution (FRET- 2CDE) estimator .....	154
References.....		155
Acknowledgments.....		169
Declaration.....		171

# List of Figures

Figure 2-1 - Protein - chaperone interactions in bacteria.....	22
Figure 2-2 - Binding affinities of protein-chaperone interactions. ....	24
Figure 2-3 - Thermodynamics underlying protein-chaperone interactions .....	27
Figure 2-4 - Outer membrane protein (OMP) biogenesis.....	30
Figure 2-5 - OMPs .....	31
Figure 2-6 - Periplasmic Chaperones.....	33
Figure 2-7 - Open questions addressed in this thesis.....	39
Figure 2-8 - Förster Resonance Energy Transfer (FRET) theory .....	41
Figure 2-9 - Schematic of the custom built multiparameter fluorescence detection (MFD) setup .....	42
Figure 2-10 - Single molecule FRET (smFRET) data.....	43
Figure 2-11 - Time-Correlated Single Photon Counting (TCSPC) .....	45
Figure 2-12 - Fluorescence correlation spectroscopy (FCS) .....	47
Figure 3-1 - Labelling Assays.....	51
Figure 3-2 - Labelling efficiencies of different outer membrane phospholipase A (OmpLA) variants.....	54
Figure 3-3 - Effects of dyes and labelling under denaturing conditions.....	56
Figure 4-1 - Unfolding OmpX <sub>1,149</sub> .....	63
Figure 4-2 - Slow interconversion among denatured OmpX conformations.....	67
Figure 4-3 - Stability of different OmpLA segments against denaturation. ....	72
Figure 4-4 - Slow interconversion between unfolded conformational states of OmpLA. .	74
Figure 5-1 - OmpX expands in an aqueous chaperone free environment while undergoing reconfiguration on sub-millisecond timescale .....	79
Figure 5-2 - FRET efficiency histograms of trimeric seventeen kilodalton protein (Skp <sub>3</sub> ) and Survival factor A (SurA) bound OmpX <sub>1,149</sub> .....	82
Figure 5-3 - Trend of chaperone complexed FRET states.....	83
Figure 5-4 – Fast chain reconfiguration among the chaperone bound states of OmpX ....	85
Figure 5-5 - Interaction between SurA and OmpX is characterised by a relatively lower entropic change .....	88
Figure 5.6 - The disaggregating property of Skp and SurA.....	92

Figure 5-7 - Summary of chaperone-OmpX interactions .....	94
Figure 6-1 - Compact conformation of unbound OmpLA.....	98
Figure 6-2 – Skp <sub>3</sub> binds to and expands specific regions of OmpLA.....	101
Figure 6-3 - OmpLA lacks distinguishable conformational change upon complexing with SurA .....	103
Figure 6-4 - Series of FRET measurements performed with OmpLA <sub>64,187</sub> and incremental Skp <sub>3</sub> concentration .....	105
Figure 6-5 - Skp <sub>3</sub> interacts with OmpLA at a relatively low entropic cost.....	107
Figure 6-6 - Frustrated regions of OmpLA are located close to its N-terminus.....	109
Figure 7-1 - Slow interconversion among the heterogeneous unfolded OMP states.....	113
Figure 7-2 - A structural and thermodynamic perspective of OMP - chaperone interactions in the periplasm.....	116
Figure 8.1-1 – Fast translational dynamics between the domains of SurA .....	122
Figure 8.1-2 - C-terminal and P2 domains of SurA lack change in distance upon addition of the substrate OMPs.....	124
Figure 8.2-1 - Differently labelled DNA origami are identified by using two acceptor fluorophores with distinguishable lifetimes.....	129
Figure 8.2-2 - Origami coupled rulers are distinguished from the uncoupled molecules by acceptor lifetime filtering.....	131
Figure 8.2-3 - Resolution of DNA hairpin dynamics can be achieved by coupling it to the origami .....	133
Figure 8.3-1 - OMP expression and purification .....	143
Figure 8.3-2 - OmpX <sub>1,149</sub> and OmpLA <sub>13,125</sub> (refolded and denatured) labelling.....	145
Figure 8.3-3 - Expression and purification of periplasmic chaperones Skp and SurA....	148
Figure 8.3-4 - Scheme employed for extraction of center positions of unbound, Skp <sub>3</sub> and SurA bound states of OmpX.....	151
Figure 8.3-5 - FCS results of aqueous, chaperone bound and aggregated OmpX.....	153

# List of Abbreviations

2CDE	two-channel kernel-based density distribution estimator
AB	antibunching (subscript)
ALEX	alternating laser excitation
APD	avalanche photodiode
ATP	adenosine triphosphate
BAM	$\beta$ -barrel assembly machinery
CD	circular Dichroism
DMSO	dimethyl sulfoxide
DNA	deoxyribonucleic acid
<i>E. coli</i>	<i>Escherichia coli</i>
EDTA	ethylenediaminetetraacetic acid
FCS	fluorescence correlation spectroscopy
FRET	Förster resonance energy transfer
GdmCl	guanidinium chloride
Hsp	heat shock protein
IPTG	isopropyl $\beta$ -D-1-thiogalactopyranoside
LDAO	lauryl dimethylamine N-oxide
LPS	lipopolysaccharide
MFD	multiparameter fluorescence detection
NMR	nuclear magnetic resonance
nsFCS	nanosecond FCS
OMP	outer membrane protein
OmpLA	outer membrane phospholipase A
P1	peptidyl-prolyl cis-trans isomerase domain 1
P2	peptidyl-prolyl cis-trans isomerase domain 2
PBS	polarising beam splitter
PDA	probability distribution analysis
PIE	pulsed-interleaved excitation
POTRA	polypeptide-transport-associated
PPiase	peptidyl-prolyl cis-trans isomerase

## List of Abbreviations

---

RASP	recurrence analysis of single particles
SDS-PAGE	sodium dodecyl sulphate–polyacrylamide gel electrophoresis
SEC	size exclusion chromatography
Skp	seventeen kilodalton protein
Skp <sub>3</sub>	Trimeric Skp
smFRET	single molecule FRET
SurA	survival factor A
TCSPC	time-correlated single photon counting
TF	trigger factor
TRIS	tris(hydroxymethyl)aminomethane
uOMP	unfolded OMP
WT	wild-type

# Chapter 1 Introduction

Cellular machinery functions by establishing several prudent interactions between cytosolic, periplasmic and membrane proteins. A fracture in any of these labyrinthine pathways could result in misfolding and aggregation of proteins disrupting the entire cellular architecture (1, 2). For this purpose, cells employ ubiquitous biomolecules called as chaperones that maintain protein homeostasis and prevent cell destruction by interacting with nascent polypeptides. They act as active or passive catalysts during protein folding and can even rescue stress induced protein aggregates (3–6). For example, Trigger factors (TF) and Heat shock proteins like Hsp70s bind to newly synthesized polypeptides co-translationally and protect them from aggregation resulting from close proximity of frustrated domains on these nascent chains (7–9). When required, they also guide them to subsequent chaperone systems like the cylindrical chaperonin complexes which provide compartments in which they can fold into a functional form (10, 11). Some chaperones like protein-export protein SecB in the cytoplasm (12, 13) and seventeen kilodalton protein (Skp) and survival factor A (SurA) in the periplasm of Gram negative bacteria (14) exhibit anti-folding activity and sequester their substrates in a folding competent state until they reach their target cellular compartments.

Intriguingly, only a meagre collection of chaperones is available to assist plentiful nascent polypeptides through a complicated protein folding landscape in either an ATP-dependent or an ATP-independent manner (15). Therefore, a complete understanding of chaperone-protein interactions requires that we not only study the structural aspects but also the biophysics underlying such intercommunication. For instance, a difference in recognition and binding mechanisms is often observed to correspond to two divergent interaction modes. While some chaperones interact with a client protein in a conformationally specific manner, some accommodate them in a structural ensemble by numerous transient non-specific interactions thereby maintaining them in a folding competent state (16–18). In energetic terms, this translates into interaction energy landscapes dominated either by an entropic or an enthalpic change upon binding.

One striking example of structurally and thermodynamically modulated protein-chaperone associations can be found in Gram-negative bacteria, mitochondria and chloroplasts which

possess a range of proteins called as outer membrane proteins (OMPs) on the outer membrane of the cell envelope. OMPs are amphipathic  $\beta$ -barrel proteins which maintain the cell viability by functioning as porins, lipases, ion channels or receptors while others play an important role in pathogenesis (19, 20). Interestingly, their biogenesis involves a well-regulated network of protein-protein interactions. Upon translocation from the inner membrane, chaperones in the periplasm assist the freshly secreted OMPs in an ATP-independent manner from the inner membrane to their destination, i.e. the outer membrane (14, 21–23). They protect the unfolded hydrophobic chains from misfolding and aggregation in the aqueous periplasm (24–27) and maintain them in a state capable of being handed over to the upstream folding machinery, thus playing a crucial role in OMP biogenesis. Skp, SurA, the serine protease DegP and FkpB binding protein A (FkpA) compose such a set of chiefly investigated chaperones found in the periplasm of Gram-negative bacteria. Among these, SurA and/or Skp have been established as the major chaperones in the biogenesis process as their absence induces envelope stress response (27–30). On approaching the outer membrane, the insertion and folding of OMPs is facilitated by the beta-barrel assembly machinery (BAM), a multi-protein complex (31, 32). Although a broad understanding of the OMP assembly pathway exists, the fundamental conformational and biophysical details governing the chaperone-OMP interactions remains unclear. Hence, a particular interest for this thesis has been to investigate the SurA - OMP and Skp - OMP interactions to the molecular detail.

Separate previous studies have demonstrated that the chaperone bound OMPs are either elongated or globular depending on the chaperone or OMP under consideration (16, 33–36). The fast conformational interconversion of the proteins observed in some of these investigations was then speculated to result in a low entropic change of binding thus fine tuning the thermodynamics of these interactions in the energy deficient periplasm (37). Despite these important insights and given the differential mechanism of their interaction with substrates, little is clear about the diversity in the conformational space and reconfiguration dynamics of the Skp and SurA bound OMP chain. Additionally, the change of enthalpy and entropy governing the affinity of periplasmic chaperones towards their substrates remain undescribed. Therefore, in this thesis, a comprehensive examination of the unbound, Skp and SurA bound state of OMPs is executed from conformational, temporal and energetic perspective. In order to achieve an impression of OMP-chaperone



interaction in the cellular context, two differently sized OMPs have been probed: OmpX (8  $\beta$ -strands) (38) and OmpLA (12  $\beta$ -strands) (39). Since OMPs are maintained in an unfolded form for extended periods of time, the denatured states of OMPs are also examined to obtain a broader perspective over the whole OMP biogenesis process. Finally, an interesting insight is gained into the action of these chaperones upon OmpX aggregates, as recent modelling studies have suggested a synergistic interaction amongst these chaperones especially under stress conditions (24, 40).

Single molecule spectroscopy is a powerful technique to resolve the heterogeneity and dynamics of the diverse conformations adopted by the chaperone bound OMPs. It also avoids oligomerization of the aggregation prone OMPs due to picomolar concentrations of the probed samples. On that account, this work uses single molecule Förster Resonance Energy Transfer (smFRET) (41–44) and Fluorescence Correlation Spectroscopy (FCS) (45, 46) to discern the intricate mechanistic details governing chaperone-OMP interactions. Fluorescence from freely diffusing double fluorophore labelled molecules was recorded on a custom-built confocal microscope setup to enable smFRET experiments with time-correlated single photon counting (TCSPC) and fluorescence anisotropy measurements (47). Such a multiparameter fluorescence detection (MFD) allowed for a thorough investigation of both the conformational and thermodynamic information intrinsic to the chaperone-OMP associations.

This study is an important step towards a better understanding of the chaperone-OMP interactions. In addition to its contribution to the growing fundamental interest in this field, it provides us with the scope to design drugs targeting the chaperone-OMP complex (48–50), a strategy aided by the rather porous nature of the bacterial outer membrane.



## Chapter 2 Theoretical Background

Interaction between proteins compose virtually every other step of the day-to-day business of cells, from folding of protein molecules themselves to the process of enzymatic catalysis, signalling and proteolysis (4, 6). Protein-chaperone interactions compose one such set of elusive protein-protein interactions. Although often unspecific, chaperones are selective and highly efficient in either actively or passively guiding their client proteins through the complex protein folding energy landscape to their native functional state (3, 4, 51). Such a process appears to be even more challenging during OMP biogenesis in outer membranes of Gram-negative bacteria, mitochondria and chloroplasts. Here, the periplasmic chaperones hold on to their client proteins: the OMPs in a folding-competent state until the latter reach the outer membrane (14).

This chapter begins with a theoretical background of protein-chaperone interactions and the forces governing them. Next, OMP biogenesis and the two important components of this work: OMPs and periplasmic chaperones: Skp and SurA are presented in greater detail. Section 2.2.4 provides an overview of the much-debated topic of chaperone-OMP interactions, along with raising the open questions this thesis aims to address. This work relies on the information obtained through smFRET and FCS experiments and the last subsection offers a brief account of these techniques and the setup used to perform them.

## 2.1 Protein - chaperone interactions

Chaperones are proteins that assist other proteins in their folding process. They either provide a platform for polypeptides to fold into their tertiary structure or maintain them in a folding competent state until they reach the location where they can be folded into a functional form (5, 52). Naturally, their expression is upregulated during cellular stress in order to maintain the integrity of cellular proteome (1, 51). It is intriguing that most chaperones bind to their substrates promiscuously and yet are known to have different mechanisms of interaction depending on the client in consideration. Thus, the molecular details of how chaperones assist protein folding have been a remarkably debatable topic.

### 2.1.1 Mechanisms of protein - chaperone interactions

The following intriguing chaperone-protein interaction mechanisms (Figure 2-1) have been discovered during the past years:

*First interaction partners use hydrophobic and electrostatic forces:* Chaperones like Trigger Factor (TF) of bacterial origin (53) and Ribosome-associated complex (RAC) (54) and nascent-chain-associated complex (NAC) (55) of eukaryotic origin are the first set of chaperones meeting a newly synthesized polypeptide (56, 57). They bind to the basic and aromatic acid rich segments of nascent chains with their hydrophobic cradle and prevent co-translational misfolding in the cytoplasm by delaying chain compaction (53). Functioning in an ATP-independent manner, TF forms multiple but transient interactions and prevents polypeptides from getting trapped in unproductive folding intermediates (58). Often for smaller proteins, burial of hydrophobic residues in the TF cradle results in the folding of proteins, preceded or followed by its release. However, larger proteins need subsequent interactions with other chaperones for assistance with folding (9). Interestingly, TF has a structure similar to SurA and is proposed to function in an analogous manner (52).

*Heterogeneous unfolded states are maintained by transient interactions:* Hsp70-Hsp40 (in eukaryotes) or DnaK-DnaJ (in prokaryotes) are the next set of co-chaperones that a nascent polypeptide might encounter (59). Unlike TF, they function in an ATP-dependent manner and bind to hydrophobic patches composed of typically 5 to 7 residues exposed by nascent chains (8). To this end, the Hsp70 binding motifs have hydrophobic residues often flanked

by basic residues resulting in not just hydrophobic but also electrostatic interactions between the chaperone and the client proteins (60). Although, the bound substrates are found in heterogeneous unfolded conformations, the chaperone is also shown to bind both extended and later stage folding intermediates (61). They reshape the energy landscape by specifically disrupting formation of tertiary structures while local structure formation is still possible (62). Multiple monomers of these chaperones facilitate folding of proteins by expansion and step-wise release (63, 64).

*Nanocages provide a confined environment for protein folding:* Chaperonins (GroEL in bacteria and chaperonin-containing T-complex (TRiC) in eukaryotes) are nanocages that are next in line when interacting with polypeptides (10, 65). The apical domain of GroEL has hydrophobic patches which leads to several simultaneous hydrophobic interactions (66). Once the client binds, ATP binding and hydrolysis results in sequential unbinding of hydrophobic patches of client protein. This results in release of the client protein into chamber of the chaperonin accompanied by closing of the chamber by GroES. The relatively slow ATP hydrolysis provides ample time for the client protein to undergo folding (67, 68). Different studies appear to show different modes of chaperonin-client interaction (69, 70). While some studies have shown that GroEL is involved only passively in protein folding of some clients by confining the substrates (71), others have shown a more active involvement (72). Yet another study suggests that the client protein binds and releases from the chaperone iteratively resulting in substrate unfolding. Such a mechanism appears to be especially useful for proteins trapped in misfolded states and for bigger proteins which cannot fit in the cage (73).

*Folding when bound to chaperones; recognition of frustrated regions:* Some chaperones like Spy along with the ones mentioned previously can even mediate folding of client proteins while still bound to them (5). For this purpose, Spy makes the first contact with its client proteins by forming long range electrostatic interactions. Next, using its amphiphilic binding surface, it makes both electrostatic and hydrophobic interactions with its client proteins along its frustrated regions and protects it from aggregation. The client explores many conformational states in its bound state and undergoes chain compaction. Once the hydrophobic core is formed, the client's release is triggered by weaker affinity between the two proteins (74, 75). It is important to note here that recognition of frustrated regions seems to be a characteristic of not just these but many other chaperone-protein interactions.

These regions act as unspecific and unstable recognition motifs which allow the substrates to adopt different conformations when still bound to the chaperone.

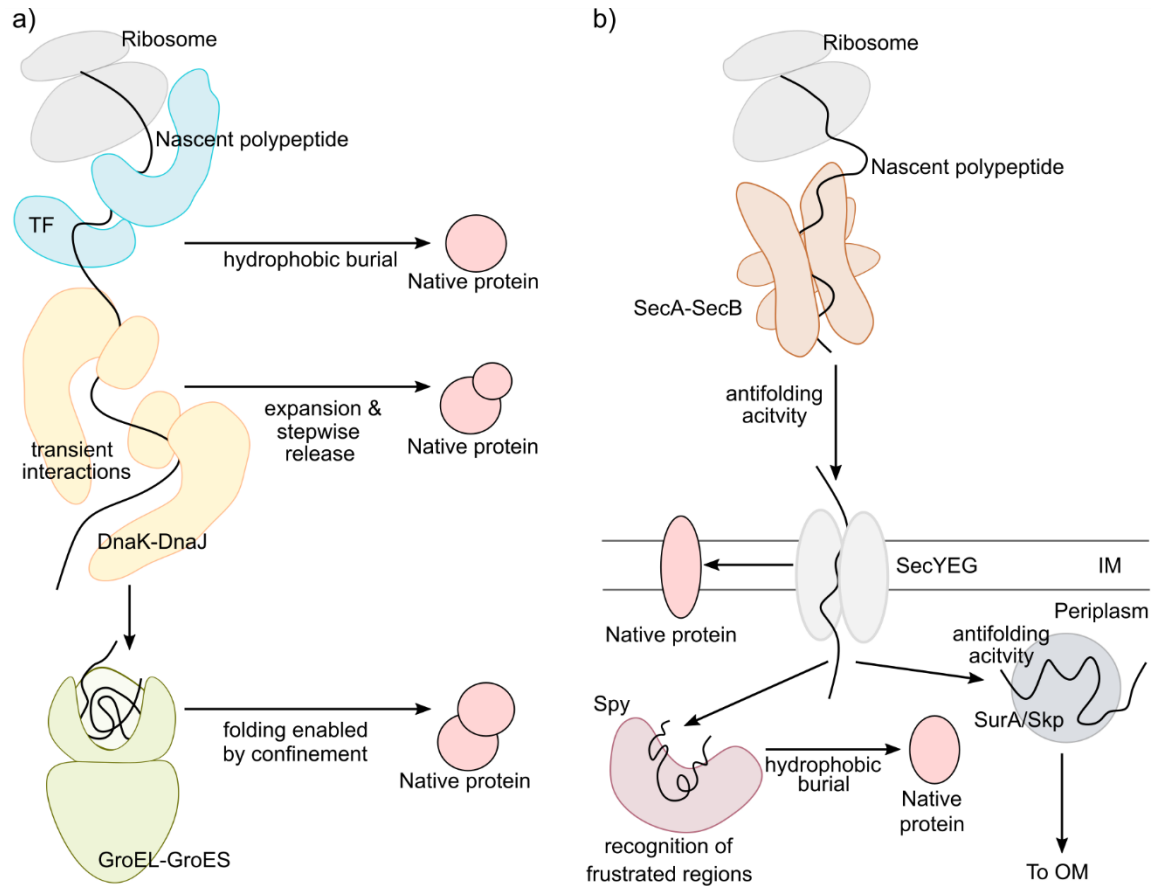


**Figure 2-1 - Protein - chaperone interactions in bacteria.** a) Nascent polypeptides synthesized on ribosome are captured co-translationally by Trigger Factor (TF) which can then pass it on to the DnaK-DnaJ chaperone system. Subsequently, the polypeptide is relayed to GroEL-GroES chaperonin. Proteins can also achieve their folded native state facilitated directly by any of these chaperone machineries without requiring the next co-chaperone. The dominating mechanism employed during each of these chaperone-protein interactions are reported as indicated in the figure (see text for details). b) Certain polypeptides are supposed to fold only after reaching their destination like the inner membrane (IM), the periplasm or the outer membrane (OM). Such polypeptides are mostly recognised by the SecA-SecB chaperones which exhibit strong anti-folding activity like the SurA/Skp chaperone in the periplasm. On the other hand, the Spy chaperone in the periplasm recognizes frustrated regions and helps fold the substrate by hydrophobic burial of residues. Figure adapted upon combining information from (2, 12, 15, 51).

*Antifolding activity of Chaperones:* Besides the ability to fold nascent proteins, chaperones like SecB, Trigger Factor, SurA, Skp and many others also exhibit antifolding activity (Figure 2-1b). Such a mode of interaction seems to be strongly modulated by kinetics and

thermodynamics of chaperone-protein interaction (18). Maintaining the proteins in a folding competent state, SecB along with SecA is involved in transfer of secretory proteins to their next destination which is often the SecYEG translocon system present on the inner membrane of bacteria (12). Being the major focus of this work, the anti-folding action of periplasmic chaperones like SurA and Skp on newly secreted OMPs is discussed later (Section 2.2.4).

Chaperones employ kinetic partitioning to steer nascent chains away from defective conformations or aggregation (3). Moreover, in addition to all these functionalities, chaperones like HSP70, DnaK, ClpB and Skp are even found to be disintegrating protein aggregates or amyloid fibrils (35, 76–78). At this point, it should be noted that these mechanistic perspectives are rather a set of observations than a consolidated story. While all are true to their experiments and the proteins involved, the reasons that underly the chosen mechanism for a particular chaperone-protein association remain unclear. As the next two subsections demonstrate, such a question can be well addressed by examining the kinetic and biophysical properties of this interaction.

### 2.1.2 Binding affinities of protein-chaperone interactions

Different modes of protein-chaperone interactions call for different binding kinetics between the two proteins. The binding affinities dictate not only the freedom of the bound substrate to fold into its functional form but also could be regulating the conformational heterogeneity of its unfolded states (17). As has been studied for the periplasmic Spy chaperone with Isothermal Titration Calorimetry (ITC) and FRET analysis, while a higher binding affinity (a tight binding) slows down the folding of its client protein SH3, a relatively weaker affinity promotes folding of the bound SH3 (79). On the other hand, an even weaker affinity is found to render chaperone incapable of regulating client protein folding or aggregation. In another example, using Surface Plasmon Resonance (SPR) and Bio-Layer Interferometry (BLI), a 100-fold lower binding affinity has been observed for SecB with Maltose Binding Protein (MBP) as compared to MBP precursor (preMBP) (18). In accordance with the previous observation for Spy and SH3, while MBP was able to fold when bound to SecB due to both higher intrinsic folding rate and weaker affinity, preMBP did not fold when bound to SecB (18). These examples demonstrate that a balance of

binding affinities is intrinsic to the functionalities of the chaperone and protein in consideration and emphasize the need for its study.

Characterizing the binding affinities of a protein-protein interaction, in this case, the protein-chaperone interaction involves describing the equilibrium reaction of the two involved partners. Let us consider  $C_{\text{free}}$  as the unbound chaperone and  $P_{\text{free}}$  as its unbound client protein in the following equilibrium reaction scheme (Figure 2-2a):

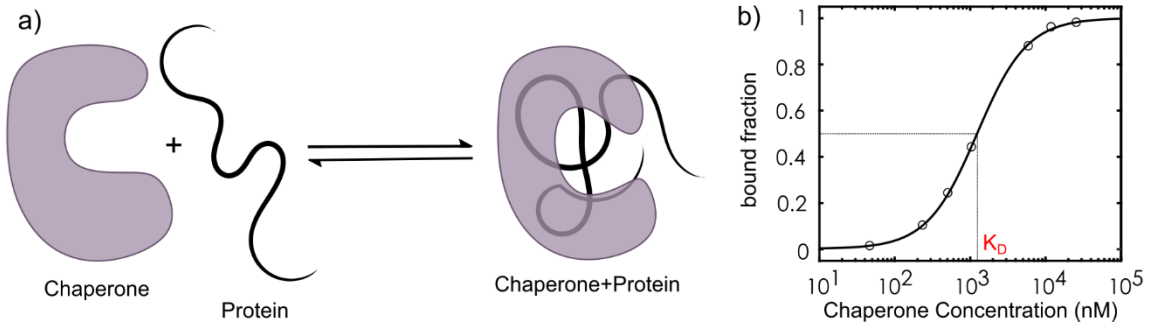


**Figure 2-2 - Binding affinities of protein-chaperone interactions.** a) A reaction scheme to represent the chaperone-protein binding. b) A theoretical fit of hill equation (eq. (7)) where  $K_D$  is the chaperone concentration when half the client protein is bound.

This equilibrium reaction is then defined by the equilibrium constant  $K_{\text{eq}}$  which can also be called as  $K_A$ , the association constant for a protein-chaperone interaction scheme. Here,

$$K_{\text{eq}} = K_A = \frac{[CP]}{[C_{\text{free}}][P_{\text{free}}]} = \frac{1}{K_D} \quad (2)$$

The square brackets represent the concentration of the particular species at equilibrium and  $K_D$  is the dissociation constant and has the convenient unit of Molarity M. Since it is difficult to obtain the  $[C_{\text{free}}]$  and  $[P_{\text{free}}]$  values in a measurement solution, it is often easier to record the total chaperone  $[C_{\text{total}}]$  and protein  $[P_{\text{total}}]$  concentration values. This converts eq. (2) into:

$$[CP] = \frac{[C_{\text{free}}][P_{\text{free}}]}{K_D} = \frac{([C_{\text{total}}] - [CP])([P_{\text{total}}] - [CP])}{K_D} \quad (3)$$

The above equation can be expressed as a quadratic equation:



$$[C_{total}][P_{total}] - ([C_{total}] + [P_{total}] + K_D)[CP] + [CP]^2 = 0 \quad (4)$$

with a solution as:

$$[CP] = \frac{([C_{total}] + [P_{total}] + K_D) - \sqrt{([C_{total}] + [P_{total}] + K_D)^2 - 4([C_{total}][P_{total}])}}{2} \quad (5)$$

Eq (5) can be used to calculate  $K_D$ , however, a simplified version can also be used in the case where  $[C_{total}]$  is in excess and the concentration of chaperone lost in complex formation is negligible. In such a case,

$$K_D = \frac{[C_{total}][P_{free}]}{[CP]} \quad (6)$$

Now, if:

$K_D \gg [C_{total}]$  then most of the client protein is unbound,

$K_D \ll [C_{total}]$  then most of the client protein is bound,

And if  $K_D = [C_{total}]$ , then 50% of the protein is bound by the chaperone. This relation is very useful when calculating  $K_D$ .

In an experiment, the chaperone is titrated against a fixed concentration of the client protein, and the concentration of the protein-chaperone complex is measured. To calculate  $K_D$ , the measurement data can be fitted using the Hill equation (80, 81):

$$[CP] = \frac{1}{\left(\frac{K_D}{[C_{total}]}\right)^n + 1} \quad (7)$$

Here,  $n$  is the hill coefficient and indicates the cooperativity of the chaperone interaction. When  $n < 1$ , the chaperone interacts non-cooperatively, i.e. the bound chaperone inhibits binding of anymore chaperone molecules to the client protein. If  $n > 1$ , the chaperone interacts cooperatively and once one chaperone is bound, it assists binding of the next chaperone to the client protein. Finally, if  $n = 1$ , the bound chaperone has no effect on binding of any more chaperones to the client protein. Eq. (7) is an important relation and will be used later on in the thesis to derive the binding affinities of the chaperone-OMP

interaction. This equation can be plotted as a sigmoidal curve on a log scale as in Figure 2-2b with  $K_D$  indicated at 0.5 bound fraction.

### 2.1.3 Thermodynamics of protein - chaperone interactions

A biophysical perspective of protein-chaperone interactions often involves studying its free energy landscape. This interaction free energy landscape is then described by two thermodynamic parameters: the enthalpic change ( $\Delta H_A$ ) and the entropic change ( $\Delta S_A$ ) of binding. Both of which are dictated by the mechanism underlying the chaperone - protein interactions such that  $\Delta H_A$  is determined by the association force between the two proteins and  $\Delta S_A$  majorly corresponds to the change in sampling of conformational space by the two proteins upon binding.

Despite the binding mechanism employed, at a given temperature  $T$ , a favourable interaction between the two proteins results in a negative Gibbs free energy of interaction or association ( $\Delta G_A$ ) which is calculated as follows:

$$\Delta G_A = \Delta H_A - T(\Delta S_A) \quad (8)$$

While  $\Delta H_A$  is the change in inter- and intra- molecular interaction energy ( $\Delta H_{inter}$  and  $\Delta H_{intra}$ , respectively),  $\Delta S_A$  is the change in entropy between the bound and unbound state and is given by:

$$\Delta S_A = S_{\text{complex}} - S_{\text{unbound}} \quad (9)$$

Thus, it is evident that for  $\Delta G_A$  to be negative, either the  $\Delta H_A$  has a large negative value or the entropy of the bound state ( $S_{\text{complex}}$ ) is greater than or equal to entropy of the unbound molecule ( $S_{\text{unbound}}$ ) leading to a very small  $\Delta S_A$ . It should be noted that there is always a small gain in entropy when the two molecules bind due to displacement of water molecules.

From the examples mentioned in the previous two sections, it can be envisioned that the chaperones and client proteins could be forming either a single conformation (Figure 2-3a) upon association or sample a large configurational space leading to formation of a multi-conformational complex (Figure 2-3b) (70). Thus, in the first case, the interaction between the two proteins is made feasible by high affinity (and thus high enthalpy change) due to

site-specific or multi-site binding resulting in  $\Delta H_{\text{inter}} \gg \Delta H_{\text{intra}}$  upon association. On the other hand, the second case suggests that despite the transient nature of interactions (and thus low  $\Delta H_A$ ) between the bound molecules, the low entropic change due to similarly populous conformational space occupied by the bound and unbound proteins ensures that the interaction is favourable (17).

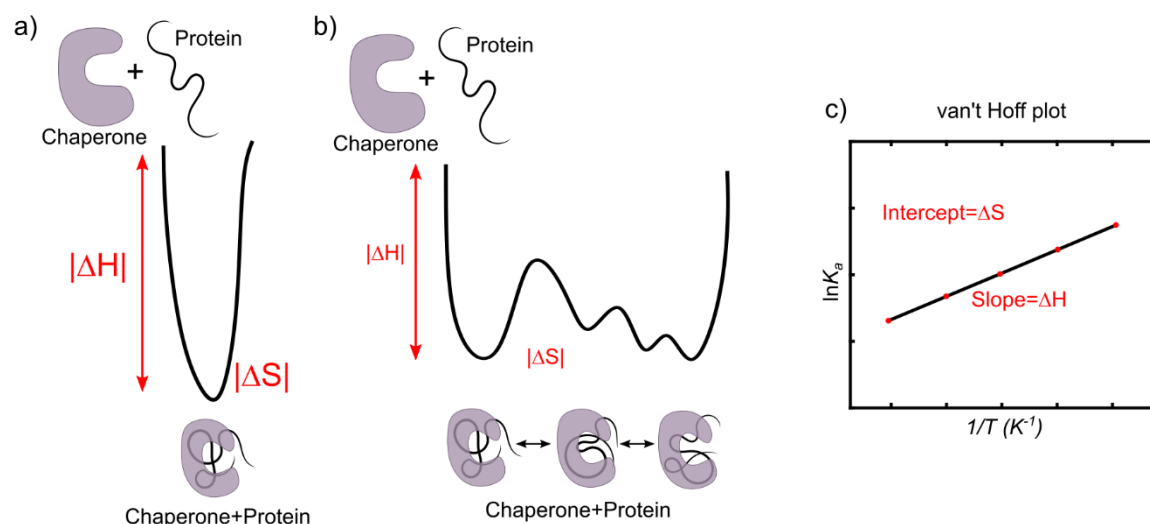


**Figure 2-3 - Thermodynamics underlying protein-chaperone interactions.** a) Specific or Multiple binding sites on the chaperone and protein lead to a high affinity of binding (high  $|\Delta H|$ ) and a unique complex conformation (high  $|\Delta S|$ ), b) Transient binding results in relatively weaker affinity (low  $|\Delta H|$ ) but higher freedom to sample multiple conformations in the bound state leading to a much lower  $|\Delta S|$ . Both the cases result in a negative  $\Delta G$  and thus a favourable interaction. Both a and b schemes are adapted from (17) c) van't Hoff plot can be used to calculate  $\Delta H$  (from the slope) and  $\Delta S$  (from the intercept) by conducting experiments so as to obtain  $K_A$  at different temperatures ( $T$ ).

In an experiment, although it is difficult to measure the enthalpic and entropic change directly, they can be estimated using a convenient relation between  $\Delta G_A$  and  $K_A$ :

$$\Delta G_A = -RT \ln K_A \quad (10)$$

Here,  $R$  is the gas constant and is equal to  $8.3145 \text{ J}\cdot\text{K}^{-1}\cdot\text{mol}^{-1}$ .

Now, combining eq. (8) and eq. (10), the following relation can be derived:

$$\ln K_A = -\frac{\Delta H_A}{RT} + \frac{\Delta S_A}{R} \quad (11)$$

This form of the van't Hoff equation can also be expressed in a differential form:

$$\frac{d}{dT} \ln K_A = \frac{\Delta H_A}{RT^2} \quad (12)$$

Measurements can be made at multiple temperatures in order to obtain a graph with  $\ln K_A$  on the y-axis and  $1/T$  on the x-axis. Such a plot called as a van't Hoff plot (Figure 2-3c) then relates to eq. (11) and can provide us with an estimation of  $\Delta H_A$  and  $\Delta S_A$ :

$$\Delta H_A = -R \times \text{slope} \quad (13)$$

$$\Delta S_A = R \times \text{intercept} \quad (14)$$

Depending on the slope of the plot, we can also decipher if the association was endothermic with a positive  $\Delta H_A$  and a negative slope or exothermic with a negative  $\Delta H_A$  and a positive slope. Thus, it is an extremely useful plot not only to obtain  $\Delta H_A$  and  $\Delta S_A$  but also to compare two different mechanisms of chaperone – client protein interaction and it will be used later on to reflect upon the periplasmic chaperone – OMP interactions.

## 2.2 Protein - chaperone interactions involved in outer membrane protein (OMP) biogenesis

Most of the soluble cytoplasmic proteins and inner membrane proteins (IMPs) need chaperones to fold into their native states. On the other hand, OMPs need a different set of chaperones which can maintain them in a folding competent state not just in the cytoplasm but also in the periplasm. The folding and insertion of outer membrane proteins is thus a challenging process and a vital one for the viability of cells and organelles having an outer membrane.

### 2.2.1 OMP biogenesis

Gram negative bacteria like *Escherichia coli* (*E. coli*), mitochondria and chloroplasts possess a cell envelope which is composed of an outer membrane, an inner membrane and a periplasm enclosed by these two layers (82, 83). Unlike the symmetric phospholipid bilayer of the inner membrane, the outer membrane is asymmetric. Inner leaflet of the outer

membrane is composed of phospholipids and the outer leaflet is made up of Lipopolysaccharide (LPS). LPS is a glycolipid typically consisting of lipid A, a core oligosaccharide and an O-antigen, it decreases the fluidity of the outer membrane and makes it relatively impermeable (84). The periplasm between the two membranes is an approximately 17 nm long ATP deficient aqueous environment with a peptidoglycan layer that maintains the cell shape. It contains many soluble proteins and chaperones that are important for cells to function properly (85).

Both the inner and outer membranes harbour proteins which maintain the viability of cells by functioning as receptors, translocons, small molecule transporters, porins, lipases and ion channels (20, 86). The nascent inner membrane polypeptides possess an anchor signal for the signal recognition particle (SRP) which facilitates co-translational folding and insertion by Sec-translocon situated on the inner membrane (87). On the other hand, the nascent outer membrane polypeptides are transported with the help of SecB to the Sec-translocon which helps the proteins to cross the inner membrane (86). The OMPs then have to be protected from aggregation in the periplasm, a challenging feat achieved by the periplasmic chaperones like Skp and SurA which bind to the outer membrane polypeptides possibly while still being secreted from the Sec-translocon and maintain them in a folding competent state until they reach the outer membrane (21–23). Here, they are finally folded and inserted with the help of the multi-protein complex,  $\beta$ -barrel assembly machinery (BAM). OMP biogenesis (Figure 2-4) is thus a well synchronized process modulated by protein–chaperone interactions at various stages.

Although a basic understanding of OMP biogenesis is well established by now, the mechanistic and biophysical aspects ruling them are still debatable and to a great extent still uncovered. To understand these interactions better, it is important to first establish a ground knowledge about the individual components of the binding complex. The next two sections look at the two interacting candidates: OMPs and periplasmic chaperones in greater detail.

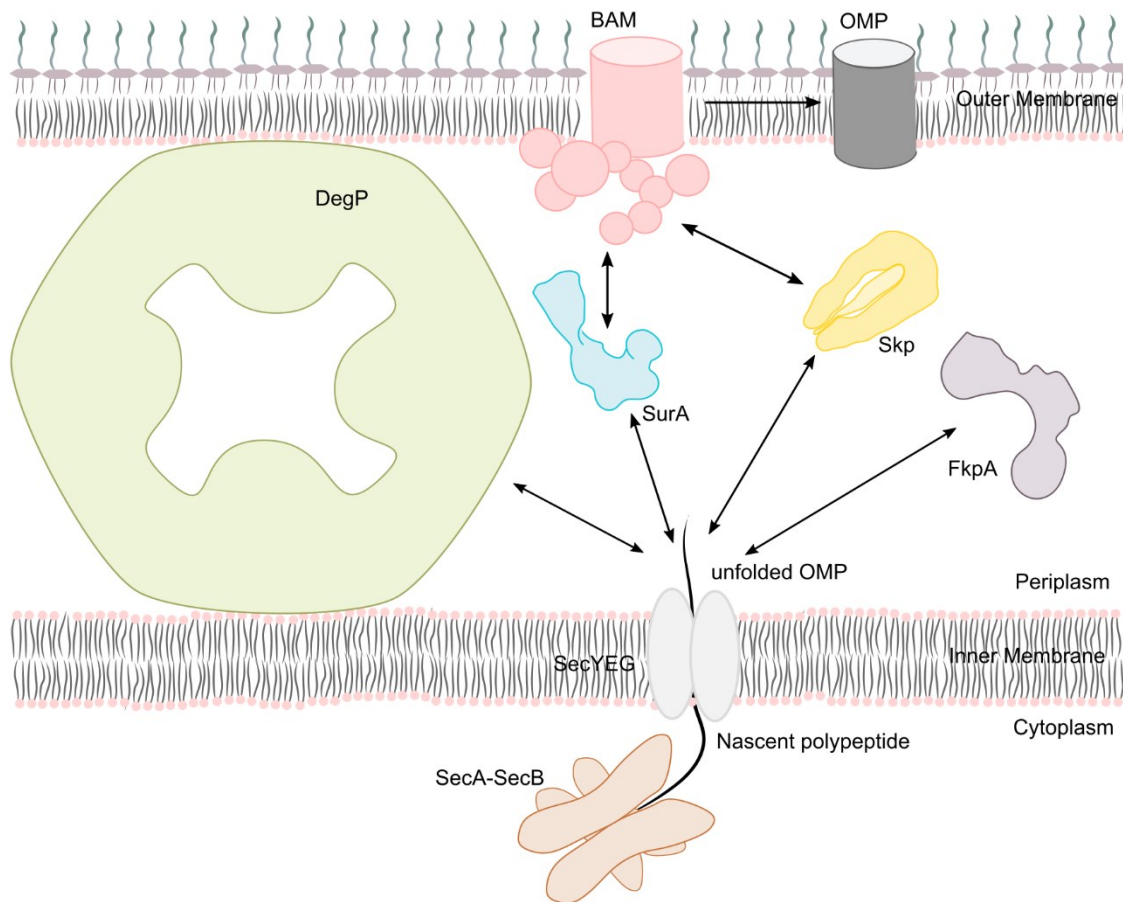


**Figure 2-4 - Outer membrane protein (OMP) biogenesis.** Secretion of nascent OMP polypeptides through the inner membrane is often facilitated by the chaperones SecA-SecB (orange) and SecYEG translocon (grey). In the periplasm, chaperones SurA (blue), Skp (yellow) and FkpA (purple) interact with the unfolded OMPs and maintain them in a folding competent state. DegP (green) is also found to be cleaving OMP aggregates under stress conditions. On reaching the outer membrane, BAM (red) facilitates folding and insertion of OMPs (dark grey) into the outer membrane. For simplicity, the peptidoglycan layer is not shown. Figure adapted from Plummer and Fleming review (23).

### 2.2.2 Beta-barrel OMPs

OMP are amphipathic proteins located on the outer membrane and are the only membrane proteins that possess a  $\beta$ -barrel structure (20). The girth of these structures is determined by the number of antiparallel  $\beta$ -strands which can range from 8 to 26  $\beta$ -strands. They often have extra-membrane domains which connect the  $\beta$ -strands and might provide additional functionalities. The cylindrical conformation with a hydrophilic interior and a lipid exposed hydrophobic exterior results in a thermodynamically stable native state. A recent study shows that the C-termini of OMPs have increased evolutionary traces as compared to their

N-termini. This suggests that the C-terminus acts as the folding nucleus or the template which guides folding of rest of the protein (88). Functionally, they can be involved in initiating pathogenesis, maintaining nutrient influx, driving locomotion or act as surface attachments, receptors and environmental sensors. They thus compose the first line of defence for Gram negative bacteria and are considered to be important drug targets (89). Certain examples of OMPs and of particular interest to this thesis are: OmpX and Outer membrane phospholipase A (OmpLA) (Figure 2-5). Below follows a short overview of their native characteristics and a few bigger OMPs (OmpF and BamA):

*OmpX* is one of the smallest OMPs with just 8  $\beta$ -strands and 171 amino acids. Some of these  $\beta$ -sheets protrude into the extra membrane domain (90). Although still unclear, based on its structure and evolutionary relation, it is proposed that OmpX promotes cell adhesion, invasion and also facilitates cellular defence against the complement system (38). *OmpLA* is a 12  $\beta$ -stranded (289 amino acids) serine hydrolase enzyme with a His142-Ser144-Asn156 catalytic triad which requires calcium to be active in its dimer form (39). Its phospholipase A1 and A2, lysophospholipase A1 and A2, and mono- and diacylglyceride lipase activity is triggered by a compromise in the integrity of the outer membrane. As the outer membrane becomes more fluid due to leakage of phospholipids, OmpLA dimerizes upon binding of substrate and calcium on the active site and hydrolyses the phospholipids making the membrane permeable for secretion of bacteriocins (91–93).

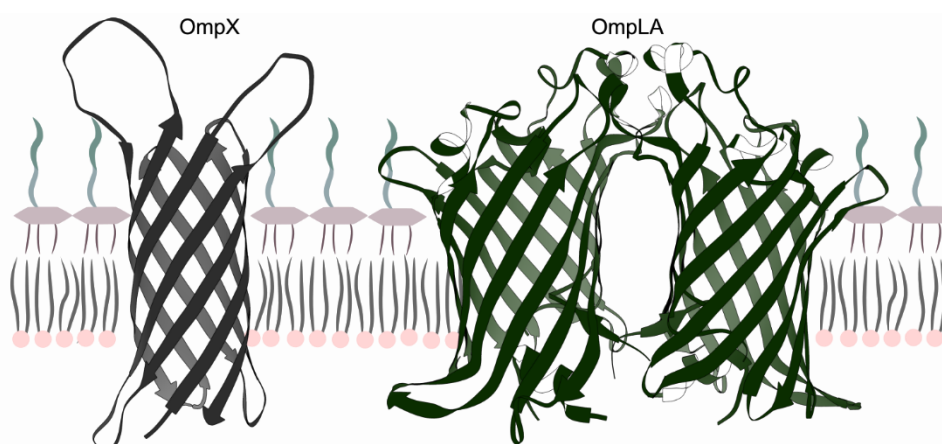


**Figure 2-5 - OMPs.** The small 8  $\beta$ -stranded OmpX (2m06.pdb, (90)) (grey) and 12  $\beta$ -stranded OmpLA (1qd6.pdb, (93)) (green) are the two model OMPs studied in this thesis.

*OmpF* is a 16  $\beta$ -stranded large OMP which forms a stable trimer and acts as a porin for diffusion of small hydrophilic molecules (94). The N-terminal extracellular domain displays eight surface antigen motifs and is proposed as a versatile vaccine candidate against certain strains of *E. coli* infection (95). *BamA* is another 16  $\beta$ -stranded OMP and one of the important components of BAM which is involved in enabling folding of other OMPs. It has two domains: the transmembrane  $\beta$ -barrel and the soluble polypeptide transport-associated (POTRA) domain composed of five motifs (96). The  $\beta$ -barrel domain is shown to exhibit lateral gating such that the first and the last  $\beta$ -strands move in order to open the protein (97). This observation has led to different models being proposed for different mechanisms by which BamA could be facilitating folding of OMPs. While some suggest that it acts as a template, others suggest that it can create a pore through which the OMP can insert and fold into the outer membrane (98, 99).

### 2.2.3 Periplasmic Chaperones

Periplasm has an oxidising environment with a pH similar to the external environment. It hosts a large number of soluble proteins including chaperones like Skp, SurA, FkpA and DegP (Figure 2-6) (27, 100, 101). These chaperones function in an ATP independent manner and sequester the incoming outer membrane polypeptides from aggregating in the aqueous crowded medium. They then deliver the bound OMP in a folding competent state possibly through transient interactions with BAM-POTRA domains (23). A brief overview of their structures and characteristics is provided in this section:

*Skp* is a seventeen kilodalton protein in its monomer form. Its crystal structure was elucidated as a trimer (1sg2.pdb, Figure 2-6a, (102)) with three double  $\alpha$ -helical arms attached to a  $\beta$ -barrel trimerization domain giving it a jelly fish like appearance. The external surface of their arms is positively charged while the internal surface contains hydrophobic patches. Skp is shown to have a holdase activity such that it accommodates small client proteins within its cavity through several weak non-covalent interactions leading to a nanomolar dissociation constant (103–105). For larger client proteins, it is demonstrated to expand its cavity and/or bind at a higher stoichiometry (104, 106). Other than binding to its client OMP, it is shown to interact with LPS and the plasma membrane as well (107). Although not much is understood about the functional utility of the Skp



monomer itself, it is interesting to note that Skp exists in an equilibrium between its trimeric and monomeric state at its periplasmic concentration of 3.9  $\mu\text{M}$  (108). Additionally, a recent investigation has shown that Skp exists in a disordered monomer form under non-stressed conditions with a shift of equilibrium towards trimerisation upon exposure to OMPs (109).

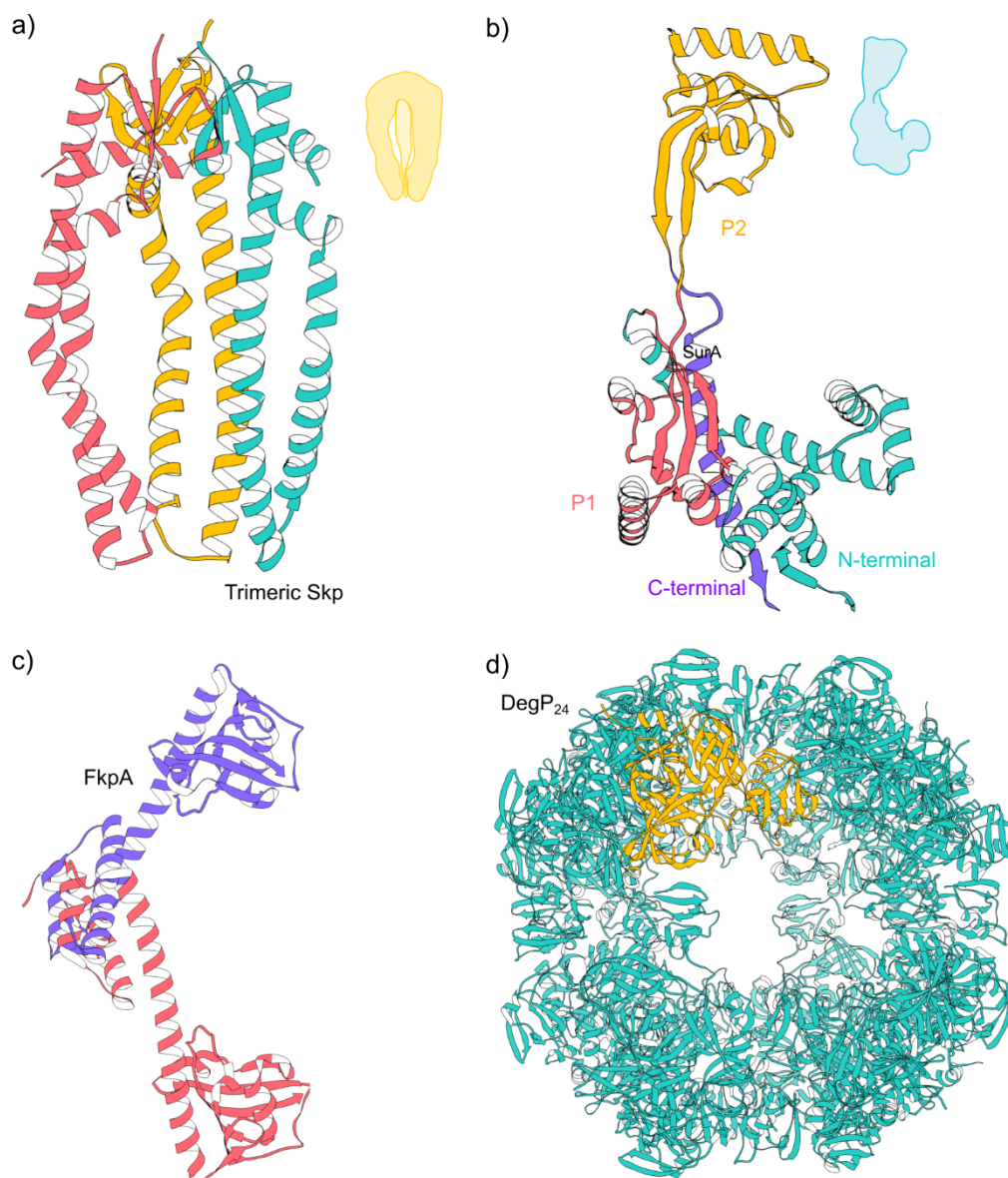


**Figure 2-6 - Periplasmic Chaperones.** a) Trimeric Skp (1sg2.pdb, (102), each monomer is coloured differently; The missing residues in two monomers were filled in using the UCSF chimera software b) SurA (1m5y.pdb, (110)) showing the PPIase domains (P1-red and P2-yellow), N-terminal (blue) and the C-terminal (purple), c) FkpA (1q6h.pdb, 104): the two monomers are coloured differently and d) DegP<sub>24</sub> (3cs0.pdb, (112): A homocomplex of 24 monomers, here one of the monomer is highlighted in yellow. Pictograms generally used to depict Skp and SurA in this thesis are shown at the Skp and SurA panels, respectively.

*SurA* is considered to be the dominant protein involved in chaperoning OMPs as its deletion has shown to induce OMP assembly defects and makes cells vulnerable to antibiotics and detergents (26, 113, 114). It has four domains: N-terminal, C-terminal and two peptidyl-prolyl cis/trans isomerase (PPIase) domains (1m5y.pdb, (110), Figure 2-6b). The N- and C-terminal domains are connected with an antiparallel  $\beta$ -sheet and are the key sites interacting with OMPs. Along with the parvulin-like PPIase 1 domain (P1), they form the core of the protein, while the PPIase 2 domain (P2) is connected flexibly to the rest of the protein (26, 110, 115). The exact role of these two domains in OMP interaction is now becoming increasingly clear as an enhancer of the chaperone activity for certain OMPs (116). *SurA* is said to recognize peptide segments with an Ar-X-Ar motif, where Ar is an aromatic residue and X can be any residue (117, 118). Moreover, recent studies have used crosslinking mass spectroscopy to identify the residue binding sites of the two protein partners (34, 36).

*FkpA* is a V shaped dimeric molecule also with both chaperone and PPIase activities. Its N-terminal domain has three  $\alpha$ -helices forming an interface by the mutual exchange of two  $\beta$ -strands between monomers and the C-terminal domain is located at its extremity (Figure 2-6c) (111, 119). Although still under debate, both the domains have been implicated in chaperoning activity while the PPIase activity is attributed just to the C-terminal domain. Similar to *Skp*, *DegP* (Figure 2-6d) is also proposed to bind to its client proteins via a cavity formed by a homo-complex of up to 24 monomers (112). It is a serine endoprotease with a chaperone activity implicated in cleaving misfolded or aggregated uOMPs (120). In its monomer state ( $\text{DegP}_3$ ) it has a protease (P) domain which forms the internal chamber and two mobile PDZ domains. The dimer of the trimer ( $\text{DegP}_6$ ) is inactive as the active site of each monomer is perturbed by a regulatory loop from the parallel trimer.  $\text{DegP}_{12}$  ( $4 \times$  trimer) and  $\text{DegP}_{24}$  ( $8 \times$  trimer) are the active oligomeric forms of the chaperone. Here, the adjacent PDZ domains of the monomers interact to keep the oligomer intact (112).

### 2.2.4 The unbound and chaperone-bound OMP

Now, we arrive at the most interesting aspect of OMP biogenesis for this thesis: the OMP-chaperone interactions.

Since OMPs remain unfolded for extended periods of time throughout their biogenesis pathway, as a first step, it is of importance to study their denatured states. Such an investigation sheds light not only the unfolded chain dynamics, but also their interactions with chaperones and subsequent release to BAM. Although little is known about the interconversion timescales of unfolded sub-populations, recent studies have shown that OMPs adapt non-random secondary structures or long-range interactions in presence of detergents under denaturing conditions. For example, using NMR, urea denatured OmpX was found to have non-native hydrophobic clusters which result in local non-random structures (121, 122). Fascinatingly, smFRET in combination with ensemble techniques like Circular Dichroism (CD) spectroscopy and Tryptophan fluorescence spectroscopy was previously employed by the Schlierf group to show that the C-terminus of OmpLA exhibits slow sampling (>100 ms) of heterogeneous conformations in presence of a denaturant (123). On the one hand, such slow chain dynamics could drive the *in vitro* folding rates of OMPs to timescale of hours as has been observed previously (123–125). On the other hand, in a cellular context, they might facilitate chaperone interaction by increasing affinity between the two proteins due to reduced entropic penalty upon binding. Moreover, upon encountering BAM, such slow conformational changes might also help them retain the folding competent states upon release (126). Thus, it will be of great value to examine if the slow interconversion dynamics of unfolded OMP sub-populations happens to be a global characteristic independent of the OMP under consideration.

Certainly, it will be of additional advantage to probe the chaperone free state of OMPs in absence of detergent and denaturant so as to better mimic *in vivo* conditions. However, despite being a requisite when comparing with chaperone bound states, the unbound states of OMPs and their interconversion dynamics still remain to be well-characterized. To this end, as a basic measure towards obtaining an overall perspective of OMP biogenesis, this thesis aims to investigate the denatured states of two differently sized OMPs: OmpX and OmpLA in greater detail along with their unbound conformations (Figure 2-7a).

A fair amount of studies has also sought to understand chaperone-bound states of OMPs. However, many of them appear to contradict each other and much of it is still widely debated in this field of science. This raises many questions regarding the chaperone-OMP interaction, especially of particular interest to this thesis, with regards to SurA-OMP and

Skp-OMP complexes. Here, a brief account of the studies till date highlights the issues this thesis endeavours to resolve:

*Are the Skp and SurA bound OMP conformations different from each other? Are they dynamic in nature?* One of the first inquiry into chaperone-OMP interactions involves the examination of the bound OMP conformations (Figure 2-7b). In this regard, the earliest studies using site-directed fluorescence spectroscopy and NMR spectroscopy in combination with biochemical experiments revealed that the entire transmembrane region of OmpA (tOmpA) is held within the cavity of chaperone Skp through both electrostatic and hydrophobic interactions in an unfolded conformation (25, 127). Conformations of tOmpA and OmpX were also probed in their Skp bound state using NMR spectroscopy by another group. They found the proteins to be entirely encapsulated within the Skp cavity with a spherical volume radius of  $\sim 2.1$  nm while undergoing sub-millisecond conformational dynamics (103). Such a fast reconfiguration of the bound substrate was suggested to be resulting from the numerous weak interactions between the two proteins. A certain smFRET study showed that Skp has substrate specific effects on the conformation of the client protein (35). For a bigger OMP protein like OmpC (16  $\beta$ -strands), while the middle segment of the protein appears to expand, the N and C-terminal of the protein becomes compact when bound to Skp. On the other hand, Skp appeared to expand OmpT (10  $\beta$ -strands) on binding, but compacted tOmpA (10  $\beta$ -strands) (35). However, the configurational space and the dynamics among the underlying bound OMP conformations were not descriptively explored in any of these studies.

Incidentally, the same study also showed that SurA bound OmpC, OmpT and tOmpA adopted a rather expanded conformation in the chaperone bound complex. Additionally, small-angle neutron scattering (SANS) experiments have suggested that SurA expands the bound tOmpA in solution (36). On the other hand, some NMR studies (103, 128) demonstrate that the SurA bound state of tOmpA and OmpX exhibit fluid-globule like states as that observed for Skp bound OMPs. A bigger OMP, FhuA is also shown to exist in dynamic conformational ensemble when bound to both the chaperones using NMR although in a conformation similar to that of Skp bound FhuA (33). The SurA bound state of OMPs and its difference to Skp bound state is thus still highly contradictory and remains to be investigated. To this end, in this work, the Skp and SurA bound states of OmpX and

OmpLA will be systematically examined for both their conformations and their reconfiguration dynamics (Figure 2-7b).

*What are the binding affinities of these chaperone-OMP interactions?* Hitherto, quite some studies indicate that the dissociation constant of Skp-OMP binding is in a nanomolar range while that for SurA-OMP binding is in the micromolar range (105, 116, 117, 129). The high affinity of Skp to its client proteins is attributed to its ability to make several transient weak interactions with the client uOMP protein (17, 103). It is speculated that in the case of SurA, the relatively low affinity is a result of region specific binding to the client OMP protein (117). Indeed, recent crosslinking experiments have demonstrated that the same sites of OmpX can interact with multiple sites of SurA and vice-versa (34, 36) suggesting presence of a transient binding. Likewise, the timescales of binding and unbinding have also garnered significant interest in the recent past, although resulting in contrasting observations. While some studies suggest lifetimes on a scale of milliseconds others have indicated that they can be as long as hours for both Skp-OMP and SurA-OMP complexes (16, 24, 40, 77, 116).

The stoichiometry of chaperones in this interaction is also a much-debated topic. The trimerization of Skp itself is speculated to be a result of OMP binding due to the presence of a significant monomer population at periplasmic conditions (108, 109). Intriguingly, for bigger OMPs, more than one Skp trimer is found to be involved in the chaperoning function (106, 108). In any case, Skp is popularly considered to be functional only in its trimeric form such that it encapsulates its substrate within its cavity (103, 104). Although little is clear about the stoichiometry of SurA when binding to its client uOMP, a few recent studies suggest multivalency in this case too. MicroScale Thermophoresis (MST) binding curves obtained for binding of SurA to unfolded OmpT were shown to fit adequately with a hill coefficient  $>1$  (116). Incidentally, many SurA binding sites are now found to be present on a single OMP (for example: OmpX and tOmpA) raising the possibility of a higher stoichiometry such that SurA holds on to the substrate in an extended manner like SecB but in a ‘beads-on-string’ fashion (18, 34, 36). In this thesis, the binding affinities and to an extent the transience of SurA-bound states and their stoichiometry will be investigated.

*What are the energetic implications of conformational sampling by chaperone bound states?* This question becomes particularly interesting for chaperone-OMP systems as in

the energy deficient environment of periplasm, thermodynamics could be playing an important role in modulating affinity between the two proteins. In the scenario of multiple bound substrate conformations, the thermodynamic concepts outlined in section 2.2.3, suggest that the free energy landscape of chaperone-OMP interaction might follow a rugged pathway. However, up till now, the energetic aspects of their associations remain undescribed (Figure 2-7c).

*Can Skp or SurA or both rescue aggregated OMPs?* *In vivo* experiments have shown that while an absence of Skp or DegP has no effect on outer membrane composition, depletion of SurA results in decrease of OMP density (27). This study has led others to suggest that SurA is the major chaperone in facilitating OMP transfer to BamA while Skp and DegP become essential only during stress conditions. One smFRET study also observed a disaggregation property for chaperone Skp (35). Yet, it is still unclear if SurA or a synergistic action by both the chaperones can disintegrate aggregated OMPs. In this light, the ability of chaperones to rescue aggregated OmpX is also investigated (Figure 2-7d) by this work.

Perceivably, an implicit argument to all the observations above is: *Do all these chaperone-OMP characteristics depend on the size of OMP under consideration?* This literature survey impresses upon us that periplasmic chaperones might employ different interaction mechanisms depending on the difference in binding kinetics and their binding functionalities. Moreover, they encounter differently sized OMPs during OMP biogenesis which necessitates that client and chaperone specific pathways are drawn when presenting a detailed view of OMP biogenesis. Indeed, a recent study observes that SurA is selective in binding certain OMPs, such that while OmpX and tOmpA have SurA binding sites, such sites were absent in OmpLA (36). Furthermore, little is known about the recognition regions harboured by OMPs for the non-specifically interacting Skp. It is certainly possible that they too possess locally frustrated regions (induced by instability in local structure due to unfavourable contacts) like Im7 and SH3 which have been found to interact with Skp irrespective of sequence or domain specificity (130). It is for this purpose that two differently sized OMPs: OmpX and OmpLA have been examined to better understand the chaperone-OMP interaction. Consequently, by charting conformational changes in different segments of OmpLA, a molecular representation of its chaperone bound state along with an insight into its recognition motif is also acquired.

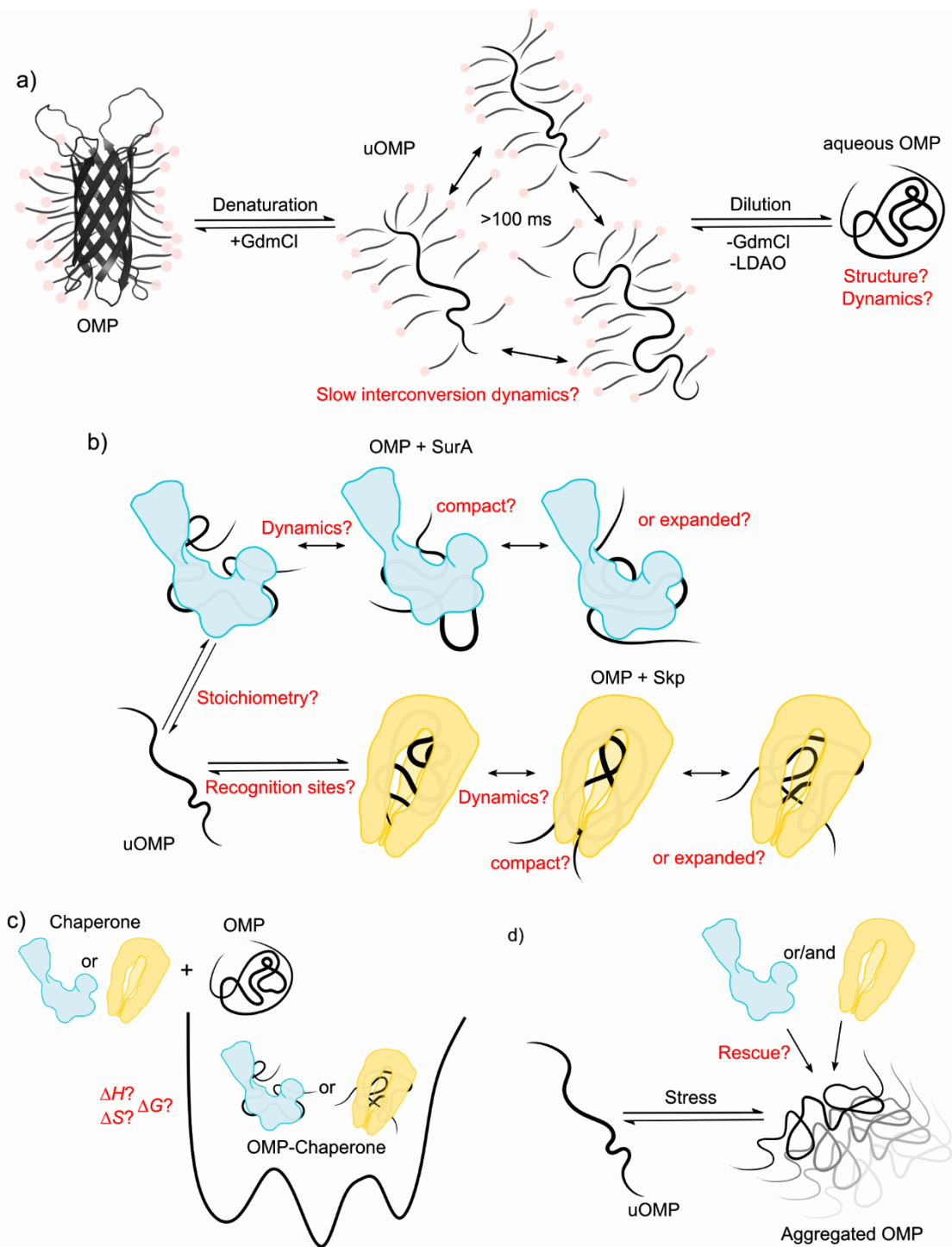


**Figure 2-7 - Open questions addressed in this thesis.** a) Is the slow unfolded chain dynamics observed for C-terminus segment of OmpLA also a feature of another OMP like OmpX? What are the conformational features of OMPs in aqueous solution? b) What do the chaperone bound conformations of OMPs look like and what is the timescale of configurational interchange among these states? Do they harbour a recognition motif for Skp? What is the stoichiometry of SurA when binding to OMPs? c) What are the thermodynamics governing chaperone-OMP interactions? ( $\Delta G$  - free energy of interaction,  $\Delta S$  - entropy change and  $\Delta H$  - enthalpy change) d) Can chaperones disintegrate aggregated OMPs? Multiple conformations adopted by different states of OMPs in each of the cases are depicted by three pictograms.

The survey above has focussed majorly on the substrate side of the chaperone-OMP interaction. Many questions arise when one starts to look at changes in chaperone conformations on binding to the client OMPs. Although out of scope for this thesis, recent research is revealing many complementary details on this aspect (34, 36, 104, 116).

### 2.3 Single molecule Förster resonance energy transfer (smFRET) to study OMP-chaperone interactions

FRET has emerged as a robust tool when probing the conformation and the conformational dynamics of proteins. Using this technique, intriguing studies have been made to understand both soluble and membrane protein folding (123, 131, 132). It is also being increasingly employed to investigate challenging protein-chaperone interactions and access the structural, temporal and biophysical features governing them (64, 133). FRET acts a spectroscopic ruler in the range of 2-10 nm such that the distance between two fluorescent dyes commonly referred to as donor and acceptor dyes corresponds to the non-radiative energy transfer between them (134). The energy transfer is a result of dipole-dipole interaction between the excited state of the donor and the ground state of the acceptor. The FRET efficiency  $E$  is related to the distance between fluorophores  $R$  as follows:

$$E = \frac{1}{1 + \left(\frac{R}{R_0}\right)^6} \quad (15)$$

where,  $R_0$  is the characteristic inter-dye distance of a particular donor-acceptor fluorophore pair resulting in 50%  $E$  and is found to be typically 5-6 nm (Figure 2-8a). A prerequisite for such a dye pair is that the emission spectrum from the donor overlaps with the absorption spectrum of the acceptor. By chemically attaching the two fluorophores to two appropriate positions on the protein of interest, one can probe the structure and the dynamics underlying a conformational population (135). For example, in Figure 2-8b, a high FRET efficiency state corresponds to a closed conformation and a low FRET efficiency state corresponds to an open conformation of the protein under study.



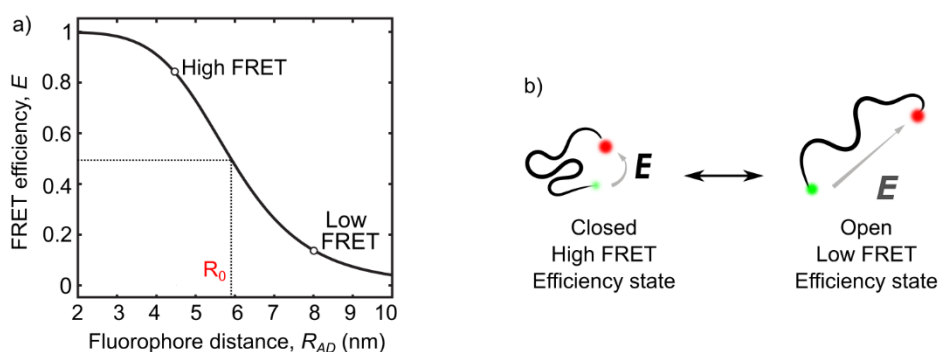


**Figure 2-8 - Förster Resonance Energy Transfer (FRET) theory.** a) The FRET efficiency,  $E$  depends on the distance between the donor (green sphere) and acceptor fluorophore (red sphere) as defined by eq. (15).  $R_0$  is the distance between the two labelling positions when  $E$  is 50%. b) In an experiment one can monitor the conformation of the protein of interest by labelling it with such a pair of dyes. Then, the closed and open conformation of the protein could correspond to a high and a low FRET efficiency state, respectively.

### 2.3.1 SmFRET based on confocal fluorescence spectroscopy

In this thesis, FRET is used at the single molecule level to probe the chaperone bound, unbound and aggregated states of OMPs. FRET when employed on a single molecule level provides additional advantages: avoidance of ensemble averaging and of aggregation due to the very low concentration (pM) of the sample under investigation. FRET measurements can be performed in solution by detecting fluorescence photon bursts from the freely diffusing labelled molecules on a confocal fluorescence microscope and has emerged as a powerful technique to probe protein conformations under diverse environmental conditions (41–44). The confined volume ( $\sim 1$  fL) resulting from a micrometre-sized pinhole ensures both a spatial and a temporal separation of the freely diffusing molecules (136). As the observation time is diffusion limited, the molecule is probed for a few milliseconds. Although, techniques like nanosecond fluorescence correlation spectroscopy (nsFCS) (132) and recurrence analysis of single particles (RASP) (137) can be implemented within the FRET measurements in order to reconstruct the timescales from a few ns to  $\sim 100$  ms.

All the smFRET experiments in this work were performed on a confocal fluorescence microscope setup incorporated with multiparameter fluorescence detection (MFD) home-built by Dr. Andreas Hartmann and Dr. Georg Krainer, a scheme of which is shown in Figure 2-9 adapted from (138). In practicality, the aforementioned FRET efficiency  $E$  is a

ratio of fluorescence emission of the donor and acceptor and is calculated from the recorded fluorescence emission by the sensitive avalanche photodiodes (APDs).

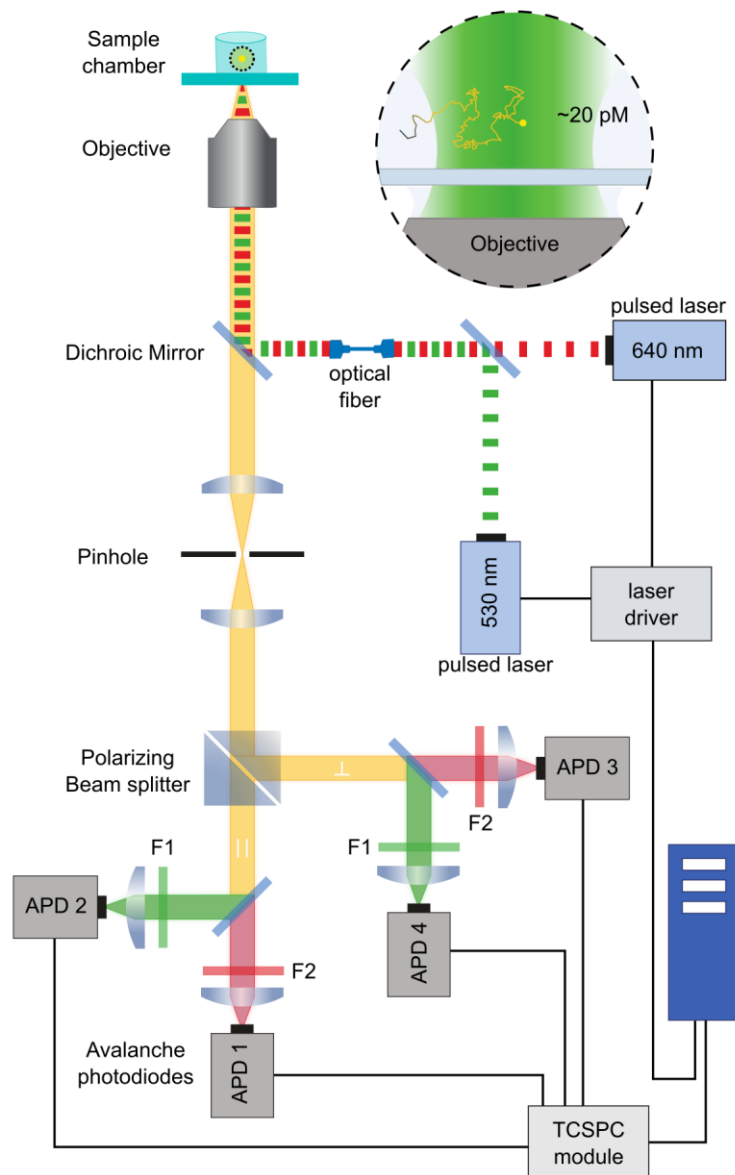


**Figure 2-9 - Schematic of the custom built multiparameter fluorescence detection (MFD) setup.** A sample chamber containing the labelled protein in low picomolar concentrations is placed on the objective and is illuminated with two linearly polarized 530 nm and 640 nm picosecond pulsed laser devices. The APDs and TCSPC modules detect and count the single photons. F1 and F2 are the bandpass filters. Such a setup enables measurement of both anisotropy and the lifetime of the dyes simultaneously (Schema adapted from the PhD thesis of Dr. Andreas Hartmann (138)).

Further, a combination of dichroic mirror and optical mirrors is used in order to disentangle signals originating only from double labelled molecules.  $E$  is then calculated as:

$$E = \frac{F_{GR} - \alpha F_{RR} - \beta F_{GG}}{F_{GR} - \alpha F_{RR} - \beta F_{GG} + \gamma F_{GG}} \quad (16)$$

where  $F_{GG}$ ,  $F_{GR}$  and  $F_{RR}$  are the background subtracted fluorescence intensities in the donor and the acceptor channel after donor excitation and in the acceptor channel after acceptor excitation, respectively.  $\alpha$ ,  $\beta$  and  $\gamma$  are the correction factors for direct excitation, spectral crosstalk and detection. The detection correction factor ( $\gamma$ ) is calculated from the detector detection efficiency ( $g_A$  and  $g_D$ ) as:

$$\gamma = \frac{g_A \phi_A}{g_D \phi_D} \quad (17)$$

where  $\phi_A$  and  $\phi_D$  are the quantum yields of the two fluorophores. A typical FRET efficiency histogram showing low and high FRET efficiencies obtained from two different position of dyes (far and close, respectively) is shown in Figure 2-10a.

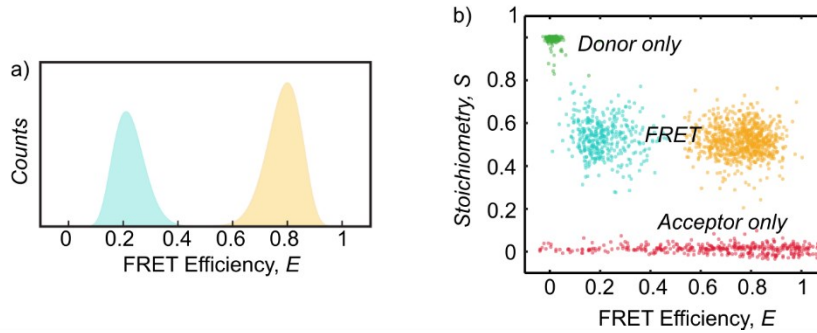


**Figure 2-10 - Single molecule FRET (smFRET) data.** a) Theoretical FRET Efficiency histograms ( $E$ ) corresponding to a high FRET efficiency (blue) and a low FRET efficiency state (yellow), b) Stoichiometry ( $S$ ) vs  $E$  plot showing acceptor only (red), donor only (green) and FRET populations (blue and yellow).

A pulse interleaved excitation (PIE) mode (139, 140) which involves a very short excitation pulse from the lasers in a repetitive manner is implemented in this setup. Accordingly, an alternate excitation is performed for the donor and acceptor fluorophores by two pulse synchronised lasers. Such an approach enables us to account for acceptor only photons. To this end, a quantity called as stoichiometry ( $S$ ) is obtained by dividing the fraction of photons originating from the green excitation with the total photons and is given by:

$$S = \frac{F_{GR} - \alpha F_{RR} - \beta F_{GG} + \gamma F_{GG}}{F_{GR} - \alpha F_{RR} - \beta F_{GG} + \gamma F_{GG} + F_{RR}} \quad (18)$$

where  $F_{RR}$  is the background corrected fluorescence intensity of the acceptor after acceptor emission, while the rest of the parameters are as defined in eq. (16). As seen in Figure 2-10b, the molecules with either donor or acceptor fluorophore appear at 1 and 0 stoichiometry, respectively. The double labelled molecules are seen around  $S$  of 0.5 and can be filtered out from the donor only or acceptor only labelled molecules.

### 2.3.2 Time-correlated single photon counting (TCSPC)

On using the PIE mode in combination with a Time-Correlated Single Photon Counting (TCSPC) module, it was also possible to record the fluorescence lifetime which provides information relating to sample heterogeneities and dynamics. It is obtained by collecting the delay time of emitted photons (microtime) over many cycles on synchronising the fluorescence emission with the preceding laser pulse (141, 142). The laser pulse is modulated to be picosecond long with a high photon density so to excite a fluorophore. The time of photon occurrence relative to the start of measurement (macrotime) is also recorded to get the time evolution of fluorescence lifetime (Figure 2-11a).  $E$  can also be expressed in terms of lifetime as:

$$E = 1 - \frac{\tau_{D(A)}}{\tau_{D(0)}} \quad (19)$$

where  $\tau_{D(A)}$  and  $\tau_{D(0)}$  are the donor lifetimes in presence and absence of acceptor.

The above relation also serves as a powerful tool to distinguish static molecules from dynamically interconverting molecules (143, 144). Here, the molecules with a fixed inter-dye distance converting on a diffusion limited timescale longer than a few milliseconds are called static, and molecules undergoing chain dynamics or conformational interconversion on a millisecond timescale are called dynamic. Furthermore, molecules can also exhibit fast-reconfiguration dynamics on a sub-millisecond timescale behaving like an unfolded polypeptide polymer resembling a Gaussian chain. In order to obtain information about the dynamics of a subpopulation, a two-dimensional (2D) plot is prepared between the intensity weighed relative lifetime of the donor ( $\tau_{D(A)}/\tau_{D(0)}$ ) vs the species weighed  $E$  (Figure 2-11b).

In this figure, the black static line is obtained from the theoretical eq. (19). In the case of a rapidly interconverting molecule, the centre of the FRET population shifts away from the static FRET line and might behave like a Gaussian chain line (red dotted line in Figure 2-11b). This powerful correlative analysis was frequently used this work to assess the dynamics of the unfolded, chaperone bound and unbound states of OMPs.

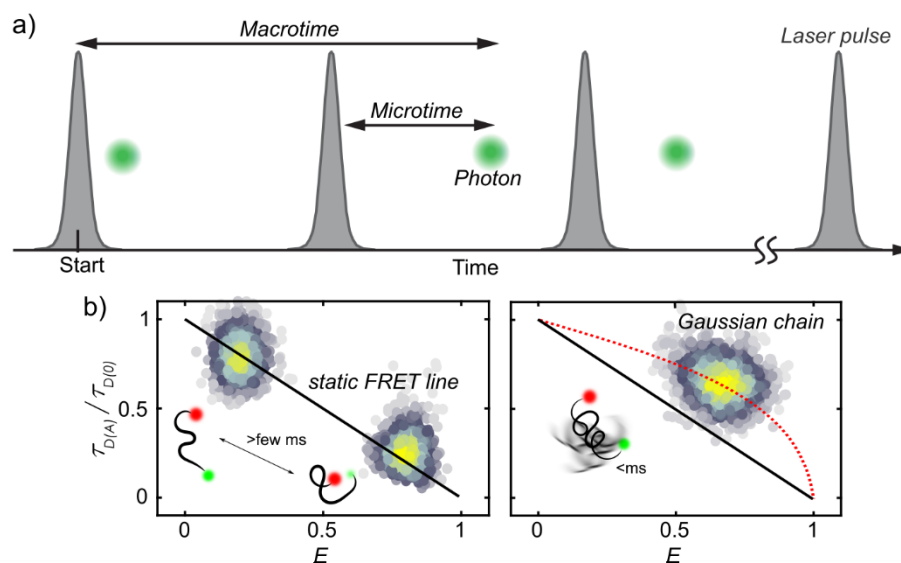


**Figure 2-11 - Time-Correlated Single Photon Counting (TCSPC).** a) A schematic of TCSPC principle with PIE mode where microtime is the delay time of the photon to the preceding laser pulse and macrotime is the time stamp of the photon (Schema adapted from the PhD thesis of Dr. Andreas Hartmann (138)), b) 2D plots between relative lifetime of donor ( $\tau_{D(A)}/\tau_{D(0)}$ ) in presence and absence of acceptor vs FRET Efficiency,  $E$  showing the static line (black line) and the Gaussian chain (red dotted) behaviour with pictograms of molecules showing the corresponding interconversion times between the subpopulations.

### 2.3.3 Fluorescence Anisotropy

It is important to check for photo physical artefacts and/or conformational artefacts of the fluorophore labelled molecules during FRET measurements. For this purpose, fluorescence anisotropy is obtained by illuminating the sample with a linear polarized laser. The intensities of light measured on the different axes of polarization provides insight into the rotational freedom of a particle (145, 146). While the emitted light will be more depolarized for a fast-rotating molecule, a slower molecule preserves the polarization of the light used for excitation. In our setup, the fluorescence emission is divided by a polarizing beam splitter into parallel and perpendicular components and is detected by two separate APDs

for both donor and acceptor channels. Insight into the rotational freedom of the dipoles can be obtained by the average rotational correlation time  $\rho$ , given by the Perrin equation (147):

$$r(\tau) = \frac{r_0}{1 + \frac{\tau_F}{\rho}} \quad (20)$$

where  $r(\tau)$  is the fluorescence anisotropy and  $\tau_F$  is the fluorescence lifetime.  $r_0$  is the fundamental anisotropy (approximately 0.4 for  $S_0 \rightarrow S_1$  excitation). When  $\rho \ll \tau_F$ , the ratio of perpendicular and parallel emission is approximately 1 and if  $\rho \gg \tau_F$ , the dipole orientation shows an excess of parallel emission indicating restricted motion. A freely diffusing fluorophore exhibits a  $\rho \sim 0.2$  ns while those tagged to a protein molecule might show a  $\rho \sim 0.7 - 1$  ns (139, 148). Higher values often indicate a hindrance in rotation and thus a possible interaction between the fluorophore and the local environment, e.g. the protein or the membrane/liposomes.

#### 2.3.4 Fluorescence Correlation Spectroscopy (FCS)

During this work, in addition to FRET measurements, the afore-mentioned setup also enabled Fluorescence Correlation Spectroscopy (FCS) experiments. FCS (45, 46) provides factual information about the size and fraction of molecules under observation and thus proved to be useful to distinguish unbound, bound and aggregated fractions of OMPs in this work.

Auto and cross-correlation functions ( $G_{ij}$ ) are obtained from fluorescence intensity fluctuations of the donor and acceptor:

$$G_{ij}(\tau) = \frac{\langle \delta F_i(t) \cdot \delta F_j(t+\tau) \rangle}{\langle F_i(t) \rangle \langle F_j(t) \rangle} \quad (21)$$

Here,  $i$  and  $j$  denote the donor (D) and acceptor (A).  $F_i(t)$  and  $F_j(t)$  are the intensities where  $F_i(t) = \langle F_i(t) \rangle + \delta F_i(t)$ .  $\langle F_i(t) \rangle$  is time averaged intensity and  $\delta F_i(t)$  is the time dependent fluorescence fluctuation. The correlation amplitude  $G_{ij}(\tau)$  is then the normalized overlap integral between  $F_i$  and  $F_j$  with  $F_j$  having a lag time of  $\tau$ . A fast diffusing (and thus smaller) molecule shows a faster decay in the autocorrelation function as compared to a slow diffusing complex or aggregate (Figure 2-12).

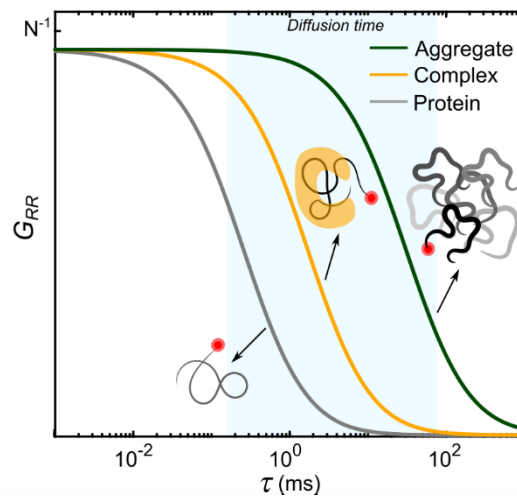


**Figure 2-12 - Fluorescence correlation spectroscopy (FCS).** An example of autocorrelation curves for a labelled molecule in its free, chaperone bound and aggregated state. While the aggregated state shows the highest diffusion time as indicated by the increase in amplitude, the chaperone bound protein complex shows relatively lower diffusion time. The lowest diffusion time is observed for the chaperone free molecule as it is the least in size. The typical diffusion (0.1 to 10 ms) times is shown through blue shaded region.





## Chapter 3    Optimisation of the labelling strategy for smFRET experiments

Monitoring the conformational changes of OMPs with smFRET experiments requires the proteins to be labelled with a suitable donor and acceptor fluorophore pair. It is beneficial to optimise the labelling protocol as a higher number of double labelled molecules requires a much lower measurement time and helps in unambiguous detection of even smaller subpopulations. Moreover, with site-specific labelling, one can avoid the effect of surrounding amino acids and the local environment on a certain sensitive dye. Such a labelling can be achieved in various manners (135): sequential labelling of cysteine residues (149), incorporation of unnatural amino acids (150, 151) and utilisation of enzymatic tags like sortase (152) among others. However, it is not a necessity when FRET is used to determine just the distances between the two labelling positions. Evaluation of the labelling efficiency and the number of double labelled molecules provides an insight into the quality of the labelled sample. Both of these are in turn dependent on the labelling assay, the type and the concentration of dyes used, the site of labelling and the characteristics of the labelling buffer. This chapter surveys the labelling strategies used during this work and solicits an optimized protocol for fluorescently labelling OMPs to perform robust smFRET experiments.

### 3.1 Refolded conformation of outer membrane phospholipase A (OmpLA) is sensitive to dimethyl sulfoxide

Site-directed mutagenesis was performed on the wild type OmpLA so as to point mutate the amino acids at positions 13 and 85 into cysteine (A13C and N85C, respectively). OmpLA<sub>13,85</sub> was then overexpressed in *E.coli*, purified from inclusion bodies and refolded in 35 mM LDAO as described in the Appendix Section 8.3.1. Different labelling assays were then used to label it (at ~5  $\mu$ M concentration) with Atto532 (ATTO-TEC) as the donor dye and Atto647N (ATTO-TEC) as the acceptor dye by maleimide reaction. At an ideal buffer pH of 6.5 to 7.5, the maleimide group on the fluorophore reacts specifically with the sulfhydryl group of cysteine on OmpLA<sub>13,85</sub> resulting in a labelled molecules with an irreversible thiol bond (153) (Figure 3-1a). Subsequently, the labelled protein molecules were separated from the free dyes via size exclusion chromatography (SEC, using Superdex 75 10/300 GL column, GE Healthcare Life Sciences) (Appendix Section 8.3.2). The obtained chromatogram was used to calculate the labelling efficiency (also called as degree of labelling or dye-to-protein ratio) for the donor and the acceptor dye using the Lambert-Beer law according to the following formula:

$$LE (\%) = \frac{\epsilon_{280}A_{\max}}{[A_{280} - (CF_{280}A_{\max})\epsilon_{\text{dye}}]} \times 100 \quad (22)$$

Here,  $LE$  is the labelling efficiency in percentage,  $\epsilon_{280}$  the extinction coefficient of the protein which is  $82280 \text{ M}^{-1}\text{cm}^{-1}$  for OmpLA wt and  $\epsilon_{\text{dye}}$  is the extinction coefficient of the maleimide dye in consideration:  $115000 \text{ M}^{-1}\text{cm}^{-1}$  and  $150000 \text{ M}^{-1}\text{cm}^{-1}$  for Atto532 and Atto647N, respectively.  $CF_{280}$  is the correction factor of the dyes at 280 nm: 0.09 for Atto532 and 0.05 for Atto647N.  $A_{280}$  and  $A_{\max}$  are the absorbance values of the protein containing fraction obtained at the chromatogram peaks for the protein and dyes, respectively.

When performing smFRET experiments with the labelled protein sample, it of greater relevance to also calculate the number of double labelled molecules. The latter can be enumerated by using the stoichiometry ( $S$ ) filter (see eq. (18), Section 2.3.1) upon the pre-analysed smFRET measurement data. To this end, single molecule events were selected from the acquired photon stream by filtering for fluorescence bursts with a maximum inter-

photon time of 50  $\mu$ s having at least 40 photons. After applying the correction factors ( $\alpha=0.054$ ,  $\beta=0.0275$  and  $\gamma=0.9$ ), the donor only labelled molecules were counted with  $0.95 < S$  and the acceptor only labelled molecules with  $S < 0.2$ . In order to obtain the double labelled molecules, an additional ALEX-2CDE filter of  $-1 < \text{ALEX-2CDE} < 10$  was applied along with the  $S$  filter of  $0.2 < S < 0.75$ . ALEX-2CDE is a brightness filter which is used in addition to the  $S$  filter to remove single labelled molecules (154) throughout this work. On normalizing the number of double labelled molecules with all the detected molecules, a percentage of double labelled OmpLA<sub>13,85</sub> or double labelling efficiency ( $DLE$ ) was calculated (Figure 3-1b and Table 3-1 on page. 50).

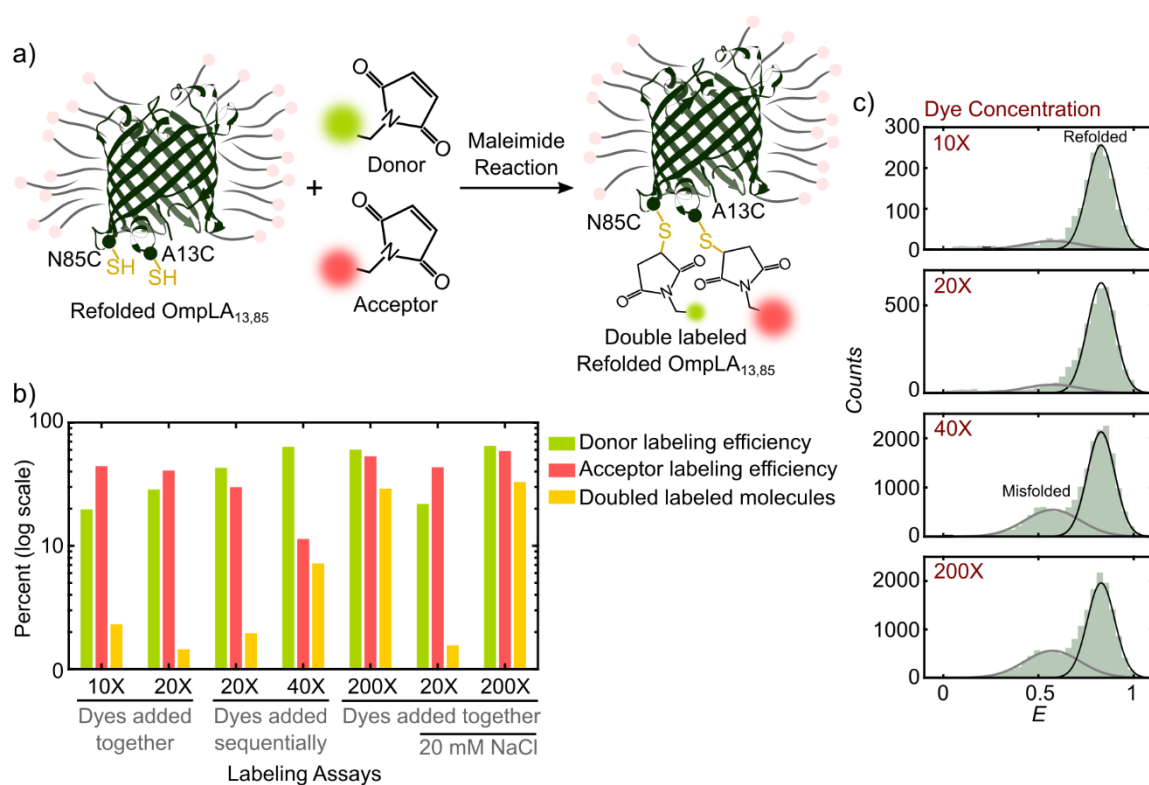


**Figure 3-1 - Labelling Assays.** a) The maleimide reaction used for labelling the refolded OmpLA<sub>13,85</sub> (1qd6.pdb, (93)) in LDAO. The positions of labelling are shown with the cysteine containing thiol group required for reacting with the maleimide functionalised donor and acceptor dyes. b) The labelling efficiency ( $LE$ ) for donor and acceptor dyes obtained from the size exclusion chromatograms and the number of double labelled molecules ( $DLE$ ) from smFRET experiments are shown for different assays as indicated in the x-axis. The reaction incubation time was 3-4 hours for all of them. It should be noted that the percentage is on the log scale for a better resolution of lower values. c) FRET histograms for measurements corresponding to different dye concentrations demonstrate that higher concentrations (40X and 200X) lead to misfolding of

refolded OmpLA<sub>13,85</sub> as shown by the Gaussian fits for the misfolded mid to high FRET efficiency population (grey curve) and high FRET efficiency refolded population (black curve).

As expected, higher concentration of dyes led to a higher labelling efficiency (Figure 3-1b and Table 3-1a). While an excess of 40X and 200X dye concentration mostly lead to *LE* of more than 50%, lower dye concentrations of 10X and 20X excess showed *LE* of less than 50% for the individual dyes. Since it was discerned that Atto532 labelled with a relatively lower competency (28.4 % with 20X dye) as compared to Atto647N (40.7 % with 20X dye), a labelling assay was designed so as to introduce the dyes sequentially: first 20X or 40X Atto532 and then 20X or 40X Atto647N after an incubation of 2 hours. As anticipated, the dye added first (Atto532) had an increased *LE*<sub>532</sub> (42.4% and 62.2% for 20X and 40X, respectively) as compared to when the dyes were added together. However, because many of the sites were now blocked by Atto532, the *LE*<sub>647N</sub> decreased (29.9% for 20X and 11.4% for 40X, respectively) as compared to the previous assay (40.7% for 20X) revealing that both the sites had similar affinity to the dyes. Furthermore, the addition of salt (20 mM NaCl) had no significant incremental or detrimental effect on the *LE* of either of the dyes Figure 3-1b and Table 3-1a.

In the next step, the true molecules of interest i.e. the double labelled molecules were evaluated from smFRET measurements along with an insight into the conformation of the labelled molecules by examining the FRET efficiency (*E*) histograms. While the dye concentrations of 20X and 40X showed a mere 10% *DLE*, higher dye concentrations indeed showed a higher *DLE* for OmpLA<sub>13,85</sub> (29.1% for 200X dyes added together). From a structural perspective, the refolded OmpLA<sub>13,85</sub> should show a narrow high FRET efficiency peak corresponding to a properly folded  $\beta$ -barrel protein. Assuredly, the refolded OmpLA<sub>13,85</sub> at 10X and 20X shows a narrow high FRET efficiency peak with an  $\langle E \rangle = 0.83$  marked by a black Gaussian curve fit in Figure 3-1c. However, misfolded OmpLA<sub>13,85</sub> becomes significantly apparent at dye concentrations of 40X and 200X with an additional mid to high FRET efficiency peak (grey curve) having  $\langle E \rangle = 0.58$ . Here  $\langle E \rangle$  is the mean FRET efficiency value obtained for each of the Gaussian curve.

At this point, it is interesting to note that dyes were dissolved in anhydrous dimethyl sulfoxide (DMSO). Hence, it is possible that higher dye concentrations and bigger dye volumes i.e. higher DMSO concentration (>0.4 mM) from the dissolved stock led to misfolding of the refolded OmpLA<sub>13,85</sub>. In the past, action of DMSO on a protein state is

found to be dependent on the protein in consideration (155–157), and yet not enough is known about its effect on OMPs. The study here indicates that exceeding a certain DMSO concentration might be harmful for their native structure. Moreover, higher concentration of dyes could also be affecting the refolded conformation of OmpLA (158). Taking into account the limitation of the dissolving ability of dyes and the effects of dyes themselves, lower dye volumes are more appropriate for maintaining the integrity of the refolded protein. Although, this could lead to a lower labelling quality, an obstacle which can be overcome by changing the buffer conditions as shown in the last section of this chapter.

### 3.2 Labelling efficiencies are site-specific

smFRET is sensitive in the range of 2-10 nm (159–161) which requires that the probed protein is labelled with the fluorophores at appropriate positions so as to fulfil the distance specification. For this purpose, it is important to choose appropriate labelling sites on the protein of interest. In the case of a folded state, the theoretical donor-acceptor distance between the chosen positions of dyes can be simply determined by inspecting it in a visualization software like VMD (162) (if structure is available). Further, on considering the unfolded polypeptide as a Gaussian chain, it is also possible to determine the distance between dyes ( $r$ ) in the unfolded state of protein as reported by Hoffmann et. al. (163):

$$\langle r^2 \rangle = 2l_p n l \quad (23)$$

Here,  $l_p$  is the persistence length which is  $\sim 1.1$  nm for a worm-like chain model,  $n$  is the number of amino acids and  $l$  is the distance between two consecutive  $\alpha$ -carbon atoms (0.38 nm). Thus, while for smaller OMPs like OmpX with 148 amino acids, the whole protein conformation could be probed by labelling at the first and last position ( $\sim 1$ -2 nm for the folded state and  $\sim 10$ -11 nm for the unfolded state), a bigger OMP like OmpLA (269 amino acids) required labelling at various sites. For this purpose, apart from positions A13C and N85C, 4 more labelling sites (K64C, D125C, D187C and H234C) were carefully chosen according to the recommendations in Appendix Section 8.3.1 (Figure 3-2a). Point mutations were done pairwise on each of these sites in order to introduce a cysteine residue and perform donor and acceptor labelling through maleimide reaction on the refolded OmpLA variants (Appendix Section 8.3.1 and 8.3.2) resulting in: OmpLA<sub>13,85,</sub>

OmpLA<sub>13,125</sub>, OmpLA<sub>64,187</sub>, OmpLA<sub>125,234</sub> and OmpLA<sub>13,234</sub>. The first two probed the first subsection of the protein, OmpLA<sub>64,187</sub> the middle and OmpLA<sub>125,234</sub> the last.

While the refolded state distances were between 1.3-2.6 nm for these variants, unfolded distance was estimated to be ~10 nm. With OmpLA<sub>13,234</sub>, the aim was to probe the global protein conformation at least in its folded form as the distance in the unfolded state might be more than 10 nm. It should be taken into account that these distances are calculated without considering the linker distances of the dye and the deviation of unfolded polypeptide from a Gaussian chain. However, the estimations verify that these variants can be probed by smFRET to get a complete picture of OmpLA conformation in its denatured, unbound and chaperone-bound state.

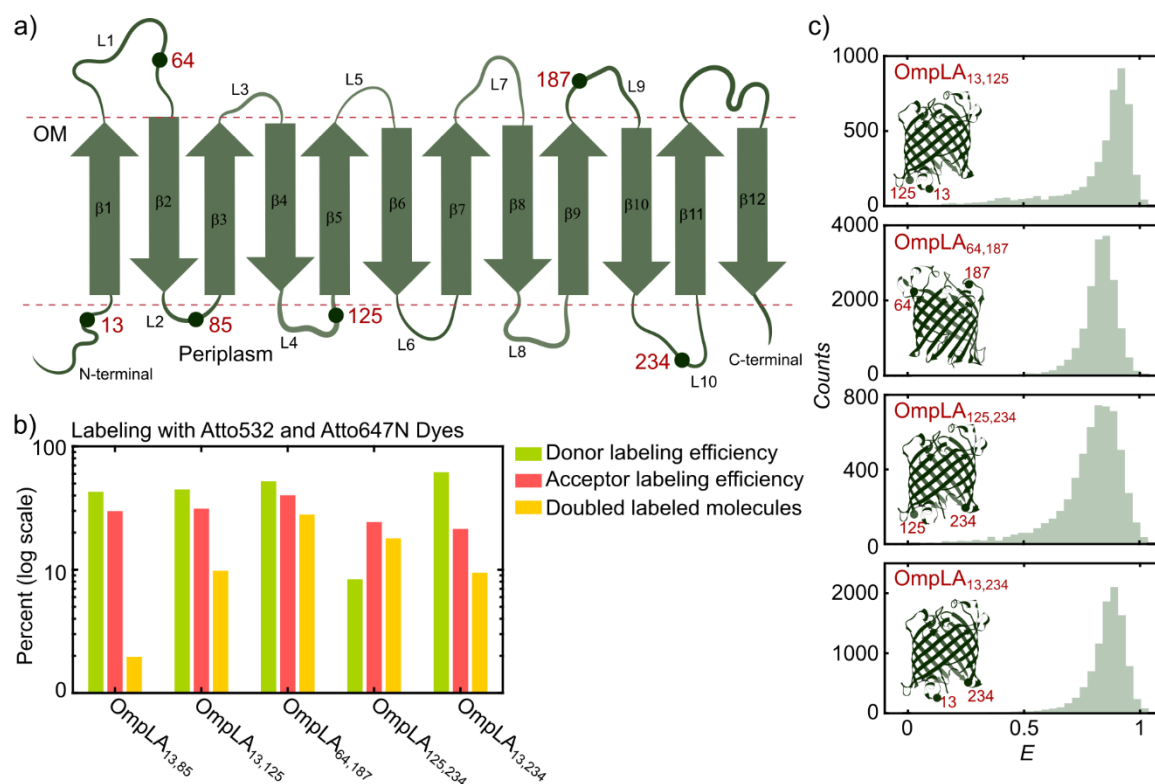


**Figure 3-2 - Labelling efficiencies of different outer membrane phospholipase A (OmpLA) variants.** a) Labelling positions (13, 64, 85, 125, 187, 234) are shown on a pictorial representation of the secondary structure map of OmpLA, b) The labelling efficiency ( $LE$ ) for donor and acceptor dyes obtained from the SEC and the percent of double labelled molecules ( $DLE$ ) from smFRET experiments are shown for the five OmpLA variants: OmpLA<sub>13,85</sub>, OmpLA<sub>13,125</sub>, OmpLA<sub>64,187</sub>, OmpLA<sub>125,234</sub> and OmpLA<sub>13,234</sub> and c) FRET histograms showing high FRET efficiency peaks of the labelled refolded OmpLA variants as indicated. The

single molecules bursts were analysed as in the previous section. The labelling positions in their native state is indicated in the protein structure (1qd6.pdb, (93)).

On keeping the protocol for labelling (both the dyes were added together at 20X concentration) and concentrations of protein (~5-10  $\mu$ M) consistent, the *LE* was calculated for each of these mutants. The analysis filters for FRET experiments were also kept the same as in previous section. Evidently, both *LE* and *DLE* appear to be dependent on the site of labelling. As seen in Figure 3-2b and Table 3-1b, while OmpLA<sub>13,85</sub> shows the least percentage of *DL* molecules (~2%), other positions appear to be better favoured especially 64, 187 and 234 (>9%). Keeping this in mind, the redundant first subsection variant OmpLA<sub>13,85</sub> is not used further for this work. Possibly due to a better exposure of the extracellular sites, OmpLA<sub>64,187</sub> has the highest *LE* on both the positions (51.3% and 40.2%) along with a much higher *DLE* (28%). All OmpLA variants are well refolded in LDAO micelles as observed by SDS-PAGE (Section 8.3.2, Figure 8.3-1) and as shown in Figure 3-2c with a corresponding high FRET efficiency state observed for all of them.

### 3.3 Denaturing conditions significantly improve labelling

Apart from choosing appropriate labelling sites, it is also important to choose suitable dyes for labelling (164). Apart from having a relevant  $R_0$  (distance corresponding to 50 % *E*) and spectral overlap for a given pair, they should also have high quantum yield and photo stability. Moreover, when studying hydrophobic proteins refolded in detergents or liposomes, their interaction with the membranes and hydrophobic regions of the protein needs to be considered so as to avoid photophysical and conformational artefacts (164). For instance, it was found by Hughes and Rawle et. al. (164) that while Atto532 (maleimide) had a much higher Membrane Interaction Factor (MIF) of  $13 \pm 1$ , Abberior Star 635P (azide) had a rather low MIF of  $0.21 \pm 0.02$ . Thus, Abberior Star 635P appears to be a better candidate for labelling hydrophobic OMPs. As explained in Section 2.3.3, during smFRET experiments, characterizing the fluorescence anisotropy is helpful to check for restricted motion of the dyes resulting from its interaction with the local environment. To this end, the rotational correlation time is calculated (according to eq. (20)) for two different acceptor dyes (Atto647N (ATTO-TEC) and Abberior Star 635P (Abberior) as shown in Figure 3-3a. Atto647N appears to show a higher rotational correlation time ( $\rho=5.665$  ns) as compared

to Abberior Star 635P (4.529 ns) for the refolded OmpLA<sub>13,125</sub>. Thus, even if  $\rho$  is not desirably perfect for either of the dyes, it is indeed better for Abberior Star 635P. But, the FRET histograms themselves show no big difference in the high FRET populations for both the cases with an  $\langle E \rangle = 0.76$  for the Atto647N labelled OmpLA<sub>13,125</sub> and  $\langle E \rangle = 0.79$  for the Abberior Star labelled OmpLA<sub>13,125</sub>. Following this finding, in many cases, the OMPs were labelled with Abberior Star 635P as the acceptor dye and Atto532 as the donor dye ( $\rho \sim 1$  ns – not shown). It should be noted that the rotational freedom of dyes depends on other factors as well like the conformation of the protein, aggregation, temperature, buffer conditions and binding partners. Thus, in this work, the rotational time of the dyes were checked wherever possible to ensure an absence of such artefacts in our FRET experiments.

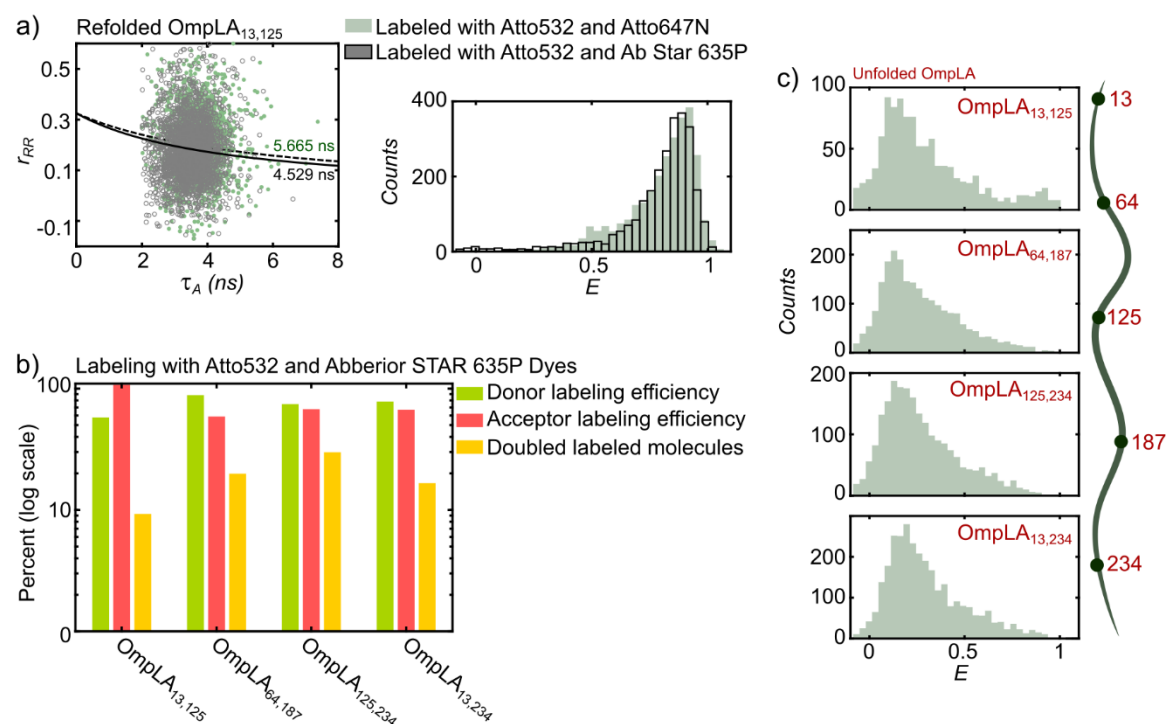


**Figure 3-3 - Effects of dyes and labelling under denaturing conditions.** a) The rotational correlation times ( $\rho$ ) as indicated were obtained from a plot between the anisotropy of the acceptor fluorophore ( $r_{RR}$ ) and  $\tau_A$  (ns), the acceptor lifetime. While  $\rho$  is 5.665 ns for Atto647N, it is rather low for Abberior Star 635P (Ab Star 635P) at 4.529 ns. Open overlapping as in the right panel, the FRET histogram for the labelled OmpLA with either Atto647N (green bars) or Abberior Star 635P (black bar outline) shows no significant difference, b) Labelling efficiencies for the donor and acceptor dye along with the percentage of double labelled molecules is shown for each variant. The labelling efficiencies seems to be rather independent of chosen position in presence of denaturants and c) FRET histograms of all the labelled variants in the denaturing labelling buffer with positions on a pictogram of the unfolded state on the right edge. As expected, a low FRET efficiency



peak is observed for all the variants indicating their unfolded state. The single molecules bursts were selected as in the previous section. Correction factors of  $\alpha=0.0881$ ,  $\beta=0.0247$  and  $\gamma=0.505$  were also used along with  $g_{GG} = 0.85152$  and  $g_{RR} = 0.82186$ .

Having now taken into account the site and dye specific effects on both the proteins and the labelling, the last step was to optimize the buffer conditions so as to increase the labelling efficiencies. Since the investigation of chaperone-bound and unbound OMPs requires that the OMPs are denatured and the detergent LDAO is absent when preparing the chaperone-OMP complex, OMPs can be labelled in a denaturing buffer (e.g. 6 M GdmCl) and used directly to measure in absence or in presence of the chaperones. Thus, the OmpLA variants were labelled in a buffer (20 mM Tris-HCl, 150 mM NaCl, pH 7.2) containing 6 M GdmCl with 20X excess of dyes at room temperature with an incubation period of 3 hours, followed by purification with SEC in the same denaturing buffer. Figure 3-3b demonstrates that labelling efficiencies increase in the unfolded state of OmpLA, possibly due to an improved exposure of the cysteine on the labelling sites. Extinction coefficient of  $\epsilon_{\text{dye}} = 120000$  and correction factor  $CF_{280} = 0.21$  was used for calculating the labelling efficiency of Abberior STAR 635P dye. Individual dye *LE* of >50% were observed for all the dyes, and up to 29.9% *DLE* was obtained for OmpLA<sub>125,234</sub> (Figure 3-3b and Table 3-1c). Compared to *DLE* in absence of denaturant (Table 3-1c), this approach appears to be beneficial for at least some variants (OmpLA<sub>125,234</sub> and OmpLA<sub>13,234</sub>), and is rather independent of the labelling position chosen. However, negligible improvements for other variants indicates that the labelling assay might still need to be improved either by increasing the dye concentration or by using a better purifying approach like Reverse Phase-High Pressure Liquid Chromatography (RP-HPLC).

Further, as expected the FRET histograms (filtered with  $0.2 < S < 0.75$  and  $0 < \text{ALEX-2CDE} < 10$ ) show a broad low FRET efficiency peak for all variants corresponding to the expected unfolded states for these proteins (Figure 3-3c). Following this finding, OmpLA variants were labelled in their denatured states and used directly to complex with chaperones to perform chaperone-bound and unbound FRET experiments.

### 3.4 Summary

This chapter focussed on establishing a labelling protocol with suitable labelling sites on OmpLA and appropriate dyes, an important venture as the quality of labelling narrates the proficiency of our FRET experiments. Equipped with the stoichiometry filter, the sample heterogeneity was quantified to reflect upon the double labelling efficiencies. Although, higher dye volumes (and thus high concentrations of dye and DMSO) incremented the labelling efficiencies, they also perturbed the refolded state of OmpLA<sub>13,85</sub> and were found to be unsuitable. Further, the LE were found to be site-specific for refolded OmpLA with the OmpLA<sub>64,187</sub> variant showing the highest labelling due a greater solvent exposure of these residues. Next, on examining the rotational freedom of dyes, Abberior Star 635P was found to be a better candidate as an acceptor dye compared to Atto647N (depends on the buffer conditions as well). Lastly, an increase in labelling efficiencies occurred when labelling was performed under denaturing conditions for at least some variants reducing the effect of chosen positions for labelling.

<b>a)</b>	<b>Labelling Assays for OmpLA<sub>13,85</sub></b>	<b>LE<sub>532</sub> (%)</b>	<b>LE<sub>647</sub> (%)</b>	<b>DL (%)</b>
<b>1</b>	10X dyes put together	19.6	44.2	2.3
<b>2</b>	20X dyes put together	28.4	40.7	1.5
<b>3</b>	20X 1st Atto532 then Atto647N put sequentially	42.4	29.9	2
<b>4</b>	40X 1st Atto532 then Atto647N put sequentially	62.2	11.4	7.2
<b>5</b>	200X dyes put together	59.1	53.1	29.1
<b>6</b>	20X put together with 20 mM NaCl	21.7	43.4	1.6
<b>7</b>	200X put together with 20 mM NaCl	63.5	58.7	32.9
<b>b)</b>	<b>Site Specificity of Labelling (with 20X dyes)</b>	<b>LE<sub>532</sub> (%)</b>	<b>LE<sub>647</sub> (%)</b>	<b>DL (%)</b>
<b>1</b>	OmpLA <sub>13,85</sub>	42.4	29.9	2
<b>2</b>	OmpLA <sub>13,125</sub>	44.2	31.3	9.8
<b>3</b>	OmpLA <sub>64,187</sub>	51.3	40.2	28
<b>4</b>	OmpLA <sub>125,234</sub>	8.3	24.3	18
<b>5</b>	OmpLA <sub>13,234</sub>	60.7	21.4	9.4
<b>c)</b>	<b>Labelling under denaturing conditions (with 20X dyes)</b>	<b>LE<sub>532</sub> (%)</b>	<b>LE<sub>635</sub> (%)</b>	<b>DL (%)</b>
<b>1</b>	OmpLA <sub>13,125</sub>	56.9	107.4	9.3

<b>2</b>	OmpLA <sub>64,187</sub>	86.1	58.8	19.9
<b>3</b>	OmpLA <sub>125,234</sub>	73	67.6	29.9
<b>4</b>	OmpLA <sub>13,234</sub>	76.6	66.8	16.7

**Table 3-1 - Labelling Efficiencies.**  $LE_{532}$  is the Labelling Efficiency for the donor Atto532 dye in %,  $LE_{647}$  is the Labelling Efficiency for the acceptor Atto647N dye in %,  $LE_{635}$  is the Labelling Efficiency ( $LE$ ) for the acceptor Abberior STAR 635P dye in % and  $DL$  is the percentage of double labelled molecules. The calculations of  $LE$  are done according to eq. (22).  $DL$  (%) is obtained on using the  $S$  filter on the FRET experiment data as explained in Section 2.3.1. a)  $LE$  for the particular labelling assays as stated in each column, b)  $LE$  for different OmpLA variants indicating site specificity of labelling and c)  $LE$  for different OmpLA variants under denaturing conditions.

*Outlook:* In general, the labelling strategies mentioned in this chapter yielded competent smFRET measurement data for further analysis. However, in future, improvements in labelling can be made by using RP-HPLC which has the ability to separate proteins based on their hydrophobicity (135). With this purification technique, even the single labelled proteins can be distinguished from the double labelled proteins on examining the ratio of peptide bond absorption (measured at 220 nm or 235 nm) to dye absorption, thus effectively increasing the double labelled population of the protein during smFRET experiments.



## Chapter 4 Denatured OMP ensembles undergo slow structural interconversion

Unfolded states of proteins provide a fundamental insight into the first few stages of a newly synthesized polypeptide (165–167). Ranging from fast nanosecond interconversion because of a random-coil like behaviour to longer millisecond chain dynamics often due to presence of residual structures, subpopulations of the denatured polypeptide also convey significant information about their cellular biogenesis process (47, 168–171). An understanding of which is especially important for OMPs which have to be maintained in an unfolded state for long time periods in the aqueous cytoplasm and the periplasm until they reach the outer membrane (21, 23, 126, 172). Using various ensemble techniques, a few studies have previously investigated different OMPs to obtain information about their structures and folding kinetics under denaturing conditions (121–123, 173–176). Many of them have found that the unfolded states of these differently sized OMPs featured non-random coil like behaviour. However, ensemble techniques generally lack the ability to resolve heterogeneities during the folding process and uncover interconversion time within the ill-defined unfolded states. In contrast, single molecule techniques provide access to different timescales of unfolded chain dynamics so as to resolve the sub-population diversity (169, 177–179). Here, smFRET in combination with kinetic analysis and recurrence analysis of single particles (RASP) (137) is used to explore the structural and biophysical aspects of OMP denaturation in presence of LDAO. By elucidating the unfolded states of two differently sized OMPs: OmpX and OmpLA, this chapter characterizes the underlying timescales among distinct conformational species along the OMP folding pathway in absence of chaperones. Such an investigation can help us to envision their interaction with chaperones and their folding mechanisms in lipid membranes.

## 4.1 Denaturing a smaller OMP: 8 $\beta$ -stranded OmpX

Using ensemble techniques, some efforts have been made towards understanding the denatured states of the 8  $\beta$ -stranded OmpX. Presence of non-random coil like features with stable hydrophobic clusters and transient secondary structures have been reported in urea denatured OmpX through NMR spectroscopy experiments (121, 122) and molecular dynamics simulations (173). Further, folding rates of OmpX into PC 10:0 liposomes have been detected on the order of  $0.01 \text{ s}^{-1}$  by various techniques including SDS PAGE, Tryptophan Fluorescence and NMR Spectroscopy (124) where the folding itself was suggested to be a two state process. Another study showed that an increase in temperature could accelerate the folding of OmpX possibly due to disruption in the lipid packing and noted a maximum folding rate at  $70 \text{ }^\circ\text{C}$  into LDAO (within first few minutes) while it was  $0.62 \text{ min}^{-1}$  at  $40 \text{ }^\circ\text{C}$  (180). Yet, a better resolution of the folding pathway with an information about the timescales of interconversion between the heterogeneous unfolded sub-species is still unclear making it necessary to study both the unfolding and the unfolded states of this protein through FRET on a single molecule level.

### 4.1.1 OmpX folds with slow kinetic rates *in vitro*

To probe OmpX folding and unfolding kinetics with smFRET experiments, a double cysteine mutant (OmpX<sub>1,149</sub>) was designed through site directed mutagenesis at positions 1 (A1C) and 149 (149C) by Mai Quynh Ma from the Schlierf group. OmpX<sub>1,149</sub> was expressed in inclusion bodies, purified, refolded into 35 mM LDAO and labelled with 20 X Atto532 (ATTO-TEC) and Abberior Star 635P (abberior) (Appendix Section 8.3.1). The double labelled OmpX<sub>1,149</sub> sample was subsequently diluted to 20-40 pM concentration in a buffer containing 20 mM Tris, 2 mM EDTA and 10 mM LDAO at pH 8 with varying concentration of the denaturant Guanidinium chloride (GdmCl). The smFRET experiments were then performed to investigate the folding kinetics in close collaboration with Dr. Andreas Hartmann. Using the home-built setup (Section. 2.3.1), fluorescence bursts were collected from single freely diffusing molecules to extract the FRET efficiencies corresponding to different conformational states of the probed molecule. For burst analysis, a maximum inter-photon time of 40  $\mu\text{s}$  with minimum 50 photons after background correction and a Lee filter window size of 4 was used. The ALEX-2CDE and stoichiometry

filters were also applied to remove the quenched and single labelled molecules (ALEX-2CDE < 7 and  $0.2 < S < 0.75$ ).

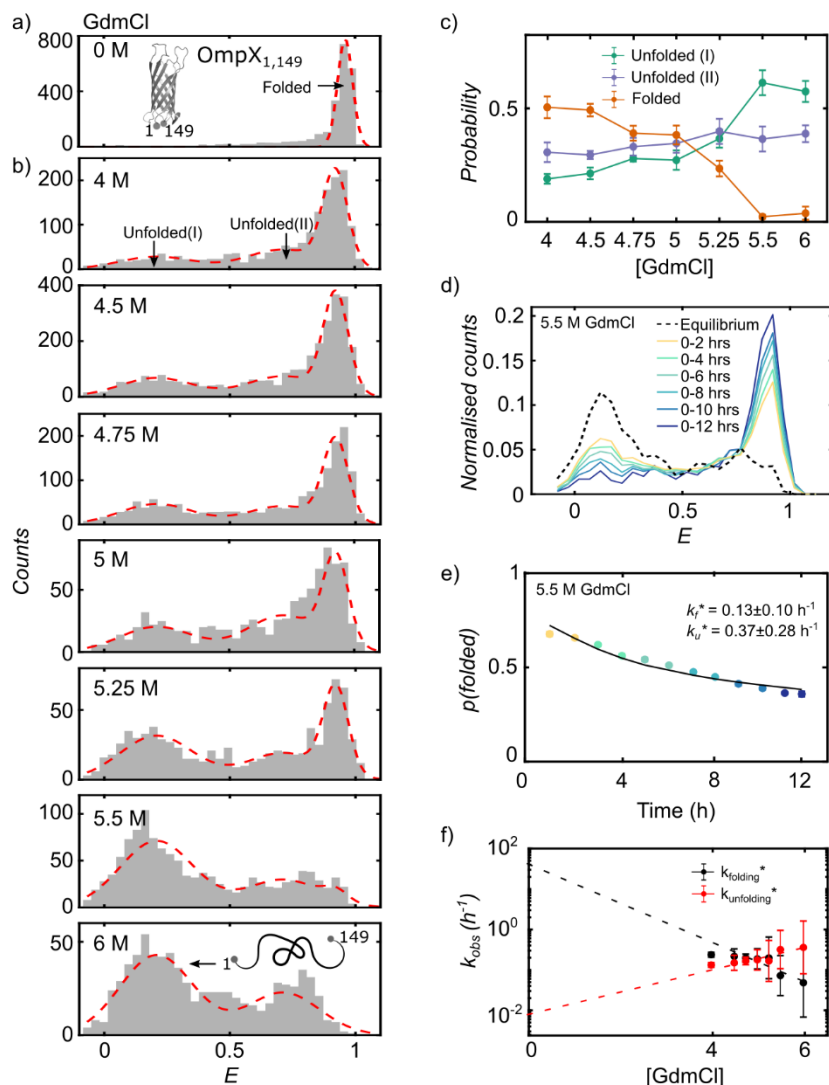


**Figure 4-1 - Unfolding OmpX<sub>1,149</sub>.** a) smFRET measurement with refolded OmpX<sub>1,149</sub> (2m06.pdb, (90)) in 10 mM LDAO shows a FRET population corresponding to high FRET efficiency as expected for a folded  $\beta$ -barrel protein. b) Equilibrium measurements of OmpX<sub>1,149</sub> at incremental GdmCl concentrations (4 M, 4.5 M, 4.75 M, 5 M, 5.25 M, 5.5 M, 6 M) as indicated in each histogram panel demonstrate decrease in the folded population with increasing denaturant concentrations. The three states during unfolding: Unfolded(I), Unfolded(II) and Folded are indicated in the first panel of the sub-figure. The red dashed line shows the Gaussian fit with three underlying states. c) The probability of those three states are shown with the folded fraction (orange line with orange error bars) clearly decreasing with increasing GdmCl concentrations while the fraction of unfolded(I) (green line with green error bars) and unfolded(II) (purple line with purple error bars) states increases. The probabilities were obtained by performing PDA considering three static states. d) The unfolding smFRET experiment performed at 5.5 M GdmCl shows that the folded fraction gets

depopulated with passage of time. Each cumulative histogram is acquired at a subsequent time interval of 2 hours as indicated in the legend. The equilibrium measurement at 5.5 M GdmCl concentration is shown by a dashed line. e) The folded fraction  $p(\textit{folded})$  is plotted against time (h) as obtained from the global cumulative PDA with the kinetic rate of folding  $k_f^*$  and kinetic rate of unfolding  $k_u^*$  being  $(0.13 \pm 0.1) \text{ h}^{-1}$  and  $(0.37 \pm 0.3) \text{ h}^{-1}$ , respectively. Here, a reaction scheme of  $U^* \leftrightarrow F$  is followed as explained in the main text. f) Global cumulative PDA was used on unfolding experiments performed for all the GdmCl concentration measurements (as before) and the kinetic rates ( $k_{\text{folding}}^*$  shown in black and  $k_{\text{unfolding}}^*$  shown in red) were obtained at each of them to reflect upon the kinetic rates in an aqueous solution by extrapolation. The kinetic rates were obtained to be  $k_f^{H_2O^*} = 11.05_{7.67}^{14.42} \text{ h}^{-1}$  or  $0.18_{0.13}^{0.24} \text{ min}^{-1}$  and  $k_u^{H_2O^*} = 0.03_{0.46}^{0.51} \text{ h}^{-1}$  or  $0.0005_{0.008}^{0.009} \text{ min}^{-1}$  in good agreement with previous works in other membrane mimetic systems (169, 181–183).

As expected for a folded  $\beta$ -barrel protein, the refolded OmpX<sub>1,149</sub> in a denaturant less buffer shows a population corresponding to high FRET efficiency (Figure 4-1a) due to close proximity of the two labelling positions. The correction factors of  $\alpha=0.881$ ,  $\beta=0.0247$  and  $\gamma=0.4907$  were used along with  $g_{GG}=0.85152$  and  $g_{RR}=0.82186$  when analysing the FRET efficiency histograms. Subsequently, the unfolding experiments were performed across a range of denaturant GdmCl concentrations (0, 4, 4.5, 4.75, 5, 5.25, 5.75 and 6 M) in a buffer (20 mM Tris, 2 mM EDTA, pH 8.0) containing 10 mM LDAO. After incubation at room temperature for ~24 hours, smFRET measurements were performed with the equilibrated denatured OmpX<sub>1,149</sub> at low picomolar concentrations (20-40 pM). All the burst analysis, correction factors and filters were set as afore-mentioned for refolded OmpX except for  $\gamma$  (~0.47, slightly varied for every GdmCl measurement, it was calculated according to Section 8.3.4, eq. (24)). As seen in Figure 4-1b, a low FRET efficiency peak corresponding to the unfolded state (Unfolded (I)) starts to get populated with increasing GdmCl concentration along with another small unfolded population (Unfolded (II)) between the folded and the unfolded (I) state suggesting presence of unfolded states. This is in contrast with the previously observed single unfolded state by Rath et. al. (124). However, in addition to the difference in membrane mimetic environment used (PC 10:0 liposomes instead of LDAO), it is possible that smFRET is able to resolve the heterogeneities in the unfolded states which were hidden from previous ensemble observations.

Subsequently, quantification of the probability of these states from each GdmCl concentration measurement was performed by Probability Density Analysis (PDA) on considering 3 static states: Unfolded-I (U(I)), Unfolded-II (U(II)) and Folded (F) (Figure



4-1c). Briefly, the experimental FRET efficiency histograms were fitted to theoretical FRET efficiency histograms obtained by Monte Carlo simulation assuming three state model with different apparent FRET efficiencies for the U(I) state ( $E_{u(I)}^*$ ) and global (i.e. same) FRET efficiencies for the U(II) ( $E_{u(II)}^*$ ) and F states ( $E_f^*$ ). The individual distances ( $R_{u(I)}$ ,  $R_{u(II)}$  and  $R_f$ ) were drawn from a Gaussian distribution probability function with  $\sigma_{u(I)}$ ,  $\sigma_{u(II)}$  and  $\sigma_f$  as the distribution width of each state: U(I), U(II) and F, respectively. This accounted for the additional widths in excess of shot-noise broadening. By performing chi-square optimisation, the probability of each state for different GdmCl concentration was determined as shown in Figure 4-1c. Such a semi-global PDA fit resulted in  $E_{u(II)}^* = 0.55 \pm 0.03$ ,  $E_f^* = 0.89 \pm 0.006$ ,  $\sigma_{u(I)} = (0.41 \pm 0.04)$  nm,  $\sigma_{u(II)} = (0.64 \pm 0.03)$  nm and  $\sigma_f = (0.53 \pm 0.05)$  nm at an average reduced  $\chi^2 = 1.91$ . The FRET efficiencies of the U(I) state along with the probabilities of each state at different GdmCl concentration are enumerated in Table 4-1. An important message to be derived from this analysis is that the probability of not only U(I), but also U(II) increases with incremental GdmCl concentration. This finding conveys that U(II) is indeed an unfolded state and can be combined with the U(I) state such that the reaction scheme  $U(I) \leftrightarrow U(II) \leftrightarrow F$  can be rewritten as  $U^* \leftrightarrow F$  where  $U^*$  is a summation of the two unfolded states. This reaction scheme can then be used to obtain the kinetic rates  $k_f^*$  and  $k_u^*$  representing the folding and unfolding rates, respectively.

In this regard, time-resolved unfolding smFRET measurements (non-equilibrated – without incubation) were made with dilution of refolded OmpX<sub>1,149</sub> into the same series of GdmCl concentration containing buffer as before. The FRET efficiency histograms at incremental time intervals ( $\Delta T = 0-2, 0-4, 0-6, 0-8, 0-10, 0-12$  hours) for the unfolding experiment conducted at 5.5 M GdmCl are shown in Figure 4-1d. It demonstrates that the folded FRET population decreases with the passage of time indicating slow interconversion between the unfolded (U(I) and U(II)) states and the folded (F) state. The burst data was further analysed for each GdmCl concentration measurement to obtain the fraction of unfolded (U(I) and U(II)) and folded (F) states. To this end, the  $E_{u(I),u(II),f}$  and  $\sigma_{u(I),u(II),f}$  obtained from a 3 free state static PDA for each unfolding experiment was obtained to ensure a better stabilisation of the fit. Next, a global cumulative PDA fit was employed on the time evolving folded fraction ( $p_{folded}$ ) so calculated to obtain the folding rates corresponding to a  $U^* \leftrightarrow F$  reaction scheme. Here, the reader is referred to the dissertation of Andreas Hartmann (138) and to

the research article about OmpLA unfolding from the Schlierf lab (123) for a detailed explanation of the analysis.

[GdmCl] (M)	$E_{u(I)}^*$	$p_f$	$p_{u(I)}$	$p_{u(II)}$	$k_f^* (h^{-1})$	$k_u^* (h^{-1})$
4	$0.19 \pm 0.01$	$0.5 \pm 0.04$	$0.31 \pm 0.04$	$0.19 \pm 0.02$	$0.30 \pm 0.03$	$0.20 \pm 0.02$
4.5	$0.19 \pm 0.01$	$0.49 \pm 0.03$	$0.29 \pm 0.02$	$0.21 \pm 0.03$	$0.28 \pm 0.08$	$0.22 \pm 0.06$
4.75	$0.18 \pm 0.01$	$0.39 \pm 0.03$	$0.33 \pm 0.04$	$0.28 \pm 0.01$	$0.26 \pm 0.04$	$0.24 \pm 0.04$
5	$0.18 \pm 0.01$	$0.38 \pm 0.04$	$0.35 \pm 0.04$	$0.27 \pm 0.04$	$0.26 \pm 0.11$	$0.24 \pm 0.11$
5.25	$0.16 \pm 0.01$	$0.23 \pm 0.03$	$0.40 \pm 0.06$	$0.37 \pm 0.04$	$0.27 \pm 0.22$	$0.23 \pm 0.19$
5.5	$0.16 \pm 0.01$	$0.02 \pm 0.01$	$0.36 \pm 0.05$	$0.61 \pm 0.06$	$0.13 \pm 0.11$	$0.37 \pm 0.28$
6	$0.16 \pm 0.01$	$0.04 \pm 0.03$	$0.39 \pm 0.04$	$0.57 \pm 0.05$	$0.10 \pm 0.13$	$0.40 \pm 0.42$

**Table 4-1 - Parameters from PDA fits for equilibrium and non-equilibrium OmpX<sub>1,149</sub> unfolding.** At each GdmCl concentration ([GdmCl] in M), the apparent FRET efficiency ( $E^*$ ) of the unfolded(I) fraction ( $E_{u(I)}$ ), the probability of the folded ( $p_f$ ), unfolded (I) ( $p_{u(I)}$ ) and the unfolded (II) ( $p_{u(II)}$ ) so obtained from the semi-global PDA (Free  $E_{u(I)}$  of Unfolded state (I) and global  $E_f$  and  $E_{u(I)}$ ) fitting of the equilibrium measurements are recorded in this table. The kinetic rates obtained from the global cumulative PDA from the non-equilibrium unfolding experiments are also noted down where  $k_f^* (h^{-1})$  and  $k_u^* (h^{-1})$  are the kinetic rates of folding and unfolding following a  $U^* \leftrightarrow F$  reaction scheme.

The decay of folded fraction for the unfolding experiment performed at 5.5 M GdmCl with the corresponding kinetic rates of  $k_f^* = (0.13 \pm 0.1) h^{-1}$  and  $k_u^* = (0.37 \pm 0.3) h^{-1}$  is shown in Figure 4-1e. By obtaining the kinetic rates ( $k_f^*$  and  $k_u^*$ ) of the unfolding experiments at each GdmCl concentration (given in Table 4-1), linear extrapolation was done to a zero denaturant concentration leading to a  $k_f^{H_2O^*} = 11.05_{7.67}^{14.42} h^{-1}$  or  $0.18_{0.13}^{0.24} min^{-1}$  and  $k_u^{H_2O^*} = 0.03_{0.46}^{0.51} h^{-1}$  or  $0.0005_{0.008}^{0.009} min^{-1}$  in a reasonable agreement with the previously obtained kinetic rates (Figure 4-1e) (124, 184, 185). It should be taken into account that the rates are influenced by the membrane mimetic environment and the buffer used. While the relatively slow folding rate resulting from heterogeneity and conformational restrictions is a rather common observation for OMPs (21, 123, 186), the slow unfolding rate testifies to the absence of need to unfold (after refolding) in a cellular context as the sequences have had no evolutionary pressure to be equipped with unfolding mechanisms (187, 188).

## 4.1.2 Denatured states of OmpX undergo slow interconversion

The dynamics within the unfolded state of OMPs dictate their binding affinity to the chaperones that carry them to the outer membrane (24, 40). Thus, in this section, the focus will be on evaluating the unfolded state of OmpX in detail. Already from the previous section, it is evident that the FRET efficiency histogram corresponding to the unfolded state is broad. On examining the measurement at 5.5 M GdmCl further, as in Figure 4-2a, it is seen that the width of the unfolded subpopulation (grey histogram of apparent FRET efficiency  $E^*$ ) is in excess of a distribution which would have been limited by shot noise (red cityscape). Interestingly, such a broad population is often attributed to slow interconversion ( $>$  inter-photon time of 50  $\mu$ s) among the unfolded states of a protein compared (169, 178, 189–191).

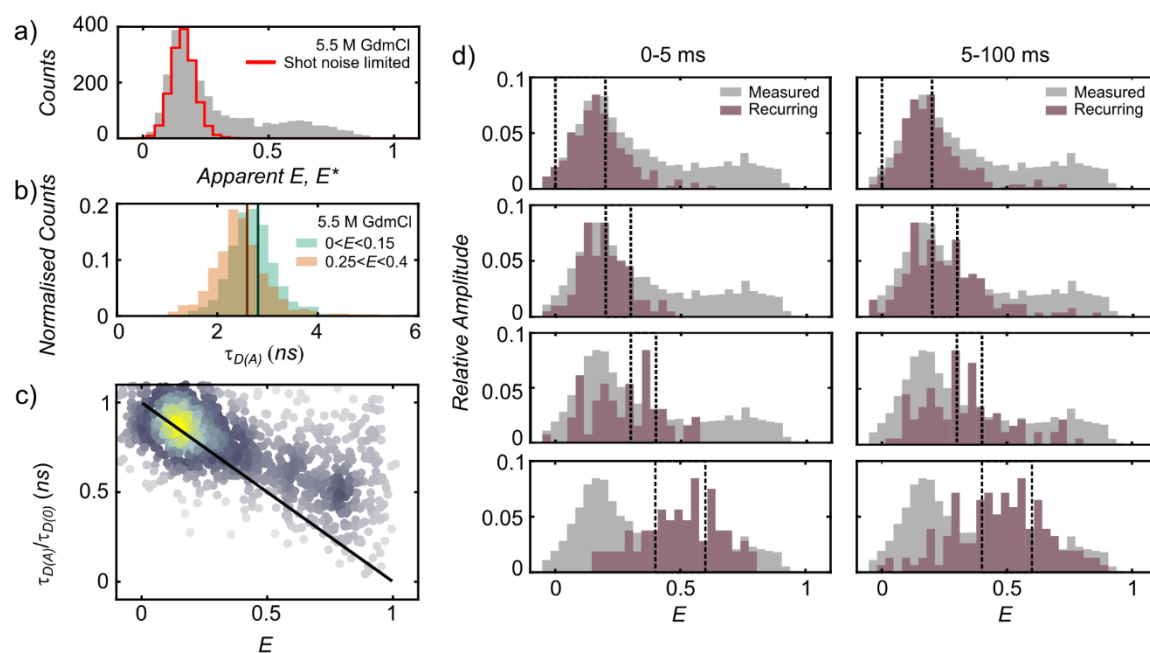


**Figure 4-2 - Slow interconversion among denatured OmpX conformations.** a) the apparent  $E$  ( $E^*$ ) histogram (grey bars) is shown with the theoretical shot noise limited distribution (red cityscape line) indicating that the unfolded population is broader than expected for an unfolded polypeptide chain behaving like a random coil. b) the lifetime of donor in presence of acceptor -  $\tau_{D(A)}$  was found to depend on the fraction corresponding to a certain range of FRET Efficiency,  $E$ . The orange  $\tau_{D(A)}$  histogram corresponds to the FRET population with  $E$  between 0 and 0.15 and the green  $\tau_{D(A)}$  histogram corresponds to the FRET population with  $E$  between 0.25 and 0.4. The mean values of  $\tau_{D(A)}$ :  $\langle \tau_{D(A)} \rangle$  indicated with dark orange and dark green line are found to be 2.81 ns and 2.59 ns, respectively. c) A 2D plot of relative lifetime of donor ( $\tau_{D(A)}/\tau_{D(0)}$ ) in presence and absence of acceptor vs  $E$  shows that the unfolded state population lies on the static FRET line

(black line) and does not undergo sub-millisecond dynamics. d) Finally, RASP analysis shows that the unfolded OmpX<sub>1,149</sub> is composed of heterogeneous conformations that have dynamics slower than 100 ms. On choosing two  $\Delta T$ : 0-5 ms and 5-100 ms with four different initial  $\Delta E$ : 0-0.2, 0.2-0.3, 0.3-0.4 and 0.4-0.6 shown subsequent to each other, the measured (grey bars) and the recurring molecule (maroon) histograms were compared. It is clear that the recurring histogram scatters around the  $\Delta E$  chosen, thus indicating interconversion on a timescale slower than 100 ms.

Further, by comparing the donor lifetimes in presence of acceptor ( $\tau_{D(A)}$ ) of different populations within the unfolded state, one can also reflect upon their dynamics. In the case of fast dynamics (<ms), the lifetime of the FRET population would be the same irrespective of the unfolded sub-fraction selected. However, we find that the lifetime of donor depends on the FRET population selected such that the mean  $\tau_{D(A)}$ :  $\langle \tau_{D(A)} \rangle = 2.81$  ns and 2.59 ns corresponds to the FRET population filtered by  $0 < E < 0.15$  and  $0.25 < E < 0.4$ , respectively. Figure 4-2b attests to this finding as the orange  $\tau_{D(A)}$  histogram is shifted from the green  $\tau_{D(A)}$  histogram for differently filtered FRET efficiencies ( $E$ ) as indicated in the plot. Such an analysis becomes clearer in a 2D plot between the ratio of average donor lifetime in presence and absence of acceptor ( $\tau_{D(A)}/\tau_{D(0)}$ ) to  $E$ . As the lifetime ratio is intensity weighed and FRET efficiency,  $E$  is species weighed, deviation from the static FRET line shown as a black line in Figure 4-2c would indicate presence of sub-millisecond dynamics. An absence of which corresponds to static sub-populations with a slow timescale (<ms) of conformational change as is the case with the unfolded population of OmpX<sub>1,149</sub>.

Lastly, using RASP, the interconversion timescale within the unfolded states was investigated. With this tool, FRET efficiency ( $E$ ) histograms of recurring molecules were compared with the measured  $E$  histograms. First, bursts were selected with different initial  $\Delta E$  in a narrow range along the unfolded peak. The bursts of recurring molecules within a given time interval ( $\Delta T$ ) after the initial bursts were also recorded. If the measured  $E$  histogram for a selected  $\Delta E$  dictates the  $E$  histogram from recurring molecules, presence of a slow interconversion can be implied. However, if the  $E$  histogram from recurring molecules is independent of the  $\Delta E$  chosen and comparably overlaps with the complete distribution, dynamics faster than the given  $\Delta T$  can be inferred. By choosing two  $\Delta T$  (0-5 ms and 5-100 ms), and four different  $\Delta E$  (0-0.2, 0.2-0.3, 0.3-0.4 and 0.5-0.7) (shown by black dashed line), it is observed that the measured (grey) and recurring histograms

(maroon) are independent of each other, such that the recurring histogram shifts with the chosen  $\Delta E$  for both the time intervals (Figure 4-2d). Hence, the conformations within the unfolded population of OmpX<sub>1,149</sub> could be undertaking conformational exchanges on a time scale longer than 100 ms. One can draw an interesting relation between the observation of transient secondary structures and hydrophobic clusters among the unfolded states of OmpX by other researchers (121, 122, 173), and the slow interconversion reported here for unfolded OmpX<sub>1,149</sub>. A similar non-random coil like behavior has been previously connected to slow interconversion of unfolded states for the last segment of OmpLA (123).

## 4.2 Denaturing a bigger OMP: 12 $\beta$ -stranded OmpLA

A strong evolutionary trace was observed in the C-terminal half of outer membrane beta-barrel proteins by Franklin et. al. (38). They reported that the sequences of 8  $\beta$ -stranded OMPs like OmpX and OmpA were conserved majorly in the C-terminal half of differently sized OMPs leading to a speculation that they might serve as the nucleation sites when folding with the help of BamA (97–99). Since OMPs are bound to chaperones in an unfolded form before they reach BamA, it is interesting to investigate if the slow dynamics observed in the unfolded states of OmpX in the previous section is a function of just the C-terminal domain of bigger OMPs or of the whole protein. Interestingly, slow interconversion was also demonstrated to be a characteristic of the C-terminal of a bigger denatured OMP – OmpLA with 12  $\beta$ -strands (16). Adding on to this finding, in this thesis, the global interconversion dynamics of the unfolded protein along with the first and middle subsections is examined. Moreover, the stability of each sub-segment against denaturation is also evaluated to speculate upon the localisation of chaperone binding region of OmpLA.

### 4.2.1 Sub-segments of OmpLA differ in their stability against denaturation

To probe different sub-segments of OmpLA, four double cysteine variants were designed: OmpLA<sub>13,125</sub>, OmpLA<sub>64,187</sub>, OmpLA<sub>125,234</sub> and OmpLA<sub>13,234</sub> probing the first, middle, last sub-segment and the whole protein, respectively (also explained in Section. 3.2). In brief, all the variants were over-expressed in *E. coli* BL21 cells and purified from inclusion bodies by solubilisation at 8 M urea. They were then refolded in 35 mM LDAO and labelled with Atto532 and Atto647N (ATTO-tec, Germany) as the donor and acceptor fluorophores,

respectively (Appendix Section 8.3.2). Each variant was then individually subjected to smFRET experiments in different concentration of denaturant (GdmCl) containing buffer (20 mM Tris-HCl, 2 mM EDTA, pH 8.0) in presence of 10 mM LDAO. All the measurements were performed at equilibrium, i.e., the OmpLA variants were incubated with the given concentration of GdmCl for ~24 hours before the experiments. On diluting them to ~20 pM in the same denaturant buffer as before, smFRET experiments were performed on the home built confocal setup (Section 2.3.1). Single molecule bursts were then identified as the ones with a minimum inter-photon time of 40  $\mu$ s having more than 50 photons. Calculation of the FRET efficiency ( $E$ ) and the stoichiometry ( $S$ ) was then performed using the correction factors of  $\alpha = 0.0587$ ,  $\beta = 0.0296$  and  $\gamma = 0.865$ . ALEX-2CDE < 12 and  $0.25 < S < 0.75$  were also applied to remove single labelled molecules with an additionally NR filter > 5 to remove multiple molecules detected in the confocal volume.

In absence of GdmCl, as expected, all the variants exhibit a high FRET efficiency ( $E$ ) peak corresponding to a refolded  $\beta$ -barrel OmpLA (Figure 4-3a, b, c and d for OmpLA<sub>13,125</sub>, OmpLA<sub>64,187</sub>, OmpLA<sub>125,234</sub> and OmpLA<sub>13,234</sub>, respectively). On increasing the concentration of denaturant, all the variants undergo unfolding as demonstrated by the decrease in high FRET efficiency population. Intriguingly, unfolded OmpLA<sub>13,234</sub> demonstrated a low FRET efficiency peak with a  $\langle E \rangle = 0.18$  despite a theoretically calculated distance of >10 nm between the two labelling positions. This substantiates the previous finding from the Schlierf lab where it was shown that OmpLA<sub>125,234</sub> possess long range tertiary interactions in its unfolded states (123). Interestingly, each variant appears to have a slight difference towards its unfolding propensity on denaturation. By using a two state (folded and unfolded) static PDA fit, the probability of unfolded OmpLA ( $p(\text{unfolded})$ ) was quantified from equilibrium measurements for each variant at different GdmCl concentration. Shortly, as done in Section 4.1.1, the basic shape of the measured FRET efficiency was fitted to a theoretical one through Monte Carlo simulation for the two states. The apparent folded and unfolded FRET efficiencies,  $E_f^*$  and  $E_u^*$ , respectively along with the standard deviation of each state ( $\sigma_u$  and  $\sigma_f$ ) so obtained during the chi square optimization for each variant are enumerated in Appendix Section 8.3.5, Table 8.3-2.

The resulting probability of unfolded fraction for each variant is plotted against the GdmCl concentration in Figure 4-4a (page no. 74). It becomes immediately clear both from Figure

4-3 and Figure 4-4a that while the middle segment of OmpLA (OmpLA<sub>64,187</sub>) appears to unfold almost completely at 4 M GdmCl, the other segments still maintain a higher fraction of low FRET efficiency structure at this concentration of denaturant. Moreover, the C-terminus of OmpLA (represented by OmpLA<sub>125,234</sub> variant) is the slowest to undergo denaturation.

On the one hand, this could simply be an influence of the labelling position chosen, while on the other hand, this could suggest that the stability of peptide in this middle region is a characteristic of the sequence, secondary structure propensity and long-range tertiary interactions in this part of the protein. It should be noted that this probed middle segment has the greatest number of loops (9) compared to other sub-segments (5 and 7 for OmpLA<sub>13,125</sub> and OmpLA<sub>125,234</sub>, respectively) possibly making it faster accessible to the denaturant molecules on average. A recent investigation by He and Hiller has shown that frustrated segments of proteins may be recognised by chaperones where they used an example of a  $\beta$ -sheet rich protein *Fyn* SH3 which appeared to have the same recognition sites for Spy, Skp and SurA (192). Further on, it will be intriguing to analyse if the middle segment of OmpLA happens to be the “frustrated region” recognisable by the chaperones Skp and SurA, as it appears to be the least stable when exposed to GdmCl. In line with this argument, it is also interesting to note that the C-terminal part of OmpLA (OmpLA<sub>125,234</sub>) appears to be the most stable segment. This suggests that at least some part of the most conserved region (considering 8  $\beta$ -strands according to ref. (88) it will be from amino acid 120 – 269 in case of OmpLA) might not distinctly harbour a chaperone binding region and be left free for interaction with BamA facilitating its folding in the outer membrane of cells.

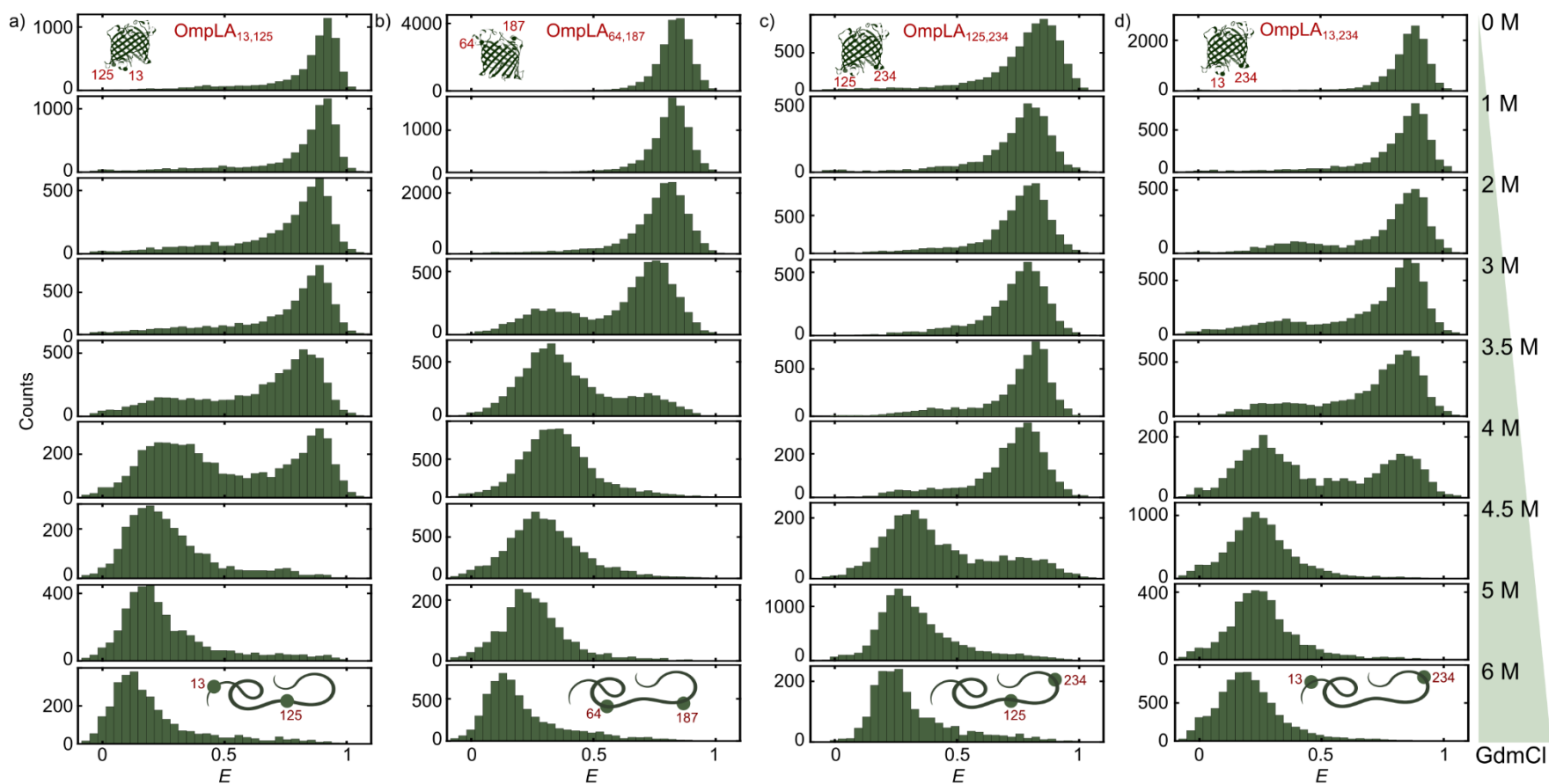


**Figure 4-3 - Stability of different OmpLA segments against denaturation.** Equilibrium smFRET measurements were performed for different variants of OmpLA with a) OmpLA<sub>13,125</sub>, b) OmpLA<sub>64,187</sub>, c) OmpLA<sub>125,234</sub> and d) OmpLA<sub>13,234</sub> at different concentration of the denaturant Guanidinium Chloride [GdmCl] as indicated in the figure. It is evident that incremental concentration of GdmCl unfolds the protein, although each segment appears to have a different stability against the denaturant. It should be noted that the data for measurements corresponding to 3.5 M, 5M and 6M GdmCl for OmpLA<sub>125,234</sub> variant was obtained from measurements by Pablo Garcia from the Schlierf group (123). The pictograms depict the refolded (1q6.pdb, (93)) and unfolded conformations with labelling positions as indicated.



#### 4.2.2 OmpLA segments possess slow unfolded chain dynamics

In a manner similar to OmpX, the next step was to analyse the dynamics of interconversion among the different sub-segments of OmpLA. To this end, the last equilibrium measurement with the highest GdmCl concentration (6 M GdmCl) was examined further for all the OmpLA variants except OmpLA<sub>125,234</sub> (already shown by Krainer et. al. (123)). Remarkably, a broad peak corresponding to the denatured state is observed for all of them (last panel of Figure 4-3), indicating that this asymmetric low-FRET efficiency peak might correspond to a slow interconverting population. Further, the width of the measured FRET efficiency histogram is indeed broader than the shot noise limited peak as seen in Figure 4-4b for the OmpLA<sub>64,187</sub> variant. Although not shown, similar extra broadening was observed for all other variants of OmpLA indicating again slower dynamics among the unfolded states. The 2 D plot of relative lifetime of donor in presence and absence of acceptor ( $\tau_{D(A)}/\tau_{D(0)}$ ) vs FRET efficiency,  $E$  was also obtained for each variant and is shown for OmpLA<sub>13,125</sub>, OmpLA<sub>64,187</sub> and OmpLA<sub>13,234</sub> measurements at 6 M GdmCl in Figure 4-4c. Discernibly, the unfolded populations of all the variants lie on the static FRET line further validating the previous inference.

To further substantiate this claim and also to obtain an insight about timescale of slow interconversion, RASP was employed on the 6 M GdmCl measurements of all the variants. The FRET efficiency histograms of the recurring molecules were compared with that of the measured histograms by choosing four different initial  $\Delta E$  (0.1-0.2, 0.2-0.3, 0.3-0.4 and 0.4-0.7) and two  $\Delta T$  (0-5 ms and 5-100 ms). Again, while an independence between the chosen initial  $\Delta E$  and the recurrence histogram is expected for a fast interconverting population, the shift of the recurrence histogram with the chosen initial  $\Delta E$  implies slower interconversion than the picked  $\Delta T$ . The latter was already observed to be the case for OmpLA<sub>125,234</sub> with a conformational interconversion among unfolded states on a timescale longer than 100 ms. Due to lack of space, such an analysis is shown here only for the OmpLA<sub>64,187</sub> variant (Figure 4-4d) with  $\Delta T = 0-5$  ms and 5-100 ms and for OmpLA<sub>13,234</sub> variant (Figure 4-4e) with  $\Delta T = 5-100$  ms with the afore-mentioned  $\Delta E$  windows. Remarkably, a similar trend suggesting very slow interconversion among the heterogeneous unfolded states was observed for all the segments of the protein. Thus, although each segment of the protein appears to have distinct stability against denaturation,

the slow conformational changes within the denatured ensemble itself emerges to be a global property of the protein.

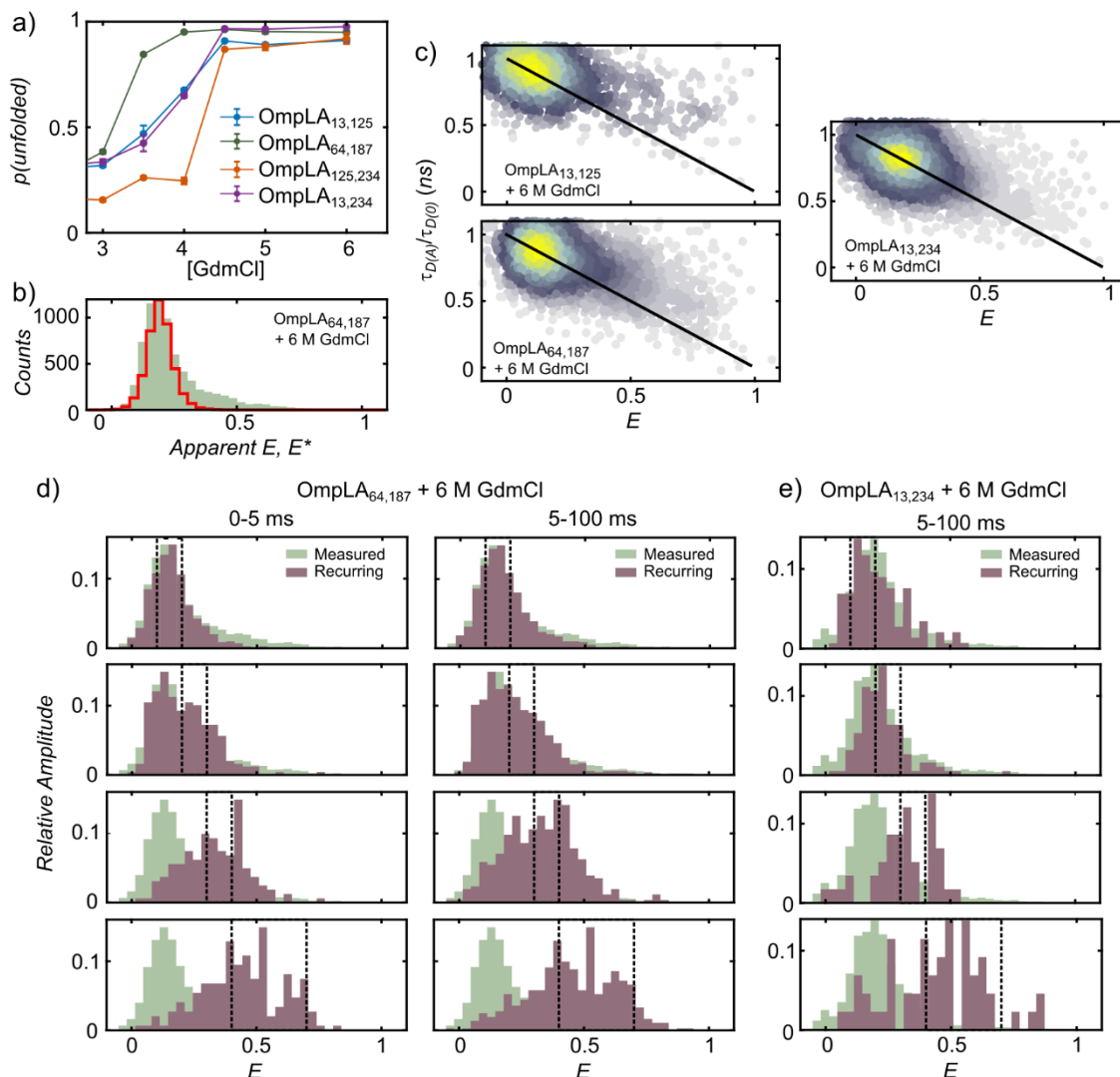


**Figure 4-4 - Slow interconversion between unfolded conformational states of OmpLA.** a) Probability of unfolded fraction ( $p(\text{unfolded})$ ) for each variant of OmpLA (OmpLA<sub>13,125</sub> – blue, OmpLA<sub>64,187</sub> – green, OmpLA<sub>125,234</sub> – orange, OmpLA<sub>13,234</sub> – purple along with respective error bars) is obtained by two state static PDA. The concentration of GdmCl is indicated in the x-axis and is shown only from 3 M GdmCl, as the measurements at lower concentration, did not show significant unfolded fraction. b) The apparent  $E$  ( $E^*$ ) histogram (green bars) is shown with the theoretical shot noise limited distribution (red cityscape line) indicating that the unfolded population is broader than expected for a fast-interconverting unfolded polypeptide chain. c) The relative lifetime of donor ( $\tau_{D(A)}/\tau_{D(0)}$ ) is plotted against FRET Efficiency,  $E$  for OmpLA<sub>13,125</sub>, OmpLA<sub>64,187</sub> and OmpLA<sub>13,234</sub> measured with 6 M GdmCl at equilibrium indicating that the unfolded sub-population appear to be static on a ms timescale for all the variants. d) RASP was performed for the middle subsegment (OmpLA<sub>64,187</sub>) with four different initial  $\Delta E$  (0.1-0.2, 0.2-0.3, 0.3-0.4 and 0.4-0.7)

for two different time intervals  $\Delta T$  (0-5 ms and 5-100 ms). Remarkably, interconversion slower than 100 ms can be inferred for the unfolded states as the recurring molecule histogram (maroon bars) depended on the initial  $\Delta E$  window chosen. e) A similar observation was also made for OmpLA<sub>13,234</sub>, indicating that the slow interconversion among the heterogeneous unfolded states is a global property of the protein.

### 4.3 Summary

Understanding the folding landscape of a protein involves not only an elucidation of the folding kinetics but also the various conformational states of the protein along the folding reaction (165, 166). Considering that the biogenesis of OMPs is a rather complicated process due to their travel across the cytoplasm, inner membrane and the periplasm in an unfolded form, it is even more important to obtain insight into their unfolded states. Furthermore, the unfolding reaction might also provide information about the structure-function relationships of the chaperone-OMP interaction in the periplasm followed by their release to the  $\beta$ -barrel assembly machinery in the outer membrane (21, 25, 31, 126, 193). By performing smFRET experiments under denaturing conditions, this section aimed to investigate the folding kinetics and the unfolded state interconversion dynamics of first a small OMP, OmpX and then a bigger OMP, OmpLA. While as anticipated, the folding kinetics were found to be slow on an order of  $11.05_{0.36}^{22.46} \text{ h}^{-1}$  or  $0.18_{0.006}^{0.37} \text{ min}^{-1}$  for OmpX<sub>1,149</sub>, the slow interconversion among the unfolded states (>100 ms) proved to be a rather significant observation. Such a finding goes hand in hand with the previous studies that have shown presence of hydrophobic clusters and secondary structures in the unfolded states of OmpX (121, 122).

Next, a bigger OMP, OmpLA was probed by choosing different labelling positions to track various sub-sections of the protein. Remarkably, the middle segment (represented by OmpLA<sub>64,187</sub>) showed the least stability against denaturation. This refers to the hypothesis that the middle segment might harbour binding sites for the periplasmic chaperones due to inherent local frustrations in its tertiary structure as was observed previously for *Fyn* SH3 (130). It will be interesting and a rather relevant point of focus in the upcoming Chapter 6, where each segment of OmpLA will be probed towards its affinity to SurA and Skp. Moreover, the last half of the protein (represented by OmpLA<sub>125,234</sub>) appeared to be rather stable against denaturation when compared to all other segments of the protein. C-terminal

sequence conservation of OMPs is supposed to be an important feature evolutionarily as it might be the nucleation site for folding. Thus, it is possible that this stability in part might play a role during the transfer of OmpLA from a periplasmic chaperone to BamA.

Lastly, the slow timescales of interconversion among the unfolded states observed for both the proteins point towards the possibility that they are not only the rate-limiting steps during protein folding but also dictate their binding competency to chaperones. For example, in energetic terms, a smaller entropic change (provided that the conformational space of bound ensemble is similar to the unbound ensemble) would increase the binding affinity between the proteins. Furthermore, under stress conditions, the preservation of folding competent states upon release from chaperones would facilitate their folding into the membrane (123, 126). Following this line of thought, the next two chapters will focus closely on the aspect of chaperone-OMP interactions for both OmpX and OmpLA and bring into the light a broader perspective upon the observations made in this chapter.

*Outlook:* It will be interesting to gain insight into OmpLA like segment-based stability of other OMPs, by performing smFRET measurements for bigger OMPs like OmpG (14  $\beta$ -strands), OmpF (16  $\beta$ -strands), BamA (16  $\beta$ -strands) and so on in presence of denaturants. This will shed light on the possible binding regions of the unfolded OMPs with both the chaperones and BamA and might help in identifying the so called “frustrated regions”.

## Chapter 5 Expanded chaperone bound OmpX displays fast chain dynamics

The smallest beta-stranded OMP – OmpX has been a well-known model when studying chaperone-OMP interactions in the periplasm. Using NMR spectroscopy, Burmann et al. showed that trimeric Skp (Skp<sub>3</sub>) encapsulated OmpX underwent rapid backbone dynamics (103). However, the conformation and dynamics of OmpX in its SurA-bound state remain unclear, especially in terms of its comparison with the Skp bound state. Interestingly, recent studies have located multiple sites of interactions on both SurA and OmpX using cross-linking experiments suggesting that the SurA complexed OmpX populates multiple conformations in a rather expanded form (34, 36). Furthermore, the timescales of reconfiguration among the chaperone bound substrates still remain to be probed directly. In actuality, such an interaction mechanism is inferred to be important both biologically and energetically (17, 34, 36, 103, 126), as it would not only avoid collapse of bound substrate but also lead to a negligible entropic change upon complexing, thus fine tuning the thermodynamics as the only source of energy in the periplasm (17). Yet, the enthalpic and entropic changes during binding remain undetermined. Furthermore, little is known about the disaggregating proteins of chaperones. A recent investigation showed that in addition to its holdase functionality, Skp also disaggregates OmpC oligomers unlike SurA (194). On the other hand, modelling studies proposed a rather synergistic interaction among different chaperones especially under conditions of stress (24, 40). Thus, many questions remain open in this field and will be addressed sequentially in this chapter starting with the unbound OmpX. It is followed by a structural and thermodynamic investigation of the chaperone bound OmpX. Lastly, an exciting insight is obtained into the disaggregation action of SurA and Skp under stress conditions. The data analysis in this chapter was developed and implemented in close collaboration with Dr. Andreas Hartmann.

## 5.1 OmpX expands on a timescale of hours in aqueous solution

Unlike ensemble techniques, smFRET permits use of picomolar concentrations of proteins, which prevents their precipitation and can thus overcome the possible artefacts in data arising from high concentrations of aggregation prone OMPs. This advantage enabled an investigation of chaperone free state of OmpX in an aqueous environment without detergent and denaturants (referred to as OmpX<sub>aq</sub> from here on). To this end, refolded double labelled OmpX<sub>1,149</sub> (in 35 mM LDAO) was first diluted in presence of 6 M GdmCl to nanomolar concentration, followed by a second dilution step (1:1000) in a buffer lacking GdmCl according to the scheme shown in Figure 5-1a. It should be noted that all the experiments in this chapter were performed using OmpX<sub>1,149</sub> labelled with Atto532 and Abberior STAR 635P as the donor and acceptor dyes. SmFRET measurements were then performed with the diluted sample over a long duration and single molecule bursts were selected as the ones with an inter-photon time of 50  $\mu$ s and a minimum photon number of 40. FRET efficiency ( $E$ ) histograms were obtained after applying filters of ALEX-2CDE < 12 and a stoichiometry filter  $S$  of  $0.2 < S < 0.75$  after background correction, and a Lee filter window size of 4. Correction factors of  $\alpha=0.0881$ ,  $\beta=0.0247$  and  $\gamma_{25^\circ\text{C}}=0.4567$ ,  $\gamma_{31^\circ\text{C}}=0.4481$  and  $\gamma_{37^\circ\text{C}}=0.4390$  were also applied.

Unlike the high FRET efficiency state of refolded OmpX<sub>1,149</sub> ( $\langle E \rangle \sim 0.95$ ) and the broad FRET efficiency state of unfolded OmpX<sub>1,149</sub> (uOmpX) in 6M GdmCl ( $\langle E \rangle \sim 0.2$ ), interestingly, OmpX<sub>aq</sub> exhibits a rather broad population in the high FRET efficiency region (grey bars with  $\langle E \rangle \sim 0.8$  in Figure 5-1b). It should also be noted that the temperature seems to have negligible influence on its conformation. As observed in Figure 5-1b, the  $E$  histograms at 31  $^\circ\text{C}$  (dark grey dashed cityscape) and 37  $^\circ\text{C}$  (black cityscape) overlay quite well with the FRET population at 25  $^\circ\text{C}$ . Subsequently, to understand subpopulation dynamics underlying this OmpX state, 2D scatter plot depicting correlation of relative fluorescence lifetime of the donor,  $\tau_{D(A)}/\tau_{D(0)}$ , (ratio of lifetime of donor in presence and absence of acceptor, respectively) with FRET efficiency,  $E$ , was prepared. Using the relation between intensity weighted fluorescence lifetime and species weighted fluorescence FRET efficiency, one can distinguish a static population with configurational changes slower than a few milliseconds from a population exhibiting fast reconfiguration dynamics on the sub-millisecond timescale. Remarkably, the plot in Figure 5-1c shows that

OmpX<sub>aq</sub> is not composed of slowly reconfiguring polypeptide conformations as the population does not lie on the static FRET line (black line). It also does not behave like a Gaussian chain (red dashed line in Figure 5-1c) possibly due to presence of transient secondary structures or hydrophobic clusters as have been detected previously for denatured OmpX (121, 122). Strikingly, it appears that the OmpX<sub>aq</sub> state is comprised of a structural ensemble undergoing fast chain reconfiguration on a sub-millisecond time scale as it lies between the two lines. In addition to the unbound population, an additional small high  $E$  peak (at a fraction of  $\sim 10\%$ ) appears in all measurements and we attribute it to a compact collapsed state (also shown by the black dashed Gaussian fit curve in Figure 5-1b).

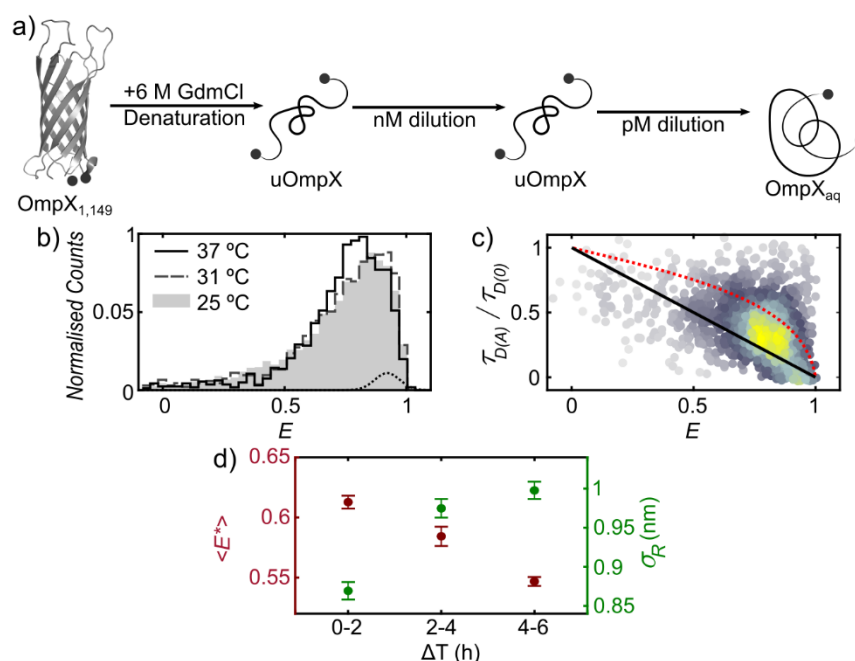


**Figure 5-1 - OmpX expands in an aqueous chaperone free environment while undergoing reconfiguration on sub-millisecond timescale.** a) Scheme of refolded double labelled OmpX<sub>1,149</sub> (2m06.pdb, (90)) dilution first to nanomolar concentration in 6 M GdmCl and then to picomolar concentration without the denaturant resulting in aqueous OmpX<sub>1,149</sub> (OmpX<sub>aq</sub>) state used for smFRET experiments in this section. b) FRET efficiency ( $E$ ) histograms of OmpX<sub>aq</sub> at three different temperatures (25 °C – grey bars, 31 °C – dashed dark grey cityscape and 37 °C – black cityscape) overlay well with each other and show a broad high FRET efficiency peak in each case. The Gaussian curve corresponding to the compact state is shown by the black dashed line. c) 2D plot between the relative lifetime of the donor ( $\tau_{D(A)}/\tau_{D(0)}$ ) and FRET Efficiency,  $E$  was created to examine interconversion dynamics of OmpX<sub>aq</sub>. The shift from the static FRET line (black line) indicates presence of sub-millisecond dynamics, although unbound OmpX does not behave like a Gaussian chain (red dashed line) either. d) The mean apparent FRET efficiencies ( $\langle E^* \rangle$ ) and distance width ( $\sigma_R$ ) of unbound state calculated at two subsequent time intervals  $\Delta T = 0-2, 2-4$  and  $4-6$  hours by applying two state PDA.

Lastly, the chaperone free OmpX population was examined as a function of time to check if the previously reported chain expansion of denatured OMPs is also a mechanism adopted by the OmpX<sub>aq</sub> to prevent aggregation. Taking into account the unbound and collapsed states, a two state Probability Distribution Analysis (PDA) was performed for populations obtained at every subsequent two hours, i.e. for the durations of 0-2, 2-4 and 4-6 hours. PDA is based on Monte-Carlo simulations which considers the limited photon statistic of measurement and enables extraction of the mean apparent FRET efficiency,  $\langle E^* \rangle$ , and the underlying width of the distance distribution,  $\sigma_R$ , of the compact and unbound state by fitting the  $E^*$  histograms with theoretical ones for each time interval (Table 5-1). The time evolution of  $\langle E^* \rangle$  and  $\sigma_R$  corresponding to the unbound state is presented in Figure 5-1d. Here, it is evident that the peak of the unbound state shifts towards lower FRET efficiencies and the population broadens (higher distance widths  $\sigma_R$ ) on the timescale of hours. It can be speculated that such an inter-conformational change possibly arises from the slow interconversion among the remaining secondary motifs of the aqueous OmpX chain.

$\Delta T$ (hours)	$p_{ub}$	$E_{ub}^*$	$E_c^*$	$\sigma_{ub}$ (nm)	$\sigma_c$ (nm)	$\chi^2$
0-2	$0.953 \pm 0.014$	$0.613 \pm 0.005$	$0.857 \pm 0.002$	$0.869 \pm 0.011$	$0.104 \pm 0.236$	5.39
2-4	$0.974 \pm 0.013$	$0.584 \pm 0.008$	$0.857 \pm 0.002$	$0.975 \pm 0.012$	$0.104 \pm 0.236$	3.06
4-6	$0.966 \pm 0.012$	$0.547 \pm 0.003$	$0.857 \pm 0.002$	$0.998 \pm 0.011$	$0.104 \pm 0.236$	1.91

**Table 5-1 - PDA fit for unbound OmpX expansion.** Probability of the unbound state ( $p_{ub}$ ), apparent FRET efficiencies of unbound ( $E_{ub}^*$ ) and compact state ( $E_c^*$ ) and the respective distance widths  $\sigma_{ub}$  (nm) and  $\sigma_c$  (nm) obtained from the two state PDA to show expansion. Best reduced chi square ( $\chi^2$ ) values are also given.

## 5.2 Trimeric Seventeen kilodalton protein (Skp<sub>3</sub>) and Survival factor A (SurA) bound OmpX is expanded and comprises of fast reconfiguring species

In order to probe the chaperone-bound conformations of OmpX, refolded and double labelled OmpX<sub>1,149</sub> was diluted as in the previous section such that the last dilution to picomolar concentration was now made in presence of different concentrations of Skp<sub>3</sub> or SurA (Figure 5-2a). Chaperone purifications were carried out as explained in Appendix Section 8.3.3. FRET efficiency ( $E$ ) histograms were then created from single molecule bursts using the same inter-photon noise (50  $\mu$ s) and minimum photon numbers of 40 as



before with  $ALEX-2CDE < 12$  and  $0.2 < S < 0.75$ . Additionally, a NG/NR filter of  $< 0.75$  and  $< 0.9$  was used for Skp<sub>3</sub> and SurA complexed OmpX<sub>1,149</sub> measurements. Gaussian fitting of either lifetime or/and FRET efficiency filtered molecules was performed to determine the peak and centre position of the individual states (chaperone bound, unbound and collapsed OmpX populations as explained in Appendix Section 8.3.6). In the first step, the bound OmpX is put to focus by discerning the  $E$  histograms of the measurements with high chaperone concentrations of 2500 nM Skp and 25000 nM SurA (last right panel of Figure 5-2b and Figure 5-2c, respectively) at the physiological temperature (37 °C). Here, unlike the high  $E$  state of unbound OmpX<sub>1,149</sub> in previous section, a lower  $E$  population corresponding to an expanded conformation representing the bound substrate is observed. Specifically, while the Skp<sub>3</sub> bound OmpX<sub>1,149</sub> demonstrates a broad peak in the low to mid  $E$  range ( $\langle E \rangle \sim 0.5$ ), SurA bound OmpX<sub>1,149</sub> covers a mid to high  $E$  region ( $\langle E \rangle \sim 0.6$ ). This indicates a difference in the end-to-end distance between the two heterogeneous chaperone-bound OmpX populations.

To evaluate the temperature dependence of chaperone complex formation and its effect on the conformation of OmpX, smFRET measurements were performed for OmpX<sub>1,149</sub> complexed with a range of chaperone concentrations and at two more temperatures (31 °C and 37 °C). The required temperature throughout the measurement was maintained using an objective collar linked to a refrigerated circulator (F25-MC, Julabo, Germany). The  $E$  histograms for measurements with Skp<sub>3</sub> and SurA at all these temperatures with different concentrations of the chaperone are shown in Figure 5-2b and Figure 5-2c, respectively. The centre positions of the FRET efficiencies which are the same as  $\langle E \rangle$  and the widths ( $\sigma_E$ ) of the bound, unbound (similar to OmpX<sub>aq</sub>) and compact states were then obtained using these  $E$  histograms. The trend followed by these two quantities is shown in Figure 5-3a and Figure 5-3b, respectively. The unbound and compact FRET states and their widths vary negligibly across temperature, concentration and the chaperone under consideration. However, strikingly, compared to the uniformity among the Skp<sub>3</sub> bound OmpX<sub>1,149</sub> (yellow error bars) across different concentrations at each temperature, the end-to-end distance increases for SurA bound OmpX<sub>1,149</sub> (blue error bars) with increasing concentration of chaperone regardless of the measurement temperature. This highlights the possibility of greater number of SurA monomers binding to the OmpX polypeptide at higher concentrations in a possible ‘beads-on-string’ fashion.

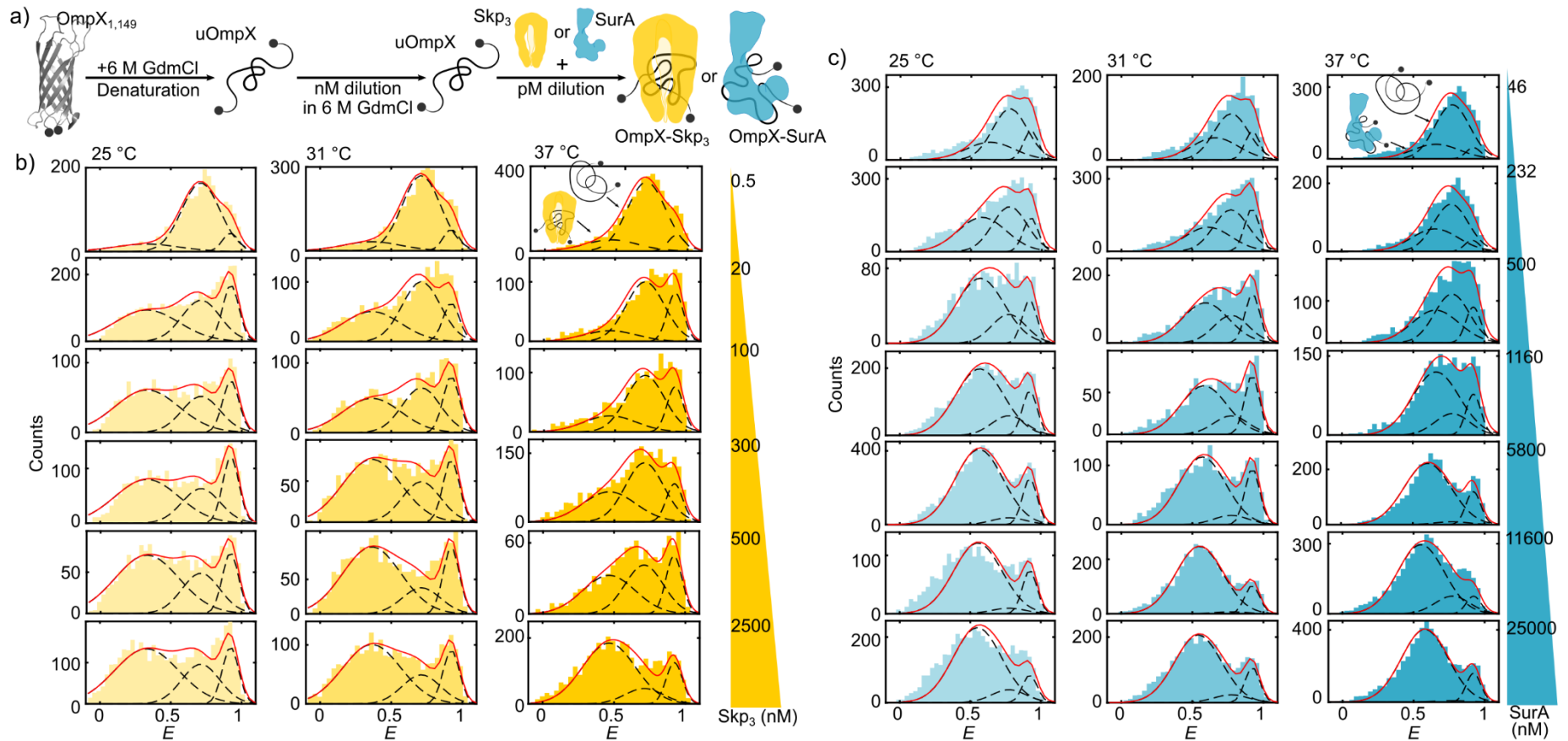


**Figure 5-2 - FRET efficiency histograms of trimeric seventeen kilodalton protein (Skp<sub>3</sub>) and Survival factor A (SurA) bound OmpX<sub>1,149</sub>.** a) Dilution scheme of refolded double labelled OmpX<sub>1,149</sub>. It was first diluted to nanomolar concentration in 6 M GdmCl and then to picomolar concentration without the denaturant in presence of different concentration of chaperone (Skp<sub>3</sub> or SurA as indicated) to perform smFRET experiments. b) FRET efficiency histograms of Skp<sub>3</sub> (0.5, 20, 100, 300, 500 and 2500 nM) complexed OmpX<sub>1,149</sub> at 25 °C, 31 °C and 37 °C c) FRET efficiency histograms of SurA (46, 232, 500, 1160, 5800, 11600 and 25000 nM) complexed OmpX<sub>1,149</sub> at 25 °C, 31 °C and 37 °C. Gaussian fits were performed according to Appendix Section 8.3.6 for the three states: bound, unbound and compact and are shown with black dashed lines along with the overall fit indicated by the red line for both Skp<sub>3</sub> and SurA containing measurements.

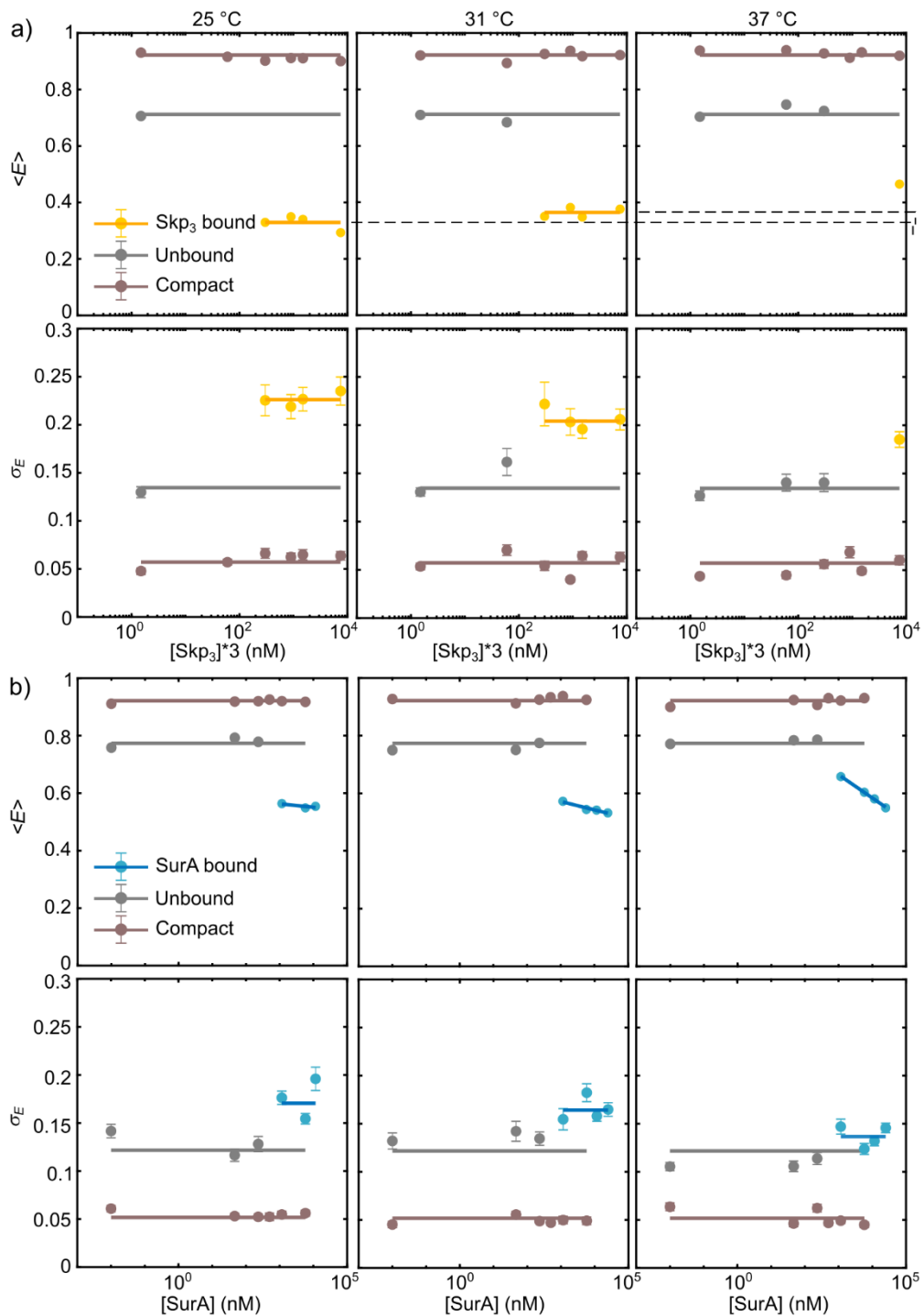


**Figure 5-3 - Trend of chaperone complexed FRET states.** a) Average FRET efficiencies of three states (Skp<sub>3</sub> bound, unbound and compact) are plotted against Skp<sub>3</sub> concentration. While the compact (maroon) and unbound FRET (grey) states and their widths ( $\sigma_E$ ) do not change with temperature or concentration, the average FRET efficiency ( $\langle E \rangle$ ) of the bound state (yellow) decreases with increase in temperature, b) Average FRET efficiencies of three states (SurA bound, unbound and compact) are plotted against SurA concentration. Similar to Skp<sub>3</sub> complexed OmpX<sub>1,149</sub> states, the compact (maroon) and unbound FRET (grey) states and their  $\sigma_E$  do not change with temperature or concentration,  $\langle E \rangle$  of the SurA bound state (blue) increases with increase in concentration at each temperature. The fit  $\langle E \rangle$  and  $\sigma_E$  are reported in Table 1-2.

Temp	$\langle E_b \rangle$	$\langle E_{ub} \rangle$	$\langle E_c \rangle$	$\langle \sigma_{E-b} \rangle$	$\langle \sigma_{E-ub} \rangle$	$\langle \sigma_{E-c} \rangle$
<b>Skp<sub>3</sub>:</b>						
25 °C	0.33 ± 0.02	0.71 ± 0.01	0.922 ± 0.003	0.226 ± 0.005	0.135 ± 0.008	0.0572 ± 0.002
31 °C	0.36 ± 0.02	0.71 ± 0.01	0.922 ± 0.003	0.204 ± 0.008	0.135 ± 0.008	0.0572 ± 0.002
37 °C	0.47 ± 0.01	0.71 ± 0.01	0.922 ± 0.003	0.185 ± 0.008	0.135 ± 0.008	0.0572 ± 0.002
<b>SurA:</b>						
25 °C	-0.00509×log([SurA]) + 0.598	0.774 ± 0.006	0.922 ± 0.002	0.17 ± 0.02	0.122 ± 0.006	0.052 ± 0.001
31 °C	-0.0127×log([SurA]) + 0.659	0.774 ± 0.006	0.922 ± 0.002	0.164 ± 0.009	0.122 ± 0.006	0.052 ± 0.001
37 °C	-0.350×log([SurA]) + 0.906	0.774 ± 0.006	0.922 ± 0.006	0.1366 ± 0.009	0.122 ± 0.006	0.052 ± 0.001

**Table 5-2 - Average FRET efficiencies of each FRET state upon complexing OmpX with chaperones.** bound:  $\langle E_b \rangle$ , unbound:  $\langle E_{ub} \rangle$  and compact:  $\langle E_c \rangle$  and their widths (bound:  $\langle \sigma_{E-b} \rangle$ , unbound:  $\langle \sigma_{E-ub} \rangle$  and compact:  $\langle \sigma_{E-c} \rangle$ ) for both Skp<sub>3</sub> and SurA binding.

Furthermore, it was found that the width of the chaperone bound OmpX population (obtained at 2500 nM Skp<sub>3</sub> and 11600 nM SurA at 37 °C) exceeded a distribution that would be limited by the average shot noise (red cityscape line) as shown in Figure 5-4a and 5-4b demonstrating that the bound polypeptide is composed of a heterogeneous structural ensemble. To gain insight into the subpopulation dynamics underlying this set of chaperone-bound diverse conformations of OmpX, 2D scatter plot between the relative lifetime of donor,  $\tau_{D(A)}/\tau_{D(0)}$  and FRET efficiency,  $E$  for 2500 nM and 11600 nM for Skp<sub>3</sub> and SurA complexed OmpX<sub>1,149</sub> measurements were created as shown in Figure 5-4c and 5-4d, respectively. From a visual inspection, it is clear that the bound states are displaced from the static FRET line suggesting that the chaperone bound substrate like unbound OmpX undergoes fast configurational changes on the sub-millisecond timescale.

Subsequently, the configurational space of the bound and unbound populations was modelled by using a log-normal distribution with distance width  $\sigma_R$  and an expected inter-dye distance  $\mu_R$  (an example of which is shown in inset of Figure 5-4e). Interestingly, Skp<sub>3</sub> bound and the SurA bound (yellow and blue in Figure 5-4e, respectively) states appear to cluster around separate dynamic lines for varying temperature and concentration. The clusters were then fitted globally with a shared  $\sigma_R$  and the floating parameter  $\mu_R(E)$  as described in Appendix Section 8.3.6. Finally, the coefficient of variance  $CV = \sqrt{e^{\sigma_R^2} - 1}$

was calculated to measure the heterogeneity of a population with varying inter-dye distances. When investigating the bound state, only the measurements containing a significant fraction of complexed molecules were inspected (with >100 nM Skp<sub>3</sub> and >1160 nM SurA as reported in Appendix Section 8.3.6). The unbound states (grey in Figure 5-4e) were obtained from the measurements in previous section.

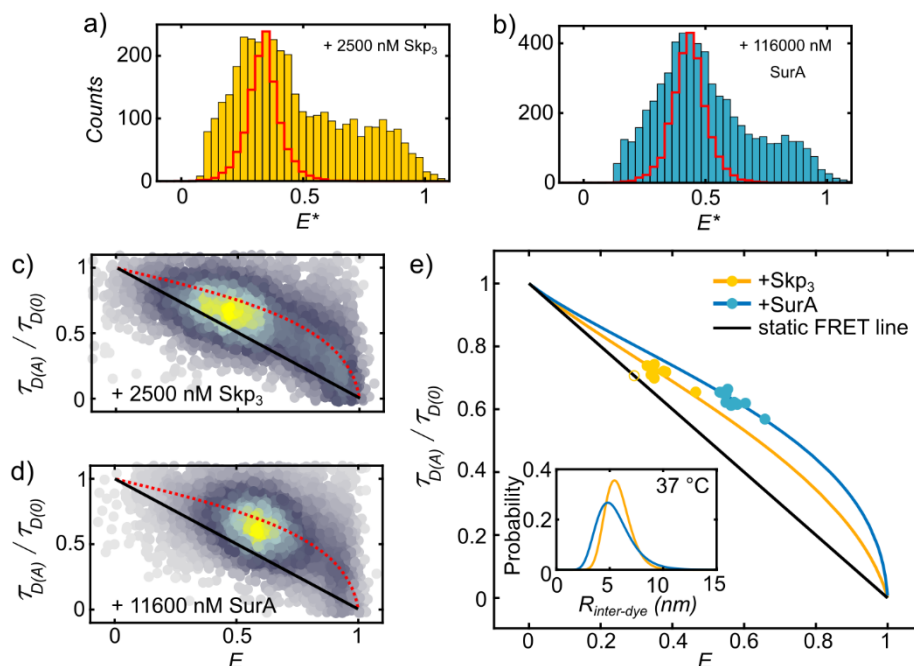


**Figure 5-4 – Fast chain reconfiguration among the chaperone bound states of OmpX.** Apparent FRET efficiency ( $E^*$ ) histogram of OmpX with a) 2500 nM Skp<sub>3</sub> (yellow bars) and b) 11600 nM SurA (blue bars) showing that the bound OmpX population is heterogeneous as it is not shot noise limited (red cityscape). 2D plot between the relative lifetime of the donor ( $\tau_{D(A)}/\tau_{D(0)}$ ) and FRET Efficiency,  $E$  was created to examine interconversion dynamics of chaperone bound OmpX for c) OmpX<sub>1,149</sub> smFRET measurement in presence of 2500 nM Skp<sub>3</sub> and d) 11600 nM SurA. The shift from the static FRET line (black line) indicates presence of sub-millisecond reconfiguration dynamics although in both the cases, bound OmpX does not behave like a Gaussian chain (red dashed line) possibly due to steric hindrance at the binding regions. e) The plot of average relative lifetime of donor ( $\langle \tau_{D(A)}/\tau_{D(0)} \rangle$ ) vs FRET efficiency ( $E$ ) for OmpX<sub>1,149</sub> measurements in presence of different concentrations of Skp<sub>3</sub> (yellow spheres) and of SurA (blue spheres) on considering that the population follows a log normal distribution. Except for OmpX complexed with 2500 nM Skp<sub>3</sub> (yellow circle), all the other data points show a shift from the static FRET such that the free OmpX lies between the Skp<sub>3</sub> and SurA bound OmpX population. The inset shows the end-to-end distance without linker correction ( $R_{inter-dye}$ ) of chaperone bound OmpX<sub>1,149</sub> (yellow and blue lines correspond to OmpX measurement with 2500 nM Skp<sub>3</sub> and 11600 nM SurA).

As seen in Figure 5-4c, remarkably, the population corresponding to unbound OmpX lies in between the Skp<sub>3</sub> and SurA bound OmpX<sub>1,149</sub>, indicating that OmpX adopts less configurations within the Skp<sub>3</sub> bound state and more in the SurA bound state compared to the unbound state. This is supported by the determined CVs of  $0.25 \pm 0.02$ ,  $0.20 \pm 0.04$  and  $0.30 \pm 0.02$  for unbound, Skp<sub>3</sub> bound and SurA bound OmpX<sub>1,149</sub>, respectively. The increased conformational space of OmpX in the SurA bound state together with its expansion upon increasing concentration of the chaperone suggests that multiple SurA monomers dissolve the remaining secondary structure and/or avoid the collapse of their substrate. In contrast, Skp<sub>3</sub> encapsulates and reduces the conformational space of OmpX while expanding its substrate possibly through multiple interactions within the cavity.

Further, the inter-dye distance of chaperone bound OmpX<sub>1,149</sub> indicates that the end-to-end distance without linker correction is higher for Skp ( $5.78 \pm 0.05$  nm) as compared to SurA ( $5.50 \pm 0.05$  nm) (inset of Figure 5-4e), a direct result of possible expansion upon chaperone association. This distance for Skp bound OmpX obtained here is in good agreement with the previously reported spherical volume radius of 21 Å on considering it as a polypeptide ensemble (103). In summary, in this section it is discerned that the binding of holdase chaperones SurA and Skp to OmpX results in latter's expansion in a dynamic manner. Remarkably, despite a difference in interaction mechanism, the two periplasmic chaperones can maintain their substrate in not only a folding competent state but also in a conformation capable of being handed over to the BAM complex.

### 5.3 SurA interacts with OmpX at a relatively low entropic cost

A comprehensive biophysical picture of chaperone-OMP binding demands that we gain a thermodynamic understanding of their interactions. As described in Section 2.2.3, the information about energetic parameters of change in enthalpy and entropy ( $\Delta S$  and  $\Delta H$ , respectively) is ciphered in the temperature dependency of the association constant,  $K_a$ . Thus, on combining the previously performed smFRET measurements for three temperatures (25 °C, 31 °C and 37 °C) and increasing chaperone concentration for a global thermodynamic analysis, it was possible to gain an insight into these two energetic parameters.

A methodological workflow of the analysis steps is shown in Figure 5-5a. Briefly, the set of histograms were globally fitted using the shared variables  $\Delta H$  and  $\Delta S$  (change in enthalpy and entropy) along with the fraction of compact state,  $f_{c,T}$ , and the maximum fraction of bound OmpX,  $f_{b,max}$ . During optimization for each pair of  $\{\Delta H, \Delta S\}$  the corresponding association constants,  $K_a(T)$ , were calculated for the respective measurement temperature using eq. (11) as illustrated by the van't Hoff plot shown in Figure 5-5a. The resulting association constants were then used to determine the individual theoretical fraction of bound OmpX,  $f_b$  by the Hill equation (eq. (7)). The Hill coefficients of binding were kept constant at 1 and 1.5 for OmpX-Skp<sub>3</sub> and OmpX-SurA interaction, respectively (34, 103, 106, 116)). It should be noted that we have considered the trimeric Skp concentration simply by dividing the monomeric concentration by 3 as it was rapidly diluted from a stock (~75  $\mu$ M) with a concentration much higher than  $c_{1/2}$  (108) as fast equilibration with OmpX was observed. Moreover, a recent study has shown that exposure of OMPs drives Skp to an active trimer form (109). Nevertheless, a case where the trimeric concentration was chosen according to the previously published data (108) is also enumerated in Table 5-3.

In the next step, using the FRET parameters (centre position and width of the individual FRET efficiency population) from the previous section and the amplitudes  $f_b(1-f_{c,T})$ ,  $(1-f_b)(1-f_{c,T})$  and  $f_{c,T}$ , FRET distribution was calculated for every measurement condition. Finally, the overall reduced Chi-square ( $\chi^2$ ) was calculated from the residuum of the theoretical and measured FRET efficiency curves. Upon varying the optimization parameters  $\{\Delta H, \Delta S, f_{c,T}, f_{b,max}\}$  the reduced  $\chi^2$  was minimized to find the best estimators for the change in enthalpy and entropy. The errors of the fitted thermodynamic parameters were derived from 200 bootstrapping steps, where for each measurement condition FRET efficiency histograms were constructed from randomly drawn bursts.

The apparent dissociation constants at the physiological temperature are determined to be  $(358.88 \pm 0.02)$  nM and  $(407.40 \pm 0.07)$  nM for Skp<sub>3</sub> and SurA, respectively which are in good agreement with the previously reported values for OMP-chaperone interactions (34, 105, 116). The best estimators of  $\Delta H$  and  $\Delta S$  values of OmpX – Skp<sub>3</sub> interaction are found to be  $(-297.74 \pm 19.06)$  kJ·mol<sup>-1</sup> and  $(-0.84 \pm 0.06)$  kJ·mol<sup>-1</sup>·K<sup>-1</sup>, respectively (yellow set in Figure 5-5b). On the other hand,  $\Delta H$  and  $\Delta S$  values for OmpX- SurA interaction are found to be  $(-132.3 \pm 24.29)$  kJ·mol<sup>-1</sup> and  $(-0.24 \pm 0.08)$  kJ·mol<sup>-1</sup>·K<sup>-1</sup>, respectively (blue

set in Figure 5-5b). All the fitting parameters and the influence of the Hill coefficient ( $n$ ) on the OmpX-SurA interaction is shown in Table 5-3.

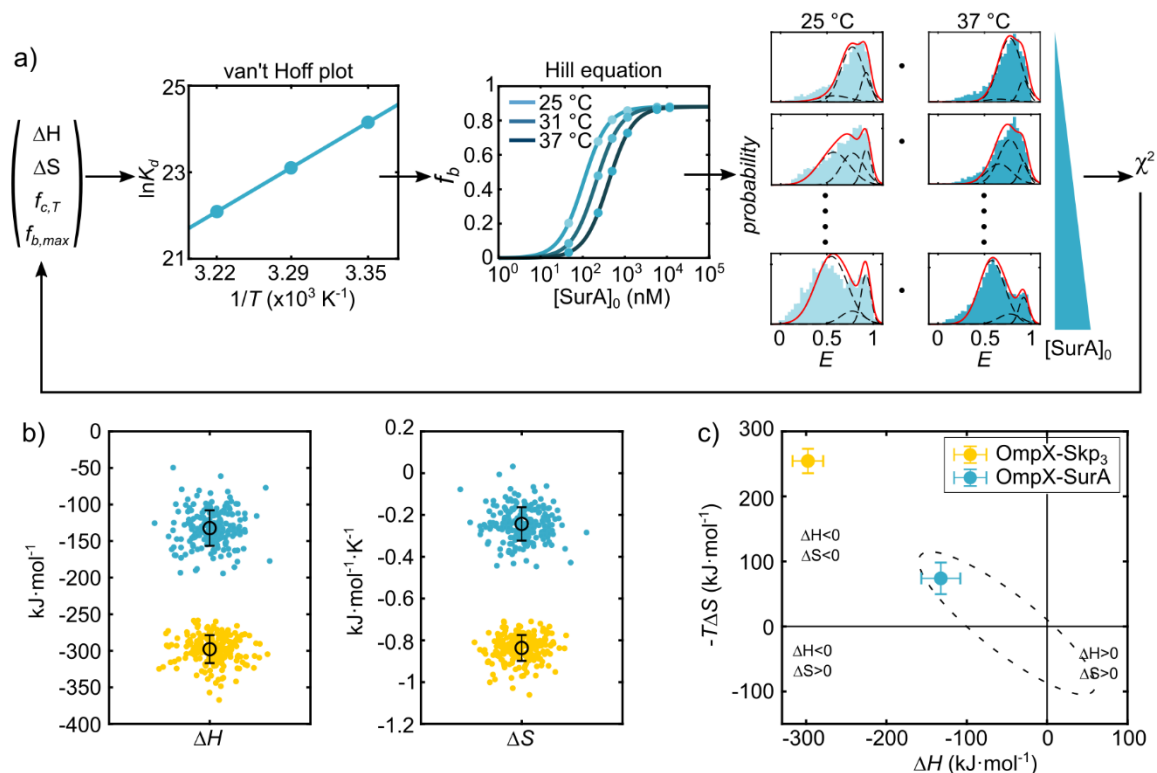


**Figure 5-5 - Interaction between SurA and OmpX is characterised by a relatively lower entropic change.** a) Scheme for global reduced  $\chi^2$  minimization to obtain enthalpic change  $\Delta H$  and entropic change  $\Delta S$  for OmpX + Skp3 and OmpX + SurA interactions with the theoretical van't Hoff plot and Hill equation fitting:  $\Delta H$ ,  $\Delta S$ ,  $f_{c,T}$  (fraction of compact OmpX at each temperature) and  $f_{b,max}$  (maximum fraction of bound OmpX) were the varying fitting parameters.  $\ln K_d$  is the natural logarithm of the dissociation constant, T is the temperature in Kelvin (K) and  $[\text{SurA}]_0$  is the initial SurA concentration in nanomolar. b) All the  $\Delta H$  ( $\text{kJ}\cdot\text{mol}^{-1}$ ) and  $\Delta S$  ( $\text{kJ}\cdot\text{mol}^{-1}\cdot\text{K}^{-1}$ ) values obtained from bootstrapping algorithm for OmpX-Skp3 (yellow) and OmpX-SurA (blue) interaction are indicated and the  $\langle \Delta H \rangle$  and  $\langle \Delta S \rangle$  are shown as a black circle with an error bar and c) The calculated  $\langle \Delta H \rangle$  and  $\langle \Delta S \rangle$  for OmpX-Skp3 and OmpX-SurA are overlaid on the spread of data points as reported in review by Heller et. al (195).

Here, the enthalpic change is defined as a characteristic of binding between the chaperone and the substrate OmpX and represents the change in inter- and intra-molecular bond energy and the entropic change majorly corresponds to the change in count of accessible configurations of OmpX. As expected, the OmpX-chaperone binding resulted in a big negative enthalpic change showing a favourable association with multiple binding regions



( $\Delta H_{inter} \ll \Delta H_{intra}$ ). The negative change in the entropy, on the other hand, suggests a reduction of the configurational space for OmpX in the bound state such that it was much lower upon binding of Skp<sub>3</sub> as compared to SurA. Interestingly, compared to Skp<sub>3</sub> – OmpX interaction which showed a relatively high negative  $\Delta H$  and  $\Delta S$ , more than two times smaller  $\Delta S$  and a decent  $\Delta H$  was observed as characteristic for small ligand binding (dashed area obtained from (Heller et al., 2015) in Figure 5-5c) for the SurA-OmpX interaction.

This suggests that while both the chaperones interact through multiple binding sites with their substrate OmpX (non-specific in case of Skp and specific in case of SurA), the SurA bound OmpX has more freedom towards conformational interconversion as compared to the Skp<sub>3</sub> encapsulated OmpX.

Chaperone	<i>n</i>	$\Delta H$ (kJ·mol <sup>-1</sup> )	$\Delta S$ (kJ·mol <sup>-1</sup> ·K <sup>-1</sup> )	$f_{c-25}$	$f_{c-31}$	$f_{c-37}$	$f_{b,max-25}$
SurA	1	-75 ± 12	-0.12 ± 0.04	0.118 ± 0.008	0.14 ± 0.01	0.11 ± 0.01	0.92 ± 0.01
SurA	1.5	-132 ± 24	-0.24 ± 0.08	0.119 ± 0.008	0.141 ± 0.009	0.111 ± 0.008	0.88 ± 0.01
Skp <sub>3</sub> ([Skp]/3)	1	-298 ± 19	-0.84 ± 0.06	0.195 ± 0.003	0.184 ± 0.007	0.179 ± 0.006	0.69 ± 0.01
Skp <sub>3</sub> (108)	1	-480 ± 21	-1.42 ± 0.07	0.195 ± 0.004	0.188 ± 0.005	0.183 ± 0.006	0.70 ± 0.01

$f_{b,max-31}$	$f_{b,max-37}$	$c_{1/2-25}$ (nM)	$c_{1/2-31}$ (nM)	$c_{1/2-37}$ (nM)	$\Delta G_{25}$ (kJ·mol <sup>-1</sup> )	$\Delta G_{31}$ (kJ·mol <sup>-1</sup> )	$\Delta G_{37}$ (kJ·mol <sup>-1</sup> )	$\chi^2$
0.92 ± 0.01	0.92 ± 0.01	109.67 ± 0.01	199.06 ± 0.02	356.05 ± 0.06	-39.7 ± 0.3	-39.0 ± 0.3	-38.3 ± 0.4	3.83
0.88 ± 0.01	0.88 ± 0.01	102.89 ± 0.02	205.94 ± 0.02	407.40 ±0.07	-59.9 ± 0.6	-58.4 ± 0.4	-56.9 ± 0.6	3.97
0.81 ± 0.02	0.998 ± 0.004	3.5536 ± 0.0009	36.993 ± 0.005	358.88 ± 0.02	-48.3 ± 0.7	-43.3 ± 0.3	-38.3 ± 0.2	3.19
0.77 ± 0.01	0.98 ± 0.05	0.0889 ± 0.0001	3.9424 ± 0.0001	154.39 ± 0.03	-57.5 ± 0.9	-49.0 ± 0.7	-40.5 ± 0.7	3.46

**Table 5-3 - Thermodynamic parameters of OmpX-chaperone interaction.** Enthalpic change ( $\Delta H$ ) and entropic change ( $\Delta S$ ) are obtained for OmpX-Skp and OmpX-SurA interactions through global  $\chi^2$  minimization.  $c_{1/2-25}$ ,  $c_{1/2-31}$  and  $c_{1/2-37}$  denotes the half association concentration at 25 °C, 31 °C and 37 °C, respectively with *n* as the hill coefficient.  $f_{c-25}$ ,  $f_{c-31}$  and  $f_{c-37}$  are the fractions of compact OmpX state at 25 °C, 31 °C and 37 °C and  $f_{b-max-25}$ ,  $f_{b-max-31}$ ,  $f_{b-max-37}$  is the fraction of chaperone bound OmpX at 25 °C, 31 °C and 37 °C, respectively. It was the same for SurA at all temperatures. The free energy of interaction so obtained at each temperature are also reported:  $\Delta G_{25}$  at 25 °C,  $\Delta G_{31}$  at 31 °C and  $\Delta G_{37}$  at 37 °C.

Yet, the balance in the enthalpic and entropic terms for both the chaperone interactions lead to a favourable  $\Delta G$  (at 37 °C) of interaction:  $(-38.28 \pm 0.18)$  kJ·mol<sup>-1</sup> and  $(-56.96 \pm 0.64)$  kJ·mol<sup>-1</sup> for OmpX-Skp<sub>3</sub> and OmpX-SurA binding, respectively. Many previous studies have reported free energy of folding for OMPs in the range of -30 to 160 kJ·mol (126, 196, 197). On the other hand, some studies have shown that the free energy of chaperone-OMP interactions resides in the range of -30 to -55 kJ·mol<sup>-1</sup> (105, 197, 198). It is indeed possible that the free energy of folding is lower than the free energy of interaction such that a sink is formed in order to enable folding of OMPs when they encounter the outer membrane. However, it must be noted that the folding of OMPs on the outer membrane is a rather complicated process with an involvement of  $\beta$ -barrel machinery as well and thus a free energy comparison based solely on folding into detergents or micelles in absence of chaperones and BAM is incomplete. For instance, an estimation of  $\Delta G$  from the OmpX<sub>1,149</sub> unfolding experiments documented in Section 4.1.1 appears to be much higher ( $\sim$ 15 kJ·mol<sup>-1</sup>) than the interaction free energies calculated for OMP-chaperone interactions in this section. Nevertheless, with regards to the developing hypothesis in this field (17, 37), our investigations here provide an exciting functional insight into the energetics of bio-molecular interactions.

## 5.4 Skp and SurA act as disaggregases under cellular stress

Stress induced over-expression of OMPs might lead to their aggregation in the periplasmic environment. Under such conditions, cells are known to employ the protease DegP to disaggregate the OMP precipitates (27, 112). However, as was recently reported, Skp might also act as a stress chaperone (194), bringing into light the need to decipher if more than one chaperone is capable of acting upon the aggregated OMPs.

In this work, to investigate the action of chaperones against aggregated OmpX (OmpX<sub>Agg</sub>), Fluorescence Correlation Spectroscopy (FCS) was used (Section 2.3.4). In a first step, OmpX<sub>1,149</sub> measurements were conducted at a low concentration (10 pM) followed by the OmpX<sub>Agg</sub> measurements at three different temperatures (25 °C, 31 °C and 37 °C). To achieve the latter, 1  $\mu$ M unlabelled unfolded OmpX (uOmpX) was mixed with 30 pM labelled uOmpX in the assembly buffer so as to enable aggregation without denaturant, chaperones and detergent (Figure 5-6a). After 10 mins of incubation, neither, either or both

Skp<sub>3</sub> and SurA in their periplasm like concentrations (2500 nM and 5800 nM, respectively) were added to examine the effect of chaperones on the OmpX<sub>Agg</sub>. FCS curves were then obtained by probing for just the acceptor photons. The autocorrelation curves (fitted according to eq. (25), Appendix Section 8.3.7) corresponding to OmpX<sub>Agg</sub> measurements without chaperones at all the temperatures show an increase in amplitude at a delay time of around 30 ms (Figure 5-6b) indicating presence of aggregates.

At the physiological temperature, while the aqueous OmpX<sub>1,149</sub> showed a diffusion time ( $\tau_D$ ) of  $(0.27 \pm 0.002)$  ms, the diffusion time of aggregated OmpX (OmpX<sub>Agg</sub>) was determined to be  $(31.6 \pm 1.3)$  ms. It should be taken into account that the afore-mentioned OmpX<sub>Agg</sub> is possibly an ensemble of differently sized oligomers or aggregates. The diffusion times of 2500 nM Skp<sub>3</sub> and 5800 nM SurA complexed OmpX<sub>1,149</sub> measurements were determined to be  $(1.79 \pm 0.05)$  ms and  $(1.38 \pm 0.03)$  ms, respectively (Figure 5-6c).

Now, having obtained the diffusion times of each species, it was possible to determine the fraction of OmpX<sub>Agg</sub>, aqueous OmpX<sub>1,149</sub>, and chaperone bound OmpX<sub>1,149</sub> from the FCS curves. All the autocorrelation curves with different reaction schemes at the physiological temperature are depicted in Figure 5-6d. Interestingly, the measurement with 1  $\mu$ M OmpX showed a significant fraction of OmpX<sub>Agg</sub> ( $0.24 \pm 0.02$  – green bar) at 37 °C, although the fraction of aggregated OmpX seemed to decrease with decreasing temperature. However, presence of aggregates at every mentioned temperature at even a micromolar concentration of OmpX, highlights the need to avoid ensemble techniques requiring micromolar concentrations when studying aggregation prone proteins like OMPs.

Upon introduction of the two chaperones separately to the aggregated OmpX sample (green bars in Figure 5-6e), it was observed that compared to Skp, SurA disaggregates OmpX<sub>Agg</sub> more efficiently as shown by a greater decrease in the aggregated fraction ( $0.13 \pm 0.01$ ) as compared to that on addition of Skp ( $0.20 \pm 0.02$ ). Strikingly, the decrease in OmpX<sub>Agg</sub> in both the cases results in a corresponding increase of the aqueous OmpX<sub>1,149</sub> fraction ( $0.87 \pm 0.08$ , grey bars in Figure 5-6e) instead of an increase in the chaperone bound OmpX fraction (purple bars in Figure 5-6e). Assuming, uniform mixing of labelled and unlabelled OmpX sample, the previous observation indicates that the chaperones have a higher affinity towards aggregated OmpX as compared to OmpX<sub>aq</sub>.

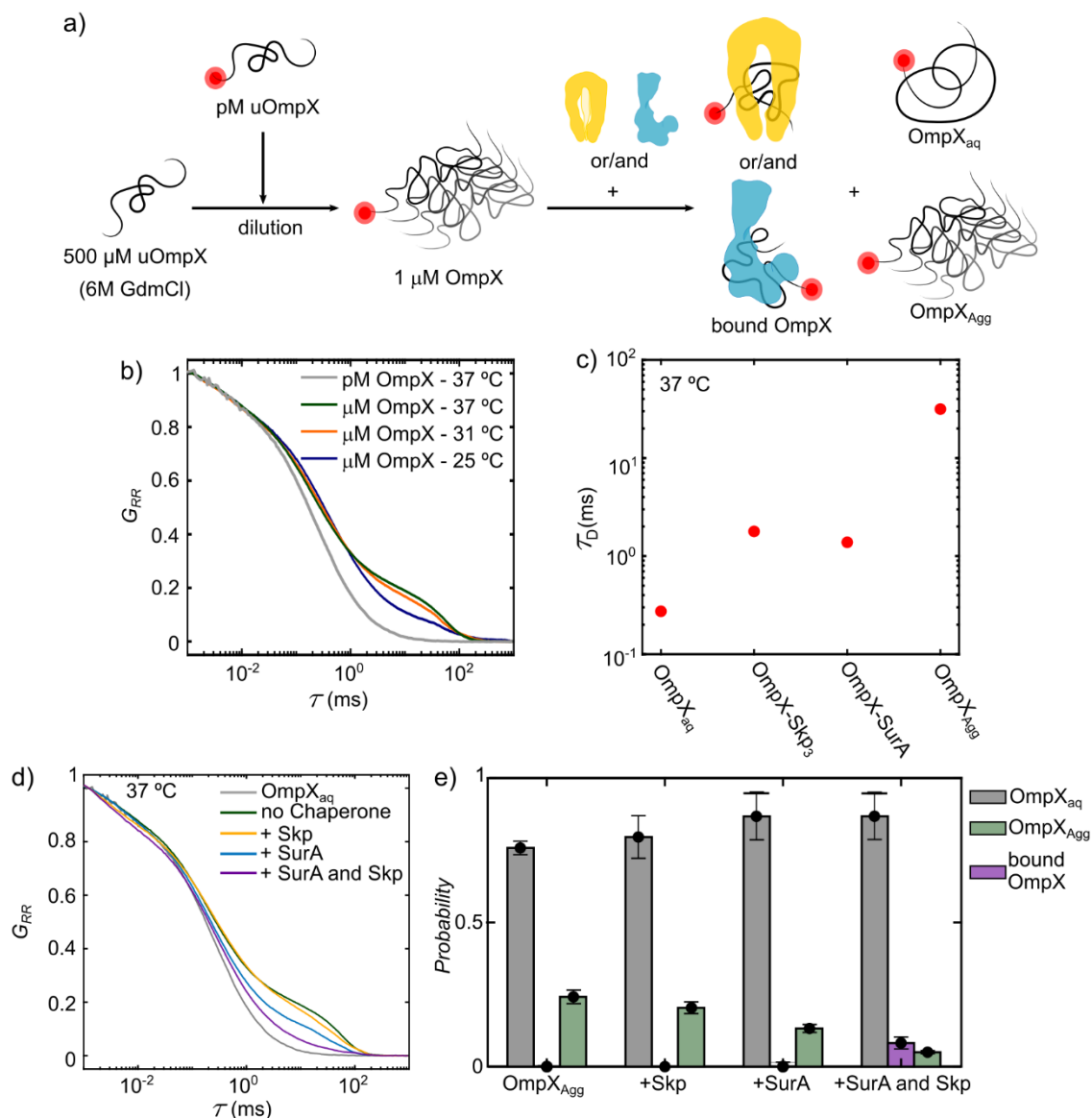


**Figure 5.6 - The disaggregating property of Skp and SurA.** a) Dilution scheme to investigate OmpX disaggregation capabilities of chaperones Skp and SurA, uOmpX denotes the unfolded OmpX, OmpX<sub>Agg</sub> is the aggregated OmpX. b) Autocorrelation curves demonstrating the diffusion times ( $\tau$ ) of OmpX<sub>Agg</sub> at three different temperatures (25 °C (blue), 31 °C (orange) and 37 °C (green)). c) Diffusion times ( $\tau_D$ ) of OmpX<sub>Aq</sub>, OmpX complexed with 2500 nM Skp<sub>3</sub> and 5800 nM SurA and OmpX<sub>Agg</sub> at 37 °C obtained from the acceptor autocorrelation curves for each of these measurements, the errors are small and not visible in the plot, but can be found in the main text. d) Autocorrelation curves demonstrating the diffusion times of OmpX aggregation at 37 °C (green line) where  $G_{RR}$  is the normalized autocorrelation coefficient of the acceptor dye and  $\tau$  is the diffusion time in ms. The disaggregating properties of chaperones Skp (blue line) and SurA (red line) individually and both together (purple line) is apparent from the autocorrelation curves for the respective measurements. e) The probability of OmpX<sub>Aq</sub> (grey bar), chaperone bound OmpX (purple bar) and OmpX<sub>Agg</sub> (green bar) in different measurement conditions as in the previous plot.

Remarkably, when both the chaperones were together added to the OmpX<sub>Agg</sub> mixture, we find that the fraction of OmpX<sub>Agg</sub> (0.05) is reduced as compared to measurements with individual chaperones. Intriguingly, it is also lower than the theoretical added fractions of individual chaperone measurements (0.09) which indicates a cooperativity between the two proteins. In addition, a small fraction of chaperone bound OmpX around 8% can also be observed for the last case. This suggests that the chaperones might elevate the binding affinity of each other to the OmpX when present together. These findings address the need for presence of two different chaperones widely speculated to be functioning redundantly. It is plausible to expect that stress induced OMP aggregates are rescued back to a folding competent OmpX form when both the chaperones function together. Indeed, SurA-Skp deletion mutants have resulted in lethal phenotypes when probed both experimentally (27) and by simulations (24). However, their cooperativity in normal condition still needs to be investigated.

## 5.5 Summary

Avoiding the artefacts due to aggregation and ensemble averaging, in this chapter, a rather comprehensive picture of SurA and Skp<sub>3</sub> action on OmpX has been deciphered. On probing the conformation of chaperone bound OmpX, it was found that both SurA and Skp<sub>3</sub> expand OmpX. Remarkably, the bound OmpX similar to unbound OmpX was also found to undergo sub-millisecond reconfiguration. Such an expansion of the bound protein might not only prevent aggregation but also facilitate recognition by the BAM complex. A mechanism prominently observed for the cytoplasmic chaperone DnaK-bound polypeptides (Kellner et al., 2014). Furthermore, the intricate balance in kinetics and energetics was seen to be maintained for chaperone action so as to keep the bound OmpX in a folding competent state. This follows from the finding that the large configurational space of the substrate OmpX when bound to SurA results in a significant lowering of entropic change despite a relatively low enthalpic change making these chaperone-OmpX interactions thermodynamically favourable. Thus, in addition to the enthalpic component contributed by multiple interactions, the resulting increase in the entropy of the bound state keeps it both unfolded and complexed to the chaperone at the same time. However, when confined within the Skp<sub>3</sub> cavity, it appears that it is indeed the multiple interactions between

OmpX and Skp<sub>3</sub> that results in a high enthalpic change making this interaction as favourable as that of OmpX with SurA.

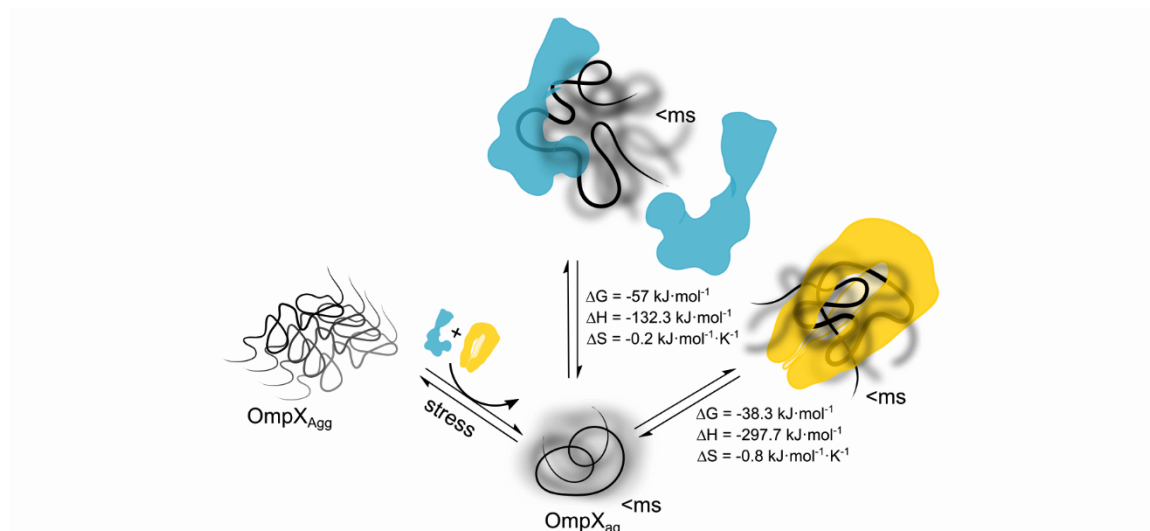


**Figure 5-7 - Summary of chaperone-OmpX interactions.** Model of Skp<sub>3</sub> and SurA chaperone action on OmpX: In this work, a thorough examination of the conformation and dynamics of OmpX with and without chaperones was performed through smFRET. It was found that OmpX exhibits sub-millisecond dynamics in aqueous solution and when bound to the chaperones. Remarkably, chaperone-bound OmpX is expanded such that the SurA bound substrate possess greater heterogeneity than both the free and Skp bound OmpX. Furthermore, the thermodynamic parameters governing these chaperone-OMP interactions were also elucidated as shown in the figure. Lastly, using FCS, it was demonstrated that OmpX aggregates even at micromolar concentration and both the chaperones can act as disaggregases under stress conditions.

Lastly, it was found that both the chaperones solubilize aggregated OmpX possibly induced under external stress conditions. Increasingly, disaggregation mechanisms are being observed in the ATP dependent cytoplasmic chaperones of Hsp70 family, raising the possibility that the periplasmic chaperones too possess such characteristics. Hence, the observation that the ATP-independent chaperones Skp and SurA can also function as disaggregases especially in presence of each other, calls for attention beyond the chaperone DegP as a disaggregase in periplasm. Periplasm thus appears to harbour a highly effective dynamic system of chaperone-OMP associations very much like the cytoplasmic systems, which not only function to protect OMPs from aggregation but can also rescue them when required. A model of these findings is shown in Figure 5-7.

*Outlook:* The analysis in this chapter was done based on a valid assumption that in these experiments, Skp was always in a trimeric state when binding and bound to OmpX. In future, it will be of great value to probe the monomer affinity and trimerization activity in presence of its substrate OmpX by increasing the incubation times of diluted Skp through smFRET experiments. Such a premise might be important to consider as a significant amount of Skp is shown to be present in a monomer concentration at cellular concentrations (108). Fascinatingly, a recent investigation used NMR spectroscopy to demonstrate that Skp exists in a disordered monomer conformation such that only upon exposure to its substrate the alpha-helices are fully folded and stapled into a trimer form (109). Furthermore, it will be interesting to see if there is any handover of the substrate OmpX between the two chaperones under normal cellular conditions as has been observed previously for a much bigger OMP: FhuA (33).





## Chapter 6 Trimeric Skp pushes and pulls OmpLA

Chaperone bound states of 12  $\beta$ -stranded OmpLA unlike many other OMPs are still not investigated to a great extent. Interestingly, bigger OMPs like OmpC, OmpF (both 16  $\beta$ -stranded) and FhuA (22  $\beta$ -stranded) have been complexed with Skp and/or SurA in a few previous studies. Using smFRET, it was reported that OmpC has chaperone specific bound conformations such that while SurA expands the protein upon binding, Skp expands only certain regions of the substrate (35), but not much was suggested in regard to the dynamics of the bound state. Through real time NMR spectroscopy, a sublime work found that FhuA was held by both Skp and SurA in a fast conformational interconversion regime while the complex itself was on the timescale of 102 and 12 min, respectively (33). However, a thermodynamic analysis of this interaction has been missing. Moreover, other studies focussed majorly on the chaperone aspect of the chaperone-OMP interaction. For example, ion mobility spectrometry – mass spectrometry (IMS-MS) and molecular dynamics simulations were used to demonstrate that OmpF and tBamA were sequestered by at least two copies of the Skp trimer (106). In conjunction, smaller OMPs like OmpX required only an expansion of the Skp cavity (104). Conformational changes were observed between the core-P1 domains of SurA on its complexation with both OmpX and OmpF (34). But the conformation of the bound substrate was not a part this interesting work. Thus, a clear lack of knowledge about the biophysical aspects of a bigger OMP client in the chaperone-OMP complex necessitates a systematic smFRET study as was done in the previous chapter for OmpX. In addition, the chaperone binding ability and the recognition sites on many of these OMPs is still unknown. That is precisely the aim of this chapter which begins first by examining the chaperone free state of the 12  $\beta$ -stranded OmpLA. The Skp and SurA complexed OmpLA are then investigated from a structural perspective along with a characterization of chaperone recognition. Subsequently, thermodynamics of Skp bound OmpLA is also explored.

## 6.1 OmpLA exhibits a compact state in aqueous environment

To comprehend the difference between the chaperone bound and unbound state, the first step was to investigate OmpLA in absence of detergent, denaturant and the chaperones. Thus, the 269 amino acid protein (without signal sequence) was designed with cysteine mutations on different sites pairwise so as to probe different segments of the protein (OmpLA<sub>13,125</sub> – first, OmpLA<sub>64,187</sub> – middle and OmpLA<sub>125,234</sub> – last) along with the whole protein conformation (OmpLA<sub>13,234</sub>) like in previous chapters. After purification and labelling under denaturing conditions (Appendix Section 8.3.2), each of the variant was first diluted to a nanomolar (nM) concentration still in presence of 6M GdmCl. It was then diluted to picomolar (pM) concentration in absence of the denaturant and chaperone so as to probe the chaperone free state of OmpLA (called as aqueous OmpLA in this text) in the assembly buffer (20 mM Tris-HCl, 150 mM NaCl and pH 8.0) by smFRET experiments. Such a dilution scheme is shown in Figure 6-1a for the OmpLA<sub>64,187</sub> variant.

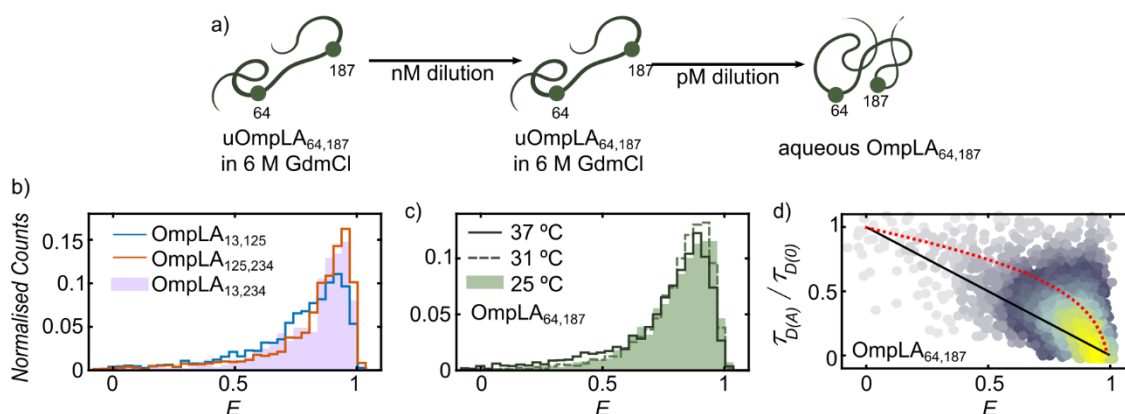


**Figure 6-1 - Compact conformation of unbound OmpLA.** a) Dilution scheme followed so as to probe the chaperone free state of OmpLA using the OmpLA<sub>64,187</sub> variant as an example—unfolded or denatured OmpLA in 6M GdmCl was first diluted to nanomolar concentration still in presence of 6 M GdmCl. It was then diluted into the assembly buffer in absence of denaturant, detergent and the chaperone to perform smFRET measurements of OmpLA in an aqueous solution. b) The FRET efficiency histograms of OmpLA<sub>13,125</sub> (blue cityscape), OmpLA<sub>125,234</sub> (orange cityscape) and OmpLA<sub>13,234</sub> (purple bars) exhibit high energy transfer states asserting that the whole protein appears to be compact in the unbound state at 25 °C. c) In agreement, the middle segment too appears to have a compact conformation, even at three different temperatures: 25 °C (green bars), 31 °C (dashed green cityscape) and 37 °C (dark green cityscape). d) Lastly, 2D plot between the relative lifetime of the donor ( $\tau_{D(A)}/\tau_{D(0)}$ ) and FRET Efficiency,  $E$  was created to examine interconversion dynamics of aqueous OmpLA<sub>64,187</sub>. The slight shift from the static FRET line (black line) indicates presence of sub-millisecond chain dynamics, although it also does not behave like a Gaussian chain (red dashed line).

From the smFRET measurements, the acquired photon stream was filtered for bursts with a maximum inter-photon time of 50  $\mu$ s and having at least 40 photons. A stoichiometry filter of  $S$  between 0.2 and 0.75 was applied along with an ALEX-2CDE filter of  $<10$  and NG/NR filter  $<1$  to remove single fluorophore labelled, quenched and multiple molecules. Further, correction factors  $\alpha= 0.0881$ ,  $\beta= 0.0247$  and  $\gamma=0.4550$  with  $g_{GG}= 0.84745$  and  $g_{RR}= 0.80809$  were used to obtain the FRET efficiency ( $E$ ) histograms. The  $E$  histograms obtained for the first (OmpLA<sub>13,125</sub> - blue cityscape line) and last (OmpLA<sub>125,234</sub> - orange cityscape line) subsection probing OmpLA variant along with the whole protein variant (OmpLA<sub>13,234</sub>) are shown in Figure 6-1b. The high FRET efficiency peaks ( $\langle E \rangle \sim 0.9$ ) obtained for all these variants makes it clear that the aqueous OmpLA is indeed a compact misfolded state. Moreover, each of these variants along with the variant representing the middle sub-section (OmpLA<sub>64,187</sub>) showed no big change in their conformation upon changing the temperature from 25 °C to 31 °C and 37 °C as observed in Figure 6-1c. The temperature was maintained using an objective collar linked to a refrigerated circulator.

In a final step, the conformational dynamics of each of these variant was probed using the 2D plot between the relative lifetime of donor ( $\tau_{D(A)}/\tau_{D(0)}$ ) vs FRET efficiency,  $E$ . Such a plot is presented for OmpLA<sub>64,187</sub> from the smFRET measurement at 25 °C. Like in previous chapters, the static FRET line (black line) depicts the theoretical relation between the intensity weighed average ratio of donor lifetimes in presence and absence of acceptor and  $E$ , while a Gaussian chain behaviour is represented by the dotted red line. Although challenging to decipher, the population corresponding to the aqueous OmpLA<sub>64,187</sub> does appear to have shifted from the static FRET line at 25 °C. OmpLA<sub>13,125</sub> also showed similar behaviour, while the FRET population of other two variants appeared to coincide with the static FRET line (not shown here). Hence, it is interesting to note that although compact, at least a sub-section of OmpLA seems to have conformational reconfiguration dynamics on timescales faster than milliseconds.

## 6.2 OmpLA is partially encapsulated by Skp<sub>3</sub> and lacks distinct conformational change upon complexing with SurA

It was recently recognised that OmpLA lacked SurA recognition sites (36). This brings into light the significance of identifying different roles for Skp and SurA in a cellular context.

Furthermore, little is known about the Skp recognition sites on OmpLA and the structural aspects of chaperone bound states of OmpLA. To this end, this section explores the conformation and where plausible the conformational dynamics of first Skp complexed and then SurA complexed states of OmpLA.

For the purpose of performing smFRET experiments probing the Skp-OmpLA interaction, the dilution scheme was modified so as to include a high concentration (3.2  $\mu\text{M}$ ) of Skp trimer (Skp<sub>3</sub>) at the last step involving picomolar dilution of OmpLA (Figure 6-2a). As discussed in the previous chapter, since Skp was diluted from a concentration higher than its  $c_{1/2}$  (108), it can be safely considered to be in its trimeric state (Skp<sub>3</sub>) when binding to the substrate. Moreover, a recent investigation found that exposure of substrate shifts the equilibrium towards Skp trimers (109). Thus, from here on, the reported concentration of Skp always corresponds to its trimeric state such that the measured concentration was simply divided by 3. Subsequently, each variant was subjected to smFRET measurements in 3.2  $\mu\text{M}$  Skp<sub>3</sub> containing assembly buffer at the physiological temperature (37 °C). The same inter-photon burst time of more than 50  $\mu\text{s}$  with more than 40 photons was used to filter for single molecule bursts. Additionally, same ALEX-2CDE filter of <10, stoichiometry filter of  $0.2 < S < 0.75$  and NG/NR filter of <1 was applied along with correction factors  $\alpha = 0.0881$  and  $\beta = 0.0247$ .  $\gamma$  slightly changed for every variant and was 0.4420, 0.4050, 0.4188 and 0.4260 for OmpLA<sub>13,125</sub>, OmpLA<sub>64,187</sub>, OmpLA<sub>125,234</sub> and OmpLA<sub>13,234</sub>, respectively.

The filtered FRET efficiency histograms so obtained were then used to compare the chaperone bound and unbound (or free) state of each OmpLA variant so as to examine region specific effect of the chaperone on the relatively big OMP. Strikingly, from Figure 6-2b, it is evident that the first segment of the protein represented by OmpLA<sub>13,125</sub> appears to have a greater distance between the two probed sites when complexed with Skp (yellow bars) as compared to its chaperone unbound state (dark green cityscape). This follows from the observation that the Skp bound OmpLA<sub>13,125</sub> has a broad FRET efficiency histogram in the mid to high  $E$  region ( $\langle E \rangle \sim 0.7$ ) unlike the relatively high FRET efficiency peak from the chaperone free OmpLA<sub>13,125</sub> measurement.

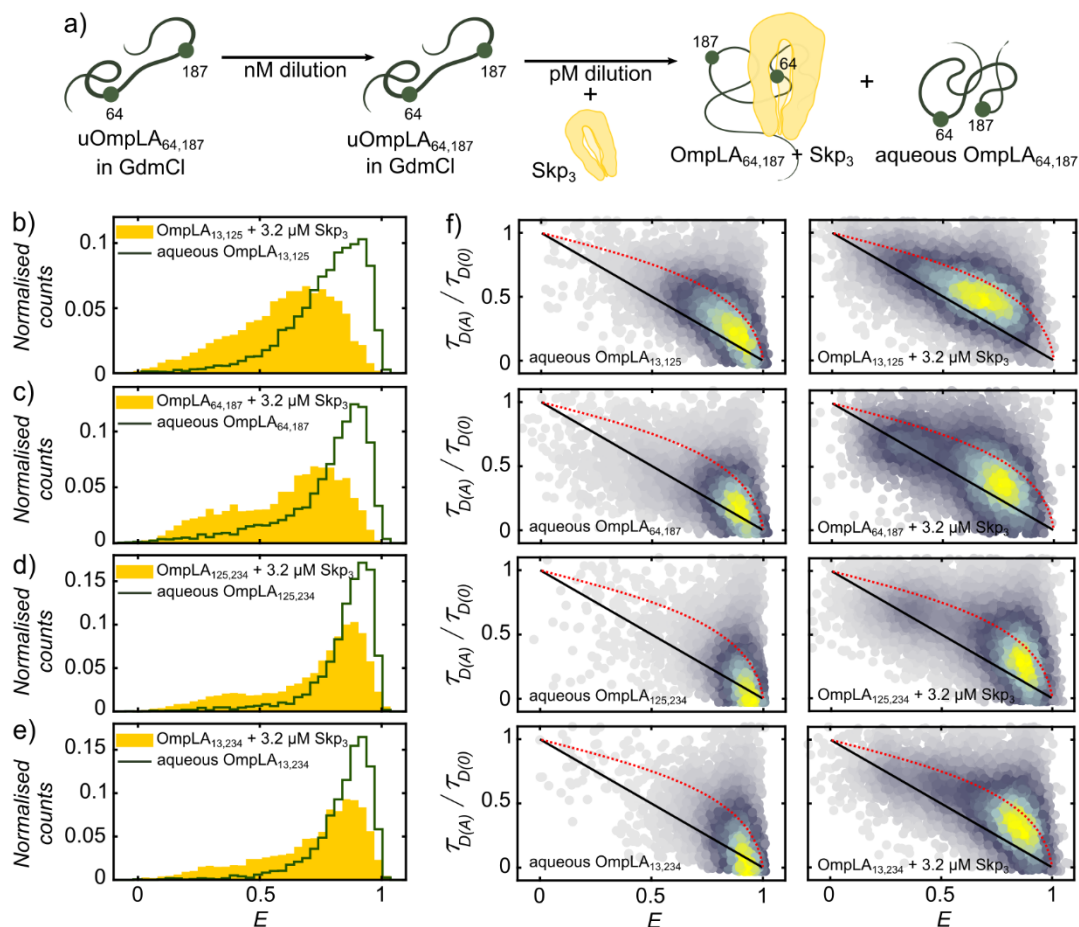


**Figure 6-2 – Skp3 binds to and expands specific regions of OmpLA.** a) Dilution scheme used to probe the chaperone bound OmpLA using the OmpLA<sub>64,187</sub> variant as an example— unfolded or denatured OmpLA (uOmpLA<sub>64,187</sub>) in 6M GdmCl was first diluted to nanomolar concentration still in presence of 6 M GdmCl. It was then diluted into the assembly buffer in absence of denaturant and in presence of 3.2  $\mu\text{M}$  Skp<sub>3</sub> to perform smFRET measurements of Skp<sub>3</sub> complexed OmpLA at 37 °C. FRET efficiency ( $E$ ) histograms of the chaperone bound (yellow bars) and chaperone unbound (green cityscape) are compared for each variant: b) OmpLA<sub>13,125</sub>, c) OmpLA<sub>64,187</sub>, d) OmpLA<sub>125,234</sub> and e) OmpLA<sub>13,234</sub>. Strikingly, the broad mid to high FRET efficiency histogram corresponding to the chaperone complexed OmpLA<sub>13,125</sub> variant appears to be different from the high FRET efficiency peak corresponding to the compact free OmpLA<sub>13,125</sub>. Further on, while the middle segment (OmpLA<sub>64,187</sub>) shows a distinguishable low to mid-FRET efficiency peak corresponding to Skp<sub>3</sub> bound conformation, OmpLA<sub>125,234</sub> and OmpLA<sub>13,234</sub> show negligible change in FRET efficiency histograms upon complexing with the chaperone. f) 2D plot between the relative lifetime of the donor ( $\tau_{D(A)}/\tau_{D(0)}$ ) and FRET Efficiency,  $E$  were again created to examine interconversion dynamics within aqueous OmpLA and chaperone complexed OmpLA population for each variant without (left panel) and with the chaperone (right panel) as indicated in the figure. Sub-millisecond dynamics were observed for the OmpLA<sub>13,125</sub> variant in presence of Skp<sub>3</sub>, while the chaperone encapsulated OmpLA<sub>64,187</sub> population appeared on the static FRET line (black line). None of the states behaved like a Gaussian chain (represented by the red dashed line).

Furthermore, the middle section of OmpLA (probed by OmpLA<sub>64,187</sub> variant in Figure 6-2c) indicates an obvious change in its conformation upon binding with Skp<sub>3</sub> as seen by the additional low to mid FRET efficiency peak (from  $E = 0.1$  to  $0.5$ , yellow bars) in comparison to just one high FRET efficiency peak (from  $E = 0.5$  to  $1$ ) corresponding to unbound OmpLA<sub>64,187</sub> (green cityscape). This suggests that the chaperone expands this part of its substrate upon association. However, from the measurements corresponding to Skp<sub>3</sub> complexed OmpLA<sub>125,234</sub>, it is clear that the last segment of the protein possesses only a limited recognition by Skp<sub>3</sub> as most fraction of the protein (~80 %) is seen to adapt a compact conformation corresponding to aqueous OmpLA<sub>125,234</sub> at the same concentration of 3.2  $\mu$ M Skp<sub>3</sub> (Figure 6-2d). Interestingly, the variant probing major part of the protein (OmpLA<sub>13,234</sub>) shows only a small expansion in its chaperone bound state as compared to its chaperone free state (Figure 6-2e). These findings suggest that Skp has a ‘pushing and pulling’ effect on OmpLA. Importantly, all the variants showed relatively broad FRET efficiency peaks in both their chaperone bound and unbound state indicating a subset of heterogeneous conformations in both populations.

Consequently, the conformational interconversion dynamics within these bound and unbound states was probed. To this end, the powerful tool of 2D plot between the relative lifetime of donor ( $\tau_{D(A)}/\tau_{D(0)}$ ) vs FRET efficiency,  $E$  was employed for each variant. In Figure 6-2f, the first panel shows plots corresponding to measurements of OmpLA variants (as indicated) without the chaperone and the second panel shows plots for OmpLA variants (as indicated) in complex with 3.2  $\mu$ M Skp<sub>3</sub> at 37 °C. A shift from the static FRET line can be observed for unbound states of both OmpLA<sub>13,125</sub> and OmpLA<sub>64,187</sub> variants but not so clearly for OmpLA<sub>125,234</sub> and OmpLA<sub>13,234</sub>. Remarkably, such a shift from the static FRET line was now observed for OmpLA<sub>13,125</sub> and OmpLA<sub>125,234</sub> in presence of Skp<sub>3</sub> although the chaperone complexed conformations of OmpLA<sub>64,187</sub> remained static. Perhaps, the C-terminus segment of the substrate is not bound or is bound only transiently to Skp<sub>3</sub> such that it now has increased freedom to undergo sub-millisecond reconfiguration dynamics since the first sub-section of the protein is already encapsulated within the Skp<sub>3</sub> cavity. In accordance, the variant probing the major part of the protein (OmpLA<sub>13,234</sub>) shows an average sub-millisecond dynamic behaviour within its chaperone bound and unbound population.

It is in this manner that Skp<sub>3</sub> is able to sequester a big OMP: while the first segment is encapsulated within the chaperone cavity by expansion resulting from multiple interactions between the proteins, the last segment remains free. In addition, this interaction mechanism ensures that OmpLA does not collapse as seen in absence of the chaperone and the conserved C-terminus is exposed so that it is easily recognised by the  $\beta$ -barrel machinery to enable folding upon reaching the outer membrane.

Next, in order to investigate the interaction of SurA with OmpLA, the dilution scheme was redesigned to include addition of 7.5  $\mu$ M SurA instead of Skp in the assembly buffer (20 mM Tris-HCl, 150 mM NaCl and pH 8.0) in the last picomolar dilution step (Figure 6-3a). FRET efficiency ( $E$ ) histograms were obtained with the same filter parameters as used previously for Skp<sub>3</sub>-OmpLA smFRET experiments at 37 °C.

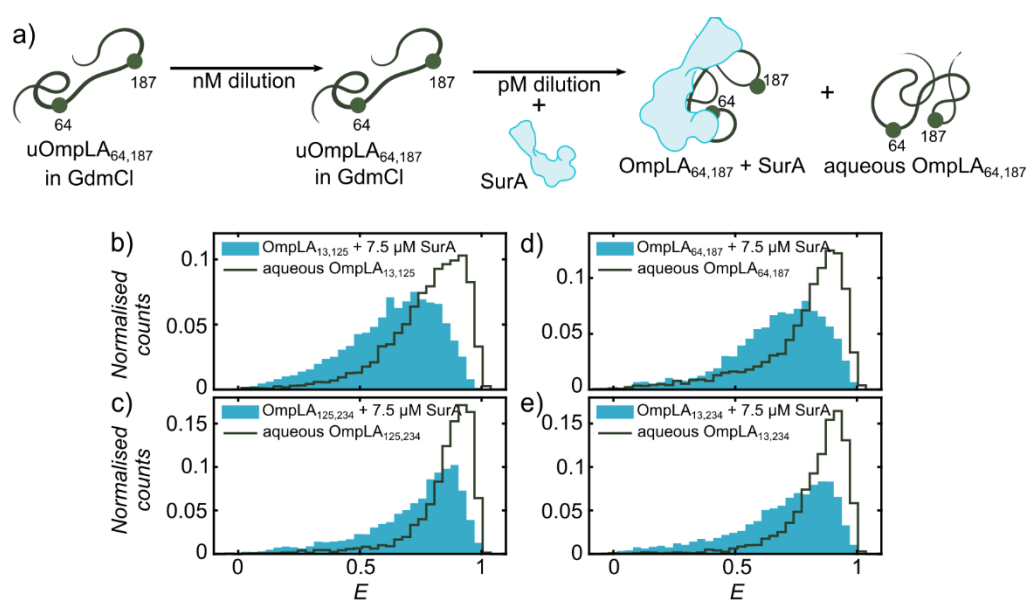


**Figure 6-3 - OmpLA lacks distinguishable conformational change upon complexing with SurA.** a) Dilution scheme used to probe the chaperone bound OmpLA using the OmpLA<sub>64,187</sub> variant as an example—unfolded or denatured OmpLA (uOmpLA<sub>64,187</sub>) in 6M GdmCl was first diluted to nanomolar concentration still in presence of 6 M GdmCl. It was then diluted into the assembly buffer in absence of denaturant and in presence of 7.5  $\mu$ M SurA to perform smFRET measurements at 37 °C. FRET efficiency ( $E$ ) histograms of the chaperone bound (yellow bars) and chaperone free (green cityscape) are compared for each variant: b) OmpLA<sub>13,125</sub>, c) OmpLA<sub>64,187</sub>, d) OmpLA<sub>125,234</sub> and e) OmpLA<sub>13,234</sub>. Intriguingly, none of the variants showed a distinguishable change in the FRET efficiency histograms in presence of 7.5  $\mu$ M SurA thus indicating that SurA might possess no specific recognition towards OmpLA.

In Figure 6-3a, Figure 6-3b, Figure 6-3c, Figure 6-3d, the FRET efficiency ( $E$ ) histograms corresponding to the smFRET measurements in absence of SurA (dark green cityscape) and in presence of SurA (blue bars) are plotted together for each variant: for OmpLA<sub>13,125</sub>, OmpLA<sub>64,187</sub>, OmpLA<sub>125,234</sub> and OmpLA<sub>13,234</sub>, respectively. It was already reported before that the chaperone unbound (free OmpLA) states appear to have a compact collapsed conformation. Astonishingly, presence of SurA appeared to show only a minor expansion of the FRET efficiency histogram corresponding to all the variants indicating that SurA possibly possess no specific recognition towards OmpLA. This observation goes in accord with a report that observed low cross linking efficiencies between OmpLA and SurA (36). Furthermore, it brings into light the possibility that the periplasmic chaperone SurA might possess selective recognition, thus highlighting that Skp and SurA might not have a redundant function as was observed in a previous work (27).

### 6.3 Skp<sub>3</sub> binds OmpLA with a relatively low entropic cost

Identification of a clear conformational change upon binding of Skp<sub>3</sub> to OmpLA, especially for the middle segment represented by OmpLA<sub>64,187</sub>, enabled a thermodynamic analysis of the Skp<sub>3</sub> – OmpLA interaction. To this end, a series of smFRET measurements were performed with OmpLA<sub>64,187</sub> and incremental concentration of Skp<sub>3</sub> (from 32 nM to 6400 nM) at three different temperatures (25 °C, 31 °C and 37 °C). Single molecule bursts were identified by using the same inter-photon time of 50  $\mu$ s and a minimum of 40 photons as in previous section. ALEX-2CDE <10, stoichiometry filter of  $0.2 < S < 0.75$  and NG/NR <1 filters were also used along with the correction factors of  $\alpha = 0.088$ ,  $\beta = 0.0247$  and  $\gamma = 0.4330, 0.4355, 0.4050$  for 25 °C, 31 °C and 37 °C, respectively to obtain the FRET efficiency ( $E$ ) histograms shown in Figure 6-4.

A global Gaussian fit was then performed for all the  $E$  histograms from each temperature to obtain  $E$  and  $\sigma$  corresponding to three populations: the Skp<sub>3</sub> bound ( $E_b, \sigma_b$ ), the unbound or free ( $E_{ub}, \sigma_{ub}$ ) and compact OmpLA<sub>64,187</sub> ( $E_c, \sigma_c$ ). The values so obtained are enumerated in Table 6-1 and the Gaussian fits for all the  $E$  histograms are shown with black dashed lines in Figure 6-4. Since no distinguishable binding was observed between OmpLA and SurA, it was unreasonable to make an energetic analysis for their interaction.



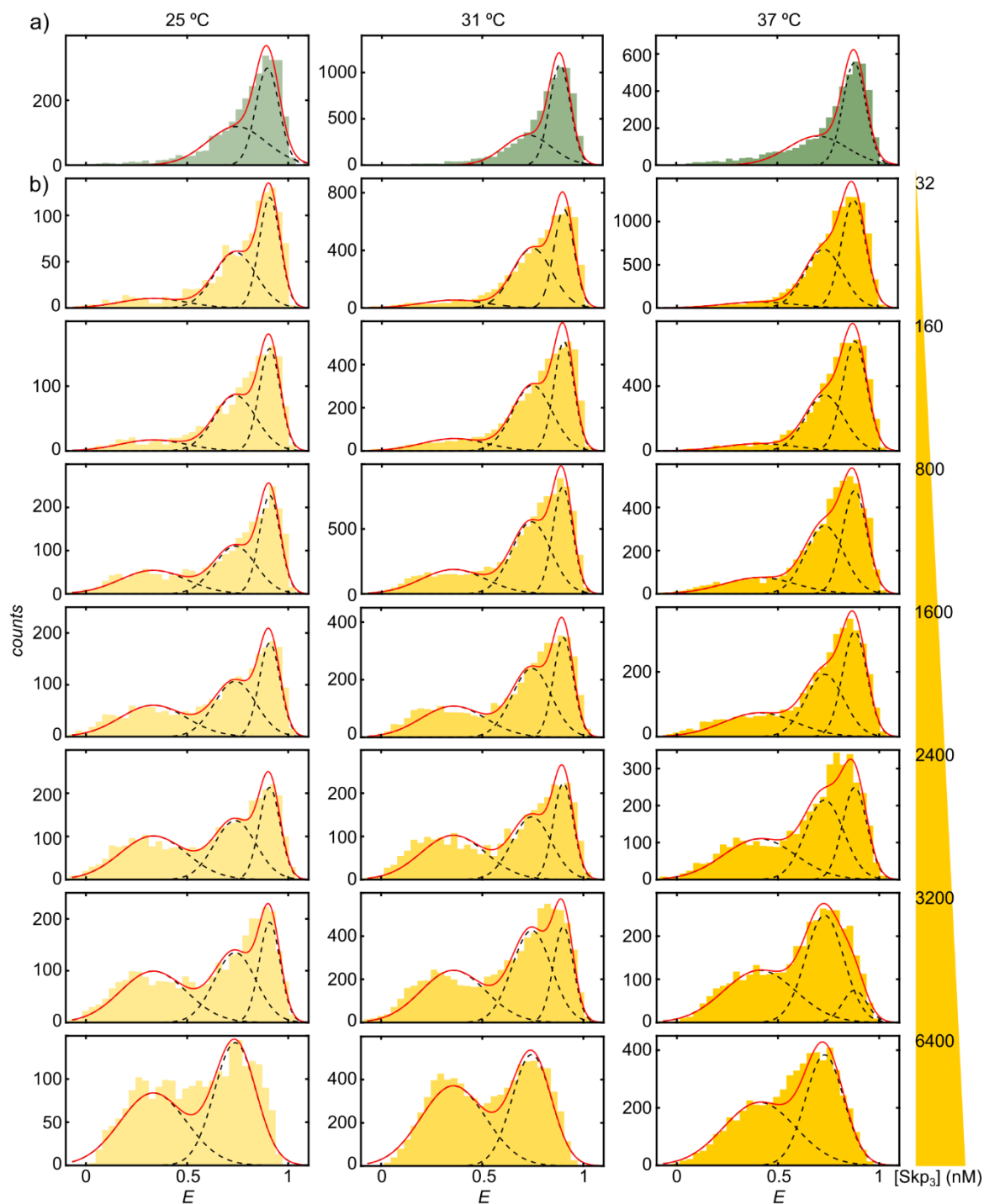


**Figure 6-4 - Series of FRET measurements performed with OmpLA<sub>64,187</sub> and incremental Skp<sub>3</sub> concentration at three different temperatures.** a) FRET efficiency ( $E$ ) histograms from the measurements of OmpLA<sub>64,187</sub> performed at each temperature in absence of the chaperone are shown for reference. b) FRET efficiency histograms from the measurements performed at each temperature with three Gaussian fits (dashed black line) for three states of OmpLA<sub>64,187</sub> : compact, unbound and Skp<sub>3</sub> bound show an obvious increase in the chaperone bound state with increasing concentration (as indicated in the figure).

Temperature	$E_b$	$\sigma_b$ (nm)	$E_{ub}$	$\sigma_{ub}$ (nm)	$E_c$	$\sigma_c$ (nm)
25 °C	0.332 ±	0.180 ±	0.738 ±	0.119 ±	0.908 ±	0.068 ±
	0.021	0.015	0.019	0.018	0.006	0.005
31 °C	0.354 ±	0.175 ±	0.744 ±	0.113 ±	0.904 ±	0.066 ±
	0.017	0.012	0.014	0.012	0.006	0.004
37 °C	0.409 ±	0.194 ±	0.730 ±	0.111 ±	0.877 ±	0.077 ±
	0.027	0.015	0.016	0.011	0.006	0.003

**Table 6-1 - The FRET parameters obtained by performing global Gaussian fit for Skp<sub>3</sub> + OmpLA<sub>64,187</sub> measurement series at each temperature (25 °C, 31 °C and 37 °C).**  $E_b$ ,  $E_{ub}$ ,  $E_c$ , are the FRET efficiency and  $\sigma_b$ ,  $\sigma_{ub}$ ,  $\sigma_c$  are the distance widths in nm for the Skp<sub>3</sub> bound, unbound and compact misfolded states of OmpLA<sub>64,187</sub>, respectively.

In order to obtain the thermodynamic parameters: change in enthalpy ( $\Delta H$ ) and change in entropy ( $\Delta S$ ) for OmpLA<sub>64,187</sub> – Skp<sub>3</sub> interaction, similar analysis algorithm was employed as done for previously for OmpX-chaperone experiments (Section 5.3). The scheme of the algorithm is also shown in Figure 6-5a with the theoretical van't Hoff plot and the fitting using Hill equation. Briefly, the FRET efficiency histograms for each OmpLA<sub>64,187</sub> + x M Skp<sub>3</sub> measurement was globally fitted using the shared variables  $\Delta H$ ,  $\Delta S$ , and  $f_{b,max}$  (maximum bound fraction) and the individual variable  $f_{c,T}$  (fraction of compact OmpLA<sub>64,187</sub>) at every temperature. Using the van't Hoff equation (eq. (11)), dissociation constants were obtained at each temperature during the optimization of  $\Delta H$  and  $\Delta S$ . Based on the Hill equation (eq. (7)), resulting  $K_d$  was then used to obtain the Skp<sub>3</sub> bound fraction ( $f_b$ ) for each measurement at all three temperatures. Next, FRET distributions were calculated for every measurement condition with the FRET parameters ( $E_c$ ,  $E_{ub}$ ,  $E_b$ ,  $\sigma_c$ ,  $\sigma_{ub}$ ,  $\sigma_b$ ) obtained previously and the amplitudes ( $f_b(1-f_{c,T})$ ,  $(1-f_b)(1-f_{c,T})$ ) and  $f_{c,T}$ .  $E_c$ ,  $E_{ub}$ ,  $\sigma_c$ ,  $\sigma_{ub}$  and  $\sigma_b$  were kept constant as little change was observed in their values across different temperatures as is evident from Table 6-1. Lastly, the reduced chi-square ( $\chi^2$ ) was calculated from the residuum of the theoretical and experimental FRET efficiency curves. By varying the initial parameters  $\{\Delta H, \Delta S, f_{b,max}$  and  $f_{c,T}\}$ , the reduced  $\chi^2$  was minimized to obtain the best fitting thermodynamic parameters:  $\Delta H$  and  $\Delta S$ . To determine the errors of the fitted parameters, 200 bootstrapping steps were performed where the FRET efficiency histograms were constructed from randomly drawn bursts for each measurement.

The dissociation constants were found to be temperature dependent and in the order of low  $\mu\text{M}$  concentration:  $K_{d,25} = (0.52 \pm 0.06) \mu\text{M}$ ,  $K_{d,31} = (1.38 \pm 0.08) \mu\text{M}$  and  $K_{d,37} = (3.52 \pm 0.13) \mu\text{M}$ . Interestingly, the resulting  $\Delta H$  and  $\Delta S$  were found to be relatively low with  $\Delta H = (-122.41 \pm -8.08) \text{kJ}\cdot\text{mol}^{-1}$  and  $\Delta S = (-0.29 \pm -0.036) \text{kJ}\cdot\text{mol}^{-1}\cdot\text{K}^{-1}$  (Figure 6-5b). This leads to a plausible explanation: the partial encapsulation of OmpLA results in a favourable high affinity interaction between the chaperone and its substrate such that all its segments occupy a large conformational space ensuring that the entropic change is lowered in absence of a big enthalpic change.

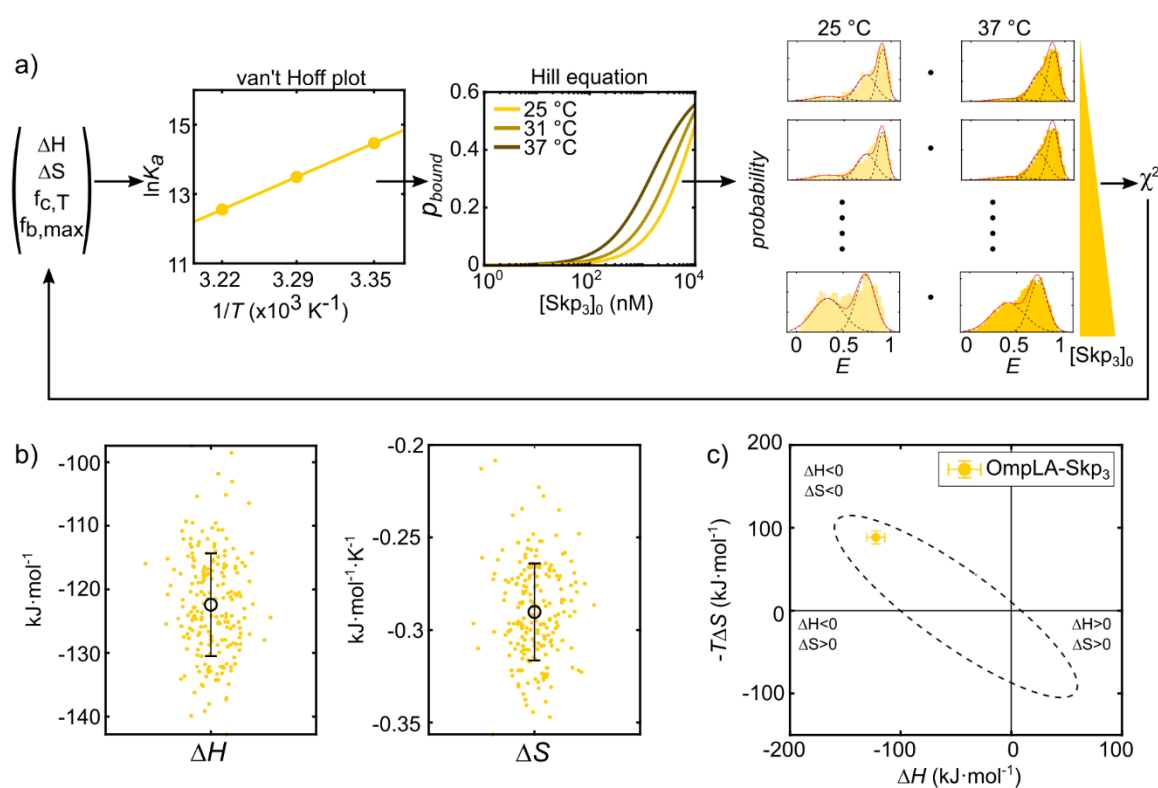


**Figure 6-5 - Skp<sub>3</sub> interacts with OmpLA at a relatively low entropic cost.** a) The algorithm used to obtain the thermodynamic parameters ( $\Delta H$  and  $\Delta S$ ) is shown with the theoretically calculated van't Hoff plot and fitting by Hill equation for OmpLA+Skp<sub>3</sub> interaction. An explanation of the steps can be found in Section 5.3. b) the enthalpic ( $\Delta H$ ) and entropic ( $\Delta S$ ) change values in  $\text{kJ}\cdot\text{mol}^{-1}$  and  $\text{kJ}\cdot\text{mol}^{-1}\cdot\text{K}^{-1}$  values obtained from bootstrapping algorithm for OmpX-Skp<sub>3</sub> and OmpX-SurA interaction are indicated as yellow dots and the  $\langle\Delta H\rangle$  and  $\langle\Delta S\rangle$  are shown as a black circle with an error bar. c) The calculated  $\langle\Delta H\rangle$  and  $\langle\Delta S\rangle$  for OmpX-Skp<sub>3</sub> and OmpX-SurA are overlaid on the spread of data points as reported in review by Heller et al (195) for protein-small molecule interactions.

Finally, the obtained values were compared with enthalpic and entropic contributions reported for protein-ligand binding as used in the review by Heller et. al (195). It appears that the thermodynamic parameters for OmpLA-Skp<sub>3</sub> interaction is within the given range of values (Figure 6-5c) and similar to OmpX-SurA interaction. However, it is in contrast with the high enthalpic and entropic change observed for OmpX-Skp<sub>3</sub> interaction. Since OmpX is a much smaller protein than OmpLA, the whole of the protein might have been encapsulated within the Skp<sub>3</sub> cavity leading to a multitude of stable interactions under confinement. This might lead to a much higher entropic and enthalpic change of the OmpX-Skp<sub>3</sub> interaction as compared to that of OmpLA and Skp<sub>3</sub>. Here, it is important to note that unfortunately, even a very high concentration of chaperone did not lead to >50% bound fraction of OmpLA<sub>64,187</sub> for 25 °C measurement, thus these results are only a discussion of the plausible parameters and need to be built upon in future. Nonetheless, the interaction between the chaperone Skp<sub>3</sub> and its substrate OmpLA was found to be a favourable one with  $\Delta G$  at 37 °C =  $(-32.38 \pm -0.28)$  kJ·mol<sup>-1</sup>.

## 6.4 Summary

Without the chaperone or denaturant, the unbound state of OmpLA was found to adapt a collapsed state in the aqueous solution. Remarkably, on complexing with Skp<sub>3</sub> only the first sub-section of OmpLA was found to expand while the rest of the protein remained compact and showed relatively low affinity to the chaperone. Here, it is also interesting to note that this was also the region found to be more unstable against a high concentration of denaturant (Section 4.2.1), raising the possibility that this might be the frustrated region of the protein (130) recognisable by chaperones. To verify this hypothesis, a freely available online tool called as AWSEM-MD Frustratometer (199) was used to quantify the local conformational frustration within the OmpLA structure. While a high frustration index (normalized using the variance of that distribution) would mean that the particular contact is unfavourable in relation to the set of all possible contacts in that location, a low frustration index emphasizes vice versa. The index value is a Z-score of the energy of the native pair compared to the N decoys. Further information about the algorithm can be found on the website and the reference paper (199) for AWSEM-MD Frustratometer. Strikingly, as shown in Figure 6-6a with a red box, most of the frustrated regions seem to be located on the first-middle segment while the second part of the protein seems to be rather

minimally frustrated, thus agreeing with the previous hypothesis that Skp<sub>3</sub> recognizes these local frustrated regions of the protein. On mapping the probable binding regions of OmpLA with chaperone Skp<sub>3</sub>, a model picture is made to visualize the chaperone bound substrate in Figure 6-6b.

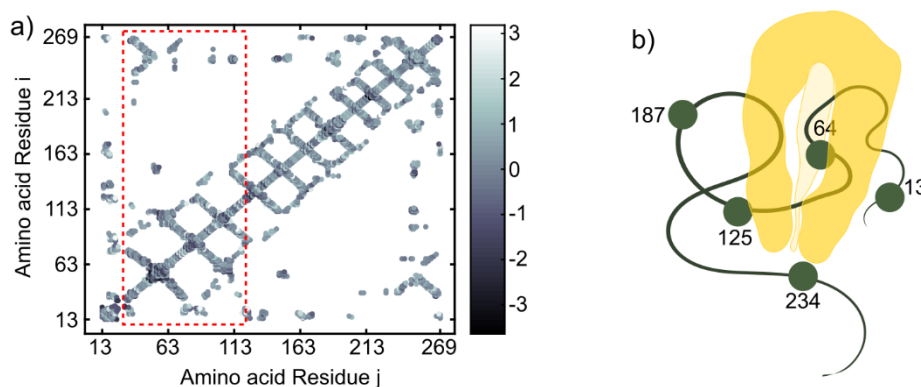


**Figure 6-6 - Frustrated regions of OmpLA are located close to its N-terminus.** a) The conformational frustration map with the frustration index of different contacts between amino acid residues  $i$  and amino acid residues  $j$  is shown on a scale of -3 to 3 with -3 being the most frustrated and 3 being the least frustrated contacts. The red box shows the region with the most frustrated contacts which intriguingly happens to be the first segment of OmpLA. b) A model of Skp<sub>3</sub> bound OmpLA is designed based on the FRET experiment data obtained in this chapter.

On examining the interconversion dynamics of the chaperone bound and unbound states, it was found that the first segment of OmpLA possessed a static heterogeneous population when bound to Skp<sub>3</sub>. Intriguingly, the C-terminus of substrate exhibited faster dynamics in its chaperone bound state as compared to the static nature of its chaperone free state. This might be a result of the increased freedom for the second half of the protein as its accessibility to the first half is now inhibited due to latter's encapsulation within the Skp<sub>3</sub> cavity. Furthermore, a coherent picture agreeing with the structural information above was drawn through analysis of the energetic parameters such that a relatively low enthalpic and entropic cost (compared to OmpX-Skp<sub>3</sub>) were determined to be contributing to the OmpLA- Skp<sub>3</sub> interaction thereby increasing the affinity between these two proteins. Finally, an absence of a distinguishable FRET efficiency change for all the segments of OmpLA on complexing with SurA suggests that Skp and SurA could be selective with respect to substrate binding thus avoiding functional redundancy.

*Outlook:* This work has established a comprehensive approach to study big OMPs in complex with chaperones. Building upon this platform, it will be interesting to identify the recognition sites of other OMPs along with their conformational and biophysical changes upon binding. Furthermore, upon combining the structural details of such smFRET experiments with molecular dynamics simulations, an atomistic picture of these chaperone-OMP interactions can be built.

## Chapter 7 Conclusion and Outlook

Protein-chaperone interactions especially between OMP and periplasmic chaperones: Skp and SurA have been challenging processes to decipher. Being one of the major determinants of cell integrity, the binding of these two chaperones to the newly secreted polypeptides ensures that their clients reach the outer membrane in a folding competent state. Despite some interesting *in vitro* investigations, studying chaperone-OMP interactions through ensemble techniques presents two critical challenges: averaging properties of composite bound substrates and aggregation tendency of the concentrated hydrophobic OMPs required to perform these experiments. In this regard, the objective of the thesis has been to overcome these obstacles and gain a comprehensive structural and thermodynamic insight into the unfolded and chaperone bound states of two differently sized OMPs: OmpX and OmpLA by employing smFRET. Furthermore, by mapping FRET efficiencies and conformational interconversion timescales of individual segments of OmpLA through different labelling variants, a volumetric structural insight is obtained into its denatured, unbound and chaperone-bound states.

### **Optimization of labelling strategies**

Certainly, the first step when intending to probe OMPs through smFRET was to construct a competent maleimide labelling protocol since an efficient donor and acceptor fluorophore tagging leads to qualitatively better measurements. As seen in Chapter 3, using the chromatograms obtained from SEC and the stoichiometry filter upon the photon bursts collected from smFRET experiments, it was possible to determine the effectiveness of OmpLA labelling assay under consideration. While a higher concentration of both dye and the dissolving solvent DMSO increased labelling efficiencies to ~30%, they also damaged the conformational integrity of refolded OmpLA. Since multiple binding positions were chosen to probe segment specific configurational changes of OmpLA upon denaturation and chaperone binding, it was vital to probe site-specificity of labelling efficiencies. Indeed, tagging the fluorophores on the refolded protein was found to be dependent on position such that the rather exposed 64 and 187 cysteine residues labelled more successfully than any other variants. Lastly, labelling under denaturing conditions proved to be advantageous for some variants (example: double labelling efficiencies increased by ~10% for OmpLA<sub>125,234</sub>) and reduced the effect of positions chosen for labelling.

### **Slow interconversion amongst the denatured structural ensemble of OMPs**

OMPs have to be maintained in an unfolded state for extended periods of time during their biogenesis. Thus, deciphering the structural characteristics of denatured OMP states provides an interesting perspective not just fundamentally but also biologically. In Chapter 4, it was demonstrated that irrespective of the OMP (or its sub-section in case of OmpLA) under examination, slow interconversion dynamics (>100 ms) within the denatured population was a common feature (illustrated in Figure 7-1). Such a chain behaviour agrees with previously found secondary structures and hydrophobic clusters in case of OmpX (121, 122) and long range tertiary interactions of denatured OmpLA (123). Consequently, such slowed sampling of competent folding states led to folding rates on order of hours (~11 h<sup>-1</sup>) for OmpX into LDAO micelles.

In a cellular setting, long timescale dynamics within unfolded states might help in reduction of the entropic cost upon binding. This argument follows from the idea that while typically chaperone binding reduces entropy substantially due to depletion in accessible



conformations, in case of Skp and SurA interaction with OMPs, the loss might be decreased as the polypeptide chain cannot access the complete conformational space even in the absence of chaperones. Thus, in thermodynamic terms, this might increase the affinity between the proteins in the ATP-deficient environment of the periplasm. Furthermore, such slow dynamic behaviour of the unfolded chain could assist the anti-folding activity of chaperones (by preventing chain collapse) and facilitate the handover of their substrates to the upstream protein folding machinery (by preserving folding competent states upon release from chaperones).

In addition to these observations, an interesting observation was also made through examination of different sub-sections of OmpLA. Here, it was revealed that the middle segment of protein (represented by OmpLA<sub>64,187</sub>) was the least stable against denaturation indicating that it might be the ‘frustrated region’ which is recognisable by Skp<sub>3</sub>. Association mechanisms facilitated through transient binding of chaperones on these locally situated non-favourable intra-substrate interactions have been shown to be playing an important role in binding of Spy, SurA, and Skp with Im7 and SH3, independent of the sequence or conformation of the specific motifs (130).

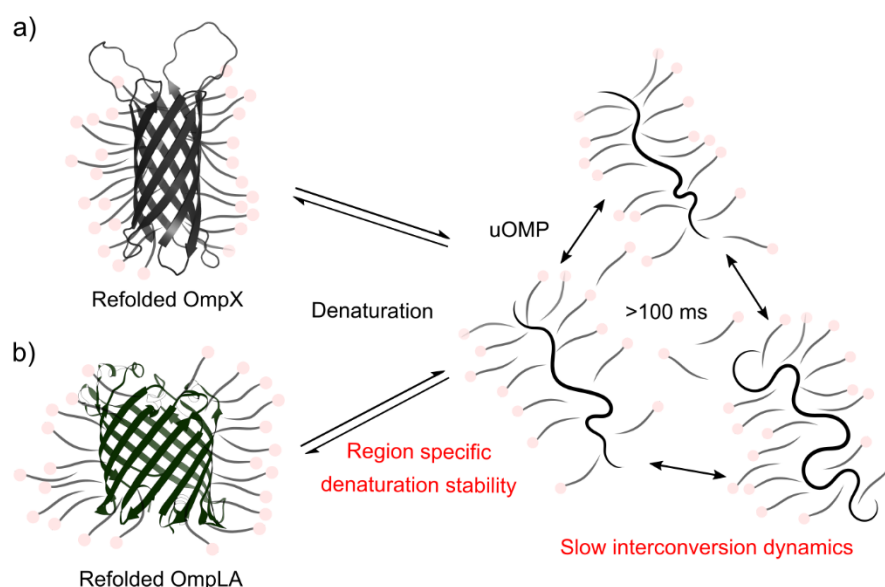


**Figure 7-1 - Slow interconversion among the heterogeneous unfolded OMP states.** Using a) OmpX and b) OmpLA as model OMPs, the denatured states were studied through smFRET. In both cases, the unfolded populations were found to possess inter-conformational changes on long timescales (>100 ms). Moreover, using different OmpLA labelling variants, it was found that the middle segment of the protein had a reduced stability against denaturation.

### **Chaperone bound OMPs are expanded and exhibit sub-millisecond conformational changes**

Unlike the rather collapsed states of unbound OMPs, chaperone bound OmpX and OmpLA appeared to possess rather expanded conformations. Importantly, because of the differential interaction mechanisms of the two proteins, it was found that their substrates occupied distinct conformational space. For instance, OmpX expanded increasingly upon gradually incrementing the concentration of SurA, suggesting that the chaperone interacts with its client in a ‘beads-on-string’ fashion demonstrating a tendency towards multivalent binding. However, an absence of such a behaviour upon increasing the concentration of Skp<sub>3</sub> follows from the previous findings (25, 104, 106, 109) that due to the small size of the substrate, Skp<sub>3</sub> is capable of encapsulating a major part of OmpX without requiring anymore chaperone molecules. Furthermore, it was observed that SurA bound OmpX adopted a larger number of configurations than both unbound and Skp<sub>3</sub> bound OmpX. Interestingly, in case of Skp<sub>3</sub> bound OmpLA, the stretching was limited to the first-middle segment of the protein corroborating with the assumption that this is the recognisable region of the protein. Strikingly, both the chaperone bound and unbound states of OMPs showed fast peptide chain reconfiguration as was predicted from denaturation experiments previously. It is intriguing to note that the sub-millisecond timescale of dynamics was also found to be a feature of the C-terminus of chaperone bound OmpLA, possibly due to absence of steric hindrance as that experienced by the largely encapsulated middle segment of the protein.

Overall, the observations made in this thesis imply that the difference in functioning mechanisms of chaperones leads to a dissimilarity in the conformational ensemble of the bound OMP in the periplasm. Multiple molecules of SurA avoid collapse of its client by binding on multiple sites of OmpX (multiple recognition sites have by now been reported between the two proteins (34, 36)), imaginably functioning in a manner analogous to Trigger Factor. In contrast, encapsulation (partial in case of OmpLA) by Skp<sub>3</sub> cavity comparatively limits the adaptable structures of the bound substrate, although numerous interactions ensure that the protein is unable to collapse and misfold. Intriguingly, Skp<sub>3</sub> possibly exposes the evolutionarily conserved C-terminal of partially bound OMPs for handover to BAM as is perceivable with OmpLA in this work. Moreover, the fast-reconfiguration of the bound polypeptide independent of the OMP sequence and chaperone

suggests that at least certain regions of the substrate are bound to Skp<sub>3</sub> and SurA in a loose and transient manner, possibly aided by the anti-folding activity of the chaperones. Ultimately, all these interaction features can also be postulated to facilitate unhindered recognition by BamA which can now easily access the specific recognisable segment of OMP (so called  $\beta$ -signal (200, 201)) within the substrate's vast chaperone bound conformational ensemble.

### **A thermodynamic insight into the OMP - chaperone interactions**

Since periplasm in an ATP-deficient environment, the affinity between the chaperones and their substrates in this space is strongly regulated by the energetics inherent to their interaction. Yet, previous studies lack a description of the thermodynamic parameters governing these protein-protein associations. Experimentally, one can elucidate the energetic contribution in terms of change in enthalpy and entropy ( $\Delta H$  and  $\Delta S$ , respectively) by determining the dissociation constants at different temperatures according to the van't Hoff equation. In this work, upon performing smFRET experiments with OmpX and OmpLA at three different temperatures (25 °C, 31 °C and 37 °C) involving chaperone titrations across a range of concentrations (from low nanomolar to micromolar), it was possible for the first time to determine  $\Delta H$  and  $\Delta S$  of chaperone-OMP interactions as shown in Figure 7-2. In context of the protein-protein interactions probed in this thesis, while a large negative  $\Delta H$  results from a bigger change in intermolecular interactions as compared to intramolecular interactions ( $\Delta H_{inter} \gg \Delta H_{intra}$ ),  $\Delta S$  majorly reflects upon the differences in the conformational space of bound and unbound states of the substrate.

Remarkably, in agreement with the structural observations of Skp<sub>3</sub> and SurA bound OmpX (relating to its configurational space), it was found that the change in entropy corresponding to interaction of SurA with OmpX ( $(-0.2 \pm 0.1) \text{ kJ}\cdot\text{mol}^{-1}\cdot\text{K}^{-1}$ ) was much smaller than that of Skp<sub>3</sub> with OmpX ( $(-0.8 \pm 0.1) \text{ kJ}\cdot\text{mol}^{-1}\cdot\text{K}^{-1}$ ). Intriguingly, the entropic change upon encapsulation of OmpLA by Skp<sub>3</sub> was much lower ( $(-0.3 \pm 0.1) \text{ kJ}\cdot\text{mol}^{-1}\cdot\text{K}^{-1}$ ) than that of OmpX, possibly due to only a partial sequestration by the chaperone. Significantly, all the chaperone-OMP interactions probed in this thesis showed a considerable  $\Delta H$  ( $(-298 \pm 19) \text{ kJ}\cdot\text{mol}^{-1}$ ,  $(-132 \pm 24) \text{ kJ}\cdot\text{mol}^{-1}$ , and  $(-122 \pm 8) \text{ kJ}\cdot\text{mol}^{-1}$  for OmpX-Skp<sub>3</sub>, OmpX-SurA and OmpLA-Skp<sub>3</sub> interactions, respectively) due to presence of multiple binding sites between

the proteins. It is plausible to presume that a relatively low  $\Delta H$  determined for OmpX-SurA and OmpLA-Skp<sub>3</sub> interaction also points towards local transient binding between the proteins, which in turn enables fast reconfiguration of the peptide chain observed previously. In conclusion, the intricate balance between the structural and thermodynamic features of complex formation led to favourable affinities between the two proteins with a negative  $\Delta G_{\text{association}}$ :  $(-38.3 \pm 0.2) \text{ kJ}\cdot\text{mol}^{-1}$  and  $(32.4 \pm 0.3) \text{ kJ}\cdot\text{mol}^{-1}$  for OmpX and OmpLA-Skp<sub>3</sub> interaction, respectively and  $(-57 \pm 1) \text{ kJ}\cdot\text{mol}^{-1}$  for OmpX-SurA interaction. All the chaperone bound OmpX and OmpLA interaction features established in Chapter 5 and Chapter 6 are summarised in Figure 7-2a and 7-2b, respectively.

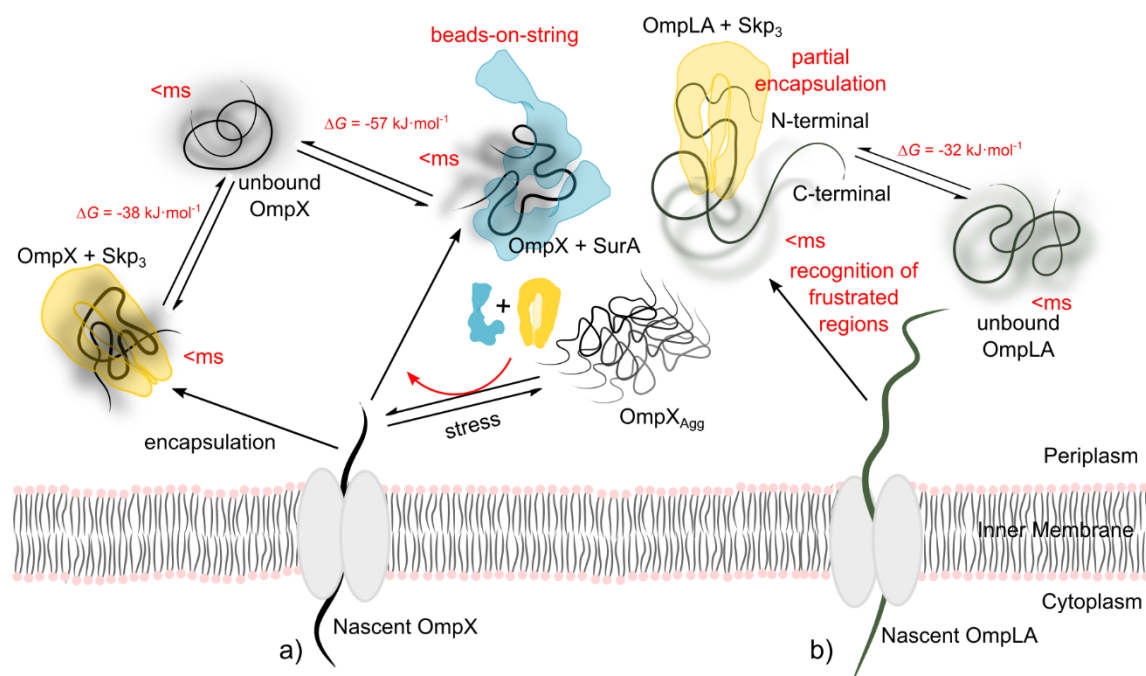


**Figure 7-2 - A structural and thermodynamic perspective of OMP - chaperone interactions in the periplasm.** With a) OmpX and b) OmpLA as the two differently sized OMPs, unbound and Skp<sub>3</sub>/SurA bound states of OMPs were deciphered during this work. It was established that both the chaperones expand the bound OMPs (or segments in case of OmpLA). A direct examination of the dynamics demonstrated that OMPs undergo fast reconfiguration dynamics on a sub-millisecond timescale in both non-complexed and complexed forms. Remarkably, it was found that the thermodynamic parameters determined during the course of this work agreed with the conformational information and strongly modulated the affinity between the two proteins. The free energy of interaction,  $\Delta G$ , is indicated for the interactions. Other energetic parameters and their errors can be found in the main text. The disaggregating property of both Skp and SurA was also brought into light in this thesis, establishing periplasm as a rather synergistic and dynamic system.

### **Disaggregation action of Skp3 and SurA**

It is possible that under conditions of stress, cells overexpress OMPs, which might increase the chances of their aggregation. Under such circumstances, it is highly likely that cell employs more than one kind of chaperone to rescue the aggregated proteins. To this end, this thesis also shed light on the disaggregation properties of Skp and SurA. First of all, it was found that even a micromolar concentration of OmpX led to its aggregation under non-denaturing conditions without a detergent. This brings into attention the need to avoid techniques using high concentration of OMPs when studying these proteins. Remarkably, upon introduction of Skp or SurA, the fraction of aggregated OmpX ( $OmpX_{Agg}$ ) was observed to reduce from 0.24 to 0.2 with Skp and to 0.13 with SurA. Furthermore, a corresponding increase in free OmpX fraction instead of the bound fraction indicated that these chaperones have a greater affinity towards aggregated OMPs as would be required by the distressed cells. In addition, it was also revealed that Skp and SurA can be functioning cooperatively towards disaggregating OMP oligomers as upon simultaneous introduction of the two chaperones, the fraction of  $OmpX_{Agg}$  determined through experiments (0.05) was much lower than that calculated theoretically (0.09). Recent studies have found that many other co-chaperone systems which were generally described to be involved in substrate solubilisation functions such as that of Human HSP70 (78, 202) and Hsc70 (203) are also able to dissolve amyloid aggregates. In this regard, it is interesting to identify that periplasm too has a dynamic and cooperative chaperone system which can be modulated according to the cellular conditions.

### ***Outlook***

Certainly, while this work answers some pressing open questions in the field, it also raises further prospects of inquiry into the subject. Combining smFRET with techniques like RASP, nsFCS, FCS or a lifetime filtering approach, one can start to build upon the folding-unfolding experiments of OMPs performed in this thesis. For this purpose, a better membrane mimicking environment can be designed by reconstituting OMPs into the recently designed asymmetric liposomes with lipopolysaccharides (204). OMPs with different number of  $\beta$ -strands can then be probed for both their region-specific stability against unfolding by partnering smFRET with techniques like molecular dynamics simulations. Furthermore, one interesting candidate to study chaperone-OMP interaction in context of bigger OMPs (with more than 12  $\beta$ -strands) would be the transmembrane part of BamA, which could shed light on the ‘chicken-egg’ problem as BamA itself also has to be transported from inner membrane and refolded into the outer membrane.

In the next step, it is conceivable to examine the chaperone-OMP interactions from the perspective of chaperones. A complete conformational and dynamic picture of the binding process can be gained by probing the structure and dynamics of chaperone domains in case of SurA and monomers in case of Skp with different substrates. To this end, a preliminary study has been initiated for examining the conformation of SurA in absence of OMPs (Appendix 8.1). Indeed, many recent works are also adding on to the knowledge in this field (34, 36, 104, 106, 109, 116). In this light, a far-reaching step would be to investigate the dynamics of SurA domains and Skp monomers as they hand over their client OMP to the  $\beta$ -barrel machinery using the liposome reconstituted BamA by Anna Svirina in the Schlierf group.

Interestingly, at the cellular concentration of Skp, a significant fraction of monomers has been detected (10). However, it is also demonstrated that in presence of substrates, the concentration of trimers is increased due to interaction with the client proteins (109). By applying the lifetime filtering strategy during smFRET experiments (as done for DNA-Origami complexed with other biomolecules – Appendix 8.2) in conjunction with FCS, one can envision a way to detect Skp trimers from Skp monomers through smFRET experiments in presence of OMPs. Furthermore, using the chemically linked Skp monomers (plasmids already exist in the Schlierf lab), it is possible to compare the

structural and thermodynamic properties between the two designs of the chaperone to reveal effects of 'forced' trimerization.

The disaggregation experiments with chaperones showed us that Skp and SurA could be working cooperatively in the periplasmic environment. It will then be intriguing to investigate if the chaperones work cooperatively or handover their substrates in a unidirectional manner in absence of aggregation. To this end, the microfluidics based setup (205) being established in the Schlierf lab with the help of Koushik Sreenivasa and Dr. Andreas Hartmann can be used.

Lastly, it will be of great value to the bio-medicinal field, if through smFRET, the effects of certain newly developing antibiotics (50, 206) on not just the OMP assembly on outer membrane but also the chaperone-OMP interactions are probed directly. Such a high throughput assay system for drug identification is currently being developed for the Cystic Fibrosis transmembrane hairpins in the Schlierf lab by Mathias Rolf Schenkel, Koushik Sreenivasa and Dr. Andreas Hartmann. On combining such findings with *in vivo* applications of microscopy, it is also possible to gain direct insights into the cellular effects of these drugs.





## Appendix 8.1 Fast inter-domain dynamics of SurA in solution

Up until now, the major part of the thesis involved understanding chaperone-OMP interactions from the perspective of OMPs. However, not much has been known about the conformational aspects of chaperone, in this case SurA, in absence and presence of its substrate. SurA is majorly composed of four domains: N-terminal, C-terminal and two parvulin-like peptidylprolyl isomerase (PPIase) domains commonly referred to as P1 and P2 domains. Despite the known crystal structure (110), the motion of domains in presence and absence of the substrate with respect to each other remained unclear for a long time. Moreover, the role of these domains in sequestering OMPs has also been of great interest (207). One study has questioned the role of PPIase domains in sequestering OMPs, as it was found that SurA can still efficiently chaperone OMPs in the absence of these domains (115). But a few previous studies have indeed found that this is not the case for certain OMPs like OmpT, where the absence of even one PPIase domain lead to its aggregation (116). Thus, to obtain an understanding from the standpoint of SurA during chaperone-OMP interaction and its conformational dynamics in solution, an additional smFRET study was also performed with double labelled SurA variants. A few recent investigations (34, 36) are found to be in good agreement with the results presented in this chapter.

### 8.1.1 SurA shows quick distance fluctuations between its C-terminal and P1 domains in absence of its substrate

To examine the conformational dynamics of SurA in solution through smFRET experiments, two double cysteine mutants were designed by site-directed mutagenesis. While one mutant – SurA<sub>197,435</sub> (S197C and S435C) aimed to examine the dynamics between the P1 and C-terminal domains, the other mutant – SurA<sub>324,435</sub> (S324C and S435C) probed the dynamics between the P2 and C-terminal domains (Figure 8.1-1a). Subsequently, the two variants were overexpressed in *E. coli* BL21 cells and purified from the cell lysate using affinity chromatography. They were subsequently refolded in reducing conditions (5 mM TCEP) and labelled with Atto532 (ATTO-TEC, Germany) and Abberior

Star 635P (abberior) as the donor and acceptor fluorophores. SEC was then used to separate the labelled protein from free dyes (Appendix Section 8.3.3). Labelled variants of SurA were then subjected to smFRET experiments at pM concentrations. To isolate the single molecule events from the spectrum, bursts with a minimum inter-photon time of 50  $\mu$ s and more than 50 photons in case of SurA<sub>197,435</sub> and more than 100 photons in case of SurA<sub>324,435</sub> were selected. The analysed burst was then filtered with ALEX-2CDE<10 and Stoichiometry of  $0.2 < S < 0.75$  parameters and correction factors of  $\alpha = 0.0881$ ,  $\beta = 0.0247$  and  $\gamma = 0.5125$  and  $0.4575$  for SurA<sub>197,435</sub> and SurA<sub>324,435</sub>, respectively.

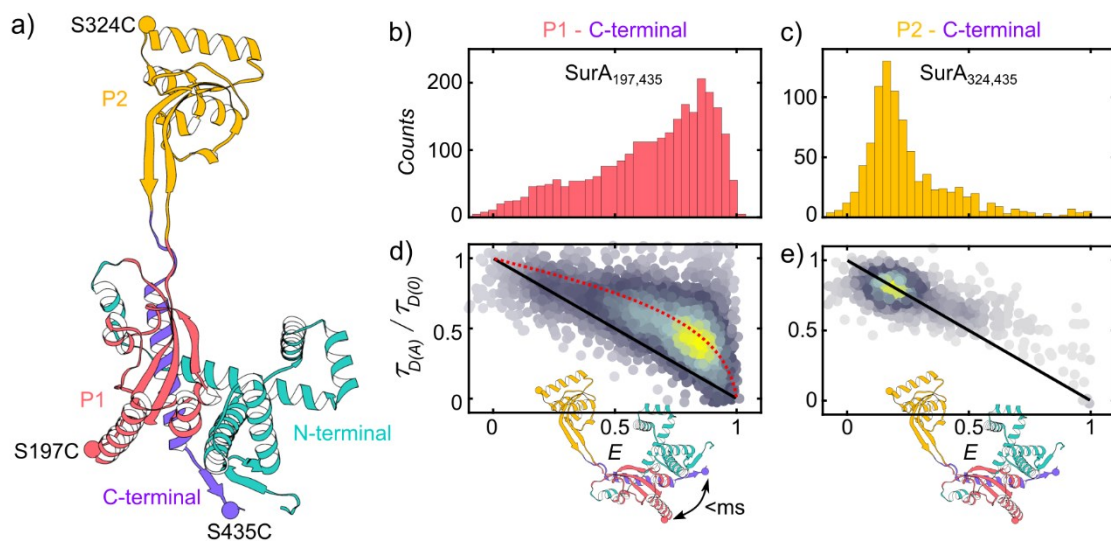


**Figure 8.1-1 – Fast translational dynamics between the domains of SurA.** a) Crystal structure of SurA (1my5.pdb, (110)) is shown with the labelling positions (S197C, S324C and S435C). The four domains are highlighted with different colours: N (green) and C-terminal (purple), peptidyl-prolyl isomerase P1 (red) and P2 (yellow). b) FRET efficiency ( $E$ ) histogram from the smFRET measurement with SurA<sub>197,435</sub> in solution (20 mM Tris-HCl, 150 mM NaCl and pH 8.0) shows a surprisingly broad population. c) FRET efficiency ( $E$ ) histogram from the smFRET measurement with SurA<sub>324,435</sub> in solution (20 mM Tris-HCl, 150 mM NaCl and pH 8.0) shows a low FRET efficiency population at an  $\langle E \rangle \sim 0.25$  corresponding to a relatively smaller distance between the two labelling positions than would be expected from the crystal structure. d) 2D plot between the relative lifetime of the donor ( $\tau_{D(A)}/\tau_{D(0)}$ ) and FRET Efficiency,  $E$  was created to examine interconversion dynamics of the broad population corresponding to SurA<sub>197,435</sub>. The population appears to behave like a Gaussian chain suggesting a sub-millisecond inter-domain movement of SurA in solution. The static FRET line (black line) and the line representing Gaussian chain (red dashed line) behaviour are also shown in the plot. e) 2D plot between the relative lifetime of the donor ( $\tau_{D(A)}/\tau_{D(0)}$ ) and FRET Efficiency,  $E$  suggests that the SurA<sub>197,435</sub> population is largely static. A pictorial representation of the possible SurA structure in solution is shown in d and e.

Figure 8.1-1b shows the FRET efficiency ( $E$ ) histogram (red bars) so obtained for the double labelled SurA<sub>197,435</sub>. Surprisingly, instead of an expected single high FRET efficiency peak, the protein appears to occupy a rather broad conformational space. On the other hand, the  $E$  histogram obtained from smFRET experiments with SurA<sub>324,435</sub> shows only a single low FRET efficiency population (yellow bars in Figure 8.1-1c). Intriguingly, the average FRET efficiency ( $\langle E \rangle \sim 0.25$ ) appears to be smaller than expected for a distance of  $\sim 10$  nm between the labelling two positions (according to the crystal structure). This indicates that the C-terminal and the P2 domain ends of the protein might be closer to each other in solution than suggested from the crystal structure (110).

In the next logical step, the interconversion dynamics of the conformations within the heterogeneous population of the two variants was examined. To this end, a 2D plot was created between the relative lifetime of donor ( $\tau_{D(A)}/\tau_{D(0)}$ ) and FRET efficiency,  $E$  with the static FRET line (black line) and the line representing a Gaussian chain behaviour (red dashed line) and is shown for SurA<sub>197,435</sub> and SurA<sub>324,435</sub> in Figure 8.1-1d and Figure 8.1-1e, respectively. It is interesting to note that the broad population belonging to SurA<sub>197,435</sub> was found to shift away from the static FRET line and seems to have reconfiguration dynamics on the timescale expected for a polypeptide behaving like a Gaussian chain (Figure 8.1-1d). Thus, the distance between the C-terminal and the P1 domain changes on a timescale of sub-milliseconds in solution. This observation is in good agreement with a recent study by Calabrese, Schiffrin and Watson et. al. (34), where they saw sub-millisecond dynamics between the core and P1 domain. However, the distance between the P2 and C-terminal end seems to be largely static in solution as the FRET population belonging to SurA<sub>324,435</sub> lies on the static FRET line (Figure 8.1-1e).

Corroborating with findings from other labs (34, 36), this study demonstrates that while the distance between the tip of P2 domain and the end of C-terminal domain remains largely static albeit lower than in the crystal structure, the distance between the C-terminal and P1 domain seems to change on an extremely fast timescale (shown as pictograms in Figure 8.1-1d and Figure 8.1-1d, respectively). Such a reorganisation of domains might not only facilitate substrate binding but also release of substrates to the  $\beta$ -barrel machinery.

### 8.1.2 Distance between ends of C-terminal and P2 domains remain unchanged upon substrate binding

A loosening of the core-P1 domain was suggested to bias SurA towards a more active state by Soltes et. al (207). Indeed, a recent study showed that SurA adopts a structure intermediate between the core-P1<sub>open</sub> and core-P1<sub>closed</sub> domain (34). Adding on to this study, here, the distance between the C-terminal and P2 domain is probed by diluting labelled SurA<sub>324,435</sub> (to pM concentration) into  $\mu\text{M}$  wild type SurA<sup>wt</sup> with the substrate of interest (pM OmpX<sup>wt</sup> or OmpLA<sup>wt</sup>) to perform smFRET experiments. Knowing the  $K_D$  for OMP-chaperone binding to be in a micromolar range (Section 5.3),  $\mu\text{M}$  SurA<sup>wt</sup> was added so as to satisfy the concentration conditions for chaperone-OMP binding, since a higher concentration of OMPs cannot be used due their propensity towards aggregation and a higher affinity of SurA to aggregated OmpX as compared to unfolded OmpX (Section 5.4).

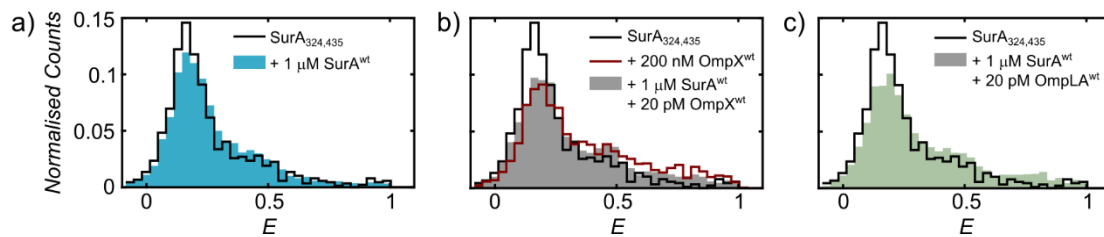


**Figure 8.1-2 - C-terminal and P2 domains of SurA lack change in distance upon addition of the substrate OMPs.** a) The FRET efficiency histogram (blue bars) of the measurement with pM SurA<sub>324,435</sub> and 1  $\mu\text{M}$  SurA wildtype (SurA<sup>wt</sup>) is used as a negative control. It demonstrates that addition of higher concentration of SurA had no visible influence on the conformation of the labelled SurA as it overlays well with the FRET efficiency ( $E$ ) histogram (black cityscape) belonging to measurement with just pM SurA<sub>324,435</sub>. b) The FRET efficiency ( $E$ ) histogram (grey bars) of the measurement with pM SurA<sub>324,435</sub>, 1  $\mu\text{M}$  SurA wildtype (SurA<sup>wt</sup>) and 20 pM OmpX<sup>wt</sup> is overlaid with  $E$  histogram (black cityscape) obtained from measurement with just SurA to show that addition of OmpX<sup>wt</sup> results in no change in distance between the two labelled positions. The maroon cityscape belongs to the FRET efficiency histogram obtained from measurement with pM SurA<sub>324,435</sub> and 200 nM OmpX<sup>wt</sup> which also suggests negligible distance change. c) Addition of 20 pM OmpLA<sup>wt</sup> to pM SurA<sub>324,435</sub> and 1  $\mu\text{M}$  SurA<sup>wt</sup> also seems to result in no change of distance between the two labelled positions upon addition of a bigger substrate.

As a negative control, a smFRET measurement of SurA<sub>324,435</sub> with  $\mu\text{M}$  wild type SurA<sup>wt</sup> was performed to check if the high concentration induced a conformational change among the SurA monomers. The FRET efficiency ( $E$ ) histogram shown for this measurement in

Figure 8.1-2a demonstrates that presence of SurA<sup>wt</sup> had no influence on the labelled SurA molecules. In the next step, 20 pM OmpX<sup>wt</sup> was added to the buffer (20 mM Tris-HCl, 150 mM NaCl and pH 8.0) with 20 pM SurA<sub>324,435</sub> and 1 μM SurA<sup>wt</sup>. The FRET efficiency histogram so obtained is shown with grey bars in Figure 8.1-2b and compared with the SurA only measurement (black cityscape). The absence of a change in FRET efficiency upon addition of OmpX<sup>wt</sup> suggests that the distance between the two positions does not change upon addition of the substrate. Similarly, addition of a bigger OMP instead of OmpX, in this case, OmpLA<sup>wt</sup> also had little effect on the distance between the two labelled positions as seen from the FRET efficiency histogram (dark green bars) in Figure 8.1-2c.

These observations suggest that there appears to be no noticeable distance change between the tip of P2 and C-terminal domain upon binding of the client OMP to SurA like was found to be the case for core-P2 domain in a previous study (34). It should be noted that the labelled chaperone molecules are 10<sup>6</sup> times more dilute than the unlabelled molecules. Thus, it is possible that statistically not many OMP-bound labelled molecules were probed during the measurement leading to a biased FRET-efficiency histogram. But one can assume that the labelled molecules are distributed evenly and thus the findings from the experiments here are inferable. Moreover, addition of 200 nM OmpX<sup>wt</sup> (possibly the maximum concentration usable while avoiding aggregation (35)) to 10 pM labelled SurA<sub>324,435</sub> also resulted in no distinguishable change in the FRET efficiency histogram (Figure 8.1-2b – maroon cityscape) agreeing with the afore-mentioned conclusion.

### 8.1.3 Summary

The results in this chapter show that SurA appears to be conformationally dynamic in solution with the distance between the C-terminal and P1 domains changing on a sub-millisecond timescale. Remarkably, the structure itself appears to be rather compact in solution than is suggested from the crystal structure of the protein (110). Furthermore, addition of differently sized substrates seems to show no perceivable influence on the distance between the tips of C-terminal and P2 domains.

*Outlook:* The next interesting step would be to probe the conformational change of SurA<sub>197,435</sub> upon addition of the substrate. This can help in investigation of the changes in

conformational distance between the P2 and C-terminal domain upon OMP binding and will be a task for future experiments. Furthermore, an insight into the change in conformation of the chaperone when releasing its substrate to the  $\beta$ -barrel machinery will be of immense value in future.

## Appendix 8.2 Lifetime based filtering of DNA-origami coupled molecules.

DNA origami (208) is a robust tool used in various fields of science. Its versatility has established its role in not only molecular lithography (209, 210) and nanotechnology (211–213) but also as a reporter (214) or a drug delivery vehicle in biomedicine (215, 216). It is also of great relevance to single molecule experiments (217–220) where it is used as a substrate for conjugation of DNA or protein biomolecules. In general, DNA origami is constructed with a long single stranded DNA-scaffold and a large number of complementary short oligonucleotides, the so-called staple strands. These staple strands can be functionalized with fluorophores (221), nanoparticles (222), proteins (223) and DNA molecules of desired sequence (224) and topology (225) thus rendering DNA origami as a useful platform with tunable positioning of molecules of interest. Furthermore, the origami structures are found to be stable at even high concentrations of GdmCl or urea (6 M) for up to 24 hours (226, 227), with a possibility of stability enhancement by enzymatic ligation (228) and photo-cross-linking (229). This opens up the opportunity to study protein folding in presence of denaturants, controlled local crowding using for example poly(ethylene glycol) (PEG) polymers (230) or with interacting partners like nucleic acids and chaperones during smFRET experiments. Moreover, as the DNA origami conjugated proteins diffuse slower, thus increasing their residence time under the confocal volume, a better resolution of fast folding proteins can be obtained by combining the two techniques. One way of coupling DNA origami with biomolecules is the biotin-streptavidin reaction whereby both the biomolecule and one of the staple strands of origami have a biotin molecule. Both of these biotins then bind to streptavidin – in this case neutravidin (with four pockets for biotin binding) in the solution resulting in a conjugation of the two molecules. However, such a coupling mechanism is not 100% efficient, thus making it essential to isolate the coupled from uncoupled molecules especially when probing through single molecule techniques like smFRET. To this end, in this chapter, a powerful lifetime-based filtering technique is employed to identify the origami complexed and un-complexed biomolecules like rulers and DNA hairpin during the smFRET experiment.

## 8.2.1 Distinguishing differently labelled DNA origami by evaluating acceptor lifetime during smFRET experiments

The setup used for measurements in this thesis was operated in a pulsed interleaved excitation (PIE) mode i.e. the donor and acceptor fluorophores were excited alternately (Section 2.3.1). As the fluorescence decays of the fluorophores did not overlap (ensured by an appropriate temporal separation of 20 ns), it was possible to detect the photons due to excitation of the donor and the acceptor fluorophore individually. Therefore, upon identification of the single molecule bursts containing a certain number of photons, average apparent lifetime of a burst can be obtained for both acceptor and donor separately. Furthermore, in the case that a particular molecule is labelled with two different acceptor fluorophores having two different lifetimes, an average lifetime of the two dyes will be reflected in the acceptor lifetime histogram resulting due to simultaneous presence of both of them during detection.

Such a system can be easily formulated using DNA origami with staple strands having two different acceptor fluorophores with distinguishable lifetimes. To this end, staple strands with ATTO647N and ALEXA647 were used in different combinations when preparing the origamis. Considering that the labelling of staple strands is not 100% efficient during DNA origami preparation (performed according to the method reported in (227, 231)), it was possible to distinguish the single labelled origami from the double labelled origami using the acceptor lifetime from each experiment. As the lifetime of ATTO647N is 3.5 ns (ATTO-TEC, Siegen, Germany) and that of ALEXA647 is 1 ns (Thermo Fisher Scientific Life Technologies GmbH, Darmstadt, Germany), it was possible to easily distinguish a molecule labelled with either (3.5 ns or 1 ns) or both the dyes (an average lifetime of the two dyes) during the smFRET experiments. The fluorescence bursts belonging to single molecules were identified by using an inter-photon time of 50  $\mu$ s with at least 400 photons. Correction factors  $\alpha = 0.054$ ,  $\beta = 0.0275$  and  $\gamma = 0.9$  were also applied during data analysis.

In Figure 8.2-1a, since the origami was labelled with only ATTO647N dye (red star) as shown in the adjacent pictogram, an average acceptor lifetime ( $\langle\tau_A\rangle$ ) of 4.04 ns was obtained by fitting the Gaussian curve on the respective population. On addition of a staple strand with ALEXA647 dye (red circle) to the origami along with the staple strand



anchored with ATTO647N fluorophore, as expected, two more lifetime peaks were detected: one belonging to the lifetime of ALEXA647 only labelled origami with  $\langle\tau_A\rangle = 0.99$  ns and one to the average lifetime of the two dyes with  $\langle\tau_A\rangle = 2.61$  ns (Figure 8.2-1b) corresponding to the double labelled molecules. Similarly, addition of two ALEXA647 dyes and three ALEXA647 dyes anchored staple strands along with one staple strand having ATTO647N, shifted the  $\langle\tau_A\rangle$  of the middle peak (2.32 ns and 1.98 ns, respectively) to further left (Figure 8.2-1c and Figure 8.2-1d, respectively). As expected, DNA origami labelled with just the ALEXA647 dye showed an average lifetime  $\langle\tau_A\rangle = 0.92$  ns. In all the cases, relevant number of Gaussian curves (1 for single labelled and 3 for double labelled origami) were fitted to report the average acceptor lifetimes.

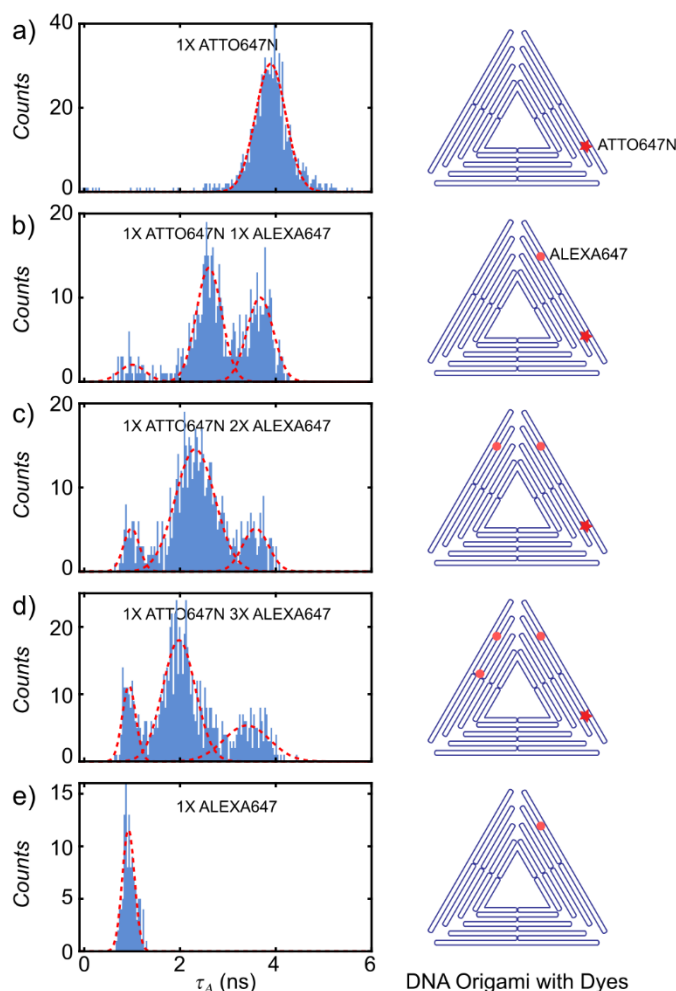


**Figure 8.2-1 - Differently labelled DNA origami are identified by using two acceptor fluorophores with distinguishable lifetimes.** a) Acceptor lifetime ( $\tau_A$ ) histogram of a DNA origami measurement with a staple strand labelled with just the ATTO647N dye was fitted with a Gaussian curve (red dashed line) showing an

average acceptor lifetime ( $\langle\tau_A\rangle$ ) of 4.03 ns. The pictogram of the origami (a triangular blue structure) with one ATTO647N fluorophore (red star) is shown adjacent to the histogram. b) Acceptor lifetime histogram of a DNA origami with one staple strand labelled with the ATTO647N dye and another with ALEXA647 dye (red circle) was fitted with three Gaussian curves showing an average acceptor lifetime ( $\langle\tau_A\rangle$ ) of 0.99 ns, 2.61 ns and 3.68 ns corresponding to ALEXA647 only, both ALEXA647 and ATTO647N and ATTO647N only labelled origami, respectively. c) and d) Acceptor lifetime histogram of a DNA origami with one staple strand labelled with the ATTO647N dye and two and three staple strands with ALEXA647 dye, respectively. The mean lifetime resulting from the DNA origami labelled with more than one ALEXA647 dye shifts the  $\langle\tau_A\rangle$  to the left ( $\langle\tau_A\rangle = 2.32$  ns and 1.98 ns for c and d, respectively). e) Acceptor lifetime histogram of a DNA origami with one staple strand labelled with ALEXA647 dye shows an expected  $\langle\tau_A\rangle = 0.92$  ns.

These results show that it is possible to distinguish a double labelled origami from a single labelled origami just by probing the acceptor lifetimes. While the single labelled molecules with a particular dye show the characteristic lifetime of that dye, a double labelled molecule with the two different fluorophores demonstrate a mean acceptor lifetime based on the number of either dyes present on the molecule.

## 8.2.2 Probing FRET efficiency of the origami coupled DNA rulers.

Indeed, the next step was to couple the DNA origami with a biomolecule labelled with a FRET pair of fluorophores and use the acceptor lifetime parameter to distinguish the coupled from the uncoupled molecules while simultaneously recording the FRET efficiency of the biomolecule. To this end, a simple reaction of biotin-neutravidin binding was used to complex the origami with DNA rulers. Two different kind of DNA rulers (sequence as in Appendix Section 8.3.8) were used: one with a distance of 9 bp between the acceptor (ATTO647N) and donor (ATTO532) fluorophore (will be referred to as 9 bp ruler further on) and one with a gap of 21 bp between the two fluorophores (will be referred to as 21 bp ruler further on). While the former shows a high FRET efficiency peak due to smaller distance between donor and acceptor, the latter shows a low FRET efficiency peak due to larger distance between the two dyes (Figure 8.2-2a). The FRET efficiency ( $E$ ) histograms were obtained upon identification of the single molecule bursts with an inter-photon time of 50  $\mu$ s and at least 75 photons. An additional ALEX-2CDE filter of less than 15 and a Stoichiometry ( $S$ ) filter of  $> 0.25$  and  $< 0.75$  was also applied along with the

correction factors mentioned previously. The pictograms representing each kind of DNA ruler is shown in Figure 8.2-2a.

In order to couple the double labelled DNA rulers with the DNA origami, both the rulers (1X) and the origami (1X) were designed with one strand having a biotin molecule (ordered from biomers). They were both incubated overnight in a solution with 1  $\mu$ M neutravidin, a molecule with four pockets for biotin. In addition to the biotin strand, DNA origami was also prepared with two ALEXA647 dye labelled staple strands, so as to enable isolation of the complexed (origami + ruler) from the uncoupled molecules (origami or ruler). Since the labelling position on the origami was chosen such that the distance between the acceptor on the origami and donor on the ruler was more than 10 nm in case of a coupled molecule, there was no energy transfer possible between these two dyes. This ensured that the FRET efficiency recorded belonged only to the double labelled ruler in consideration. Thus, following the observation from the previous section, while a coupled molecule would show a mean acceptor lifetime of ATTO647N + ALEXA647 dyes, uncoupled molecules would show a mean lifetime of either dyes depending on if it is the ruler (thus ATTO647N) or the origami (thus ALEXA647) being probed in the confocal volume at that instant.

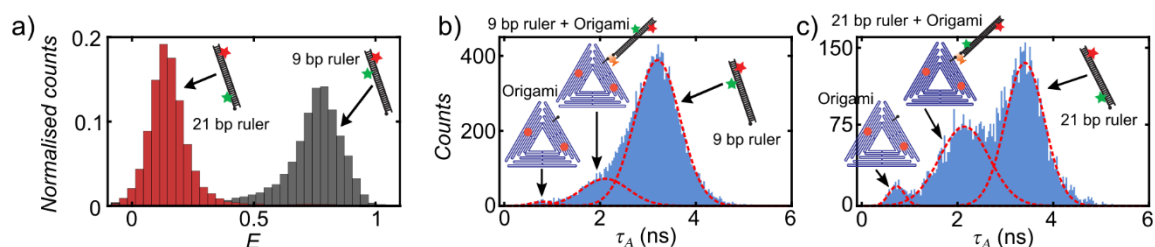


**Figure 8.2-2 - Origami coupled rulers are distinguished from the uncoupled molecules by acceptor lifetime filtering.** a) The FRET efficiency ( $E$ ) histogram of a DNA ruler measurement labelled with donor and acceptor fluorophore at a distance of 9 base pairs (9 bp ruler – grey bars) shows a high FRET efficiency state as compared to the low FRET efficiency population (red bars) of a 21 bp ruler with the two fluorophores situated at a gap of 21 base pairs. b) and c) Acceptor lifetime ( $\tau_A$ ) histogram shows three populations corresponding to ruler only, ruler coupled to origami and origami only species belonging to 9 bp ruler complexed with origami and 21 bp complexed with origami experiments, respectively. Average acceptor lifetimes obtained from the Gaussian curve fitting (red dashed line) for each population is reported in the main text. The pictograms corresponding to each species are shown in the figure, the rulers are showed as ladders with ATTO532 (donor – green star) and ATTO647N (acceptor -red star) dyes. DNA origami is shown as a triangular structure as in the previous figure with two ALEXA dyes (red spheres). The conjugated molecules can be distinguished in the heterogeneous sample by filtering for the particular acceptor lifetimes.

Figure 8.2-2b demonstrates an acceptor lifetime histogram belonging to a measurement of DNA origami complexed with 9 bp ruler. The three possible species (DNA origami only, DNA ruler only and origami complexed DNA ruler) in such an experiment are shown as pictograms in the same figure. While the Gaussian curve of the acceptor lifetime population belonging to an uncoupled origami and ruler showed an  $\langle\tau_A\rangle = 0.82$  ns and 3.20 ns, respectively, as anticipated, the acceptor lifetime peak belonging to a coupled molecule showed a  $\langle\tau_A\rangle = 2.11$  ns (Figure 8.2-2b). Similarly, when a 21 bp DNA ruler was used instead of the 9 bp ruler,  $\langle\tau_A\rangle$  of 0.74 ns, 2.07 ns and 3.45 ns were obtained corresponding to origami only, ruler + origami and ruler only molecules (Figure 8.2-2c).

Due to the apparent difference in the average lifetimes of conjugated and unconjugated molecules, it was possible to quantify the efficiency of conjugation. For this purpose, lifetime filters were applied such that  $-0.1$  ns  $< \tau_A < 1.2$  ns corresponded to the origami only molecules,  $1.2$  ns  $< \tau_A < 3$  ns corresponded to the coupled molecules and  $3$  ns  $< \tau_A < 100$  ns corresponded to the ruler only molecules. It was found that the efficiency of 9 bp ruler - origami coupling was 30 % and 21 bp ruler – origami coupling was 37 %. Moreover, as expected the average burst duration ( $\langle T_b \rangle$ ), an indicator of the residence time of a molecule in confocal volume was found to increase from 2.50 ns to 5.30 ns upon successful conjugation (not shown). This is an important aspect of origami conjugation which will be examined in the next section.

### 8.2.3 Conformational states of DNA hairpin are not perturbed upon coupling to DNA origami

DNA hairpins are simple nucleic acid structures that consist of inverse repeats of single-stranded DNA which is connected by a non-complementary loop region. The opening and closing kinetics of DNA hairpins has been extensively studied by Schlierf group previously (232). As shown in Figure 8.2-3a, depending on the salt condition and the hairpin used (in this with a T21 loop, sequence in Appendix Section 8.3.8), the hairpin could undergo interconversion between the open and closed state on a millisecond timescale. In a smFRET experiment, such millisecond dynamics can be detected by plotting *FRET-2CDE* (Appendix Section 8.3.9) against FRET efficiency, *E*. If a molecule is undergoing structural

interconversion on a millisecond timescale, the FRET efficiency peak corresponding to the dynamic molecules will lie above a FRET-2CDE value of 20. This appears to be the case for the hairpin used in the smFRET experiments in this work at a concentration of 2mM MgCl<sub>2</sub> (and 1 X TAE buffer, pH 8.0). Figure 8.2-3b demonstrates the FRET efficiency ( $E$ ) histogram obtained from the hairpin measurement and Figure 8.2-3c shows the corresponding  $FRET-2CDE$  vs  $E$  plot. The parameters for isolation of single molecule bursts and analysis of FRET efficiency histograms were the same as for the rulers.

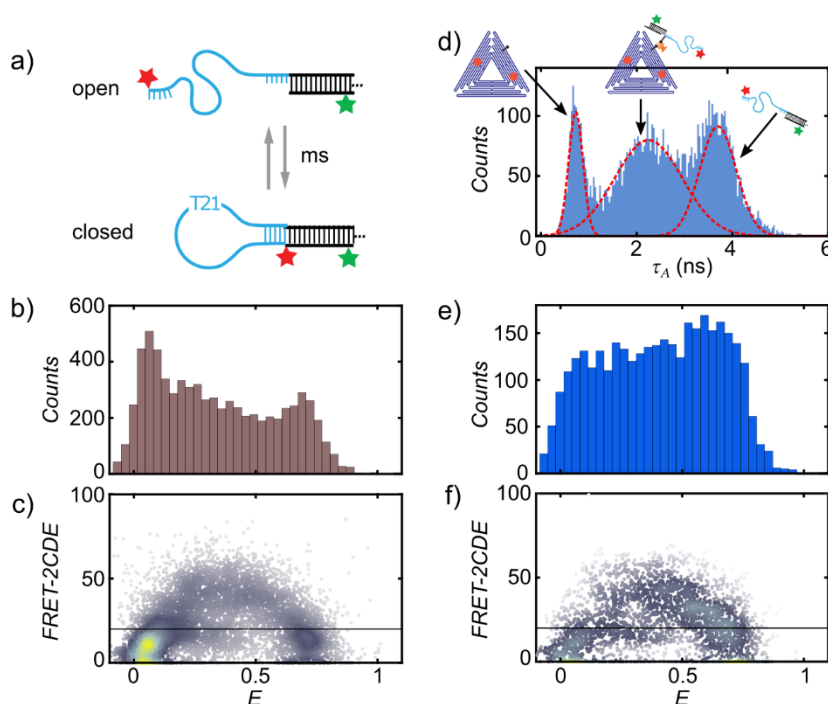


**Figure 8.2-3 - Resolution of DNA hairpin dynamics can be achieved by coupling it to the origami.** a) DNA hairpin (shown with ATTO532 – green star and ATTO647N – red star fluorophores) can interconvert between the open and closed states on a millisecond timescale depending upon the salt concentration. b) The FRET efficiency ( $E$ ) histogram from the hairpin smFRET experiment indicates a third population between the open and closed state. c) This third state appears above the threshold of 20 on a  $FRET-2CDE$  vs  $E$  plot indicating sub-millisecond dynamics between the two populations. d) Acceptor lifetime ( $\tau_A$ ) histogram of the origami complexed hairpin measurement shows three species: origami only (labelled with two ALEXA647 dyes), origami coupled hairpin, and hairpin only. For each species, a pictogram is shown with the respective peak. The red dashed lines indicate the Gaussian fits for each population. e) The FRET efficiency ( $E$ ) histogram of the origami coupled hairpin after filtering for the acceptor lifetime corresponding to the complexed molecules ( $1.2 < \tau_A < 3$  ns). f)  $FRET-2CDE$  vs  $E$  plot for the origami coupled hairpins also show sub-millisecond interconversion between the open and closed states. An increase in the middle state shows the effect of increase in residence time of the coupled molecules.

Due to the fast diffusion of hairpins through confocal volume (because of their small size), it is not possible to resolve the various fast interconverting (<ms) conformations of the hairpin when passing through the confocal volume. To this end, attaching the hairpin to the origami provides an opportunity to increase the effective size of the molecule in focus as increasing its diffusion time enables a better structural resolution of the coupled hairpin molecules. By complexing the hairpin with the origami through an overnight biotin-streptavidin coupling reaction, the dynamics of the coupled molecules were inferred by applying the acceptor lifetime filtering approach by labelling the hairpin with ATTO532 and ATTO647N as the donor and acceptor fluorophore, respectively while the origami was labelled with two ALEXA647 acceptor dyes. SmFRET experiment was then performed with the complexed sample at a concentration of 2 mM MgCl<sub>2</sub> as that was the salt concentration at which hairpin was found to undergo millisecond dynamics. As shown in Figure 8.2-3d with the pictograms corresponding to the species in each population, while the  $\langle\tau_A\rangle$  of origami only and hairpin only molecules was found to be 0.73 ns and 3.70 ns, respectively, the coupled molecules had a  $\langle\tau_A\rangle = 2.25$  ns. On applying the same acceptor filters as in the previous section, a coupling efficiency of 39 % was obtained. Furthermore, as expected an increase in residence time was observed for coupled molecules such that  $\langle T_b \rangle$  increased from 2.81 ns to 5.34 ns for hairpin molecules upon coupling.

Remarkably, an increase in the middle population can be seen among the coupled molecules due to a better resolution of the hairpin dynamics upon slower diffusion. This is evident from both the FRET efficiency ( $E$ ) histogram in Figure 8.2-3e and the  $FRET-2CDE$  vs  $E$  plot in Figure 8.2-3f corresponding to the origami coupled hairpin molecules. Using dynamic two-state PDA (readers are referred to (232) for explanation of the analysis algorithm), the kinetic rates of opening and closing were also obtained for the hairpin and origami coupled hairpin molecules. The  $k_{open}$  (representing kinetic rate of opening) and the  $k_{close}$  (representing kinetic rate of closing) between the open and closed states were found to be  $(0.89 \pm 0.04)$  ms<sup>-1</sup> and  $(0.80 \pm 0.04)$  ms<sup>-1</sup>, respectively for the origami coupled hairpin. The apparent FRET efficiencies from the fitting were:  $E_{open}^* = 0.122 \pm 0.004$  (for the open state) and  $E_{close}^* = 0.749 \pm 0.006$  (for the closed state). The dynamic PDA analysis on the hairpin only measurement resulted in kinetic rates of  $(0.71 \pm 0.01)$  ms<sup>-1</sup> and  $(0.91 \pm 0.02)$  ms<sup>-1</sup>, respectively with  $E_{open}^* = 0.105 \pm 0.001$  and  $E_{close}^* = 0.728 \pm 0.002$ . This demonstrates that origami coupled hairpins slightly favour the open state possibly due to

steric hindrance or salt concentration bias induced by the bulky DNA origami. However, the conformational states of the hairpin remain unaffected in presence of the origami as indicated by the respective FRET efficiencies.

## 8.2.4 Summary

DNA origami promises to be an extremely useful substrate when probing conformation of biomolecules under different controlled conditions during smFRET experiments. In this regard, this chapter provided a robust and clean approach to distinguish origami coupled molecules from the uncoupled molecules. Using DNA hairpin as a dynamic conformational system, it was shown that it is also possible to increase the residence time of the molecules leading to a better resolution of the dynamic states.

*Outlook:* Previous experiments in the group (performed by Xiaoyue Shang) show that such a system can also be used for identification of protein molecules coupled to DNA origami without affecting their conformational states. However, the coupling reactions need to be optimized so as to not only probe the individual proteins but also protein-protein interactions and effects of molecular crowding on DNA origami. Moreover, it is interesting to note that such a tool can also be applied to study other interaction mechanisms where the labelling positions can be ensured to be sufficiently far ( $> 10$  nm).





## Appendix 8.3 Materials and Methods

This appendix chapter provides an account of materials and the detailed protocol for designing double mutant OMPs (OmpX, OmpLA) and double cysteine mutants of SurA. The expression, purification and labelling of OMPs (OmpX and OmpLA) and periplasmic chaperones (Skp and SurA) is also described. Additionally, measurement schemes for OMP unfolding, chaperone complexation and aggregation formation are also explained.

### 8.3.1 Site directed Mutagenesis

Studying conformational changes through smFRET requires that the protein of interest is double labelled with an acceptor and donor fluorophore. Of the many approaches, this thesis used maleimide chemistry based stochastic labelling technique. For this purpose, OMPs and SurA were mutated at various positions so as to introduce the cysteine residue into the protein sequence by either point mutation or extension of the sequence by a cysteine residue. Double mutation of OmpLA to OmpLA<sub>13,85</sub>, OmpLA<sub>125,234</sub> and OmpLA<sub>13,234</sub> was done by Pablo Gracia and that of OmpX<sub>1,149</sub> was done by Mai Quynh Ma in the Schlierf group. During this thesis work, double mutants OmpLA<sub>13,125</sub>, OmpLA<sub>64,187</sub>, SurA<sub>197,435</sub> and SurA<sub>324,435</sub> were created from OmpLA wt and SurA wt plasmids (made previously by Dr. Georg Krainer from Schlierf group), respectively. A general step-by-step protocol for site directed mutagenesis, transformation and test expression is as follows:

1. Designing Sequences: The sequence of interest was obtained from UniProt. For designing mutants, the mutation sites were identified such that the amino acid to be replaced is: on the loop/turn region, preferably a serine/aspartate/lysine and not a part of active domain or involved in the functioning of the protein. A table of all the protein sequences with the corresponding mutations are provided in Table 8.1.
2. Primer for site directed mutagenesis:
  - 2.1. 1x forward and 1x reverse primer were designed according to the following rules:
    - a. Primers were 20-40 nucleotides long.
    - b. Primers had a GC content of 40-60%.
    - c. Primer pairs did not share complementary sequences at the 3' end.
    - d. The melting temperatures had a difference of approx. 3 °C.
    - e. When designing double mutants, both the primers were ensured to be on the same strand.

2.2. The QuickChange Primer Design (<https://www.agilent.com/store/primerDesignProgram.jsp>) website was used for designing primers. Primers were then ordered from Biomers company (biomers.net).

3. Polymerase Chain Reaction (PCR) was then performed with 25  $\mu$ l reaction mix with following concentrations/volumes:

10X reaction buffer	1X - 2.5 $\mu$ l
QuickSolution reagent	1 $\mu$ l
Template plasmid	100 ng (x $\mu$ l)
Primers	100 - 125 ng each (x $\mu$ l)
dNTP mix	1 $\mu$ l
Enzyme blend – should be added last	1 $\mu$ l
ddH <sub>2</sub> O	Added to make up the volume to 25 $\mu$ l

PCR protocol generally used:

Heat lid to 95 °C.

Maintain 95 °C for 2 mins.

Start cycle (30X):

Temp 95 °C for 25''

Temp 55 °C for 35 ''

Temp 65 °C for 3'5''

Close cycle

Maintain 65 °C for 5 mins.

4. After PCR, DNA sample was incubated on ice for 2 mins and then 1  $\mu$ l Dpn1 enzyme was added. The sample was then spin down and incubated at 37 °C for 15 mins.
5. Transformation:
  - i. *E. coli* XL10 ultracompetent cells (from Agilent Technologies) were thawed on ice.
  - ii. 2  $\mu$ l ligated DNA was mixed into 45 ml XL10 cells.
  - iii. The mixture was then placed on ice for 30 mins.
  - iv. Meanwhile SOC medium was incubated on 42 °C water bath.
  - v. Heat shock was done at 42 °C in a water bath for 30 sec.
  - vi. The cells were then incubated on ice for 2 min.
  - vii. 1 ml SOC medium was then added and the cells were grown for at least 1 hour at 37 °C.
  - viii. Max. 500 ml of culture was plated on a LB + Kanamycin plate and incubated overnight at 37 °C.
6. In order to check for successful transformation, a few colonies were picked and used to make 5-10 ml suspension culture overnight in a shaker at 37 °C.
7. Plasmid isolation was performed using the MiniPrep kit in order to send for sequencing: Both reverse and forward T7 Primers were used for sequencing as the insert size was bigger than 800 bp in most cases.

## Materials and Methods

8. The sequence was checked and if correct, the isolated plasmid was transformed into BL21 (DE3) cells according to the protocol above. Glycerol stocks were then made of the correct XL10 and BL21 clones.
9. Test Expression: The 10 ml suspension culture so obtained after transformation was used as preculture. 50 ml LB Medium + Antibiotic (Kanamycin) was inoculated with the preculture till an OD of 0.6-0.8 was reached. Overnight induction of expression was performed with 0.4 mM IPTG at 20 °C. SDS PAGE was then performed to check for the expression of the desired protein.

Protein	Amino acid sequence	Primers used
<b>OmpX wt</b>	ATSTVTGGYAQSDAQGMNKMGGFNLKYREEDNSPLGVIGSFTY TEKSRTASSGDYKNQYYGITAGPAYRINDWASIYGVVGVGYGKF QTTEYPYKHDTSDYGFSGAGLQFNPMENVALDFSYEQSRIRSVD VGTWIAGVGYRF	
<b>OmpX<sub>1,149</sub></b> (A1C, 149C)	<b>C</b> TSTVTGGYAQSDAQGMNKMGGFNLKYREEDNSPLGVIGSFTY TEKSRTASSGDYKNQYYGITAGPAYRINDWASIYGVVGVGYGKF QTTEYPYKHDTSDYGFSGAGLQFNPMENVALDFSYEQSRIRSVD VGTWIAGVGYRF <b>C</b>	*OmpX_A1C: 5'gatccatgggggcacttctactgta actggcgg 3' OmpX_149C 5'gatcctcgagttaacagaagcggtaa ccaacacc 3'
<b>OmpLA wt</b>	QEATVKEVHDAPAVRGSIIANMLQEHDNPFTLYPYDTNYLIYTQTSD LNKEAIASYDWAENARKDEVKFLSLAFPLWRGILGPNSVLGASYT QKSWWQLSNSEESSPFRETNYPQLFLGFATDYRFAGWTLRDVEM GYNHDSNGRSDPTSRSWNRLYTRLMAENGNWLVEVKPWYVVGNT DDNPDITKYMGGYQLKIGYHLGDAVLSAKGQYNWNTGYGGAELG LSYPITKHVRLYTQVYSGYGESLIDYFNQTRVGVGVMMLNDF	
<b>OmpLA<sub>13,85</sub></b> (A13C, N85C)	QEATVKEVHDAP <b>C</b> VRGSIIANMLQEHDNPFTLYPYDTNYLIYTQTSD LNKEAIASYDWAENARKDEVKFLSLAFPLWRGILGP <b>C</b> SVLGASYT QKSWWQLSNSEESSPFRETNYPQLFLGFATDYRFAGWTLRDVEM GYNHDSNGRSDPTSRSWNRLYTRLMAENGNWLVEVKPWYVVGNT DDNPDITKYMGGYQLKIGYHLGDAVLSAKGQYNWNTGYGGAELG LSYPITKHVRLYTQVYSGYGESLIDYFNQTRVGVGVMMLNDF	
<b>OmpLA<sub>13,125</sub></b> (A13C, D125C)	QEATVKEVHDAP <b>C</b> VRGSIIANMLQEHDNPFTLYPYDTNYLIYTQTSD LNKEAIASYDWAENARKDEVKFLSLAFPLWRGILGPNSVLGASYT QKSWWQLSNSEESSPFRETNYPQLFLGFAT <b>C</b> YRFAGWTLRDVEMG YNHDSNGRSDPTSRSWNRLYTRLMAENGNWLVEVKPWYVVGNTD DNPDITKYMGGYQLKIGYHLGDAVLSAKGQYNWNTGYGGAELGL SYPITKHVRLYTQVYSGYGESLIDYFNQTRVGVGVMMLNDF	OmpLA_A13C: 5'ggatcatgacgcgcctatgctgctg gcagtatta3' OmpLA_D125C: 5'gttcctcggtttgccacgtttacaact ttgctgctg3'
<b>OmpLA<sub>64,187</sub></b> (K64C, D187C)	QEATVKEVHDAPAVRGSIIANMLQEHDNPFTLYPYDTNYLIYTQTSD LNKEAIASYDWAENAR <b>C</b> DEVKFLSLAFPLWRGILGPNSVLGASYT QKSWWQLSNSEESSPFRETNYPQLFLGFATDYRFAGWTLRDVEM GYNHDSNGRSDPTSRSWNRLYTRLMAENGNWLVEVKPWYVVGNT DDNP <b>C</b> ITKYMGGYQLKIGYHLGDAVLSAKGQYNWNTGYGGAELG LSYPITKHVRLYTQVYSGYGESLIDYFNQTRVGVGVMMLNDF	OmpLA_K64C: 5'tcaactgaaactttactcatcgcaac gcgcatctccgccagt 3' OmpLA_D187C: 5'gccatataattggatgcacgggta tcgtccgtatc 3'
<b>OmpLA<sub>125,234</sub></b> (D125C, H234C)	QEATVKEVHDAPAVRGSIIANMLQEHDNPFTLYPYDTNYLIYTQTSD LNKEAIASYDWAENARKDEVKFLSLAFPLWRGILGPNSVLGASYT QKSWWQLSNSEESSPFRETNYPQLFLGFAT <b>C</b> YRFAGWTLRDVEMG YNHDSNGRSDPTSRSWNRLYTRLMAENGNWLVEVKPWYVVGNTD	

	DNPDITKYMGGYYQLKIGYHLGDAVLSAKGQYNWNTGYGGAELGL SYPTIKCVRLYTQVYSGYGESLIDYNFNQTRVGVGVMNLDF	
<b>OmpLA</b> <sub>13,234</sub> ( A13C, H234C)	QEATVKEVHDAPCVRGSIIANMLQEHDNPFITYDYDNYLIYTQTS LNKEAIASYDWAENARKDEVKFLSLAFPLWRGILGPNVSLGASYT QKSWWQLSNSEESSPFRETNYPQLFLGFATDYRFAGWTLRDVEM GYNHDSNGRSDPSTRSWNRLYTRLMAENGNWLVEVKPWYVVGNT DDNPDITKYMGGYYQLKIGYHLGDAVLSAKGQYNWNTGYGGAELG LSYPTIKCVRLYTQVYSGYGESLIDYNFNQTRVGVGVMNLDF	
<b>SurA wt</b>	APQVVDKVAADVNNNGVVLESVDGLMQSVKLNAAQARQLPDDA TLRHQIMERLIMDQIILQMGQKMGVKISDEQLDQAIANIAKQNNMT LDQMRSRLAYDGLNYNTYRNQIRKEMIISEVRNNEVRRRITILPQEV ESLAQQVGNQNDASTELNLSHILIPENPTSDQVNEAESQARAIVD QARNGADFGKLAIAHSADQQALNGGQMGWGRIQELPGIFAQALST AKKGDIVGPIRSVGFHILKVNDLRGESKNISVTEVHARHILLKPSPI MTDEQARVKLEQIAADIKSGKTTFAAAAKEFSQDPSANQGGDLG WATPDIFDPAFRDALTRLNKGQMSAPVHSSFGWHLIELLDTRNVDK TDAAQKDRAYRMLMNRKFSEEAASWMQEQRASAYVKILSN	
<b>SurA</b> <sub>197,435</sub> ( S197C, S435C)	APQVVDKVAADVNNNGVVLESVDGLMQSVKLNAAQARQLPDDA TLRHQIMERLIMDQIILQMGQKMGVKISDEQLDQAIANIAKQNNMT LDQMRSRLAYDGLNYNTYRNQIRKEMIISEVRNNEVRRRITILPQEV ESLAQQVGNQNDASTELNLSHILIPENPTCDQVNEAESQARAIVD QARNGADFGKLAIAHSADQQALNGGQMGWGRIQELPGIFAQALST AKKGDIVGPIRSVGFHILKVNDLRGESKNISVTEVHARHILLKPSPI MTDEQARVKLEQIAADIKSGKTTFAAAAKEFSQDPSANQGGDLG WATPDIFDPAFRDALTRLNKGQMSAPVHSSFGWHLIELLDTRNVDK TDAAQKDRAYRMLMNRKFSEEAASWMQEQRASAYVKILCN	SurA_S197C: 5'ccgaaaacccgacctgtgatcaggt gaac3' SurA_S435C: 5'ctacgttaaatcctgtgcaactaac cgagaac3'
<b>SurA</b> <sub>324,435</sub> (S324C, S435C)	APQVVDKVAADVNNNGVVLESVDGLMQSVKLNAAQARQLPDDA TLRHQIMERLIMDQIILQMGQKMGVKISDEQLDQAIANIAKQNNMT LDQMRSRLAYDGLNYNTYRNQIRKEMIISEVRNNEVRRRITILPQEV ESLAQQVGNQNDASTELNLSHILIPENPTSDQVNEAESQARAIVD QARNGADFGKLAIAHSADQQALNGGQMGWGRIQELPGIFAQALST AKKGDIVGPIRSVGFHILKVNDLRGESKNISVTEVHARHILLKPSPI MTDEQARVKLEQIAADIKCGKTTFAAAAKEFSQDPSANQGGDLG WATPDIFDPAFRDALTRLNKGQMSAPVHSSFGWHLIELLDTRNVDK TDAAQKDRAYRMLMNRKFSEEAASWMQEQRASAYVKILCN	SurA_S324C: 5'gattgctgctgatatcaagtgtgtaaa acgacttttgc 3' SurA_S435C: 5'ctacgttaaatcctgtgcaactaac cgagaac 3'
<b>Skp wt</b>	ADKIAIVNMGSLFQVVAQKTGVSNTLENEFKGRASELQRMETDLQA KMKKLQSMKAGSDRTKLEKDVMARQTFAQKAQAFEQDRARRSN EERGLVTRIQTAVKSVANSQDIDLVDANAVAYNSSDVKDITADV LKQVK	

**Table 8.3-1 - Sequences of proteins, single and double cysteine mutants designed used in this work along with the primers** designed during this work are reported in the table. The primers for OmpX<sub>1,149</sub> were made by Mai Quynh Ma. The signal sequences were absent for the proteins and the chaperones had a His tag in addition. The red letters indicate the mutated residue. The unmentioned primers are the ones not designed during this work. In this case, the already transformed OmpLA expressing glycerol stocks of *E. coli* from the Schlierf lab were used.

### 8.3.2 Expression, purification, refolding and labelling of OMPs

OMP<sub>s</sub> were overexpressed in inclusion bodies (IB<sub>s</sub>). After extraction, IB<sub>s</sub> were solubilised with 8M Urea and the purified OMP<sub>s</sub> were then subjected to refolding. Below are the steps followed for large scale expression, purification and refolding of OmpX and OmpLA:

1. Large scale expression:

*Materials:*

LB medium: 50 ml+1 L

Kanamycin: 50 µg/ml

IPTG: 0.4 mM (400 µl from 1M Stock for 1L cell culture)

NaCl: 154 mM

*Method:*

- i. Preculture (PC): 50 mL LB/Kan was inoculated with OMP expressing *E. coli* BL21 cells using an inoculation loop. Overnight incubation at 37 °C was done on a shaker (180 rpm) and OD was recorded.
- ii. 1 L LB/Kan culture was inoculated with the overnight preculture to an OD (600 nm) of 0.1-0.2.
- iii. The main culture (MC) was cultivated at 37°C on a shaker until an OD (600 nm) of 0.6-0.8 was reached. OD was recorded with 500 µl of the culture.
- iv. Gene expression was then induced with 0.4 mM IPTG and the culture was incubated at 37 °C on a shaker for 2-4 hours and then overnight at 20 °C.
- v. OD was again recorded the next day, after which the cells were harvested by centrifuging the cultures for 15 min at 4 °C and 6317g with Beckman Coulter centrifuge.
- vi. The supernatant was discarded and the cells were resuspended in 40 ml 154 mM NaCl.
- vii. The cell-suspension was then transferred into two 50 ml falcons: 20 ml in each (weigh the falcons before use).
- viii. The washed cells were then harvested by centrifugation for 10 min at 4°C and 7197g (max speed, Eppendorf centrifuge). The supernatant was discarded and the wet weight of the cell pellets was recorded (generally between 2-4 g).
- ix. The cell pellets were frozen for future use. (Either at -20 °C for short time periods (approx. 1-3 months) or at -80 °C for longer time periods).
- x. A sample of at least 500 µl was collected at each point so as to check for protein expression through SDS PAGE (Figure 8.3-1a and d for OmpX<sub>1,149</sub> and OmpLA<sub>13,125</sub>, respectively).

2. Purification, solubilisation and refolding:

*Buffers required for cell wt of approx 2.5 g:*

Breakage Buffer (BB) (50 ml): 50 mM Tris, 40 mM EDTA, pH 8.0, 25% (w/v) sucrose

Washing Buffer (WB) (50 ml): 10 mM Tris, 1mM EDTA, pH 8.0

Solubilization Buffer (SB) (50 ml): 8 M Urea, 100 mM Glycine, 20 mM Tris, 2 mM EDTA, pH 8.3

Refolding Buffer (RB): 20 mM Tris, 2 mM EDTA, 0.87 M Urea, 35 mM LDAO, 5 mM TCEP, pH 8.3

### *Cell Breakage:*

- i. Cell pellets were thawed on ice and resuspended in 1:10 (w/v) ice-cold breakage buffer (10 ml/g cell material).
- ii. The cell mass was passed through French Press (EmulsiFlex-C3, Avestin) 2 times at an air pressure of 12000 bar in cold room (4 °C) and B-TCM was collected.
- iii. Brij 25 at 0.1% w/v was mixed after the 2<sup>nd</sup> time and the cell mass was passed three more times.
- iv. A sample of total cell material: TCM was collected.

### *Solubilisation:*

- v. TCM was centrifuged for 45 min at 4 °C and 7000 x g.
- vi. The supernatant was retained and a sample of soluble fraction SF was collected, followed by pellet resuspension in 40 ml washing buffer and of that a sample insoluble fraction IF was collected.
- vii. Next, washed IF was centrifuged for 30 min at 4 °C and 7000 x g and a sample of the supernatant: Washing fraction WF was collected.
- viii. The pellet was then solubilized overnight or for at least 3-4 hours in 20 ml solubilisation buffer overnight at 4 °C on a rotor (vortexing was avoided at this step).
- ix. A sample called solubilised inclusion bodies SIB was collected and the sample was centrifuged for 30-40 min at 4 °C and 7000 x g.
- x. Subsequently, a sample of the supernatant: Soluble fraction II (SF II) containing the denatured/unfolded OMP was collected while the pellet was resuspended in 5 ml SB and a sample of the insoluble fraction (IF II) was collected.

### *Refolding:*

- xi. The total volume of OMP (x ml) was adjusted so as to refold it at an optimal concentration of 0.33 mg/ml.
- xii. The thus calculated unfolded SFII was added to the refolding buffer by rapid drop dilution under stirring (T = 50 °C).
- xiii. The refolding solution was incubated overnight for 16 h at 50 °C under stirring, after which a sample of the possibly refolded OMP was collected.
- xiv. The precipitate formed during the refolding process (RF(P)) was separated from the refolded solution by centrifugation at 4 °C, 7000 x g for at least 15 mins. The supernatant was filtered by syringe filters 0.45 µm (Carl Roth). A sample of which was then collected as RF(F).

SDS PAGE was then run for all the collected samples to check for purification and refolding (Figure 8.3-1a and d for OmpX<sub>1,149</sub> and OmpLA<sub>13,125</sub>, respectively).

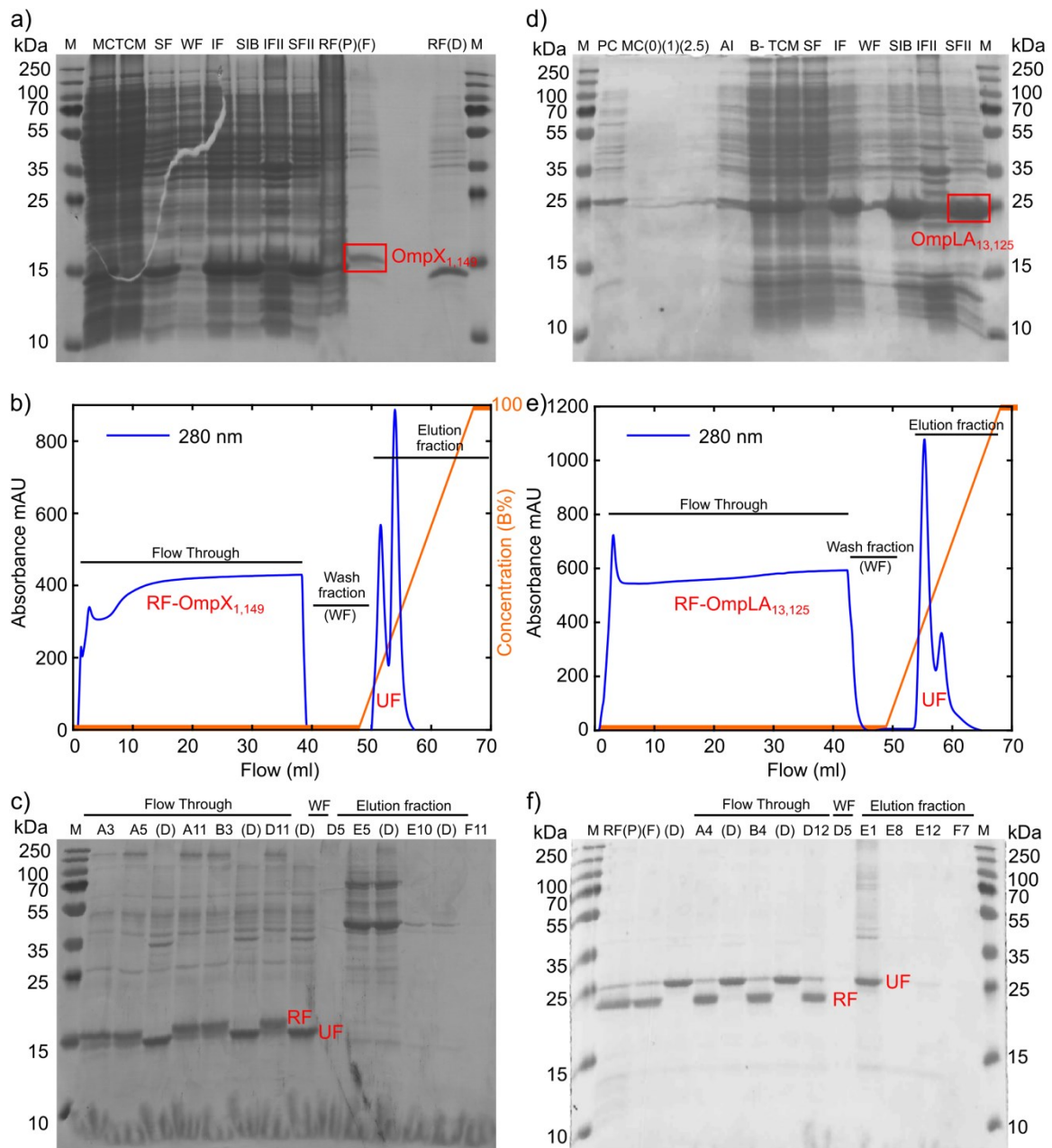


**Figure 8.3-1 - OMP expression and purification.** a) SDS PAGE with OmpX<sub>1,149</sub> expression and purification fractions: M-marker, MC-Main Culture, TCM – Total Cell Mass, SF – Soluble Fraction, WF – Wash Fraction (expression), IF - Insoluble fraction, SIB – Solubilised Inclusion Bodies, IFII – Insoluble Fraction II, RF(P) – Pellet after Refolding, RF(F) – Filtered Refolded OmpX<sub>1,149</sub> and RF(D) – Heat Denatured Refolded OmpX<sub>1,149</sub>. The OmpX fraction (mol wt. 16.4 kDa) can be identified above 15 kDa in the relevant fractions and is shown by the red box in the RF(F) fraction. b) Chromatogram from HiPrep DEAE 1ml anion exchange column run to separate refolded and unfolded fraction – RF-OmpX<sub>1,149</sub> is the refolded OmpX<sub>1,149</sub> eluted in the flow through and UF is the unfolded fraction in the elution fraction shown on a linear gradient of elution buffer (B%) shown with an orange line. The blue line is the absorbance of the protein at 280 nm. c) SDS gel showing the fractions from Flow through, wash fraction (purification) and elution fraction as indicated in the figure. The refolded fraction can be distinguished from the unfolded fraction due to their difference in

migration. d) SDS gel with OmpLA<sub>13,125</sub> expression and purification fractions: M-marker, PC-PreCulture, B-TCM – Total Cell Mass before and after addition of Brij detergent, all the other fractions are like for OmpX<sub>1,149</sub>. The OmpLA<sub>13,125</sub> (mol wt. 30.84 kDa) fraction can be identified around 25 kDa as indicated in the figure. e) Chromatogram from HiPrep DEAE 1ml anion exchange column run – RF-OmpLA<sub>13,125</sub> is the refolded OmpLA<sub>13,125</sub> eluted in the flow through. f) SDS gel showing the fractions from flow through, wash fraction (purification) and elution fraction as indicated. The refolded fraction can be distinguished from the unfolded fraction due to their difference in migration and are indicated on the gel.

### 3. Separation and Labelling of Refolded OMP:

#### *Buffers required for 50 ml RF-F sample:*

Binding Buffer: 20 mM Tris, 35 mM LDAO, 2 mM EDTA, 5mM TCEP; pH 9.5.

Elution Buffer: 20 mM Tris, 35 mM LDAO, 2 mM EDTA, 1.5 M KCl, 5mM TCEP; pH 9.5.

Pre-labelling Buffer: 20 mM Tris, 2 mM EDTA; pH 5

Labelling Buffer: 20 mM Tris, 2mM Tris, 17.5 mM LDAO; pH 7.5

#### *Purification/Separation of RF OMP from UF by weak anion exchange chromatography:*

Column used: DEAE - Sepharose HP 1 ml with ÄKTApurifier and other equipments from GE Healthcare Life Sciences

- i. The column was washed and equilibrated with 20% Ethanol, Water and Binding Buffer with at least 10 CV (10 ml). Meanwhile, the sample was loaded in a 50 ml Superloop.
- ii. The superloop was set up and the prewritten program for 1ml DEAE HP column was started to separate the refolded OMP from the unfolded OMP on a linear gradient. While the flow through contained the refolded OMP, the elution fraction contained the unfolded OMP.
- iii. After the program finished, the column was washed again with elution buffer, water and 20% ethanol.
- iv. Important fractions were collected and SDS PAGE was run to confirm purification of refolded OMP from unfolded OMP. On confirmation, the concentration of refolded OMP (RF) was recorded and when required it was further concentrated with a Vivaspin 500 (10,000 MWCO) spin centrifuge tube from Sartorius. The chromatograms and the gel result for OmpX<sub>1,149</sub> and one of the OmpLA variant (OmpLA<sub>13,125</sub>) are shown in Figure 8.3-1b,c and e,f for OmpX<sub>1,149</sub> and OmpLA<sub>13,125</sub>, respectively.

#### *Labelling reaction of Refolded OMP*

- i. The RF OMP was diluted 1:2 with the Pre-labelling Buffer so as to lower the concentration of LDAO, TCEP and pH to an optimal labelling pH of approx. 7.25-7.5.
- ii. The final volume of the reaction mixture did not exceed 500 µl.
- iii. Accordingly, 20X ATTO532 and 20 XATTO647N (Attotec) or Abberior Star 635P dye (abberior) concentrations were calculated.



- iv. The protein was first labelled with 20X ATTO532 for 2 hours and then 20X ATTO647N was introduced into the above labelling reaction and the mixture was incubated for 2 more hours.

*Free dye separation by Size Exclusion Chromatography (SEC):*

Column: 75/100 300-GE Healthcare Life Sciences

- i. In the meantime, the column was preequilibrated with 20 % ethanol, water and labelling buffer with at least 2CV.
- ii. The reaction sample was injected into the column with a 500 µl Hamilton syringe.
- iii. After the SEC run, the labelled OMP was separated from the free dyes as evident from the chromatogram for OmpX<sub>1,149</sub> and OmpLA<sub>13,125</sub> in Fig. 2a and Fig. 2b, respectively. The concentration of double labelled OMP was measured and concentrated when required with a Vivaspin 500 (10,000 MWCO) spin centrifuge tube from Sartorius. Aliquots were then prepared and stored at 4 °C. The peak values of absorbance at 280 nm (for protein), 532 nm (for Atto532 dye), 647N (for Atto647N dye) and 635P (for Abberior Star 635P) were noted down to reflect upon the labelling efficiencies as in Chapter 3.
- iv. At the end of the run, the column was equilibrated again with the labelling buffer, water and 20% ethanol.

*Labelling reaction of Unfolded OMP:* When labelling unfolded OmpLA, SF II of each variant was directly used. First it was exchanged into a 6M GdmCl containing buffer (20 mM Tris and 150 mM NaCl) and then labelling reaction was done with 20X dyes added together. The labelled OmpLA was then separated from free dyes using SEC as before (Figure 8.3-2).

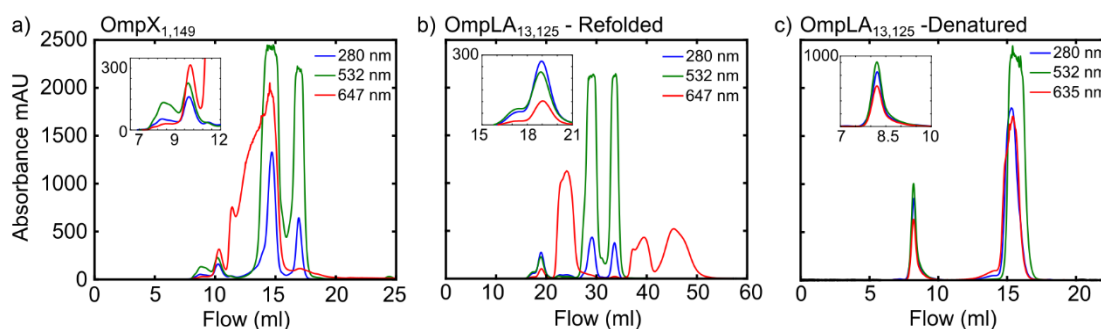


**Figure 8.3-2 - OmpX<sub>1,149</sub> and OmpLA<sub>13,125</sub> (refolded and denatured) labelling.** a) Chromatogram obtained after Size Exclusion Chromatography of the labelled OmpX<sub>1,149</sub>. The inset shows the magnified double labelled OmpX<sub>1,149</sub> fraction. b) Chromatogram obtained after Size Exclusion Chromatography of the labelled OmpLA<sub>13,125</sub>. The inset shows the magnified double labelled OmpLA<sub>13,125</sub> fraction. c) Chromatogram obtained after Size Exclusion Chromatography of the labelled denatured OmpLA<sub>13,125</sub>. The inset shows the magnified double labelled denatured OmpLA<sub>13,125</sub> fraction. The blue, green and red line shows the absorbance

at 280 nm (protein), 532 nm (donor) and 647 or 635 nm (acceptor - as indicated), respectively. The peak positions were noted down from the chromatograms to reflect upon the labelling efficiencies as in Chapter 3.

Note 1: Any variation in the labelling assay as noted in Chapter 3 was adopted at the labelling reaction step while the rest of the steps remained the same.

Note 2: Temperatures below 4 °C denatures the OMP. Thus, long term storage was done at 4 °C to avoid cold denaturation.

Note 3: 5mM TCEP was always included after solubilisation when purifying double cysteine variants.

### 8.3.3 Expression, purification, refolding and labelling of chaperones

A protocol based on the one used by Schiffrin et. al (106) with some modifications was used for both Skp and SurA expression and purification:

#### 1. Large scale expression:

##### *Materials:*

LB medium: 50 ml+1 L

Kanamycin: 50 ug/ml

IPTG: 0.4 mM (400 µl from 1M Stock for 1L cell culture)

##### *Method:*

- i. Preculture: 50 mL LB/Kan was inoculated with *E. coli* BL21 cells using an inoculation loop expressing Skp or SurA.
- ii. After overnight incubation at 37 °C on a shaker (180 rpm), OD was recorded.
- iii. 1 L LB/Kan was inoculated with the overnight preculture to an OD (600 nm) of 0.1-0.2.
- iv. The culture was cultivated at 37°C on a shaker (180 rpm) until an OD (600 nm) of 0.6-0.8 was reached (approx. 3-4 hours). OD was recorded with 500 µl of the culture.
- v. Gene expression was induced with 0.4 mM IPTG and the culture was incubated on a shaker overnight at 20 °C.
- vi. OD was again recorded the next day, after which the cells were harvested by centrifuging the cultures for 15 min at 4 °C and 6317g with Beckman Coulter centrifuge.
- vii. Pellet was resuspended in 50 ml Buffer A, pH 7.2 and complete EDTA free protease inhibitor tablet (Roche). While half of it was stored in -80 °C for long term, the rest was stored at -20 °C for short term.
- viii. SDS PAGE was run for all the samples at each step to check for expression of chaperones (Figure 8.3-3a and c for Skp and SurA, respectively).

### 2. Purification and refolding by dialysis

#### *Buffers:*

Buffer a (pH 7.2): 20 mM Imidazole, 20 mM Tris HCl, and 150 mM NaCl

Buffer B (pH 7.2): 500 mM Imidazole, 20 mM Tris HCl, and 150 mM NaCl

Assembly Buffer (pH 7.2): 150 mM NaCl, 20 mM Tris HCl.

#### *Method:*

- i. When needed, the cell pellet was thawed and passed through EmulsiFlex-C3, Avestin 4 times to break the cells.
- ii. The cell lysate was centrifuged at 4 °C, 18000 x g for 30 mins with Optima™ L-80 XP Ultracentrifuge. The supernatant was retained. While half of it (12.5 ml) was mixed with Buffer A + 6M GdmCl, the rest was stored at -20 °C for later use. The former sample was then rotated for at least 24 hours at 4 °C.
- iii. As the chaperones had a His-tag, they were purified from other proteins using a 5ml His Trap HP column on an ÄKTApurifier system from GE Healthcare Life Sciences.
- iv. The column was preequilibrated with 20% ethanol, water and Buffer A+6M GdmCl and then the sample was introduced with the help of a Superloop (GE Healthcare Life Sciences).
- v. Using Buffer B as the elution buffer, a step gradient of 0-100% was applied with steps at 0,50 and 75 and 100%. The chromatogram shows the typical volume and concentration gradient at which Skp and SurA were eluted (Figure 8.3-3b and d, respectively). SDS gel was run with important fractions to confirm the fraction containing chaperone, it was especially important for Skp as it had no tryptophan and showed little absorption at 280 nm.
- vi. The chaperone containing fractions were pooled and refolded overnight at 4 °C with the assembly buffer using dialysis bags with MWCO of 3.5 kDa (Spectrum Labs). The bag was first equilibrated by soaking in the assembly buffer and the protein was added after. The 200 X v/v buffer was exchanged at least 2 times during the dialysis process. If any precipitation was present, the dialysed sample was centrifuged at 10000 rpm for 15 mins at 4 °C. Refolded chaperone was shock frozen and stored at -80 °C for long term while for short term purposes it was stored at 4 °C.
- vii. Whenever required, the refolded chaperones were thawed and concentrated with Vivaspin 500 (10,000 MWCO) spin centrifuge tube from Sartorius.
- viii. In order to clean them for performing smFRET experiments, the buffer of the sample was exchanged with a cleaner assembly buffer by Micro Bio-Spin 6 columns (Bio-Rad Laboratories, Inc.).
- ix. Due to absence of tryptophan in Skp, it was difficult to obtain the true concentration through absorbance at 280 nm. Therefore, BCA Assay (BCA™ protein Assay Kit by Thermo Scientific) was performed to determine the concentration of Skp after every purification. The protocol was followed according the manual from the company.
- x. Labelling: Labelling (reaction and free dye separation) of double cysteine variants of SurA was done in a manner similar to OMPs (with 20X Atto532 and Abberior Star 635P dyes).

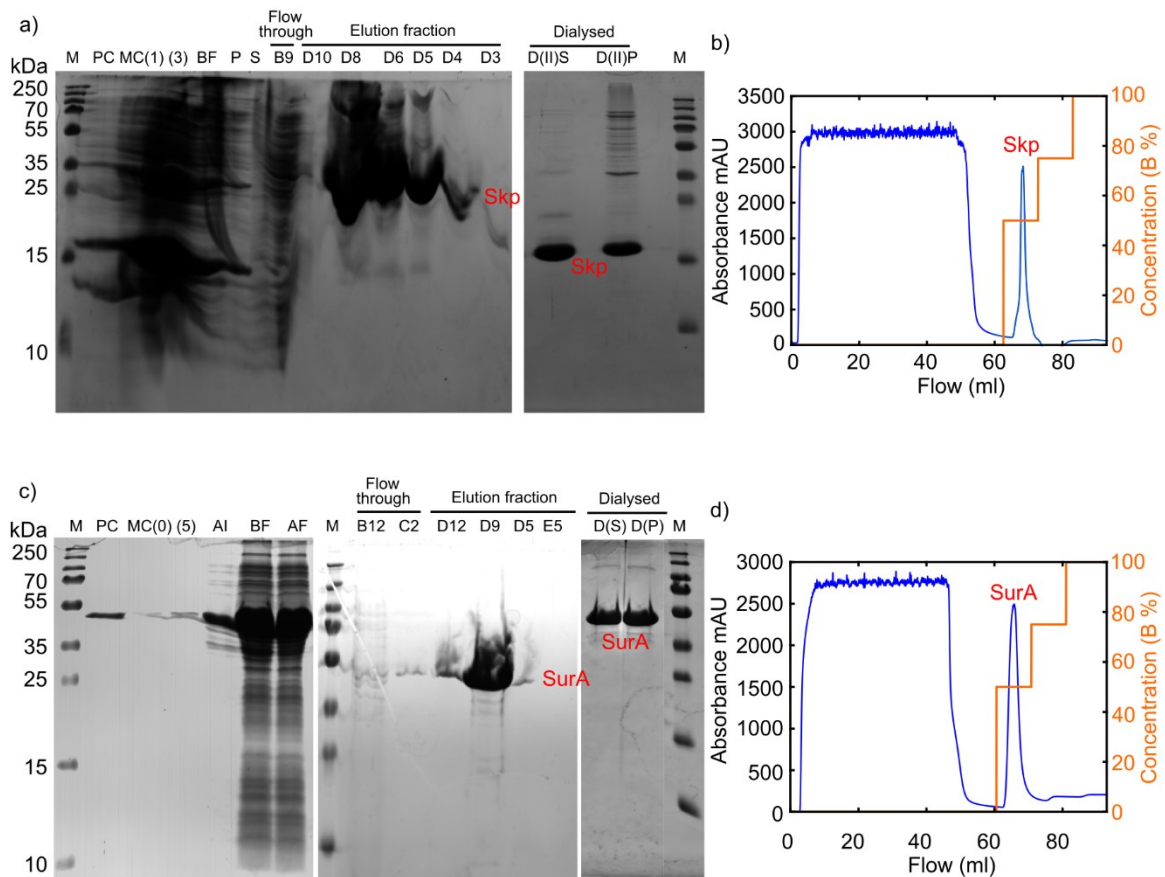


**Figure 8.3-3 - Expression and purification of periplasmic chaperones Skp and SurA.** a) SDS PAGE with samples collected during Skp expression and purification. M-Marker, PC-Preculture, MC(1) – Main Culture after 1 hour, MC(3) – Main Culture after 3 hours, BF – Before French Press, P – Pellet of cell lysate, S – Supernatant of cell lysate, all the other fractions are as indicated in the figure. Due to presence of denaturant (6 M GdmCl) in the His Trap fractions, the gel did not run properly, but a big fraction of Skp can be detected in the elution fraction. The dialysed supernatant fraction (S-Supernatant and P-Pellet) shows presence of purified Skp slightly above 15 kDa. b) Chromatograms from the His Trap HP 5 ml affinity column run to purify Skp from other proteins. The fractions so obtained were then collected and the Skp fractions in the elution fraction were dialysed. The orange line shows the concentration step gradient of the elution buffer (B %) at 0, 50, 75 and 100%. c) SDS PAGE with samples collected during SurA expression and purification. The fraction after induction (AI), AF – After French Press and the dialysed supernatant fraction (S-Supernatant and P-Pellet) shows presence of purified SurA around 55 kDa. d) Chromatograms from the His Trap HP 5 ml affinity column run to purify SurA from other proteins. The fractions so obtained were then collected and the SurA fractions in the elution fraction were dialysed e. The orange line shows the concentration step gradient of the elution buffer (B %) at 0, 50, 75 and 100%.

### 8.3.4 Derivation of correction factor, $\gamma$

The correction factor  $\gamma$ , which accounts for differences in detection efficiency and quantum yield was calculated for every measurement condition (GdmCl concentration or temperature) as mentioned in the main text in case of OMPs labelled with Atto532 and Abberior STAR 635P as the donor and acceptor dyes. The donor and acceptor lifetimes ( $\tau_{D(0)}$  and  $\tau_A$ , respectively) obtained from experiments were used to correct for their quenching and obtain the theoretical  $\gamma$ ,  $\gamma^*$  according to the following equation:

$$\gamma^* = \frac{\tau_A}{\tau_{A,theo}} \frac{\tau_{D(0),theo}}{\tau_{D(0)}} \gamma \quad (24)$$

Here,  $\tau_{A,theo}$  and  $\tau_{D(0),theo}$  are the theoretical lifetimes of acceptor and donor.

### 8.3.5 Probability density analysis (PDA) results of denaturant concentration range with OmpLA variants

A Monte Carlo simulation based two state PDA fitting was performed for the static folded and unfolded states of OmpLA variants to obtain the fraction of molecules in each state.

#### OmpLA<sub>13,125</sub>:

[GdmCl] (M)	$E_u^*$	$E_f^*$	$\sigma_u$ (nm)	$\sigma_f$ (nm)	$p(\text{unfolded})$	$\chi^2$
0	-	0.903 ± 0.001	-	0.453 ± 0.016	-	25.6
1	0.543 ± 0.015	0.899 ± 0.001	0.986 ± 0.044	0.279 ± 0.008	0.282 ± 0.008	7.8
2	0.475 ± 0.010	0.871 ± 0.002	0.852 ± 0.057	0.398 ± 0.012	0.289 ± 0.013	5.0
3	0.416 ± 0.006	0.865 ± 0.002	0.910 ± 0.025	0.396 ± 0.016	0.319 ± 0.013	5.4
3.5	0.411 ± 0.026	0.837 ± 0.006	0.979 ± 0.068	0.362 ± 0.005	0.469 ± 0.039	4.5
4	0.348 ± 0.005	0.867 ± 0.003	0.726 ± 0.022	0.362 ± 0.026	0.676 ± 0.009	3.8
4.5	0.260 ± 0.002	0.722 ± 0.009	0.525 ± 0.018	0.431 ± 0.082	0.909 ± 0.004	1.6
5	0.232 ± 0.002	0.758 ± 0.005	0.611 ± 0.019	0.650 ± 0.053	0.891 ± 0.007	1.8
6	0.180 ± 0.003	0.735 ± 0.017	0.728 ± 0.021	0.746 ± 0.121	0.911 ± 0.010	1.1

#### OmpLA<sub>64,187</sub>:

[GdmCl] (M)	$E_u^*$	$E_f^*$	$\sigma_u$ (nm)	$\sigma_f$ (nm)	$p(\text{unfolded})$	$\chi^2$
0	-	0.832 ± 0.000	-	0.236 ± 0.003	-	12.2
1	0.522 ± 0.015	0.822 ± 0.151	0.968 ± 0.361	0.230 ± 0.317	0.059 ± 0.429	3.2

## Materials and Methods

2	0.573 ± 0.125	0.796 ± 0.067	0.964 ± 0.265	0.963 ± 0.012	0.176 ± 0.217	5.2
3	0.364 ± 0.007	0.756 ± 0.002	0.558 ± 0.029	0.285 ± 0.006	0.383 ± 0.009	2.5
3.5	0.362 ± 0.001	0.757 ± 0.003	0.467 ± 0.012	0.279 ± 0.021	0.845 ± 0.004	3.5
4	0.363 ± 0.001	0.734 ± 0.018	0.441 ± 0.006	0.493 ± 0.041	0.951 ± 0.006	5.4
4.5	0.320 ± 0.002	0.730 ± 0.022	0.549 ± 0.012	0.651 ± 0.163	0.963 ± 0.005	4.7
5	0.266 ± 0.002	0.721 ± 0.030	0.473 ± 0.054	0.468 ± 0.108	0.953 ± 0.010	2.0
6	0.212 ± 0.002	0.724 ± 0.005	0.640 ± 0.029	0.414 ± 0.108	0.950 ± 0.010	7.2

### OmpLA<sub>125,234</sub>:

[GdmCl] (M)	$E_u^*$	$E_f^*$	$\sigma_u$ (nm)	$\sigma_f$ (nm)	$p(\text{unfolded})$	$\chi^2$
0	-	0.815 ± 0.002	-	0.490 ± 0.008	-	15.9
1	0.254 ± 0.030	0.790 ± 0.020	0.585 ± 0.363	0.389 ± 0.072	0.076 ± 0.009	5.0
2	0.389 ± 0.072	0.791 ± 0.003	0.989 ± 0.147	0.317 ± 0.020	0.169 ± 0.033	5.8
3	0.490 ± 0.006	0.783 ± 0.001	0.710 ± 0.030	0.322 ± 0.009	0.156 ± 0.009	2.6
3.5	0.472 ± 0.006	0.775 ± 0.001	0.806 ± 0.030	0.288 ± 0.006	0.261 ± 0.007	2.1
4	0.522 ± 0.021	0.820 ± 0.003	0.831 ± 0.030	0.373 ± 0.017	0.246 ± 0.016	4.0
4.5	0.341 ± 0.003	0.838 ± 0.004	0.577 ± 0.011	0.467 ± 0.026	0.869 ± 0.002	2.5
5	0.268 ± 0.003	0.642 ± 0.033	0.504 ± 0.015	0.618 ± 0.041	0.881 ± 0.016	6.8
6	0.248 ± 0.004	0.714 ± 0.065	0.551 ± 0.043	0.626 ± 0.073	0.920 ± 0.026	2.5

### For OmpLA<sub>13,234</sub>:

[GdmCl] (M)	$E_u^*$	$E_f^*$	$\sigma_u$ (nm)	$\sigma_f$ (nm)	$p(\text{unfolded})$	$\chi^2$
0	-	0.871 ± 0.001	-	0.306 ± 0.005	-	22.7
1	0.484 ± 0.020	0.875 ± 0.001	0.811 ± 0.060	0.371 ± 0.010	0.150 ± 0.011	5.6
2	0.472 ± 0.006	0.870 ± 0.001	0.693 ± 0.010	0.329 ± 0.007	0.302 ± 0.009	4.4
3	0.388 ± 0.009	0.848 ± 0.002	0.817 ± 0.036	0.365 ± 0.002	0.336 ± 0.012	5.2
3.5	0.530 ± 0.029	0.845 ± 0.001	0.832 ± 0.040	0.333 ± 0.026	0.424 ± 0.039	5.8
4	0.309 ± 0.004	0.819 ± 0.007	0.441 ± 0.006	0.566 ± 0.027	0.426 ± 0.022	2.0
4.5	0.270 ± 0.003	0.732 ± 0.016	0.528 ± 0.012	0.531 ± 0.065	0.967 ± 0.004	6.2
5	0.265 ± 0.002	0.733 ± 0.011	0.520 ± 0.032	0.554 ± 0.091	0.965 ± 0.004	3.5
6	0.216 ± 0.002	0.672 ± 0.016	0.631 ± 0.022	0.457 ± 0.072	0.976 ± 0.003	5.4

**Table 8.3-2 - Parameters obtained from PDA fit for all OmpLA variants with a range of GdmCl concentration.** ([GdmCl] reported in Molar):  $E_u^*$  and  $E_f^*$  are the apparent FRET efficiencies of unfolded and folded state,  $\sigma_u$  and  $\sigma_f$  are the distance widths of unfolded and folded states and  $p(\text{unfolded})$  is the probability of unfolded state at a particular GdmCl concentration as reported.

### 8.3.6 Modelling the aqueous and chaperone bound OmpX state heterogeneity

First, the center positions of unbound, Skp- and SurA-bound OmpX distributions were extracted as illustrated in Figure 8.3-4. In a next step, the resulting coordinates were used to analyse the underlying inter-dye distance distribution showing interconversion dynamics on the sub-millisecond timescale. To this end, the inter-dye distance was modelled with a log-normal distribution:

$$P(r) = \frac{1}{\sqrt{2\pi}\sigma_R r} \exp\left(-\frac{(\ln(r) - \mu_R)^2}{2\sigma_R^2}\right) \quad (25)$$

with  $\sqrt{e^{\sigma_R^2}-1}$  being the coefficient of variance, CV, and  $e^{\mu + \frac{1}{2}\sigma_R^2}$  the expected distance of the distribution. A corresponding coordinate of donor lifetime,  $\tau_{D(A)}$ , and FRET efficiency,  $E$ , is then obtained by integration over time and distance, respectively, as described by Soranno et. al. (172). In the global fit, for each variation of  $\sigma_R$ , a dynamic curve was calculated for the range  $\mu_R = \{0.1-20\}$  nm so as to record the Chi-square value. Finally, the most likely width,  $\sigma_R$ , of the log-normal distribution corresponding to the minimal Chi-square were obtained for the unbound, Skp- and SurA-bound states of OmpX.

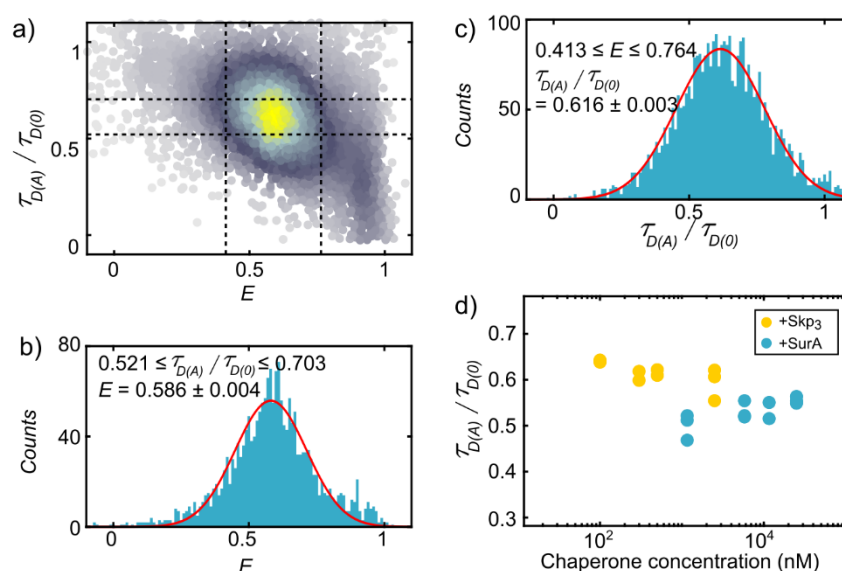


**Figure 8.3-4 - Scheme employed for extraction of center positions of unbound, Skp<sub>3</sub> and SurA bound states of OmpX.** a) 2D plot between relative lifetime of donor ( $\tau_{D(A)}/\tau_{D(0)}$ ) in presence and absence of acceptor vs FRET Efficiency,  $E$  with black dashed lines showing the range of filters applied to get the center position corresponding to b) FRET efficiency,  $E$  and c)  $\tau_{D(A)}/\tau_{D(0)}$  as reported in the respective figures. d) Center

positions of all the Skp<sub>3</sub>- (yellow spheres) and SurA- bound (blue spheres) OmpX at all three temperatures (25 °C, 31 °C and 37 °C). It should be noted that the center positions for chaperone bound species were calculated only for measurements which had a significant fraction of the same (>100 nM [Skp<sub>3</sub>] at 25 °C and 31 °C and >2500 nM [Skp<sub>3</sub>] at 37 °C and >1160 nM [SurA] at all three temperatures except for 11600 nM [SurA] at 25 °C).

### 8.3.7 Calculation of autocorrelation function

For the purpose of quantifying the fraction of OmpX aggregates in the solution, first the diffusion time of OmpX was characterized in absence of Skp and/or SurA, respectively, at low protein concentration (~10pM). To this end, the autocorrelation function ( $G(\tau)$ ) was calculated from the collected acceptor photons (red PIE pulse) of the FRET measurements and fitted by following equation:

$$G(\tau) = \frac{\sum_{i=1}^k (Q_i^2) F_i g_i(\tau)}{N (\sum_{i=1}^k Q_i F_i)^2} \left( 1 + \frac{T}{1-T} \exp\left(-\frac{\tau}{\tau_T}\right) \right) \quad (26)$$

$$\text{where } g_i(\tau) = \left( 1 + \frac{\tau}{\tau_{Di}} \right)^{-1} \left( 1 + \frac{\tau}{\kappa^2 \tau_{Di}} \right)^{\frac{1}{2}}$$

with  $F_i$  and  $\tau_{Di}$  being the fraction and diffusion time of species  $i$ , respectively and  $N$  denotes the average number of molecules in the spot. It should be noted, that a similar triplet state fraction,  $T$ , and characteristic triplet time,  $\tau_T$ , was assumed for both the bound and unbound state. In the presence of chaperones two diffusion components ( $k=2$ ) were used to model the extracted correlation curve. The molecular brightness,  $Q_i$ , of state  $i$  of the corresponding FRET distribution was directly derived from the same measurement by applying a FRET filter. The autocorrelation curves for all the fits are shown in Figure 8.3-5.

The resulting fit parameters together with the molecular brightness and triplet state values are reported in Table 8.3-3. In a next step, the measurements of aggregated OmpX in absence of Skp and/or SurA, respectively, were analysed using the aforementioned parameters. Here the ensemble of aggregated OmpX was summarized with different coexisting size in a single diffusion time. While the correlation curve of ~1  $\mu$ M OmpX without chaperones was fitted with two diffusion components ( $k=2$ ), three diffusion components ( $k=3$ ) were used in the presence of chaperones. In the case where both chaperones were present at the same time only three components were used due to the quite



similar diffusion times of the Skp and SurA bound state. For the error calculation a Jack-knifing approach was employed, where randomly chosen chunks of the photon stream were removed to measure the variance of the extracted fractions.

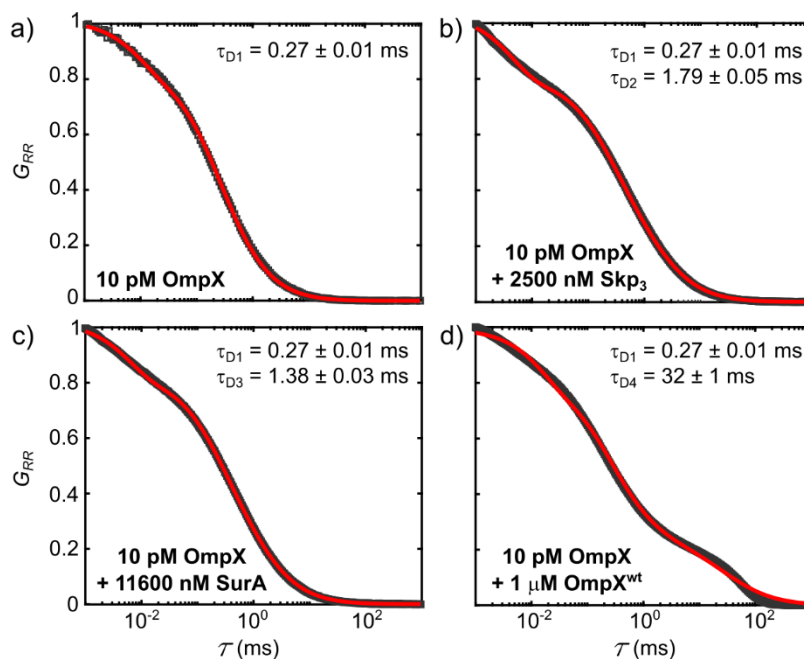


**Figure 8.3-5 - FCS results of aqueous, chaperone bound and aggregated OmpX.** Autocorrelation curve from measurements as indicated to obtain diffusion times ( $\tau_D$ ) corresponding to a) aqueous OmpX ( $\text{OmpX}_{\text{aq}}$ ) with  $\tau_{D1}$ , b) Skp<sub>3</sub> complexed OmpX with  $\tau_{D2}$ , c) SurA complexed OmpX with  $\tau_{D3}$  and aggregated OmpX ( $\text{OmpX}_{\text{Agg}}$ ) with  $\tau_{D4}$ .  $G_{RR}$  is the autocorrelation coefficient corresponding to acceptor photons. The data is shown by the black squares and the fit is shown by the red line.

Measurement	$Q$ (kHz)	$\tau_D$ (ms)	$\tau_T$ ( $\mu$ s)	$T$
<b>OmpX<sub>aq</sub></b>	48.79	$0.27 \pm 0.01$	$9.3 \pm 0.4$	$0.164 \pm 0.003$
<b>OmpX-SurA</b>	52.82 ( $-0.1 < E < 0.75$ )	$1.38 \pm 0.03$	$5.9 \pm 0.1$	$0.191 \pm 0.001$
<b>OmpX- Skp<sub>3</sub></b>	47.85 ( $-0.1 < E < 0.6$ )	$1.79 \pm 0.05$	$4.4 \pm 0.1$	$0.223 \pm 0.001$
<b>OmpX<sub>Agg</sub></b>	52.66	$32 \pm 1$	$1.5 \pm 0.1$	$0.185 \pm 0.001$

**Table 8.3-3 - FCS results** of aqueous OmpX ( $\text{OmpX}_{\text{aq}}$ ) i.e., without chaperones, OmpX in complex with SurA (OmpX-SurA), or Skp<sub>3</sub> (OmpX-Skp<sub>3</sub>) and aggregated OmpX ( $\text{OmpX}_{\text{Agg}}$ ).  $Q$  is the brightness in kHz,  $\tau_D$  the diffusion time in ms,  $\tau_T$  is the characteristic triplet time in  $\mu$ s and  $T$  is the triplet fraction of each state.

### 8.3.8 Sequence of DNA rulers and hairpin

Sequence of 9 bp DNA ruler:

(Biotin)-5'-GCA TCA **X**CC AAG CGA CAC AAA CAG ACA ACC-3'

3'-CGT AGT AGG TTC GC**X** GTG TTT GTC TGT TGG-5'

Sequence of 21 bp DNA ruler:

(Biotin)-5'-GCA TCA **X**CC AAG CGA CAC AAA CAG ACA ACC-3'

3'-CGT AGT AGG TTC GCT GTG TTT GTC TG**X** TGG-5'

Sequence of DNA hairpin:

5'-TAA GTT TGT GAT AGT TTG GAC TGG T**X**T GTG AAG AA-3'

3'-**X**GG TTT TTT TTT TTT TTT TTT TTA ACC A-Biotin-5'

Here **X** is the position of labelling.

### 8.3.9 Calculation of FRET-two-channel kernel-based density distribution (FRET-2CDE) estimator

FRET-2CDE is a score calculated using the donor and acceptor photon arrival times ( $t_{\{D\}}$  and  $t_{\{A\}}$ , respectively) and average FRET efficiency of the burst determined by the photon densities with respect to the donor ( $(E)_D$ ) and acceptor channel ( $(1-E)_A$ ) according to the following relation:

$$FRET-2CDE(t_{\{D\}}, t_{\{A\}}) = 110 - 100 \cdot [(E)_D + (1-E)_A] \quad (27)$$

Further details about all the parameters can be found in (232). If the score is lower than 20, the underlying population is said to be composed of static molecules while that larger than this threshold corresponds to molecules possibly undergoing millisecond interconversion. The arc-shaped distribution due to such fast dynamics is a typical signature of such a population as shown for hairpin in Appendix Section 8.2.3.

## References

1. P. Walter, D. Ron, The Unfolded Protein Response: From Stress Pathway to Homeostatic Regulation. *Science* 334, 1081-1086 (2011).
2. C. L. Klaips, G. G. Jayaraj, F. U. Hartl, Pathways of cellular proteostasis in aging and disease. *J. Cell Biol.* 217, 51–63 (2018).
3. F. U. Hartl, Molecular Chaperones in the Cytosol: from Nascent Chain to Folded Protein. *Science* 295, 1852–1858 (2002).
4. B. Bukau, J. Weissman, A. Horwich, Molecular Chaperones and Protein Quality Control. *Cell* 125, 443–451 (2006).
5. S. Horowitz, P. Koldewey, F. Stull, J. C. Bardwell, Folding while bound to chaperones. *Curr. Opin. Struct. Biol.* 48, 1–5 (2018).
6. H. R. Saibil, Chaperone machines in action. *Curr. Opin. Struct. Biol.* 18, 35–42 (2008).
7. A. Hoffmann, B. Bukau, G. Kramer, Structure and function of the molecular chaperone Trigger Factor. *Biochim. Biophys. Acta BBA - Mol. Cell Res.* 1803, 650–661 (2010).
8. E. M. Clerico, J. M. Tilitzky, W. Meng, L. M. Gierasch, How Hsp70 Molecular Machines Interact with Their Substrates to Mediate Diverse Physiological Functions. *J. Mol. Biol.* 427, 1575–1588 (2015).
9. V. R. Agashe, S. Guha, H. Chang, P. Genevoux, M. Hayer-Hartl, M. Stemp, C. Georgopoulos, F. U. Hartl, and J. M. Barral, Function of Trigger Factor and DnaK in Multidomain Protein Folding: Increase in Yield at the Expense of Folding Speed. *Cell* 117, 199–209 (2004).
10. M. Hayer-Hartl, A. Bracher, F. U. Hartl, The GroEL–GroES Chaperonin Machine: A Nano-Cage for Protein Folding. *Spec. Issue 40 Years TiBS* 41, 62–76 (2016).
11. A. L. Horwich, W. A. Fenton, Chaperonin-mediated protein folding: using a central cavity to kinetically assist polypeptide chain folding. *Q. Rev. Biophys.* 42, 83–116 (2009).
12. A. Sala, P. Bordes, P. Genevoux, Multitasking SecB chaperones in bacteria. *Front. Microbiol.* 5, 666 (2014).
13. P. Bechtluft, N. Nouwen, S. J. Tans, A. J. M. Driessen, SecB—A chaperone dedicated to protein translocation. *Mol BioSyst* 6, 620–627 (2010).
14. J. De Geyter, A. Tsirigotaki, G. Orfanoudaki, V. Zorzini, A. Economou, and S. Karamanou, Protein folding in the cell envelope of Escherichia coli. *Nat. Microbiol.* 1-13, 16107 (2016).
15. J. C. Young, V. R. Agashe, K. Siegers, F. U. Hartl, Pathways of chaperone-mediated protein folding in the cytosol. *Nat. Rev. Mol. Cell Biol.* 5, 781–791 (2004).
16. B. M. Burmann, C. Wang, S. Hiller, Conformation and dynamics of the periplasmic membrane-protein–chaperone complexes OmpX–Skp and tOmpA–Skp. *Nat. Struct. Mol. Biol.* 20, 1265–1272 (2013).
17. S. Hiller, Chaperone-Bound Clients: The Importance of Being Dynamic. *Trends Biochem. Sci.* 44, 517–527 (2019).

18. C. Huang, P. Rossi, T. Saio, C. G. Kalodimos, Structural basis for the antifolding activity of a molecular chaperone. *Nature* 537, 202–206 (2016).
19. W. C. Wimley, The versatile  $\beta$ -barrel membrane protein. *Curr. Opin. Struct. Biol.* 13, 404–411 (2003).
20. G. E. Schulz,  $\beta$ -Barrel membrane proteins. *Curr. Opin. Struct. Biol.* 10, 443–447 (2000).
21. L. M. McMorran, D. J. Brockwell, S. E. Radford, Mechanistic studies of the biogenesis and folding of outer membrane proteins in vitro and in vivo: What have we learned to date? *Arch. Biochem. Biophys.* 564, 265–280 (2014).
22. S. E. Rollauer, M. A. Soreshjani, N. Noinaj, S. K. Buchanan, Outer membrane protein biogenesis in Gram-negative bacteria. *Philos. Trans. R. Soc. B Biol. Sci.* 370, 20150023 (2015).
23. A. M. Plummer, K. G. Fleming, From Chaperones to the Membrane with a BAM! *Trends Biochem. Sci.* 41, 872–882 (2016).
24. S. M. Costello, A. M. Plummer, P. J. Fleming, K. G. Fleming, Dynamic periplasmic chaperone reservoir facilitates biogenesis of outer membrane proteins. *Proc. Natl. Acad. Sci.* 113, E4794–E4800 (2016).
25. T. A. Walton, C. M. Sandoval, C. A. Fowler, A. Pardi, M. C. Sousa, The cavity-chaperone Skp protects its substrate from aggregation but allows independent folding of substrate domains. *Proc. Natl. Acad. Sci.* 106, 1772–1777 (2009).
26. S. W. Lazar, R. Kolter, SurA assists the folding of Escherichia coli outer membrane proteins. *J. Bacteriol.* 178, 1770–1773 (1996).
27. J. G. Sklar, T. Wu, D. Kahne, T. J. Silhavy, Defining the roles of the periplasmic chaperones SurA, Skp, and DegP in Escherichia coli. *Genes Amp Dev.* 21, 2473–2484 (2007).
28. B. Schiffrin, A. N. Calabrese, A. J. Higgins, J. R. Humes, A. E. Ashcroft, A. C. Kalli, D. J. Brockwell, and S. E. Radford, Effects of Periplasmic Chaperones and Membrane Thickness on BamA-Catalyzed Outer-Membrane Protein Folding. *J. Mol. Biol.* 429, 3776–3792 (2017).
29. G. Mas, J. Thoma, S. Hiller, “The Periplasmic Chaperones Skp and SurA” in *Bacterial Cell Walls and Membranes*, A. Kuhn, Ed. Springer International Publishing 169–186 (2019).
30. V. A. Rhodius, W. C. Suh, G. Nonaka, J. West, C. A. Gross, Conserved and Variable Functions of the  $\sigma$ E Stress Response in Related Genomes. *PLoS Biol.* 4, e2 (2005).
31. N. Noinaj, J. C. Gumbart, S. K. Buchanan, The  $\beta$ -barrel assembly machinery in motion. *Nat. Rev. Microbiol.* 15, 197–204 (2017).
32. T. Wu, J. Malinverni, N. Ruiz, S. Kim, T. J. Silhavy, D. Kahne, Identification of a Multicomponent Complex Required for Outer Membrane Biogenesis in Escherichia coli. *Cell* 121, 235–245 (2005).
33. J. Thoma, B. M. Burmann, S. Hiller, D. J. Müller, Impact of holdase chaperones Skp and SurA on the folding of  $\beta$ -barrel outer-membrane proteins. *Nat. Struct. Mol. Biol.* 22, 795–802 (2015).
34. A. N. Calabrese, B. Schiffrin, M. Watson, T.K. Karamanos, M. Walko, J.R. Humes, J.E. Horne, P. White, A.J. Wilson, A.C. Kalli, and R. Tuma, Inter-domain dynamics in the chaperone SurA and multi-site binding to its outer membrane protein clients. *Nat. Commun.* 11(1), 1–16, (2020).
35. G. Li, C. He, P. Bu, H. Bi, S. Pan, R. Sun, X.S. Zhao. Single-Molecule Detection Reveals Different Roles of Skp and SurA as Chaperones. *ACS Chem. Biol.* 13, 1082–1089 (2018).

36. D. C. Marx, A. M. Plummer, A. M. Faustino, T. Devlin, M. A. Roskopf, M. J. Leblanc, H. J. Lessen, B. T. Amann, P. J. Fleming, S. Krueger, S. D. Fried, K. G. Fleming, SurA is a cryptically grooved chaperone that expands unfolded outer membrane proteins. *Proc. Natl. Acad. Sci.* 117, 28026 (2020).
37. G. Mas, S. Hiller, Conformational plasticity of molecular chaperones involved in periplasmic and outer membrane protein folding. *FEMS Microbiol. Lett.* 365 (2018).
38. J. Vogt, G. E. Schulz, The structure of the outer membrane protein OmpX from *Escherichia coli* reveals possible mechanisms of virulence. *Structure* 7, 1301–1309 (1999).
39. N. Dekker, Outer-membrane phospholipase A: known structure, unknown biological function. *Mol. Microbiol.* 35, 711–717 (2000).
40. A. P. Chum, S. R. Shoemaker, P. J. Fleming, K. G. Fleming, Plasticity and transient binding are key ingredients of the periplasmic chaperone network. *Protein Sci.*, 28 (7) 1340-1349. (2019).
41. S. Weiss, Fluorescence Spectroscopy of Single Biomolecules. *Science* 283, 1676–1683 (1999).
42. R. Roy, S. Hohng, T. Ha, A practical guide to single-molecule FRET. *Nat. Methods* 5, 507–516 (2008).
43. T. Ha, Single-Molecule Fluorescence Resonance Energy Transfer. *Methods* 25, 78–86 (2001).
44. T. Ha, T. Enderle, D. F. Ogletree, D. S. Chemla, P. R. Selvin, and S. Weiss, Probing the interaction between two single molecules: fluorescence resonance energy transfer between a single donor and a single acceptor. *Proc. Natl. Acad. Sci.* 93, 6264–6268 (1996).
45. D. Magde, E. Elson, W. W. Webb, Thermodynamic Fluctuations in a Reacting System—Measurement by Fluorescence Correlation Spectroscopy. *Phys. Rev. Lett.* 29, 705–708 (1972).
46. E. Haustein, P. Schwille, Fluorescence Correlation Spectroscopy: Novel Variations of an Established Technique. *Annu. Rev. Biophys. Biomol. Struct.* 36, 151–169 (2007).
47. A. Hartmann, G. Krainer, S. Keller, M. Schlierf, Quantification of Millisecond Protein-Folding Dynamics in Membrane-Mimetic Environments by Single-Molecule Förster Resonance Energy Transfer Spectroscopy. *Anal. Chem.* 87, 11224–11232 (2015).
48. E. M. Hart, A. M. Mitchell, A. Konovalova, M. Grabowicz, J. Sheng, X. Han, F. P. Rodriguez-Rivera, A. G. Schwaid, J. C. Malinverni, C. J. Balibar, S. Bodea, Q. Si, H. Wang, M. F. Homsher, Ronald E. Painter, A. K. Ogawa, H. Sutterlin, T. Roemer, T. A. Black, D. M. Rothman, S. S. Walker, T. J. Silhavy A small-molecule inhibitor of BamA impervious to efflux and the outer membrane permeability barrier. *Proc. Natl. Acad. Sci.* 116, 21748–21757 (2019)
49. Y. Imai, K. J. Meyer, A. Iinishi, Q. Favre-Godal, R. Green, S. Manuse, M. Caboni, M. Mori, S. Niles, M. Ghiglieri, C. Honrao, A new antibiotic selectively kills Gram-negative pathogens. *Nature* 576, 459–464 (2019).
50. A. Luther, *et al.*, Chimeric peptidomimetic antibiotics against Gram-negative bacteria. *Nature* 576, 452–458 (2019).
51. Y. E. Kim, M. S. Hipp, A. Bracher, M. Hayer-Hartl, F. Ulrich Hartl, Molecular Chaperone Functions in Protein Folding and Proteostasis. *Annu. Rev. Biochem.* 82, 323–355 (2013).
52. E. Deuerling, B. Bukau, Chaperone-Assisted Folding of Newly Synthesized Proteins in the Cytosol. *Crit. Rev. Biochem. Mol. Biol.* 39, 261–277 (2004).
53. T. Maier, L. Ferbitz, E. Deuerling, N. Ban, A cradle for new proteins: trigger factor at the ribosome. *Curr. Opin. Struct. Biol.* 15, 204–212 (2005).

54. M. Chiabudini, C. Conz, F. Reckmann, S. Rospert, Ribosome-Associated Complex and Ssb Are Required for Translational Repression Induced by Polylysine Segments within Nascent Chains. *Mol. Cell. Biol.* 32, 4769–4779 (2012).
55. J. Kirstein-Miles, A. Scior, E. Deuerling, R. I. Morimoto, The nascent polypeptide-associated complex is a key regulator of proteostasis. *EMBO J.* 32, 1451–1468 (2013).
56. S. Preissler, E. Deuerling, Ribosome-associated chaperones as key players in proteostasis. *Trends Biochem. Sci.* 37, 274–283 (2012).
57. B. Bukau, E. Deuerling, C. Pfund, E. A. Craig, Getting Newly Synthesized Proteins into Shape. *Cell* 101, 119–122 (2000).
58. F. Merz, A. Hoffmann, A. Rutkowska, B. Zachmann-Brand, B. Bukau, and E. Deuerling, The C-terminal Domain of *Escherichia coli* Trigger Factor Represents the Central Module of Its Chaperone Activity. *J. Biol. Chem.* 281, 31963–31971 (2006).
59. G. Calloni, T. Chen, S. M. Schermann, H.n Chang, P. Genevoux, F. Agostini, G. G. Tartaglia, M. Hayer-Hartl, and F. Ulrich Hartl, DnaK Functions as a Central Hub in the E. coli Chaperone Network. *Cell Rep.* 1, 251–264 (2012).
60. A. Sekhar, R. Rosenzweig, G. Bouvignies, L. E. Kay, Mapping the conformation of a client protein through the Hsp70 functional cycle. *Proc. Natl. Acad. Sci.* 112, 10395 (2015).
61. M. Marcinowski, M. Rosam, C. Seitz, J. Elferich, J. Behnke, C. Bello, M. J. Feige, C. FW Becker, I. Antes, J. Buchner, Conformational Selection in Substrate Recognition by Hsp70 Chaperones. *J. Mol. Biol.* 425, 466–474 (2013).
62. A. Sekhar, R. Rosenzweig, G. Bouvignies, L. E. Kay, Hsp70 biases the folding pathways of client proteins. *Proc. Natl. Acad. Sci.* 113, E2794-801 (2016).
63. D. Balchin, M. Hayer-Hartl, F. U. Hartl, Recent advances in understanding catalysis of protein folding by molecular chaperones. *FEBS Lett.*, 594: 2770-2781. (2020).
64. R. Kellner, H. Hofmann, A. Barducci, B. Wunderlich, D. Nettels, and B. Schuler, Single-molecule spectroscopy reveals chaperone-mediated expansion of substrate protein. *Proc. Natl. Acad. Sci.* 111, 13355–13360 (2014).
65. A. Leitner, L. A. Joachimiak, A. Bracher, L. Mönkemeyer, T. Walzthoeni, B. Chen, S. Pechmann, S. Holmes, Y. Cong, B. Ma, S. Ludtke, The Molecular Architecture of the Eukaryotic Chaperonin TRiC/CCT. *Structure* 20, 814–825 (2012).
66. H. R. Saibil, W. A. Fenton, D. K. Clare, A. L. Horwich, Structure and Allostery of the Chaperonin GroEL. *J. Mol. Biol.* 425, 1476–1487 (2013).
67. F. Motojima, How do chaperonins fold protein? *Biophysics* 11, 93–102 (2015).
68. L. Skjaerven, J. Cuellar, A. Martinez, J. M. Valpuesta, Dynamics, flexibility, and allostery in molecular chaperonins. *FEBS Lett.* 589, 2522–2532 (2015).
69. A. Sirur, R. B. Best, Effects of Interactions with the GroEL Cavity on Protein Folding Rates. *Biophys. J.* 104, 1098–1106 (2013).
70. P. Koldewey, S. Horowitz, J. C. A. Bardwell, Chaperone-client interactions: Non-specificity engenders multifunctionality. *J. Biol. Chem.* 292, 12010–12017 (2017).
71. A. C. Apetri, A. L. Horwich, Chaperonin chamber accelerates protein folding through passive action of preventing aggregation. *Proc. Natl. Acad. Sci.* 105, 17351–17355 (2008).

72. F. Georgescauld, K. Popova, A. J. Gupta, A. Bracher, J. R. Engen, M. Hayer-Hartl, and F. Ulrich Hartl, GroEL/ES Chaperonin Modulates the Mechanism and Accelerates the Rate of TIM-Barrel Domain Folding. *Cell* 157, 922–934 (2014).
73. D. S. Libich, V. Tugarinov, G. M. Clore, Intrinsic unfoldase/foldase activity of the chaperonin GroEL directly demonstrated using multinuclear relaxation-based NMR. *Proc. Natl. Acad. Sci.* 112, 8817–8823 (2015).
74. C. Lee, H. Kim, J. C. A. Bardwell, Electrostatic interactions are important for chaperone–client interaction in vivo. *Microbiology* 164, 992–997 (2018).
75. P. Koldewey, F. Stull, S. Horowitz, R. Martin, J. C. A. Bardwell, Forces Driving Chaperone Action. *Cell* 166, 369–379 (2016).
76. A. Mogk, Identification of thermolabile *Escherichia coli* proteins: prevention and reversion of aggregation by DnaK and ClpB. *EMBO J.* 18, 6934–6949 (1999).
77. S. Wu, X. Ge, Z. Lv, Z. Zhi, Z. Chang, X. S. Zhao, Interaction between bacterial outer membrane proteins and periplasmic quality control factors: a kinetic partitioning mechanism. *Biochem. J.* 438, 505–511 (2011).
78. A. S. Wentink, M. Carroni, C. Nussbaum-Krammer, A. Mogk, N. B. Nillegoda, A. Szlachcic, D. Lys Guilbride, H. R. Saibil, M. P. Mayer, and B. Bukau., Molecular dissection of amyloid disaggregation by human HSP70. *Nature* (2020) <https://doi.org/10.1038/s41586-020-2904-6> (November 16, 2020).
79. K. Wu, F. Stull, C. Lee, J. C. A. Bardwell, Protein folding while chaperone bound is dependent on weak interactions. *Nat. Commun.* 10(1), 1-10 (2019).
80. A. V. Hill, The combinations of haemoglobin with oxygen and with carbon mon-oxide. *Biochemical Journal* 7, 5, 471-480 (1913).
81. H. P. Erickson, Principles of Protein–Protein Association (IOP Publishing, 2019) <https://doi.org/10.1088/2053-2563/ab19ba>.
82. N. Ruiz, D. Kahne, T. J. Silhavy, Advances in understanding bacterial outer-membrane biogenesis. *Nat. Rev. Microbiol.* 4, 57–66 (2006).
83. T. J. Silhavy, D. Kahne, S. Walker, The Bacterial Cell Envelope. *Cold Spring Harb. Perspect. Biol.* 2, a000414 (2010).
84. N. Ruiz, D. Kahne, T. J. Silhavy, Transport of lipopolysaccharide across the cell envelope: the long road of discovery. *Nat. Rev. Microbiol.* 7, 677–683 (2009).
85. D. Missiakas, J.-M. Betton, S. Raina, New components of protein folding in extracytoplasmic compartments of *Escherichia coli* SurA, FkpA and Skp/OmpH. *Mol. Microbiol.* 21, 871–884 (1996).
86. E. R. Green, J. Meccas, Bacterial Secretion Systems: An Overview. *Microbiol. Spectr.* 4 (2016).
87. K. Beck, Discrimination between SRP- and SecA/SecB-dependent substrates involves selective recognition of nascent chains by SRP and trigger factor. *EMBO J.* 19, 134–143 (2000).
88. M. W. Franklin, S. Nepomnyachyi, R. Feehan, N. Ben-Tal, R. Kolodny, and J. S. G. Slusky, Evolutionary pathways of repeat protein topology in bacterial outer membrane proteins. *eLife* 7, e40308 (2018).

89. J. Weirich, C. Bräutigam, M. Mühlenkamp, M. Franz-Wachtel, B. Macek, I. Meuskens, M. Skurnik, K. Leskinen, E. Bohn, I. Autenrieth & M. Schütz Identifying components required for OMP biogenesis as novel targets for anti-infective drugs. *Virulence* 8, 1170–1188 (2017).
90. F. Hagn, M. Etzkorn, T. Raschle, G. Wagner, Optimized Phospholipid Bilayer Nanodiscs Facilitate High-Resolution Structure Determination of Membrane Proteins. *J. Am. Chem. Soc.* 135, 1919–1925 (2013).
91. M. Rangl, L. Rima, J. Klement, A. Miyagi, S. Keller, and S. Scheuring. Real-time Visualization of Phospholipid Degradation by Outer Membrane Phospholipase A using High-Speed Atomic Force Microscopy. *J. Mol. Biol.* 429, 977–986 (2017).
92. H. J. Snijder, B. W. Dijkstra, Bacterial phospholipase A: structure and function of an integral membrane phospholipase. *Biochim. Biophys. Acta BBA - Mol. Cell Biol. Lipids* 1488, 91–101 (2000).
93. H. J. Snijder, I. Ubarretxena-Belandia, M. Blaauw, K. H. Kalk, H. M. Verheij, M. R. Egmond, N. Dekker & B. W. Dijkstra, Structural evidence for dimerization-regulated activation of an integral membrane phospholipase. 401, 717–721 (1999).
94. E. Yamashita, M. V. Zhalnina, S. D. Zakharov, O. Sharma, W. A. Cramer, Crystal structures of the OmpF porin: function in a colicin translocon. *EMBO J.* 27, 2171–2180 (2008).
95. X. Wang, D. Teng, Q. Guan, R. Mao, Y. Hao, X. Wang, J. Yao, and J. Wang, Escherichia coli outer membrane protein F (OmpF): an immunogenic protein induces cross-reactive antibodies against Escherichia coli and Shigella. *AMB Express* 7, 155 (2017).
96. K. H. Kim, S. Aulakh, M. Paetzel, The bacterial outer membrane  $\beta$ -barrel assembly machinery. *Protein Sci.* 21, 751–768 (2012).
97. P. A. Doerner, M. C. Sousa, Extreme Dynamics in the BamA  $\beta$ -Barrel Seam. *Biochemistry* 56, 3142–3149 (2017).
98. L. James, D. Tomasek, T. M. Santos, M. D. May, I. Meuskens, and D. Kahne, Formation of a  $\beta$ -barrel membrane protein is catalyzed by the interior surface of the assembly machine protein BamA. *eLife* 8, e49787 (2019).
99. N. Noinaj, A. J. Kuszak, C. Balusek, J. C. Gumbart, S. K. Buchanan, Lateral Opening and Exit Pore Formation Are Required for BamA Function. *Structure* 22, 1055–1062 (2014).
100. S. Behrens, Periplasmic Chaperones—New Structural and Functional Insights. *Structure* 10, 1469–1471 (2002).
101. F. Stull, J.-M. Betton, J. C. A. Bardwell, Periplasmic Chaperones and Prolyl Isomerases. *EcoSal Plus* 8 (2018).
102. T. A. Walton, M. C. Sousa, Crystal Structure of Skp, a Prefoldin-like Chaperone that Protects Soluble and Membrane Proteins from Aggregation. *Mol. Cell* 15, 367–374 (2004).
103. B. M. Burmann, C. Wang, S. Hiller, Conformation and dynamics of the periplasmic membrane-protein-chaperone complexes OmpX–Skp and tOmpA–Skp. *Nat. Struct. Mol. Biol.* 20, 1265–1272 (2013).
104. D. A. Holdbrook, B. M. Burmann, R. G. Huber, M. V. Petoukhov, D. I. Svergun, S. Hiller, and P.J. Bond, A Spring-Loaded Mechanism Governs the Clamp-like Dynamics of the Skp Chaperone. *Structure* 25, 1079–1088.e3 (2017).



105. J. Qu, C. Mayer, S. Behrens, O. Holst, J. H. Kleinschmidt, The Trimeric Periplasmic Chaperone Skp of *Escherichia coli* Forms 1:1 Complexes with Outer Membrane Proteins via Hydrophobic and Electrostatic Interactions. *J. Mol. Biol.* 374, 91–105 (2007).
106. B. Schiffrin, A. N. Calabrese, P. W. A. Devine, S. A. Harris, A. E. Ashcroft, D. J. Brockwell, and S. E. Radford, Skp is a multivalent chaperone of outer-membrane proteins. *Nat. Struct. Mol. Biol.* 23, 786–793 (2016).
107. B. M. Burmann, D. A. Holdbrook, M. Callon, P. J. Bond, S. Hiller, Revisiting the Interaction between the Chaperone Skp and Lipopolysaccharide. *Biophys. J.* 108, 1516–1526 (2015).
108. C. W. Sandlin, N. R. Zaccai, K. G. Fleming, Skp Trimer Formation Is Insensitive to Salts in the Physiological Range. *Biochemistry* 54, 7059–7062 (2015).
109. G. Mas, B. M. Burmann, T. Sharpe, B. Claudi, D. Bumann, and S. Hiller., Regulation of chaperone function by coupled folding and oligomerization. *Sci. Adv.* 6, eabc5822 (2020).
110. E. Bitto, D. B. McKay, Crystallographic Structure of SurA, a Molecular Chaperone that Facilitates Folding of Outer Membrane Porins. *Structure* 10, 1489–1498 (2002).
111. F. A. Saul, J-P. Arié, B. Vulliez-le Normand, R. Kahn, J-M. Betton, and G. A. Bentley, Structural and Functional Studies of FkpA from *Escherichia coli*, a cis/trans Peptidyl-prolyl Isomerase with Chaperone Activity. *J. Mol. Biol.* 335, 595–608 (2004).
112. T. Krojer, J. Sawa, E. Schäfer, H. R. Saibil, M. Ehrmann, and T. Clausen., Structural basis for the regulated protease and chaperone function of DegP. *Nature* 453, 885–890 (2008).
113. D. Vertommen, N. Ruiz, P. Leverrier, T. J. Silhavy, J.-F. Collet, Characterization of the role of the *Escherichia coli* periplasmic chaperone SurA using differential proteomics. *PROTEOMICS* 9, 2432–2443 (2009).
114. S. S. Justice, D. A. Hunstad, J. R. Harper, A. R. Duguay, J. S. Pinkner, J. Bann, C. Frieden, T. J. Silhavy, and S. J. Hultgren. "Periplasmic peptidyl prolyl cis-trans isomerases are not essential for viability, but SurA is required for pilus biogenesis in *Escherichia coli*. *J. Bacteriol.* 187, 7680 (2005).
115. S. Behrens, The SurA periplasmic PPIase lacking its parvulin domains functions in vivo and has chaperone activity. *EMBO J.* 20, 285–294 (2001).
116. J. R. Humes, B. Schiffrin, A. N. Calabrese, A. J. Higgins, D. R. Westhead, D. J. Brockwell, and S. E. Radford. The Role of SurA PPIase Domains in Preventing Aggregation of the Outer-Membrane Proteins tOmpA and OmpT. *J. Mol. Biol.* 431, 1267–1283 (2019).
117. E. Bitto, D. B. McKay, Binding of phage-display-selected peptides to the periplasmic chaperone protein SurA mimics binding of unfolded outer membrane proteins. *FEBS Lett.* 568, 94–98 (2004).
118. X. Xu, S. Wang, Y.-X. Hu, D. B. McKay, The Periplasmic Bacterial Molecular Chaperone SurA Adapts its Structure to Bind Peptides in Different Conformations to Assert a Sequence Preference for Aromatic Residues. *J. Mol. Biol.* 373, 367–381 (2007).
119. J.-P. Arié, N. Sassoon, J.-M. Betton, Chaperone function of FkpA, a heat shock prolyl isomerase, in the periplasm of *Escherichia coli*. *Mol. Microbiol.* 39, 199–210 (2001).
120. M. Meltzer, S. Hasenbein, P. Hauske, N. Kucz, M. Merdanovic, S. Grau, A. Beil, D. Jones, T. Krojer., T. Clausen, M. Ehrmann, Allosteric Activation of HtrA Protease DegP by Stress Signals during Bacterial Protein Quality Control. *Angew. Chem. Int. Ed.* 47, 1332–1334 (2008).
121. H. Tafer, S. Hiller, C. Hilty, C. Fernández, K. Wüthrich, Nonrandom Structure in the Urea-Unfolded *Escherichia coli* Outer Membrane Protein X (OmpX) †. *Biochemistry* 43, 860–869 (2004).

122. S. Hiller, G. Wider, L. L. Imbach, K. Wüthrich, Interactions with Hydrophobic Clusters in the Urea-Unfolded Membrane Protein OmpX. *Angew. Chem. Int. Ed.* 47, 977–981 (2008).
123. G. Krainer, P. Gracia, E. Frotscher, A. Hartmann, P. Gröger, S. Keller, and M. Schlierf, Slow Interconversion in a Heterogeneous Unfolded-State Ensemble of Outer-Membrane Phospholipase A. *Biophys. J.* 113, 1280–1289 (2017).
124. P. Rath, T. Sharpe, B. Kohl, S. Hiller, Two-State Folding of the Outer Membrane Protein X into a Lipid Bilayer Membrane. *Angew. Chem. Int. Ed.* 58, 2665–2669 (2019).
125. N. K. Burgess, T. P. Dao, A. M. Stanley, K. G. Fleming,  $\beta$ -Barrel Proteins That Reside in the *Escherichia coli* Outer Membrane *in Vivo* Demonstrate Varied Folding Behavior *in Vitro*. *J. Biol. Chem.* 283, 26748–26758 (2008).
126. B. Schiffrin, D. J. Brockwell, S. E. Radford, Outer membrane protein folding from an energy landscape perspective. *BMC Biol.* 15, 123 (2017).
127. J. Qu, S. Behrens-Kneip, O. Holst, J. H. Kleinschmidt, Binding Regions of Outer Membrane Protein A in Complexes with the Periplasmic Chaperone Skp. A Site-Directed Fluorescence Study. *Biochemistry* 48, 4926–4936 (2009).
128. B. M. Burmann, S. Hiller, Solution NMR Studies of Membrane-Protein–Chaperone Complexes. *Chim. Int. J. Chem.* 66, 759–763 (2012).
129. E. Bitto, D. B. McKay, The Periplasmic Molecular Chaperone Protein SurA Binds a Peptide Motif That Is Characteristic of Integral Outer Membrane Proteins. *J. Biol. Chem.* 278, 49316–49322 (2003).
130. L. He, S. Hiller, Frustrated Interfaces Facilitate Dynamic Interactions between Native Client Proteins and Holdase Chaperones. *ChemBioChem* 20, 2803–2806 (2019).
131. G. Krainer, A. Hartmann, A. Anandamurugan, P. Gracia, S. Keller, and M. Schlierf, Ultrafast Protein Folding in Membrane-Mimetic Environments. *J. Mol. Biol.* 430, 554–564 (2018).
132. D. Nettels, I. V. Gopich, A. Hoffmann, B. Schuler, Ultrafast dynamics of protein collapse from single-molecule photon statistics. *Proc. Natl. Acad. Sci.* 104, 2655–2660 (2007).
133. A. Mashaghi, G. Kramer, D. C. Lamb, M. P. Mayer, S. J. Tans, Chaperone Action at the Single-Molecule Level. *Chem. Rev.* 114, 660–676 (2014).
134. Th. Förster, Zwischenmolekulare Energiewanderung und Fluoreszenz. *Ann. Phys.* 437, 55–75 (1948).
135. F. Zosel, A. Holla, B. Schuler, Labeling of proteins for single-molecule fluorescence spectroscopy. 24. *ChemRxiv* (2020)
136. M. Minsky, Microscopy apparatus. US3013467 A, (1961).
137. A. Hoffmann, D. Nettels, J. Clark, A. Borgia, S. E. Radford, J. Clarke, and B. Schuler, Quantifying heterogeneity and conformational dynamics from single molecule FRET of diffusing molecules: recurrence analysis of single particles (RASP). *Phys. Chem. Chem. Phys.* 13, 1857 (2011).
138. A. Hartmann, “Observing Biomolecular Dynamics from Nanoseconds to Hours with Single-Molecule Fluorescence Spectroscopy,” Technische Universität Dresden (2017).
139. V. Kudryavtsev, M. Sikor, S. Kalinin, D. Mokranjac, C. AM Seidel, and D. C. Lamb, Combining MFD and PIE for Accurate Single-Pair Förster Resonance Energy Transfer Measurements. *ChemPhysChem* 13, 1060–1078 (2012).

140. J. Hendrix, D. C. Lamb, “Chapter Nine - Pulsed Interleaved Excitation: Principles and Applications” in *Methods in Enzymology*, S. Y. Tetin, Ed. (Academic Press, 2013), pp. 205–243.
141. D. O’Connor, *Time-correlated single photon counting* (Academic Press, 2012).
142. M. Wahl, Time-Correlated Single Photon Counting. *Tech. Note - PicoQuant*, 1–14, (2014).
143. I. V. Gopich, A. Szabo, Theory of the energy transfer efficiency and fluorescence lifetime distribution in single-molecule FRET. *Proc. Natl. Acad. Sci.* 109, 7747–7752 (2012).
144. S. Kalinin, A. Valeri, M. Antonik, S. Felekyan, C. A. M. Seidel, Detection of Structural Dynamics by FRET: A Photon Distribution and Fluorescence Lifetime Analysis of Systems with Multiple States. *J. Phys. Chem. B* 114, 7983–7995 (2010).
145. M. Ameloot, M. vandeVen, A. U. Acuña, B. Valeur, Fluorescence anisotropy measurements in solution: Methods and reference materials (IUPAC Technical Report). *Pure Appl. Chem.* 85, 589–608 (2013).
146. J. Schaffer, A. Volkmer, C. Eggeling, V. Subramaniam, G. Striker, and C. A. M. Seidel, Identification of Single Molecules in Aqueous Solution by Time-Resolved Fluorescence Anisotropy. *J. Phys. Chem. A* 103, 331–336 (1999).
147. J. Perrin, Mouvement brownien et molécules. *J. Phys. Théorique Appliquée* 9, 5–39 (1910).
148. S. Sindbert, S. Kalinin, H. Nguyen, A. Kienzler, L. Clima, W. Bannwarth, B. Appel, S. Müller, and C. A. M. Seide, Accurate Distance Determination of Nucleic Acids via Förster Resonance Energy Transfer: Implications of Dye Linker Length and Rigidity. *J. Am. Chem. Soc.* 133, 2463–2480 (2011).
149. Y. Kim, S. O. Ho, N. R. Gassman, Y. Korlann, E. V. Landorf, F. R. Collart, and S. Weiss. Efficient Site-Specific Labeling of Proteins via Cysteines. *Bioconjug. Chem.* 19, 786–791 (2008).
150. E. M. Brustad, E. A. Lemke, P. G. Schultz, A. A. Deniz, A General and Efficient Method for the Site-Specific Dual-Labeling of Proteins for Single Molecule Fluorescence Resonance Energy Transfer. *J. Am. Chem. Soc.* 130, 17664–17665 (2008).
151. E. A. Lemke, “Site-Specific Labeling of Proteins for Single-Molecule FRET Measurements Using Genetically Encoded Ketone Functionalities” in *Bioconjugation Protocols*, S. S. Mark, Ed. (Humana Press), 3–15 (2011).
152. M. W.-L. Popp, “Site-Specific Labeling of Proteins via Sortase: Protocols for the Molecular Biologist” in *Site-Specific Protein Labeling*, A. Gautier, M. J. Hinner, Eds. (Springer New York, 2015), pp. 185–198.
153. V. Ratner, E. Kahana, M. Eichler, E. Haas, A General Strategy for Site-Specific Double Labeling of Globular Proteins for Kinetic FRET Studies. *Bioconjug. Chem.* 13, 1163–1170 (2002).
154. T. E. Tomov, Disentangling Subpopulations in Single-Molecule FRET and ALEX Experiments with Photon Distribution Analysis. *Biophys. J.*, 11.
155. D. S.-H. Chan, M. E. Kavanagh, K. J. McLean, A. W. Munro, D. Matak-Vinković, A. G. Coyne, C. Abell, Effect of DMSO on Protein Structure and Interactions Assessed by Collision-Induced Dissociation and Unfolding. *Anal. Chem.* 89, 9976–9983 (2017).
156. T. Arakawa, Y. Kita, S. N. Timasheff, Protein precipitation and denaturation by dimethyl sulfoxide. *Biophys. Chem.* 131, 62–70 (2007).
157. A. Tjernberg, N. Markova, W. J. Griffiths, D. Hallén, DMSO-Related Effects in Protein Characterization. *J. Biomol. Screen.* 11, 131–137 (2006).

158. C. Sánchez-Rico, L. Voith von Voithenberg, L. Warner, D. C. Lamb, M. Sattler, Effects of Fluorophore Attachment on Protein Conformation and Dynamics Studied by spFRET and NMR Spectroscopy. *Chem. - Eur. J.* 23, 14267–14277 (2017).
159. C. Joo, H. Balci, Y. Ishitsuka, C. Buranachai, T. Ha, Advances in Single-Molecule Fluorescence Methods for Molecular Biology. *Annu. Rev. Biochem.* 77, 51–76 (2008).
160. B. Schuler, W. A. Eaton, Protein folding studied by single-molecule FRET. *Curr. Opin. Struct. Biol.* 18, 16–26 (2008).
161. E. Sisamakris, A. Valeri, S. Kalinin, P. J. Rothwell, C. A. M. Seidel, “Accurate Single-Molecule FRET Studies Using Multiparameter Fluorescence Detection” in *Methods in Enzymology*, (Elsevier, 2010), pp. 455–514.
162. W. Humphrey, A. Dalke, K. Schulten, VMD: Visual molecular dynamics. *J. Mol. Graph.* 14, 33–38 (1996).
163. A. Hoffmann, A. Kane, D. Nettels, D. E. Hertzog, P. Baumgärtel, J. Lengefeld, G. Reichardt, D. A. Horsley, R. Seckler, O. Bakajin, B. Schuler, Mapping protein collapse with single-molecule fluorescence and kinetic synchrotron radiation circular dichroism spectroscopy. *Proc. Natl. Acad. Sci.* 104, 105–110 (2007).
164. L. D. Hughes, R. J. Rawle, S. G. Boxer, Choose Your Label Wisely: Water-Soluble Fluorophores Often Interact with Lipid Bilayers. *PLoS ONE* 9, e87649 (2014).
165. K. A. Dill, S. B. Ozkan, M. S. Shell, T. R. Weikel, The Protein Folding Problem. *Annu. Rev. Biophys.* 37, 289–316 (2008).
166. P. Wolynes, J. Onuchic, D. Thirumalai, Navigating the folding routes. *Science* 267, 1619–1620 (1995).
167. A. S̃ali, E. Shakhnovich, M. Karplus, How does a protein fold? *Nature* 369, 248–251 (1994).
168. A. Borgia, W. Zheng, K. Buholzer, M. B. Borgia, A. Schüler, H. Hofmann, A. Soranno, D. Nettels, K. Gast, A. Grishaev, R. B. Best, and B. Schuler, Consistent View of Polypeptide Chain Expansion in Chemical Denaturants from Multiple Experimental Methods. *J. Am. Chem. Soc.* 138, 11714–11726 (2016).
169. M. Aznauryan, L. Delgado, A. Soranno, D. Nettels, J. Huang, A. M. Labhardt, S. Grzesiek, and B. Schuler., Comprehensive structural and dynamical view of an unfolded protein from the combination of single-molecule FRET, NMR, and SAXS. *Proc. Natl. Acad. Sci.* 113, E5389–E5398 (2016).
170. D. Shortle, Persistence of Native-Like Topology in a Denatured Protein in 8 M Urea. *Science* 293, 487–489 (2001).
171. J. Klein-Seetharaman, Long-Range Interactions Within a Nonnative Protein. *Science* 295, 1719–1722 (2002).
172. M. P. Bos, V. Robert, J. Tommassen, Biogenesis of the Gram-Negative Bacterial Outer Membrane. *Annu. Rev. Microbiol.* 61, 191–214 (2007).
173. V. Kräutler, S. Hiller, P. H. Hünenberger, Residual structure in a peptide fragment of the outer membrane protein X under denaturing conditions: a molecular dynamics study. *Eur. Biophys. J.* 39, 1421–1432 (2010).
174. K. K. Andersen, H. Wang, D. E. Otzen, A Kinetic Analysis of the Folding and Unfolding of OmpA in Urea and Guanidinium Chloride: Single and Parallel Pathways. *Biochemistry* 51, 8371–8383 (2012).

175. J. E. Kim, G. Arjara, J. H. Richards, H. B. Gray, J. R. Winkler, Probing Folded and Unfolded States of Outer Membrane Protein A with Steady-State and Time-Resolved Tryptophan Fluorescence. *J. Phys. Chem. B* 110, 17656–17662 (2006).
176. N. K. Burgess, T. P. Dao, A. M. Stanley, K. G. Fleming,  $\beta$ -Barrel Proteins That Reside in the *Escherichia coli* Outer Membrane *in Vivo* Demonstrate Varied Folding Behavior *in Vitro*. *J. Biol. Chem.* 283, 26748–26758 (2008).
177. G.-N. Gomes, C. C. Gradinaru, Insights into the conformations and dynamics of intrinsically disordered proteins using single-molecule fluorescence. *Biophys. Can.* 1865, 1696–1706 (2017).
178. A. Soranno, B. Buchli, D. Nettels, R. R. Cheng, S. Müller-Späth, S. H. Pfeil, A. Hoffmann, Everett A. Lipman, D. E. Makarov, and B. Schuler, Quantifying internal friction in unfolded and intrinsically disordered proteins with single-molecule spectroscopy. *Proc. Natl. Acad. Sci.* 109, 17800–17806 (2012).
179. I. König, A. Zarrine-Afsar, M. Aznauryan, A. Soranno, B. Wunderlich, F. Dingfelder, J. C. Stüber, A. Plückthun, D. Nettels, and B. Schuler, Single-molecule spectroscopy of protein conformational dynamics in live eukaryotic cells. *Nat. Methods* 12, 773–779 (2015).
180. S. R. Maurya, D. Chaturvedi, R. Mahalakshmi, Modulating lipid dynamics and membrane fluidity to drive rapid folding of a transmembrane barrel. *Sci. Rep.* 3, 1989 (2013).
181. E. Sherman, G. Haran, Coil-globule transition in the denatured state of a small protein. *Proc. Natl. Acad. Sci.* 103, 11539–11543 (2006).
182. G. Haran, How, when and why proteins collapse: the relation to folding. *Curr. Opin. Struct. Biol.* 22, 14–20 (2012).
183. B. Schuler, A. Soranno, H. Hofmann, D. Nettels, Single-Molecule FRET Spectroscopy and the Polymer Physics of Unfolded and Intrinsically Disordered Proteins. *Annu. Rev. Biophys.* 45, 207–231 (2016).
184. N. K. Burgess, T. P. Dao, A. M. Stanley, K. G. Fleming,  $\beta$ -Barrel Proteins That Reside in the *Escherichia coli* Outer Membrane *in Vivo* Demonstrate Varied Folding Behavior *in Vitro*. *J. Biol. Chem.* 283, 26748–26758 (2008).
185. D. Chaturvedi, R. Mahalakshmi, Methionine Mutations of Outer Membrane Protein X Influence Structural Stability and Beta-Barrel Unfolding. *PLoS ONE* 8, e79351 (2013).
186. T. Raschle, P. Rios Flores, C. Opitz, D. J. Müller, S. Hiller, Monitoring Backbone Hydrogen-Bond Formation in  $\beta$ -Barrel Membrane Protein Folding. *Angew. Chem. Int. Ed.* 55, 5952–5955 (2016).
187. S. K. McDonald, K. G. Fleming, Negative Charge Neutralization in the Loops and Turns of Outer Membrane Phospholipase A Impacts Folding Hysteresis at Neutral pH. *Biochemistry* 55, 6133–6137 (2016).
188. T. Henry, S. Pommier, L. Journet, A. Bernadac, J. Gorvel, and R. Llobès, Improved methods for producing outer membrane vesicles in Gram-negative bacteria. *Res. Microbiol.* 155, 437–446 (2004).
189. E. V. Kuzmenkina, C. D. Heyes, G. Ulrich Nienhaus, Single-molecule FRET Study of Denaturant Induced Unfolding of RNase H. *J. Mol. Biol.* 357, 313–324 (2006).
190. K. A. Merchant, R. B. Best, J. M. Louis, I. V. Gopich, W. A. Eaton, Characterizing the unfolded states of proteins using single-molecule FRET spectroscopy and molecular simulations. *Proc. Natl. Acad. Sci.* 104, 1528–1533 (2007).

191. B. Schuler, E. A. Lipman, W. A. Eaton, Probing the free-energy surface for protein folding with single-molecule fluorescence spectroscopy. *Nature* 419, 743–747 (2002).
192. L. He, S. Hiller, Common Patterns in Chaperone Interactions with a Native Client Protein. *Angew. Chem. Int. Ed.* 57, 5921–5924 (2018).
193. C. Goemans, K. Denoncin, J.-F. Collet, Folding mechanisms of periplasmic proteins. *Biochim. Biophys. Acta BBA - Mol. Cell Res.* 1843, 1517–1528 (2014).
194. G. Li, C. He, P. Bu, H. Bi, S. Pan, R. Sun, X. S. Zhao, Single-Molecule Detection Reveals Different Roles of Skp and SurA as Chaperones. *ACS Chem. Biol.* 13, 1082–1089 (2018).
195. G. T. Heller, P. Sormanni, M. Vendruscolo, Targeting disordered proteins with small molecules using entropy. *Trends Biochem. Sci.* 40, 491–496 (2015).
196. K. G. Fleming, Energetics of Membrane Protein Folding. *Annu. Rev. Biophys.* 43, 233–255 (2014).
197. C. P. Moon, N. R. Zaccai, P. J. Fleming, D. Gessmann, K. G. Fleming, Membrane protein thermodynamic stability may serve as the energy sink for sorting in the periplasm. *Proc. Natl. Acad. Sci.* 110, 4285–4290 (2013).
198. K. G. Fleming, A combined kinetic push and thermodynamic pull as driving forces for outer membrane protein sorting and folding in bacteria. *Philos. Trans. R. Soc. B Biol. Sci.* 370, 20150026 (2015).
199. R. G. Parra, N. P. Schafer, L. G. Radusky, M. Tsai, A. B. Guzovsky, P. G. Wolynes, and D. U. Ferreira, Protein Frustratometer 2: a tool to localize energetic frustration in protein molecules, now with electrostatics. *Nucleic Acids Res.* 44, W356–W360 (2016).
200. V. Robert, E. B. Volokhina, F. Senf, M. P. Bos, P. Van Gelder, and J. Tommassen, Assembly Factor Omp85 Recognizes Its Outer Membrane Protein Substrates by a Species-Specific C-Terminal Motif. *PLoS Biol.* 4, e377 (2006).
201. S. Kutik, D. Stojanovski, L. Becker, T. Becker, M. Meinecke, V. Krüger, C. Prinz, C. Meisinger, B. Guiard, R. Wagner, N. Pfanner, N. Wiedemann, Dissecting Membrane Insertion of Mitochondrial  $\beta$ -Barrel Proteins. *Cell* 132, 1011–1024 (2008).
202. N. B. Nillegoda, J. Kirstein, A. Szlachcic, M. Berynskyy, A. Stank, F. Stengel, K. Arnsburg, X. Gao, A. Scior, R. Aebersold, D. L. Guilbride, Crucial HSP70 co-chaperone complex unlocks metazoan protein disaggregation. *Nature* 524, 247–251 (2015).
203. M. M. Schneider, S. Gautam, T. W. Herling, E. Andrzejwska, G. Krainer, A. M. Miller, A. Q. Peter, F. S. Ruggeri, M. Vendruscolo, A. Bracher, C.M. Dobson, The Hsc70 Disaggregation Machinery Removes Monomer Units Directly from  $\alpha$ -Synuclein Fibril Ends. *bioRxiv*, 2020.11.02.365825 (2020).
204. L. Paulowski, A. Donoghue, C. Nehls, S. Groth, M. Koistinen, S. O. Hagge, A. Böhling, M. Winterhalter, and T. Gutschmann. The Beauty of Asymmetric Membranes: Reconstitution of the Outer Membrane of Gram-Negative Bacteria. *Front. Cell Dev. Biol.* 8, 586 (2020).
205. B. Wunderlich, D. Nettels, S. Benke, J. Clark, S. Weidner, H. Hofmann, S. H. Pfeil, B. Schuler, Microfluidic mixer designed for performing single-molecule kinetics with confocal detection on timescales from milliseconds to minutes. *Nat. Protoc.* 8, 1459–1474 (2013).
206. M. Urfer, J. Bogdanovic, F. L. Monte, K. Moehle, K. Zerbe, U. Omasits, C. H. Ahrens, G. Pessi, L. Eberl, and J. A. Robinson, A Peptidomimetic Antibiotic Targets Outer Membrane Proteins and Disrupts Selectively the Outer Membrane in *Escherichia coli*. *J. Biol. Chem.* 291, 1921–1932 (2016).

207. G. R. Soltés, J. Schwalm, D. P. Ricci, T. J. Silhavy, The Activity of Escherichia coli Chaperone SurA Is Regulated by Conformational Changes Involving a Parvulin Domain. *J. Bacteriol.* 198, 921–929 (2016).
208. P. W. K. Rothemund, Folding DNA to create nanoscale shapes and patterns. *Nature* 440, 297–302 (2006).
209. S. P. Surwade, F. Zhou, Z. Li, A. Powell, C. O'Donnell and H. Liu, Nanoscale patterning of self-assembled monolayers using DNA nanostructure templates. *Chem. Commun.* 52, 1677–1680 (2016).
210. S. Ramakrishnan, S. Subramaniam, A. F. Stewart, G. Grundmeier, A. Keller, Regular Nanoscale Protein Patterns via Directed Adsorption through Self-Assembled DNA Origami Masks. *ACS Appl. Mater. Interfaces* 8, 31239–31247 (2016).
211. M.-K. Nguyen, V. H. Nguyen, A. K. Natarajan, Y. Huang, J. Ryssy, B. Shen, and A. Kuzyk. Ultrathin Silica Coating of DNA Origami Nanostructures. *Chem. Mater.* 32, 6657–6665 (2020).
212. T. R. Westover, B. R. Aryal, D. R. Ranasinghe, B. Uprety, J. N. Harb, A. T. Woolley, and R. C. Davis, Impact of Polymer-Constrained Annealing on the Properties of DNA Origami-Templated Gold Nanowires. *Langmuir* 36, 6661–6667 (2020).
213. A. C. Pearson, J. Liu, E. Pound, B. Uprety, A. T. Woolley, R. C. Davis, and J. N. Harb, DNA Origami Metallized Site Specifically to Form Electrically Conductive Nanowires. *J. Phys. Chem. B* 116, 10551–10560 (2012).
214. Y. Choi, C. Schmidt, P. Tinnefeld, I. Bald, S. Rödiger, A new reporter design based on DNA origami nanostructures for quantification of short oligonucleotides using microbeads. *Sci. Rep.* 9, 4769 (2019).
215. Y.-X. Zhao, A. Shaw, X. Zeng, E. Benson, A. M. Nystrom, and B. Hogberg, DNA Origami Delivery System for Cancer Therapy with Tunable Release Properties. *ACS Nano* 6, 8684–8691 (2012).
216. M. Cao, Y. Sun, M. Xiao, L. Li, X. Liu, H. Jin, H. Pei, Multivalent Aptamer-modified DNA Origami as Drug Delivery System for Targeted Cancer Therapy. *Chem. Res. Chin. Univ.* 36, 254–260 (2020).
217. N. V. Voigt, T. Tørring, A. Rotaru, M.F. Jacobsen, J. B. Ravnsbæk, R. Subramani, W. Mamdouh, J. Kjems, A. Mokhir, F. Besenbacher and K. V. Gothelf, Single-molecule chemical reactions on DNA origami. *Nat. Nanotechnol.* 5, 200–203 (2010).
218. K. Kramm, T. Schröder, J. Gouge, A. M. Vera, K. Gupta, F. n B. Heiss, T. Liedl, C. Engel, I. Berger, A. Vannini, P. Tinnefeld, D. Grohmann, DNA origami-based single-molecule force spectroscopy elucidates RNA Polymerase III pre-initiation complex stability. *Nat. Commun.* 11, 2828 (2020).
219. M. Endo, H. Sugiyama, Single-Molecule Imaging of Dynamic Motions of Biomolecules in DNA Origami Nanostructures Using High-Speed Atomic Force Microscopy. *Acc. Chem. Res.* 47, 1645–1653 (2014).
220. A. Rajendran, M. Endo, H. Sugiyama, Single-Molecule Analysis Using DNA Origami. *Angew. Chem. Int. Ed.* 51, 874–890 (2012).
221. C. Steinhauer, R. Jungmann, T. Sobey, F. Simmel, P. Tinnefeld, DNA Origami as a Nanoscopic Ruler for Super-Resolution Microscopy. *Angew. Chem. Int. Ed.* 48, 8870–8873 (2009).
222. J. Li, T. S. Deng, X. Liu, J.A. Dolan, N. F. Scherer, P. F. Nealey, Hierarchical Assembly of Plasmonic Nanoparticle Heterodimer Arrays with Tunable Sub-5 nm Nanogaps. *Nano Lett.* 19, 4314–4320 (2019).

223. T. Yamazaki, J. G. Heddle, A. Kuzuya, M. Komiyama, Orthogonal enzyme arrays on a DNA origami scaffold bearing size-tunable wells. *Nanoscale* 6, 9122–9126 (2014).
224. A. Keller, J. Rackwitz, E. Cauët, J. Liévin, T. Körzdörfer, A. Rotaru, K. V. Gothelf, F. Besenbacher, and I. Bald, Sequence dependence of electron-induced DNA strand breakage revealed by DNA nanoarrays. *Sci. Rep.* 4, 7391 (2015).
225. A. Rajendran, M. Endo, K. Hidaka, H. Sugiyama, Direct and Single-Molecule Visualization of the Solution-State Structures of G-Hairpin and G-Triplex Intermediates. *Angew. Chem. Int. Ed.* 53, 4107–4112 (2014).
226. S. Ramakrishnan, G. Krainer, G. Grundmeier, M. Schlierf, A. Keller, Cation-Induced Stabilization and Denaturation of DNA Origami Nanostructures in Urea and Guanidinium Chloride. *Small* 13, 1702100 (2017).
227. S. Ramakrishnan, G. Krainer, G. Grundmeier, M. Schlierf, A. Keller, Structural stability of DNA origami nanostructures in the presence of chaotropic agents. *Nanoscale* 8, 10398–10405 (2016).
228. S. Ramakrishnan, L. Schärfer, K. Hunold, S. Fricke, G. Grundmeier, M. Schlierf, A. Keller, G. Krainer, Enhancing the stability of DNA origami nanostructures: staple strand redesign *versus* enzymatic ligation. *Nanoscale* 11, 16270–16276 (2019).
229. A. Rajendran, M. Endo, Y. Katsuda, K. Hidaka, H. Sugiyama, Photo-Cross-Linking-Assisted Thermal Stability of DNA Origami Structures and Its Application for Higher-Temperature Self-Assembly. *J. Am. Chem. Soc.* 133, 14488–14491 (2011).
230. N. P. Agarwal, M. Matthies, F. N. Gür, K. Osada, T. L. Schmidt, Block Copolymer Micellization as a Protection Strategy for DNA Origami. *Angew. Chem.* 129, 5552–5556 (2017).
231. A. Keller, I. Bald, A. Rotaru, E. Cauët, K. V. Gothelf, and F. Besenbacher, Probing Electron-Induced Bond Cleavage at the Single-Molecule Level Using DNA Origami Templates. *ACS Nano* 6, 4392–4399 (2012).
232. A. Hartmann, G. Krainer, M. Schlierf, Different Fluorophore Labeling Strategies and Designs Affect Millisecond Kinetics of DNA Hairpins. *Molecules* 19, 13735–13754 (2014).



# Acknowledgments

First and foremost, I would like to express my deep and sincere gratitude to Prof. Dr. Michael Schlierf for recruiting me as a PhD student in his group to work on this exciting project. It was your enthusiastic scientific guidance, support and patience that allowed me to grasp working in an experimental laboratory and get accustomed to both biochemistry and biophysics. I greatly appreciate that you enabled me to visit other laboratories to learn protocols, attend and present at many conferences and provided with the independence to pursue and develop ideas. Your constant feedback at different professional levels is much valued.

I would like to thank my thesis advisory and doctoral committee members, Prof. Dr. Stefan Diez and Prof. Dr. Karim Fahmy for their feedback every year, it helped me gain a bigger perspective on the whole project. I am also grateful to Prof. Thorsten Mascher for agreeing to be the head of my doctoral commission.

Accomplishing this thesis would not have been possible without the professional presence of a number of people. I am extremely thankful to Dr. Andreas Hartmann for all the data analysis algorithms, setup construction and alignments and his scientific rigour at demanding junctions of this work. The close collaborations with you have been of great benefit especially regarding OmpX and chaperone experiments. On the same note, I would also like to thank Dr. Georg Krainer, whose ideas, viewpoints and involvement have been of extreme help throughout this work. A special note of thanks also goes to Kristin Hunold and Abhinaya Anandamurugan, who patiently taught me the ways of wet lab and setup usage in the very beginning of PhD. I also thank Prof. Dr. Sandro Keller and Dr. Jessica Klement for hosting and teaching me OmpLA purification. All the supervising experiences I have had with Master students: Mai Qunyh Ma and Xiaoyue Shang have been delightful and in turn taught me a lot, and I am grateful for it. I also thank Andreas, Dr. Anja Buttstedt, Anna Svirina, Mathias Rolf Schenkel and Simon Ollmann for their valuable feedback on the thesis draft.

I express my sincere gratitude to the Dresden International PhD program, DIGS-BB office (Dr. Arantxa Sánchez Fernández, Marleen Franke, Melina Bohla) and the international office (Anja Glenk, Vera Geyer) for their support with getting settled in Dresden in the

beginning, for financial aid at different points of PhD and administrative help with submission of the dissertation.

On a personal note, I would like to extend an immense gratitude to all the people I encountered during this journey. It was the amazing environment of the Schlierf lab and the friends outside that made it a one to cherish. The infectious music and knowledge mania of Anna, Kristin, Mai, Marta, Mathias and Vadim Bogatyr in the wet lab; the many dinner gatherings with heart-warming food by Adeeba Fathima VT; and the long discussions about academia and the world outside with them and other members (including César a. Quintana-Cataño, Mordjane Alissa Boukhet, Melanie Haensel, Simon, Andreas and Georg) of the Schlierf lab made living and working in Dresden a gratifying experience. Likewise, I also thank Alena Uvizl, Dalileh Nabi, Dr. Francesco Vincenzo Reddavide and Stephan Heiden for the refreshing fun times away from the lab.

It was the past guidance and motivation from Dr. Suman Chakrabarty that encouraged me to pursue a PhD here, and I am grateful for the same. I am also thankful to Dr. A Sri Ramya, Dr. Amit Kumawat, Dr. Harini Swaminathan, Pravesh Parekh, Saumya Bhagat, Shilpi Verma, Shruti Chandra, Dr. Sneha Menon and Sudhanshu Gupta who have been of great comfort, support and influence during the many years before PhD and now.

The close company of Andreas in the last few years has been endearing and of huge creative inspiration. I cannot thank you enough for your continuous support (especially so for the last few months) and the joy and affection you brought into my life. Finally, I express eternal gratitude to my family back in India. To my father: who never stopped believing in me and despite his absence has always been present. To my brother: Nikhil, who with his generous heart and understanding kept me free from any burden or worries related to home. To my amma: to who I owe so much, and without who I would not have made it this far.

# Declaration

## **Declaration according to §5.5 of the doctorate regulations**

I herewith declare that I have produced this thesis without the prohibited assistance of third parties and without making use of aids other than those specified; notions taken over directly or indirectly from other sources have been identified as such. This paper has not previously been presented in identical or similar form to any other German or foreign examination board.

The thesis work was conducted from 12.11.2016 to 19.11.2020 under the supervision of Prof. Dr. Michael Schlierf, B CUBE - Center for Molecular Bioengineering, Technische Universität Dresden.

I declare that I have not undertaken any previous unsuccessful doctorate proceedings.

I declare that I recognize the doctorate regulations of the Bereich für Mathematik und Naturwissenschaften of the Technische Universität Dresden.

---

*Date, Place*

*Signature*

## **Erklärung entsprechend §5.5 der Promotionsordnung**

Hiermit versichere ich, dass ich die vorliegende Arbeit ohne unzulässige Hilfe Dritter und ohne Benutzung anderer als der angegebenen Hilfsmittel angefertigt habe; die aus fremden Quellen direkt oder indirekt übernommenen Gedanken sind als solche kenntlich gemacht. Die Arbeit wurde bisher weder im Inland noch im Ausland in gleicher oder ähnlicher Form einer anderen Prüfungsbehörde vorgelegt.

Die Dissertation wurde im Zeitraum vom 12.11.2016 bis 19.11.2020 verfasst und von Prof. Dr. Michael Schlierf, B CUBE - Center for Molecular Bioengineering, Technische Universität Dresden, betreut.

Meine Person betreffend erkläre ich hiermit, dass keine früheren erfolglosen Promotionsverfahren stattgefunden haben.

Ich erkenne die Promotionsordnung des Bereiches für Mathematik und Naturwissenschaften, Technische Universität Dresden an.

---

*Datum, Ort*

*Unterschrift*